THE UNIVERSITY *of* EDINBURGH

One-Dimensional and Two-Dimensional Green-Naghdi Equation Solvers for Shallow Flow over Uniform and non-Uniform Beds

Mohammad Reza Jalali

A thesis submitted for the degree of

Doctor of Philosophy

The University of Edinburgh

2016

Abstract

Numerical simulation of wave behaviour in shallow and deep water is often a key aspect of ocean, coastal, and river hydrodynamic studies. This thesis derives nonlinear one- and two-dimensional level I Green-Naghdi (GN) equations that model the motions of free surface waves in shallow water over non-uniform bed topography. By assuming fitted velocity profiles through the depth, GN equations are simpler than Boussinesq equations, while retaining the wave dispersion property. Implicit matrix solvers are used to solve the spatially discretised 1D and 2D GN equations, with a 4^{th} order Runge Kutta scheme used for time integration. To verify the developed numerical solvers of 1D GN equations, a series of simulations are undertaken for standard benchmark tests including sloshing in a tank and solitary wave propagation over a flat bed. In all cases, grid convergence tests were conducted. In the sloshing test, both numerical schemes and the analytical solution were in complete agreement for small-amplitude free surface motions. At larger values of initial sloshing amplitude, the nonlinear effects caused the free surface waves to steepen, and eventually the numerical simulations became unstable. This could be resolved in future using a shock-capturing scheme. Excellent agreement was achieved between the numerical predictions and analytical solution for solitary waves propagating.

The 2D GN equation solver was then verified for the benchmark tests of Gaussian hump sloshing and solitary wave propagation in closed basin. The predicted free surface motions for Gaussian hump sloshing were in good agreement with linear Fourier analytical solutions for a certain initial period, after which nonlinear effects started to dominate the numerical solution. A reversibility check was undertaken. Nonlinear effects were investigated by increasing the amplitude of the hump, and applying harmonic separation (by comparison against slosh predictions for a corresponding Gaussian trough). It was found that the even harmonic components provided a useful indication of the nonlinear behaviour of the 2D GN equations. 2D GN simulations of a 0.6 m amplitude solitary wave propagation in 1 m deep water over a flat, horizontal bed confirmed that nonlinear interaction was correctly modelled, when the solitary wave hit a solid wall and its runup reached 2.36 m which was 0.36m more than the linear analytical solution and almost identical to a second order solution.

Acknowledgments

Having had the great opportunity to be a research student of Professor Alistair Borthwick for 3 years, I would like to express my respect and gratitude to him for his thoughtful advice as well as financial support. During my study in Ireland and Scotland, he was not only my true friend, but also the greatest supervisor a PhD student can have. He nourished me with his unique knowledge like a gardener who waters and grows his flowers. He gave me confidence to fly in the vast skies of science and knowledge on my own. Due to his experience and expertise in coastal engineering and numerical modeling, I never feared, even for a moment, to face a major, unsolvable technical problem in my research. Undoubtedly, we made a wonderful team together. I believe he is a national treasure for his country. His kindness and friendship will always remain in my mind, since his humanity really captured my heart and soul. It is my honor to be his student. Last but not least, I would like to thank my parents. My mother and father were always supportive of me in different stages of my life, and they are my role model. As their son I hope I can follow their footsteps as a fantastic academic member and I wish to make them proud. It is my great honor to dedicate this thesis to my knowledgeable supervisor, my lovely mother, and my supportive father.

Declaration

I confirm that the present thesis is based on my PhD researches under the supervision of Professor Alistair Borthwick. All the simulations and results are obtained by means of the developed numerical and analytical models. This thesis is prepared for degree of Doctor of Philosophy from University of Edinburgh.

Mohammad Reza Jalali 27 July 2016

1D and 2D Green-Naghdi equations for sloshing in shallow basins

(Paper accepted in journal of Engineering and Computational Mechanics)

Mohammad Reza Jalali, BSc, MSc
PhD candidate, Institute for Energy Systems, The University of Edinburgh, Edinburgh, UK
(Corresponding author: reza.jalali@ed.ac.uk)

Alistair Borthwick, PhD, DSc, CEng, FICE, FREng, FRSE
Professor, Institute for Energy Systems, The University of Edinburgh, Edinburgh, UK

This paper presents a verified model of weakly nonlinear wave sloshing in shallow basins, based on Level I Green-Naghdi (GN) mass and momentum equations derived for mild-sloped beds. The model is verified for sloshing of an initially sinusoidal free surface perturbation in a square tank with a horizontal bed. The model is also used to investigate free surface sloshing of an initial Gaussian hump in closed square basins, over horizontal and non-uniform bed topographies. Analysis of the free surface slosh motions demonstrates that the model gives predictions in satisfactory agreement with the analytical solution obtained by [Lamb H. (1916) *Hydrodynamics*. 4th Ed., Cambridge University Press, Cambridge, UK] from linearised shallow water theory. Discrepancies between the GN predictions and the linear analytical solutions arise from the effect of wave nonlinearities arising from the wave amplitude itself and wave-wave interactions.

1. Introduction

Slosh motions occur in the liquid ballast tanks of ships, LNG tankers, and containers subject to seismic excitation. The response of the liquid free surface depends on the amplitude of the initial disturbance and the natural frequencies of motion, and involves complex fluid-structure interactions (Ibrahim, 2005). In practice, civil engineers may use sloshing tests to assess the likelihood of such phenomena occurring in oil tanks, elevated water towers, and in reservoirs. The earliest theories of progressive and sloshing waves were developed by Airy (1841) and Stokes (1847, 1880), and which were based on potential theory idealisations. Airy's theory was linear, so that it was strictly derived for waves of zero amplitude. Stokes extended the theory to deal with waves of finite amplitude, and he obtained series solutions that were later computed to high order by many hydrodynamicists in the late 20thC (Sarpkaya and Isaacson, 1981). To extend to more realistic domains, computational methods have become widely used. These include: (1) boundary element and finite element potential flow solvers; (2) CFD – Navier-Stokes solvers with volume of fluid treatment of the free surface, Navier-Stokes solvers with level-set treatment of the free surface, Navier-Stokes solvers with mappings of the free surface; and (3) smoothed-particle-hydrodynamics. The above- mentioned 3D computational methods undergo inherently high computational expense, therefore, considerable effort has gone into depth-averaged approaches being cheaper to compute and yet capturing much of the physics. Examples of such approaches include Shallow Water Equations (SWEs) (see e.g. Lamb 1879), and more recently Green-Naghdi (GN) equations (1974). Nonlinear SWEs are the depth-averaged form of continuity and Navier-Stokes momentum equations. Since SWEs neglect vertical motions and the consequent hydrostatic pressure, these equations are usually restricted to long wave behaviour. Thus, SWEs is limited to shallow depth (surf zone) of the ocean (Bonneton et al., 2011 and Nadiga et al., 1996). Green and Naghdi (1976) pioneered the development of nonlinear equations for two-dimensional incompressible inviscid fluid sheets. Green

and Naghdi proposed a theory of fluid sheets known as (GN theory) to model the two dimensional continuum of unsteady inviscid three-dimensional flows. The theory facilitated prediction of unsteady, non-periodic, free surface flows. GN theory utilises some aspects of perturbation analysis in building up first-, second-, and higher-order approximations (called **levels**) to layer-averaged mass and momentum equations. According to Webster and Shields (1991) the GN approach assumes a particular flow kinematic structure in the vertical direction for shallow water problems. The fluid velocity profile is a finite sum of coefficients depending on space and time multiplied by a weighting function. GN fluid sheet theory reduces the dimensions from three to two, yielding equations that can be solved efficiently so that no scale is introduced and no term is deleted (Webster and Shields, 1991). Nevertheless, the lowest level of GN theory permits the kinematic boundary conditions to be satisfied. There are two types of GN theory: restricted and unrestricted. The former successfully models irrotational shallow water flow field. Restricted GN theory was derived from the first level of the direct theory by means of a constrained director (Shields and Webster, 1988). Later, this procedure was extended to the k^{th} level theory (Demirbilek and Webster, 1992). In other words, in a restricted GN theory, the k components of the two-dimensional velocity components are constrained. Demirbilek and Webster (1992) developed an unrestricted version of GN theory of shallow water by enforcing conservation of mass and momentum in the vertical direction and implementing exact boundary conditions. They demonstrated that GN theory can appropriately predict the behaviour of nonlinear numerical wave tank. According to Webster and Shields (1991), Green-Naghdi (GN) sheet theory is placed between classical perturbation methods and pure numerical schemes. Webster and Shields note that for classical perturbation methods, there is usually no evidence that the assumed series is convergent. However, in certain flow problems, such as two-dimensional water waves in both shallow and deep water addressed by GN theory, there is ample evidence of convergence. There is another difference between classical perturbation methods and GN theory. The former exactly satisfies field equation but partially satisfy boundary conditions. Thus, the classical perturbation methods show inconsistencies, while GN theory is self-consistent since the boundary conditions are exactly satisfied, when the field equations are partially approximated. With regard to Coastal Engineering, the present GN model is merely applicable to the shallow depth (before the surf zone) and the intermediate depth of ocean (Jalali, 2016). GN levels higher than I can be used for the deep water ocean (Webster and Shields (1991)). The present paper describes the application of 2D and 1D level I GN equations (according to Jalali, 2016) to free surface sloshing in closed square basins, with horizontal and non-uniform bed topographies. Sections 2 and 3 present the derivation of governing equations. Section 4, 5 and 6 outline the numerical implementation. Section 7 presents the results for initial sinusoidal and Gaussian free surface perturbations. Section 8 is the summary of the main findings.

2. Derivation of continuity equation of level I GN equation

In a 3D Cartesian system, the classical mass conservation equation is applied to drive GN continuity equation:

1. $$\frac{\partial u}{\partial x}+\frac{\partial v}{\partial y}+\frac{\partial w}{\partial z}=0$$

In which u, v, w are the velocity components in the *x, y, z* directions. In present derivation of GN Eqns the total depth, h, is $h = h_0 + \zeta$. Here h_0 is the still water depth and ζ is the free surface elevation above still water level. The elevation of free surface above the fixed horizontal datum, η, is $\eta = h + z_b$. Here, z_b is the bed elevation above a fixed horizontal datum.

The kinematic bed and free surface boundary condition are as follows:

2. $$d\big|_b = \frac{\partial z_b}{\partial t} + u\frac{\partial z_b}{\partial x} + v\frac{\partial z_b}{\partial y}$$

3. $$d\big|_s = \frac{\partial \eta}{\partial t} + u\frac{\partial \eta}{\partial x} + v\frac{\partial \eta}{\partial y}$$

where $d\big|_b$ is kinematic bed boundary condition and $d\big|_s$ is kinematic free surface boundary condition. In order to derive the GN continuity equation, it is assumed that the velocity vector, $\boldsymbol{V}$, can be written as follows:

4. $$\boldsymbol{V}(x,y,z,t) = \sum_{n=0}^{e} \overrightarrow{W_n}(x,y,t)\,\lambda_n(z)$$

where $\overrightarrow{W_n} = (u_n, v_n, w_n)$ is a vector of velocity component approximations at level n, $\lambda_n$are assumed shape functions depending on z-direction, and e is the level of approximation of GN theory. Expansion of Eqn. (4) for level I gives the following velocity parameters:

5. $$\begin{aligned} u(x,y,z,t) &= u_0(x,y,t) \\ v(x,y,z,t) &= v_0(x,y,t) \\ w(x,y,z,t) &= w_0(x,y,t) + w_1(x,y,z,t)\,(z - z_b) \end{aligned}$$

In which:

$\lambda_{0\,x} = \lambda_{0\,y} = \lambda_{0\,z} = 1$, $\lambda_{1\,x} = \lambda_{1\,y} = \lambda_{1\,z} = (z - z_b)$

and

$u_1(x,y,t) = v_1(x,y,t) = 0$ (for more details see Demirbilek and Webster, 1992)

By applying Eqn. (5) in Eqn. (1), (2) values of w_1 and w_0 are obtained:

6. $$w_1 = -\left(\frac{\partial u_0}{\partial x} + \frac{\partial v_0}{\partial y}\right)$$

7. $$w_0 = \frac{\partial z_b}{\partial t} + u_0\frac{\partial z_b}{\partial x} + v_0\frac{\partial z_b}{\partial y}$$

By using Eqn. (5) in Eqn. (3) and replacing Eqn. (6) and (7) into the resulted Eqn, the 2D level I GN continuity Eqn is derived:

8. $$\frac{\partial h}{\partial t} + \frac{\partial u_0 h}{\partial x} + \frac{\partial v_0 h}{\partial y} = 0$$

in which h is the total depth, and (u_0, v_0) are horizontal velocity components at a particular point (x,y) and time t.

3. Derivation of *x*-direction momentum of level I GN equation

The general momentum conservation equation expanded in the x-directions is as follows:

9. $$\frac{\partial \rho u}{\partial t} + \frac{\partial \rho u u}{\partial x} + \frac{\partial \rho u v}{\partial y} + \frac{\partial \rho u w}{\partial z} = -\frac{\partial P}{\partial x}$$

in which ρ is water density. Depth integration of Eqn. (9), then using the chain rule for fourth term and applying the Leibnitz Rule for right hand side term yields:

$$10.\quad \int_{z_b}^{\eta}\frac{\partial \rho u}{\partial t}\lambda_n dz+\int_{z_b}^{\eta}\frac{\partial \rho v}{\partial t}\lambda_n dz+\rho uw\lambda_n\Big|_{z_b}^{\eta}-\int_{z_b}^{\eta}\rho uw\lambda_n' dz=-\frac{\partial P_n}{\partial x}+\hat{P}\frac{\partial \eta}{\partial x}\lambda_n\big|_{\eta}-\bar{P}\frac{\partial z_b}{\partial x}\lambda_n\big|_{z_b}$$

where $P_n=\frac{\partial\left(\int_{z_b}^{\eta}P\lambda_n dz\right)}{\partial x}$, $\hat{P}$ is pressure at the free surface (here $\hat{P}=0$), and $\bar{P}$ is pressure at the bottom. Applying Eqn. (4) for Eqn. (10)

$$11.\quad \sum_{m=0}^{e=1}\rho\frac{\partial u_m}{\partial t}y_{mn}+\sum_{m=0}^{e=1}\sum_{r=0}^{e=1}\rho\frac{\partial u_m u_r}{\partial x}y_{mrn}+\sum_{m=0}^{e=1}\sum_{r=0}^{e=1}\rho\frac{\partial u_m v_r}{\partial y}y_{mrn}+\sum_{m=0}^{e=1}\sum_{r=0}^{e=1}\rho u_m w_r\,\lambda_m\lambda_r\lambda_n\Big|_{z_b}^{\eta}$$

$$-\sum_{m=0}^{e=1}\sum_{r=0}^{e=1}\rho u_m w_r\,y_{mr}^{n}=-\frac{\partial P_n}{\partial x}+\hat{P}\frac{\partial \eta}{\partial x}\lambda_n\big|_{\eta}-\bar{P}\frac{\partial z_b}{\partial x}\lambda_n\big|_{z_b}$$

where $y_{mn}=\int_{z_b}^{\eta}\lambda_m\lambda_n\,dz$, $y_{mrn}=\int_{z_b}^{\eta}\lambda_m\lambda_r\lambda_n\,dz$

and $y_{mr}^{n}=\int_{z_b}^{\eta}\lambda_m\lambda_r\lambda_n'\,dz$ (for more details see chapter 2 of PhD thesis by Jalali, 2016 and chapter 4 of PhD thesis by Haniffah, 2013).

Applying Eqn. (4) in Eqn. (1) and using the Krylov-Kantorovich method for third term of the obtained Eqn result:

$$12.\quad \sum_{r=0}^{e=1}\frac{\partial u_r}{\partial x}\lambda_r+\sum_{r=0}^{e=1}\frac{\partial v_r}{\partial y}\lambda_r+\sum_{r=0}^{e=1}w_r\lambda_n'=0$$

Here, the index *n* changes to *r* in Eqn. (4). By summing over *m*, then applying depth integrating Eqn. (12) becomes:

$$13.\quad \sum_{m=0}^{e=1}\sum_{r=0}^{e=1}\frac{\partial u_r}{\partial x}y_{mnr}=-\sum_{m=0}^{e=1}\sum_{r=0}^{e=1}\frac{\partial v_r}{\partial y}y_{mrn}-\sum_{m=0}^{e=1}\sum_{r=0}^{e=1}w_r\,y_{mn}^{r}$$

By inserting Eqn. (13) in Eqn. (11) and implementing the chain rule for the second and third terms of Eqn. (11), the constrained *x*-direction momentum equation of level I GN Eqn is derived:

$$14.\quad \sum_{m=0}^{e=1}\rho\frac{\partial u_m}{\partial t}y_{mn}+\sum_{m=0}^{e=1}\sum_{r=0}^{e=1}\rho\frac{\partial u_m}{\partial x}u_r\,y_{mrn}+\sum_{m=0}^{e=1}\sum_{r=0}^{e=1}\rho\frac{\partial u_m}{\partial y}v_r\,y_{mrn}+\sum_{m=0}^{e=1}\sum_{r=0}^{e=1}\rho u_m w_r\,y_{nr}^{m}$$
$$=-\frac{\partial P_n}{\partial x}-\bar{P}\frac{\partial z_b}{\partial x}\lambda_n\big|_{z_b}$$

Derivation of GN Eqn in *z*-direction is similar to the derivation of GN Eqn in *x*-direction, therefore; detailed derivation is not included here for brevity. The constrained *z*-direction momentum equation of level I GN Eqn is:

$$15.\quad \sum_{m=0}^{e=1}\rho\frac{\partial w_m}{\partial t}\,y_{mn}+\sum_{m=0}^{e=1}\sum_{r=0}^{e=1}\rho\frac{\partial w_m}{\partial x}u_r\,y_{mrn}+\sum_{m=0}^{e=1}\sum_{r=0}^{e=1}\rho\frac{\partial w_m}{\partial y}v_r\,y_{mrn}+\sum_{m=0}^{e=1}\sum_{r=0}^{e=1}\rho\,w_m w_r\,y_{rn}^{m}$$
$$=\bar{P}\lambda_n\big|_{z_b}+P_n'-\rho g y_n$$

where $P_n' = \int_{z_b}^{\eta} P\lambda_n' \, dz$ and g is the gravitational acceleration.

(To learn more about the derivation of GN momentum Eqns in this paper, refer to PhD theses by Jalali, 2016 and Haniffah, 2013).

Eqn. (14) and Eqn. (15) are expanded for level I $\{(u_0, u_1), (v_0, v_1), (w_0, w_1)\}$. In z-momentum GN Eqn. (15), w_0 and w_1 are replaced by Eqns. (6) and (7). Two sets of Eqns are derived for x- and z-momentum GN Eqns (n = 0, level 0, and n = 1, level I,). In z-momentum GN Eqn.(15) , $P_0' = 0$ and $P_1' = P_0$. For eliminating the effect of P_0 differentiation is applied with respect to x for n = 1 set of z-momentum GN Eqn and the obtained Eqn is added to the n = 0 set of x-momentum GN Eqn. Also, the effect of bottom pressure term, $\bar{P}$, is eliminated by multiplying $(\frac{\partial z_b}{\partial x})$ to the n = 0 set of z-momentum GN Eqn and adding the resulted Eqn to the n = 1 set of z-momentum GN Eqn. Finally, the 2D level I x-momentum GN Eqn for stationary bed, $(\frac{\partial z_b}{\partial t} = \frac{\partial^2 z_b}{\partial x \partial t} = \frac{\partial^2 z_b}{\partial y \partial t} = 0)$, and non-uniform bathymetry is derived:

16.
$$\begin{aligned}
&\frac{\partial \eta}{\partial x}\left[\frac{\partial z_b}{\partial x}\left(\frac{\partial u_0}{\partial t} + v_0\,\frac{\partial u_0}{\partial y} - u_0\frac{\partial v_0}{\partial y}\right) + u_0^2\,\frac{\partial^2 z_b}{\partial x^2} + \frac{\partial z_b}{\partial y}\left(\frac{\partial v_0}{\partial t} + u_0\,\frac{\partial v_0}{\partial x} - v_0\,\frac{\partial u_0}{\partial x}\right) + v_0^2\,\frac{\partial^2 z_b}{\partial y^2}\right.\\
&\left. +2u_0v_0\,\frac{\partial^2 z_b}{\partial x \partial y} + g\right] + \frac{h}{2}\left[\frac{\partial z_b}{\partial x}\left(\frac{\partial^2 u_0}{\partial x \partial t} + \frac{\partial v_0}{\partial x}\frac{\partial u_0}{\partial y} + v_0\frac{\partial^2 u_0}{\partial x \partial y} - \frac{\partial u_0}{\partial x}\frac{\partial v_0}{\partial y} - u_0\,\frac{\partial^2 v_0}{\partial x \partial y}\right)\right.\\
&+\frac{\partial^2 z_b}{\partial x^2}\left(\frac{\partial u_0}{\partial t} + 2u_0\,\frac{\partial u_0}{\partial x} + v_0\,\frac{\partial u_0}{\partial y} - u_0\frac{\partial v_0}{\partial y}\right) + \frac{\partial z_b}{\partial y}\left(\frac{\partial^2 v_0}{\partial x \partial t} + u_0\,\frac{\partial^2 v_0}{\partial x^2} - v_0\,\frac{\partial^2 u_0}{\partial x^2}\right)\\
&\left.+\frac{\partial^2 z_b}{\partial x \partial y}\left(\frac{\partial v_0}{\partial t} + 3u_0\,\frac{\partial v_0}{\partial x} + v_0\,\frac{\partial u_0}{\partial x}\right) + u_0^2\,\frac{\partial^3 z_b}{\partial x^3} + 2u_0v_0\,\frac{\partial^3 z_b}{\partial x^2 \partial y} + 2v_0\,\frac{\partial v_0}{\partial x}\,\frac{\partial^2 z_b}{\partial y^2} + v_0^2\,\frac{\partial^3 z_b}{\partial x \partial y^2}\right]\\
&+h\,\frac{\partial\left(h + \frac{z_b}{2}\right)}{\partial x}\left[-\frac{\partial^2 u_0}{\partial x \partial t} - \frac{\partial^2 v_0}{\partial y \partial t} - u_0\,\frac{\partial^2 u_0}{\partial x^2} - \frac{\partial^2 (u_0 v_0)}{\partial x \partial y} - v_0\,\frac{\partial^2 v_0}{\partial y^2} + \left(\frac{\partial u_0}{\partial x} + \frac{\partial v_0}{\partial y}\right)^2\right]\\
&+\frac{h^2}{3}\left[-\frac{\partial^3 u_0}{\partial x^2 \partial t} - \frac{\partial^3 v_0}{\partial x \partial y \partial t} - u_0\,\frac{\partial^3 u_0}{\partial x^3} - \frac{\partial^3 (u_0 v_0)}{\partial x^2 \partial y} - v_0\,\frac{\partial^3 v_0}{\partial x \partial y^2} - \frac{\partial v_0}{\partial x}\left(\frac{\partial^2 u_0}{\partial x \partial y} + \frac{\partial^2 v_0}{\partial y^2}\right)\right.\\
&\left.+\left(\frac{\partial u_0}{\partial x} + 2\frac{\partial v_0}{\partial y}\right)\left(\frac{\partial^2 v_0}{\partial x \partial y} + \frac{\partial^2 u_0}{\partial x^2}\right)\right] + \left(\frac{\partial u_0}{\partial t} + u_0\,\frac{\partial u_0}{\partial x} + v_0\,\frac{\partial u_0}{\partial y}\right) = 0
\end{aligned}$$

By simplifying Eqn. (16), the 2D level I x-momentum GN equation for uniform bathymetry is:

17.
$$\begin{aligned}
&g\frac{\partial \eta}{\partial x} + h\left(\frac{\partial h}{\partial x}\right)\left[-\frac{\partial^2 u_0}{\partial x \partial t} - \frac{\partial^2 v_0}{\partial y \partial t} - u_0\,\frac{\partial^2 u_0}{\partial x^2} - v_0\frac{\partial^2 v_0}{\partial y^2} - \frac{\partial^2 u_0 v_0}{\partial x \partial y} + \left(\frac{\partial u_0}{\partial x} + \frac{\partial v_0}{\partial y}\right)^2\right]\\
&+\frac{h^2}{3}\left[-\frac{\partial^3 u_0}{\partial x^2 \partial t} - \frac{\partial^3 v_0}{\partial x \partial y \partial t} - u_0\frac{\partial^3 u_0}{\partial x^3} - \frac{\partial^3 u_0 v_0}{\partial x^2 \partial y} - v_0\frac{\partial^3 v_0}{\partial x \partial y^2} - \frac{\partial v_0}{\partial x}\left(\frac{\partial^2 u_0}{\partial x \partial y} + \frac{\partial^2 v_0}{\partial y^2}\right)\right.\\
&\left.+\left(\frac{\partial u_0}{\partial x} + 2\frac{\partial v_0}{\partial y}\right)\left(\frac{\partial^2 v_0}{\partial x \partial y} + \frac{\partial^2 u_0}{\partial x^2}\right)\right] + \left(\frac{\partial u_0}{\partial t} + u_0\,\frac{\partial u_0}{\partial x} + v_0\,\frac{\partial u_0}{\partial y}\right) = 0
\end{aligned}$$

2D level I y-direction momentum GN Eqn and its derivation are not included here for brevity (For complete detailed derivations of level I GN Eqns see PhD theses by Jalali 2016 and Haniffah 2013). The corresponding 1D level I x-momentum GN Eqn for and uniform bathymetry is:

18.
$$\begin{aligned}
&g\frac{\partial \eta}{\partial x} + h\left(\frac{\partial h}{\partial x}\right)\left[-\frac{\partial^2 u_0}{\partial x \partial t} - u_0\,\frac{\partial^2 u_0}{\partial x^2} + \left(\frac{\partial u_0}{\partial x}\right)^2\right] + \frac{h^2}{3}\left[-\frac{\partial^3 u_0}{\partial x^2 \partial t} - u_0\,\frac{\partial^3 u_0}{\partial x^3} + \frac{\partial u_0}{\partial x}\frac{\partial^2 u_0}{\partial x^2}\right]\\
&+\left(\frac{\partial u_0}{\partial t} + u_0\,\frac{\partial u_0}{\partial x}\right) = 0
\end{aligned}$$

The corresponding 1D level I GN continuity Eqn is:

19. $$\frac{\partial h}{\partial t}+\frac{\partial u_0 h}{\partial x}=0$$

4. Numerical implementation

To develop a valid numerical solver of 2D level I GN Eqns, the researchers discretised Eqns. (8) and (17) using second-order central finite differences (numerical solver of 2D level I GN momentum equation for non-uniform bathymetry, Eqn. (16), is presented in chapter 3 of PhD thesis by Jalali, 2016). In the present numerical solver two different sections were developed to deal with the continuity equation and momentum equations. Continuity equation do not have any cross-derivative terms; therefore, an explicit second-order finite difference solves the equations properly. On the other hand, momentum equations contain cross-derivatives terms ($\frac{\partial^2 u_0}{\partial x \partial t}$ and $\frac{\partial^3 u_0}{\partial x^2 \partial t}$). Since an explicit predictor-corrector scheme is incapable of solving this kind of equations, implicit finite difference scheme is used to solve the GN momentum equations. Herein, implicit tridiagonal matrix inversion scheme is utilised to solve GN momentum equations (for more details see Chapter 3 of PhD thesis by Jalali, 2016). Nevertheless, other numerical schemes such as finite volume or finite element may be capable of solving the continuity and momentum equations simultaneously. The developed numerical solver is based on finite difference that cannot solve these equations simultaneously. The 2D GN continuity Eqn (8) is discretised by applying second-order central difference:

20. $$\frac{\partial h}{\partial t}\Big|_{ij}^{t}=-\left[\left(\frac{{u_0}_{i+1\,j}^{t}\,h_{i+1\,j}^{t}-{u_0}_{i-1\,j}^{t}\,h_{i-1\,j}^{t}}{2\Delta x}\right)+\left(\frac{{v_0}_{i\,j+1}^{t}\,h_{i\,j+1}^{t}-{v_0}_{i\,j-1}^{t}\,h_{i\,j-1}^{t}}{2\Delta y}\right)\right]$$

The 2D level I GN *x*-direction momentum Eqn. (17) are rearranged and solved using an implicit scheme. To handle Eqn. (17), let

21. $$\mathrm{F}=\frac{\partial u_0}{\partial t}-h\left(\frac{\partial h}{\partial x}\right)\frac{\partial}{\partial x}\left(\frac{\partial u_0}{\partial t}\right)-\frac{h^2}{3}\frac{\partial^2}{\partial x^2}\left(\frac{\partial u_0}{\partial t}\right)$$

In second-order central differences this becomes

22. $$\mathrm{F}_{ij}^{t}=\left[h_{ij}^{t}\left(\frac{h_{i+1\,j}^{t}-h_{i-1\,j}^{t}}{4\Delta x^2}\right)-\frac{(h_{ij}^{t})^2}{3\Delta x^2}\right]\hat{u}_{0_{i-1\,j}}^{t}+\left[1+\frac{2(h_{ij}^{t})^2}{3\Delta x^2}\right]\hat{u}_{0_{ij}}^{t}$$
$$+\left[-h_{ij}^{t}\left(\frac{h_{i+1\,j}^{t}-h_{i-1\,j}^{t}}{4\Delta x^2}\right)-\frac{(h_{ij}^{t})^2}{3\Delta x^2}\right]\hat{u}_{0_{i+1\,j}}^{t}$$

where $\hat{u}_{0_{ij}}^{t}=\frac{\partial u_0}{\partial t}\Big|_{ij}^{t}$. The discretised equation is rewritten as

23. $$\mathrm{F}_{ij}^{t}=a_{ij}^{t}\,\hat{u}_{0_{i-1\,j}}^{t}+b_{ij}^{t}\,\hat{u}_{0_{ij}}^{t}+c_{ij}^{t}\,\hat{u}_{0_{i+1\,j}}^{t}$$

where a_{ij}^{t}, b_{ij}^{t} and c_{ij}^{t} are the tridiagonal matrix coefficients for *x*-direction. Here, i refers to *x*-direction, j is *y*-direction and *t* is time. F is also equal to the remaining spatial derivative terms in Eqn. (17). These terms are also discretised in Eqn. (17) by using second-order central differences, giving:

24. $$\mathrm{F}_{ij}^{t} = -\left[{u_0}_{ij}^{t}\frac{\partial u_0}{\partial x}\Big|_{ij}^{t} + {v_0}_{ij}^{t}\frac{\partial u_0}{\partial y}\Big|_{ij}^{t} + g\frac{\partial \eta}{\partial x}\Big|_{ij}^{t}\right] + h_{ij}^{t}\frac{\partial h}{\partial x}\Big|_{ij}^{t}\frac{\partial}{\partial y}\left(\frac{\partial v_0}{\partial t}\right)\Big|_{ij}^{t} + \frac{{h_{ij}^{t}}^2}{3}\frac{\partial^2}{\partial x\partial y}\left(\frac{\partial v_0}{\partial t}\right)\Big|_{ij}^{t}$$

$$+h_{ij}^{t}\frac{\partial h}{\partial x}\Big|_{ij}^{t}\left[{u_0}_{ij}^{t}\frac{\partial^2 u_0}{\partial x^2}\Big|_{ij}^{t} + \frac{\partial^2(u_0v_0)}{\partial x\partial y}\Big|_{ij}^{t} + {v_0}_{ij}^{t}\frac{\partial^2 v_0}{\partial y^2}\Big|_{ij}^{t} - \left(\frac{\partial u_0}{\partial x}\Big|_{ij}^{t} + \frac{\partial v_0}{\partial y}\Big|_{ij}^{t}\right)^2\right]$$

$$+\frac{{h_{ij}^{t}}^2}{3}\left[{u_0}_{ij}^{t}\frac{\partial^3 u_0}{\partial x^3}\Big|_{ij}^{t} + \frac{\partial^3 u_0 v_0}{\partial x^2\partial y}\Big|_{ij}^{t} + \frac{\partial v_0}{\partial x}\Big|_{ij}^{t}\left(\frac{\partial^2 u_0}{\partial x\partial y}\Big|_{ij}^{t} + \frac{\partial^2 v_0}{\partial y^2}\Big|_{ij}^{t}\right) + {v_0}_{ij}^{t}\frac{\partial^3 v_0}{\partial x\partial y^2}\Big|_{ij}^{t}\right.$$

$$\left.-\left(\frac{\partial u_0}{\partial x}\Big|_{ij}^{t} + 2\frac{\partial v_0}{\partial y}\Big|_{ij}^{t}\right)\left(\frac{\partial^2 v_0}{\partial x\partial y}\Big|_{ij}^{t} + \frac{\partial^2 u_0}{\partial x^2}\Big|_{ij}^{t}\right)\right]$$

The above sets of discretised equations form the tridiagonal matrix system. The unknown values $\hat{u}_{0_{ij}}^{t}$ are obtained for $j = 2, \ldots, j_{\max}-1$ and $i = 1, \ldots, i_{\max}$ using the Thomas algorithm (Press *et al*. 2007). It should be mentioned that i_{max} and j_{max} refer to the max number of grid points in *x*- ad *y*-directions. Similar numerical approach was applied to 2D level I GN *y*-momentum Eqn (for detailed development of GN numerical solver refer to chapter 3 of PhD thesis by Jalali, 2016). Iteration is then used to centre correctly (in space and time) the cross-derivative terms that appear in both the *x*- and *y*-direction momentum Eqns. Runge-Kutta fourth-order (Rk4) time-integration is used to update the total depth and horizontal velocity components each time step.

5. Boundary conditions

To solve the 2D GN equations, it is necessary to impose flexible and compatible boundary conditions. For instance, solid wall boundaries are located at the ends of the domain when simulating sloshing of waves in a tank. The surface elevation at the boundary obtained by cubic Lagrange interpolation of interior values is assigned according to Haniffah, 2013. The velocity is set to zero at solid wall boundaries. Additional ghost grid points are located outside the boundaries, with anti-symmetry imposed for horizontal velocity (u) on *y*-direction and symmetry on *x*-direction. The velocity boundary conditions on *x*-direction for numerical solver of 2D GN Eqns are:

$$\frac{\partial u_0}{\partial t}\Big|_{1,j}^{t} = 0, \quad \frac{\partial u_0}{\partial t}\Big|_{0,j}^{t} = -\frac{\partial u_0}{\partial t}\Big|_{2,j}^{t}, \quad \frac{\partial u_0}{\partial t}\Big|_{-1,j}^{t} = -\frac{\partial u_0}{\partial t}\Big|_{3,j}^{t}$$

$$\frac{\partial u_0}{\partial t}\Big|_{i_{max},j}^{t} = 0\,, \qquad \frac{\partial u_0}{\partial t}\Big|_{i_{max}+1,j}^{t} = -\frac{\partial u_0}{\partial t}\Big|_{i_{max}-1,j}^{t}$$

$$\frac{\partial u_0}{\partial t}\Big|_{i_{max}+2,j}^{t} = -\frac{\partial u_0}{\partial t}\Big|_{i_{max}-2,j}^{t}\,, \qquad \frac{\partial u_0}{\partial t}\Big|_{i,1}^{t} = 0$$

$$\frac{\partial u_0}{\partial t}\Big|_{i,0}^{t} = \frac{\partial u_0}{\partial t}\Big|_{i,2}^{t}\,, \quad \frac{\partial u_0}{\partial t}\Big|_{i,-1}^{t} = \frac{\partial u_0}{\partial t}\Big|_{i,3}^{t}\,, \quad \frac{\partial u_0}{\partial t}\Big|_{i,j_{max}}^{t} = 0$$

$$\frac{\partial u_0}{\partial t}\Big|_{i,j_{max}+1}^{t} = \frac{\partial u_0}{\partial t}\Big|_{i,j_{max}-1}^{t}\,, \frac{\partial u_0}{\partial t}\Big|_{i,j_{max}+2}^{t} = \frac{\partial u_0}{\partial t}\Big|_{i,j_{max}-2}^{t}$$

Here, index 1, i_{max} and j_{max}, presents the location of wall, index 2, 3, i_{max}-1, i_{max}-2, j_{max}-1 and j_{max}-2 indicate grid points located in side of computational boundary (before the wall), and index -1, 0, i_{max}+1, i_{max}+2, j_{max}+1 and j_{max}+2 show ghost points located outside of computational boundary (after the wall). The velocity boundary conditions on

y-direction are not included here for brevity (for more details see Jalali, 2016). The symmetry boundaries imposed for surface elevation are:

$$\frac{\partial h}{\partial t}\Big|_{0,j}^{t} = \frac{\partial h}{\partial t}\Big|_{2,j}^{t} \;, \qquad \frac{\partial h}{\partial t}\Big|_{i_{max}+1,j}^{t} = \frac{\partial h}{\partial t}\Big|_{i_{max}-1,j}^{t}$$

$$\frac{\partial h}{\partial t}\Big|_{1,j}^{t} = 4\frac{\partial h}{\partial t}\Big|_{2,j}^{t} - 6\frac{\partial h}{\partial t}\Big|_{3,j}^{t} + 4\frac{\partial h}{\partial t}\Big|_{4,j}^{t} - \frac{\partial h}{\partial t}\Big|_{5,j}^{t}$$

$$\frac{\partial h}{\partial t}\Big|_{i_{max},j}^{t} = 4\frac{\partial h}{\partial t}\Big|_{i_{max}-1,j}^{t} - 6\frac{\partial h}{\partial t}\Big|_{i_{max}-2,j}^{t} + 4\frac{\partial h}{\partial t}\Big|_{i_{max}-3,j}^{t} - \frac{\partial h}{\partial t}\Big|_{i_{max}-4,j}^{t}$$

$$\frac{\partial h}{\partial t}\Big|_{i,0}^{t} = \frac{\partial h}{\partial t}\Big|_{i,2}^{t} \;, \qquad \frac{\partial h}{\partial t}\Big|_{i,j_{max}+1}^{t} = \frac{\partial h}{\partial t}\Big|_{i,j_{max}-1}^{t}$$

$$\frac{\partial h}{\partial t}\Big|_{i,1}^{t} = 4\frac{\partial h}{\partial t}\Big|_{i,2}^{t} - 6\frac{\partial h}{\partial t}\Big|_{i,3}^{t} + 4\frac{\partial h}{\partial t}\Big|_{i,4}^{t} - \frac{\partial h}{\partial t}\Big|_{i,5}^{t}$$

$$\frac{\partial h}{\partial t}\Big|_{i,j_{max}}^{t} = 4\frac{\partial h}{\partial t}\Big|_{i,j_{max}-1}^{t} - 6\frac{\partial h}{\partial t}\Big|_{i,j_{max}-2}^{t} + 4\frac{\partial h}{\partial t}\Big|_{i,j_{max}-3}^{t} - \frac{\partial h}{\partial t}\Big|_{i,j_{max}-4}^{t}$$

In 1D level I GN numerical solver, Eqn. (18) and Eqn. (19) are governing Eqns. The 1D GN continuity Eqn (19) is discretised by applying second-order central difference:

25. $$\frac{\partial h}{\partial t}\Big|_{i}^{t} = -\left(\frac{{u_0}_{i+1}^{t}\, h_{i+1}^{t} - {u_0}_{i-1}^{t}\, h_{i-1}^{t}}{2\Delta x}\right)$$

In Eqn. (18), cross -derivative terms of *x* and *t* are rearranged and solved by using an implicit scheme. Similar to the procedure followed for Eqn. (21). The discretised equation is:

26. $$\mathrm{F}_i^t = a_i^t\ \hat{u}_{0_{i-1}}^t + b_i^t\ \hat{u}_{0_i}^t + c_i^t\ \hat{u}_{0_{i+1}}^t$$

F is also equal to the remaining spatial derivative terms in Eqn. (18). Using second-order central differences discretisises the terms in Eqn. (18) and gives:

27. $$\mathrm{F}_i^t = -{u_0}_i^t\ \frac{\partial u_0}{\partial x}\Big|_i^t - g\frac{\partial \eta}{\partial x}\Big|_i^t + h_i^t\ \frac{\partial h}{\partial x}\Big|_i^t \left[{u_0}_i^t\ \frac{\partial^2 u_0}{\partial x^2}\Big|_i^t - \left(\frac{\partial u_0}{\partial x}\right)^2\Big|_i^t\right] + \frac{{h_i^t}^2}{3}\left[{u_0}_i^t\ \frac{\partial^3 u_0}{\partial x^3}\Big|_i^t - \frac{\partial u_0}{\partial x}\Big|_i^t \frac{\partial^2 u_0}{\partial x^2}\Big|_i^t\right]$$

The velocity boundary conditions for solver of 1D GN Eqn are:

$$\frac{\partial u_0}{\partial t}\Big|_1^t = 0\,, \quad \frac{\partial u_0}{\partial t}\Big|_0^t = -\frac{\partial u_0}{\partial t}\Big|_2^t\,, \quad \frac{\partial u_0}{\partial t}\Big|_{-1}^t = -\frac{\partial u_0}{\partial t}\Big|_3^t$$

$$\frac{\partial u_0}{\partial t}\Big|_{i_{max}}^t = 0\,, \qquad \frac{\partial u_0}{\partial t}\Big|_{i_{max}+1}^t = -\frac{\partial u_0}{\partial t}\Big|_{i_{max}-1}^t\,, \qquad \frac{\partial u_0}{\partial t}\Big|_{i_{max}+2}^t = -\frac{\partial u_0}{\partial t}\Big|_{i_{max}-2}^t$$

In 1D GN numerical solver the symmetry boundaries imposed for surface elevation are:

$$\frac{\partial h}{\partial t}\Big|_0^t = \frac{\partial h}{\partial t}\Big|_2^t \quad , \quad \frac{\partial h}{\partial t}\Big|_{i_{max}+1}^t = \frac{\partial h}{\partial t}\Big|_{i_{max}-1}^t$$

$$\frac{\partial h}{\partial t}\Big|_1^t = 4\frac{\partial h}{\partial t}\Big|_2^t - 6\frac{\partial h}{\partial t}\Big|_3^t + 4\frac{\partial h}{\partial t}\Big|_4^t - \frac{\partial h}{\partial t}\Big|_5^t$$

$$\frac{\partial h}{\partial t}\Big|_{i_{max}}^t = 4\frac{\partial h}{\partial t}\Big|_{i_{max}-1}^t - 6\frac{\partial h}{\partial t}\Big|_{i_{max}-2}^t + 4\frac{\partial h}{\partial t}\Big|_{i_{max}-3}^t - \frac{\partial h}{\partial t}\Big|_{i_{max}-4}^t$$

For more details details see chapter 3 of PhD thesis by Jalali, 2016 and chapter 4 of PhD thesis by Haniffah, 2013.

6. Numerical Procedure

The GN program comprises four main subroutines: input, calculation, update and output. For each test case, the following initial values are put into the program: bed elevation, initial water depth, amplitude, length and width of the study basin, number of grid points, time step, and duration of simulation time. The initial conditions supply for the bed elevation above fixed horizontal datum, local depth, and local horizontal velocity components throughout the tank. Solving the discretised continuity equation provides new water depth values throughout the grid. Then, the discretised momentum equations are solved. Iteration is used to solve the cross-derivative velocity terms in the momentum equation. Next, boundary conditions are invoked. The values of *u, v* and *h* are updated after each time step. The calculation process is repeated until the simulation is complete. The two benchmark tests comprise: sloshing in a square tank and free surface sloshing of an initial Gaussian hump in a square basin. In sloshing in a square tank to test for grid independence, the time history of wave elevation at the corner of the tank (in positive *x*-direction) was obtained on grids of increasingly fine resolution (Δx = 25 m (coarse grids), Δx = 10 m (medium grids), and Δx = 1 m (fine grids)) and a fixed time step Δt = 1 s. The results demonstrated that Δx = 1 m was sufficient to achieve a converged solution. Three time steps are chosen (Δt = 0.25, 1.0 and 2.0 s) on the converged grid with Δx = 1 m. There was a close agreement between the results, therefore; Δt = 1 s was selected as a fixed time step in simulation of sloshing in the tank (see chapter 4 of PhD thesis by Jalali, 2016). To determine the number of the grid points required to produce accurate simulation of free surface sloshing of an initial Gaussian hump, grid convergence test was performed. To this end, 3D visualisations and contour maps of the free surface elevation patterns in the basin were obtained on increasingly grid size with $\Delta x = \Delta y$ = 0.15 m (coarse grids), $\Delta x = \Delta y$ = 0.0375 m (medium grids), and $\Delta x = \Delta y = 7.5\times10^{-3}$ m (fine grids). The medium grid size $\Delta x = \Delta y$ = 0.0375 m is sufficient to convergence. Therefore, $\Delta x = \Delta y$ = 0.0375 m were chosen for numerical simulations. The numerical predictions of free surface sloshing of an initial Gaussian hump for different time steps (Δt = 0.05, 0.1 and 0.2 s) showed that Δt = 0.05 s was sufficient for producing an accurate simulations (see chapter 5 of PhD thesis by Jalali, 2016).

7. Model verification against analytical solution

7.1 Sloshing in a Tank

First, the benchmark test of sinusoidal free surface sloshing in a square tank is considered. The wavelength *L* is 1000 m and the still water depth h_0 is 5 m. Sloshing motions may even occur by using very small number of amplitude disturbance. For the present test case the amplitudes are *a* = 0.005 m and 0.05 m. These small numbers

of wave amplitude are applied in order to create minimum nonlinear behaviour by the sloshing wave. The first order analytical solution for the depth profile evolution in space and time of a standing wave in a tank (see e.g. Dean and Dalrymple, 2004) is

28. $\zeta_c = h_c - h_0 = a\ \cos(kx)\cos(\omega t + \phi)$

Here, ζ_c refers to the crest-induced free surface elevation time series, a is the amplitude of the standing wave, k is the wave number, ω is the angular frequency of the wave, x is distance along the tank, t is time, and ϕ is the phase. Wave angular frequency ω is obtained by means of dispersion relation:

29. $\omega = \sqrt{gk \tanh kh_0}$

In this case: $\omega = 0.044$ rad/s, T (period) = $2\pi/\omega$ = 142.8 s and f = (frequency) = 0.007 Hz.

Figure 1and Figure 2 are obtained by applying the numerical solver of 1D GN equations. This program was specifically developed to deal with sloshing in the tank, so it is necessary to measure free surface elevation of time history at two different locations: (a) the corner of tank (b) the centre of the tank. Figure 1 (a) presents crest-induced water level time histories at the corner of the tank (in positive x-direction) for a sloshing wave of a small-amplitude disturbance $a = 0.005$ m with phase $\phi = 0$. Here, ζ_c/a = 1 at time t = 0 s for free surface elevation of time history at corner of tank. Excellent agreement is obtained between the first-order analytical solution and the numerical prediction in which cross symbols (numerical prediction) essentially overlay the solid line (analytical solution). The standing wave behaviour is periodic and of constant amplitude. This case verifies that the numerical scheme gives a correct representation of the underlying mathematical description, provided the waves are nearly linear. Figure 1 (b) depicts the numerical prediction of the crest-induced free surface elevation time history at the corner of the tank for a = 0.05 m. The free surface elevation time history displayed in Figure 1 (b) is shorter than that in Figure 1 (a) because nonlinear effects eventually cause shock-like steepening of the wave profiles (becoming visible at about t = 2000 s) in the larger amplitude case leading to the numerical model becoming unstable. A shock-capturing scheme would be needed to overcome this problem, and is recommended for future implementation. Figure 1 (c) presents the numerically predicted trough-induced free surface elevation time history at the corner of the tank in which $\zeta_t = -a\ \cos(kx)\cos(\omega t)$. The results are qualitatively almost the same as for the crest-induced case (i.e. Figure1 (b)). Nonlinearity can be presented by even harmonics ($\frac{\zeta_c+\zeta_t}{2a}$). To separate even harmonics, harmonics are treated as orthogonal functions. Figure 1 (d) shows the numerically predicted free surface elevation time history of the even harmonic components (obtained by taking the average of results obtained for $\phi = 0$ and π) for the amplitude $a = 0.05$ m. Here, the amplitude of the second-order harmonics grows monotonically with time until the point at which numerical instability occurs. It is worth noting that the (linear) analytical solution is not capable to show the nonlinear behaviour of even harmonics. The developed numerical model is also applied to simulate other possible predictions for sloshing wave in the centre of tank. In this case, the wavelength is 1000 m and the still water depth h_0 is 1 m. Two values of wave amplitude, $a = 0.005$ m and 0.015 m, are selected. In this case: $\omega = 0.0197$ rad/s, T = 319.28 s and f = 0.003 Hz.

Figure 2 (a) shows satisfactory agreement between numerical prediction (cross symbols) and analytical solution (solid line) of the crest-induced free surface elevation time histories at the centre of the tank by applying a = 0.005m. Here, $\zeta_c/a = -1$ at time t = 0 s for the crest-induced free surface elevation of time history at the centre of the tank. Figure 2 (b) depicts numerically predicted crest-induced free surface elevation time history for $a = 0.015$ m. It is clear that the numerical solver is unable to simulate the long term sloshing behaviour of wave, with high-order even

harmonic oscillations appearing after t = 1735 s. The nonlinear effects eventually caused shock-like steepening of the wave profiles. Therefore, a shock-capturing scheme is required to overcome this problem. Figure 2 (c) reveals the numerically predicted free surface elevation time history of the trough-induced sloshing at the centre of the tank for $a = 0.015$ m. The results are qualitatively almost the same as for the crest-induced case (i.e. Figure 2 (b)). Figure 2 (d) shows the numerically predicted free surface elevation time history of the even harmonic components (obtained by $\frac{\zeta_c+\zeta_t}{2a}$) for a = 0.015m. The effect of nonlinearity increases as the initial slosh amplitude increases, as would be expected (for more details see Chapter 4 of PhD thesis by Jalali, 2016).

7.2 Free surface sloshing of an initial Gaussian hump in a closed square, flat-bottomed basin

The numerical solver of the 2D GN equations is now verified for nonlinear free surface sloshing motions arising from an initial Gaussian hump free surface profile in a closed basin. The well-established analytical solution (Lamb 1916, Wei and Kirby 1995, Yao 2007) of the linearised shallow water equations for the evolution of an initial hump in a closed square basin is

30. $$\zeta(x,y,t) = \sum_{p=0}\sum_{q=0} \tilde{\zeta}_{pq} e^{-i\omega t} * \cos\left(\frac{p\pi}{L_x}x\right)\cos\left(\frac{q\pi}{L_y}y\right)$$

Here, ζ is the free surface elevation above still water level,
where:

31. $$\tilde{\zeta}_{pq} = \frac{4}{(1+\sigma_{p0})(1+\sigma_{q0})L_xL_y}\int_{-L_y}^{L_y}\int_{-L_x}^{L_x}\zeta_0(x,y)\cos\left(\frac{p\pi}{L_x}x\right)\cos\left(\frac{q\pi}{L_y}y\right)dxdy$$

In Eqn. (30), $i = \sqrt{-1}$, L_x and L_y are the length and width of the basin, ω is angular frequency, p and q are the number of wave components, σ_{pq} is the Kronecker delta function, and

32. $$\zeta_0(x,y) = a\exp\left\{-b\left[\left(x-\frac{L_x}{2}\right)^2+\left(y-\frac{L_y}{2}\right)^2\right]\right\}$$

where a is the wave amplitude and b is spreading parameter.
Consider a basin of 7.5 m length and 7.5 m width. The constant water depth is h_0 = 0.45 m. The initial amplitude of the hump a is 0.045 m and the spreading parameter b = 2 m^{-2}. In order to obtain an accurate estimate of the analytical solution, different numbers of wave components (p and q) and grid size (Δx and Δy) are selected to solve the double Fourier series in Eqn. (30). Table 1 presents initial elevation of analytically predicted free surface perturbation ζ_c/a at the centre of the basin at time t = 0 s for different numbers of wave components (p, q) and grid size (Δx, Δy). This table reveals that using $p = q$ = 51 and $\Delta x = \Delta y$ = 0.075 m is sufficient to obtain a converged analytical solution. In the present GN numerical solver, 4 iterations on the medium grid size, $\Delta x = \Delta y$ = 0.0375 m, are sufficient for the numerical predictions to be in satisfactory agreement with the analytical results. A time step of Δt = 0.05 s is found to be sufficient to achieve accurate and stable results. Figure 3 compares the numerical free surface elevation time history with the analytical solution at the centre of the basin for a total simulation time of 70s after release of the initial hump. Here, ζ_c/a = 1 at time t = 0 s for free surface elevation of time history at centre of basin. There is close agreement between the numerical and analytical results for about 10 s after the initial hump is released, after which differences are discernible between the numerical predictions and analytical solution. The foregoing discrepancies are largely due to nonlinear (second- and higher-order) wave interactions which are modelled by the 2D level I GN equations, but neglected in the analytical solution of the linearised shallow water equations. The even harmonics of the sloshing motions induced by the initial Gaussian hump can be determined by

simulating the free surface time series resulting from releasing the initial hump, and the corresponding free surface time histories driven by an initial trough of equal but opposite shape to the hump (following the separation of harmonics method utilised by Johannessen and Swan (2001), Hunt et al. (2004), and Borthwick et al. (2006) amongst others). Here, the harmonics are treated as orthogonal functions, and the even harmonics obtained by addition as $\left(\frac{\zeta_c+\zeta_t}{2}\right)$ where ζ_c refers to the free surface elevation time series of the initial Gaussian hump and ζ_t to the equivalent time series for the initial Gaussian trough. Figure 4 reveals that for a relatively large amplitude hump ($a = h_0/2 = 0.225$ m), it is possible to see evidence of the nonlinear effect produced by even harmonics, which are non-dimensionalised with respect to the amplitude of the initial hump. The even harmonics have amplitudes of up to about 20% that of the initial hump, and are perhaps growing slightly over the duration of the simulation. Figure5 presents comparison of analytically predicted FFT spectrum for the free surface elevation time history of the initial Gaussian hump and numerically predicted FFT spectrum for the free surface elevation time history of even harmonic components. It can be observed that all five peaks of numerical even harmonics occur at the same frequency of the analytically predicted peaks of Gaussian hump. Table 2 lists the resonant frequencies associated with different modes for the basin (r and s): the first peak occurs at mode $r = 2$ and $s = 0$; the second peak at mode $r = 2$ and $s = 2$, the third peak at mode $r = 3$ and $s = 2$, the fourth peak at mode $r = 4$ and $s = 0$; and finally the fifth peak at mode $r = 5$ and $s = 1$.

Figure 6 and Figure 7 compare the numerical simulations with the analytical solutions for sloshing in the basin, using 3D visualisations of the water surface at times $t = 1$, 5, 10, and 20 s. Corresponding contour maps are given in Figure 8 and Figure 9. Although satisfactory agreement is achieved between the numerical predictions and analytical solution at $t = 1$ and 5 s, discrepancies between the numerical and analytical simulations become evident at $t = 10$ s, and grow with simulation time, as can be seen at $t = 20$ s where phase differences are observable. Figure10 shows numerically predicted velocity vectors and magnitude contours for the water surface at times $t =$ 1, 5, 10, and 20 s after releasing the Gaussian hump in the flat-bottomed basin. Here, the velocity vectors indicate the direction of water particles and magnitude contours show the value of velocity in different sections of the basin. Slosh motions evolve in the basin from the initial hump as it rapidly drops under its own weight, causing a deep trough at the centre of the basin with an associated circular wave front. The initial free surface motions are remarkably similar to those generated by the collapse of a liquid column, as modelled by Toro (2001) amongst others, except that the central oscillations do not die away as quickly. The balance between potential and kinetic energy drives repeated up and down motions at the centre of the basin, generating circular waves that propagate radially away from the centre of the basin and reflect with the basin walls. The repeated reflections between the waves with each other and the walls promote increasingly complicated sloshing modes dominated by waves whose wavelength is half the length of the basin.

Figure 11 compares long time simulation of the numerical free surface elevation time history with the analytical solution at the centre of the basin for very small-amplitude disturbance ($a = 0.001$ m) and spreading parameter ($b = 0.2$ m^{-2}). Here, complete agreement between the numerical and analytical simulations are obtained since the effect of nonlinear second-order wave interactions is quite small. Corresponding FFT plots are given in Figure 12. The reversibility of the simulations is now considered. The Gaussian hump is released at $t = 0$ s and the numerical solution then propagated forward in time until 20 s, after which the time step is made negative and the numerical scheme forced to simulate the backward propagation of the water surface until time zero is again reached. The results should be in almost identical agreement, given that the problem is thermodynamically reversible. There is no viscosity present, no turbulence, no surface tension, and no sources of friction (e.g. from the basin walls or bed).

Figure 13 examines reversibility by plotting the free surface elevation time history at the centre of the basin. The forward part of the simulation is shown by the solid line, the backward by means of cross symbols. For the vast majority of the simulation, the agreement between the forward and backward processes is excellent. Discrepancies only occur when recovering the last 3 s of simulation. It seems likely that by travelling forward and backward in time, the accumulated dissipative error of the numerical scheme is responsible for causing the recovered hump to lose amplitude. Increasing number of grid, increasing number of iterations and selecting very small time step did not reduce the magnitude of this accumulated dissipative error at the last 3 s of simulation. Figures 14 indicates the effect of reversibility on free surface elevation time history simulation at the centre of the basin for very small-amplitude disturbance, a = 0.001m, and spreading parameter b = 0.2 m^{-2}. Excellent agreement is obtained between forward and backward propagations of the water surface since the effect of nonlinearity is neglected.

7.3 Parameter tests for sloshing in a square basin with non-uniform bathymetry

Simulations are now considered of the sloshing behaviour of an initial Gaussian hump of water released in a square basin with non-uniform bathymetry. Here, the bed elevation is given by

$$33. \quad z_b(x,y) = a_{z_b} \exp\left\{-b_{z_b}\left[\left(x-\frac{L_x}{2}\right)^2+\left(y-\frac{L_y}{2}\right)^2\right]\right\}$$

where a_{z_b} is the bed amplitude and b_{z_b} = 2 m^{-2} is a bed spreading parameter. The initial local free surface elevation is:

$$34. \quad \zeta_0(x,y) = -a_{z_b} \exp\left\{-b_{z_b}\left[\left(x-\frac{L_x}{2}\right)^2+\left(y-\frac{L_y}{2}\right)^2\right]\right\} + a \exp\left\{-b\left[\left(x-\frac{L_x}{2}\right)^2+\left(y-\frac{L_y}{2}\right)^2\right]\right\}$$

where a is the amplitude of the initial Gaussian hump in free surface elevation, and b = 2 m^{-2} is a measure of its spread. Figure 15 and Figure 16 respectively depict 3D visualisation and contour maps of the water surface at times t = 1, 5, 10 and 20 s for relatively large values of bed hump amplitude (a_{z_b} = 0.225 m) and Gaussian hump amplitude (a = 0.225 m). It is worth mentioning that bed hump amplitude, a_z, is obtained through trial-error method (for more details see chapter 5 of PhD thesis by Jalali, 2016). Figure 17 presents velocity vectors and magnitude contours for the water surface at times t = 1, 5, 10, and 20 s where the bed topography contains a central hump. The effect of the bed hump on the evolution of the water free surface is most obvious at the centre of the basin exactly where the bed hump has its peak. At first the Gaussian free surface hump drops rapidly to form a trough at the centre of the basin, releasing a circular ring-like wave that propagates towards the basin walls, where reflections occur. The plunging free surface at the centre of the basin interacts with the bed hump, leading to the recovery of a second clapotis-like hump which peaks and releases a second circular wave. After several cycles of central peaks and troughs, the water surface motions immediately above the hump degenerate into a patch of small waves that heave up and down over the hump (after $t \sim 10$ s); elsewhere the sloshing behaviour is similar to that of the corresponding case without a bed hump, particularly the presence of sloshing components whose wavelength is half the length of the basin.

Figure 18 and Figure 19 respectively show 3D visualisation and contour maps of the evolution of the water surface over a Gaussian trough in the bed ($a_{z_b} = -0.225$ m). Figure 20 shows velocity vectors and magnitude contours for the water surface at (a) t = 1 s, (b) t = 5 s, (c) t = 10 s and (d) t = 20 s where the bed topography contains a central trough. The bed trough has greatest effect at the centre of the basin, coincident with the peak position of the initial Gaussian free surface hump. The water free surface at the centre of the basin is able to fall further than for the

corresponding bed hump case, before interacting with the bed; localised sloshing of circular waves develops above the bed trough; the slosh behaviour away from the basin centre is similar to that in the corresponding basin with a flat bed, with modes at half basin wave length dominating.

8. Conclusions

This study has presented Level I GN equations for shallow flow over uniform and non-uniform bed topography in the context of slosh motions in a container. It has been demonstrated that level I GN equations can represent sloshing in a closed square basin resulting from initial sinusoidal and initial Gaussian free surface perturbations. Satisfactory agreement was obtained between the model predictions and the linear analytical solution for relatively small initial wave amplitude ($a \leq 0.005$ m). At larger amplitudes of initial disturbance, the numerically predicted free surface elevation time history steepened up and eventually began to develop a saw-tooth profile. Nonlinear effects were particularly noticeable in the even harmonic slosh components. For $a = 0.045$ m and $b = 2$ m^{-2} satisfactory agreement was also obtained between the numerical predictions and semi-analytical solution of the early stages of free surface motions in a square, flat-bottomed basin after the initial release of the Gaussian hump. Discrepancies later evolved partly because of nonlinear wave interaction effects which were not described by the analytical theory. It was found that the non-uniform bathymetry has a localised effect on the slosh motions.

9. Acknowledgements

The first author was partly funded by the University of Edinburgh.

10. References

1. Bonneton P, Chazel F, Lannes D, Marche F, Tissier M (2011) A splitting approach for the fully nonlinear and weakly dispersive Green–Naghdi model. Journal of Computational Physics, **230**: 1479-1498.

2. Borthwick AGL, Hunt AC, Feng T, Taylor PH, and Stansby PK (2006) Flow kinematics of focused wave groups on a plane beach in the UK. Coastal Research Facility. Coastal Engineering, 53(12): 1033-1044.

3. Dean RG and Dalrymple RA (2004) Coastal Processes with Engineering Applications. Modeling of Beaches and Shorelines. Cambridge University Press, Cambridge, UK.

4. Demirbilek Z and Webster WC (1992) Application of the Green-Naghdi theory of fluid sheets to shallow-water wave problems, Report 1. Model Development. US Army Engineers Waterways Experiment Station, Coastal Engineering Research Center, USA, Technical Report CERC–92–11.

5. Green AE and Naghdi PM (1976) Directed Fluid Sheets. Proceedings of the Royal Society of London. Series A, Mathematical and Physical Sciences, **347**: 447–473.

6. Haniffah MRM (2013) Wave Evolution on Gentle Slopes-Statistical Analysis and Green-Naghdi Modelling. D.Phil. Thesis, University of Oxford, UK.

7. Hunt AC, Taylor PH, Borthwick AGL and Stansby PK (2004) Phase inversion and the identification of harmonic structure in coastal engineering experiments. In Proceedings of the ASCE 29th International Conference on Coastal Engineering, Lisbon, pp. 1047–1059.

8. Ibrahim RA (2005) Liquid sloshing dynamics theory and applications. Cambridge University Press, Cambridge, UK.

9. Jalali MR (2016) One-Dimensional and Two-Dimensional Green-Naghdi Equation Solvers for Shallow Flow over Uniform and non-Uniform Beds. PhD Thesis, University of the Edinburgh, UK.

10. Johannessen T and Swan C (2001) A laboratory study of the focusing of transient and directionally spread surface water waves. Proceedings of the Royal Society of London. Series A, Mathematical, Physical and Engineering Sciences, **457**: 971–1006.

11. Lamb H (1916) Hydrodynamics. *Tidal Waves*. 4th Ed., Cambridge University Press, Cambridge, UK, pp. 274–276.

12. Nadiga BT, Margolin LG, Smolarkiewicz PK (1996) Different approximations of shallow fluid flow over an obstacle. American Institute of Physics, Phys. Fluids, **8:** 2066-2077.

13. Press WH, Teukolsky SA, Vetterling WT and Flannery BP (2007). Numerical recipes the art of scientific computing. Solution of linear algebraic equations. Cambridge University Press, Cambridge, UK, pp. 56 – 57.

14. Sarpkaya T and Isaacson M (1981) Mechanics of Wave Forces on Offshore Structures. Van Nostrand Reinhold, New York, USA.

15. Shields JJ and Webster WC (1988) On direct methods in water-wave theory. Journal of Fluid Mechanics, **197**: 171–199.

16. Toro EF (2001) Shock-Capturing Methods for Free-Surface Shallow Flows. John Wiley and Sons Ltd, UK.

17. Webster WC and Shields JJ (1991) Applications of high-level Green-Naghdi theory to fluid flow problems. IUTAM Symposium. On the Dynamics of Marine Vehicles and Structures in Waves. (Ed. Price WG, Temarel P and Keane AJ) Elsevier Science Publishers B.V. Brunel University, London, UK.

18. Wei G and Kirby JT (1995) Time-dependent numerical code for extended Boussinesq equations. Journal of Waterway, Port, Coastal, and Engineering, **121**: 251–261.

19. Yao Y (2007) Boussinesq-type Modelling of Gently Shoaling Extreme Ocean Waves. D.Phil. Thesis, University of Oxford, UK.

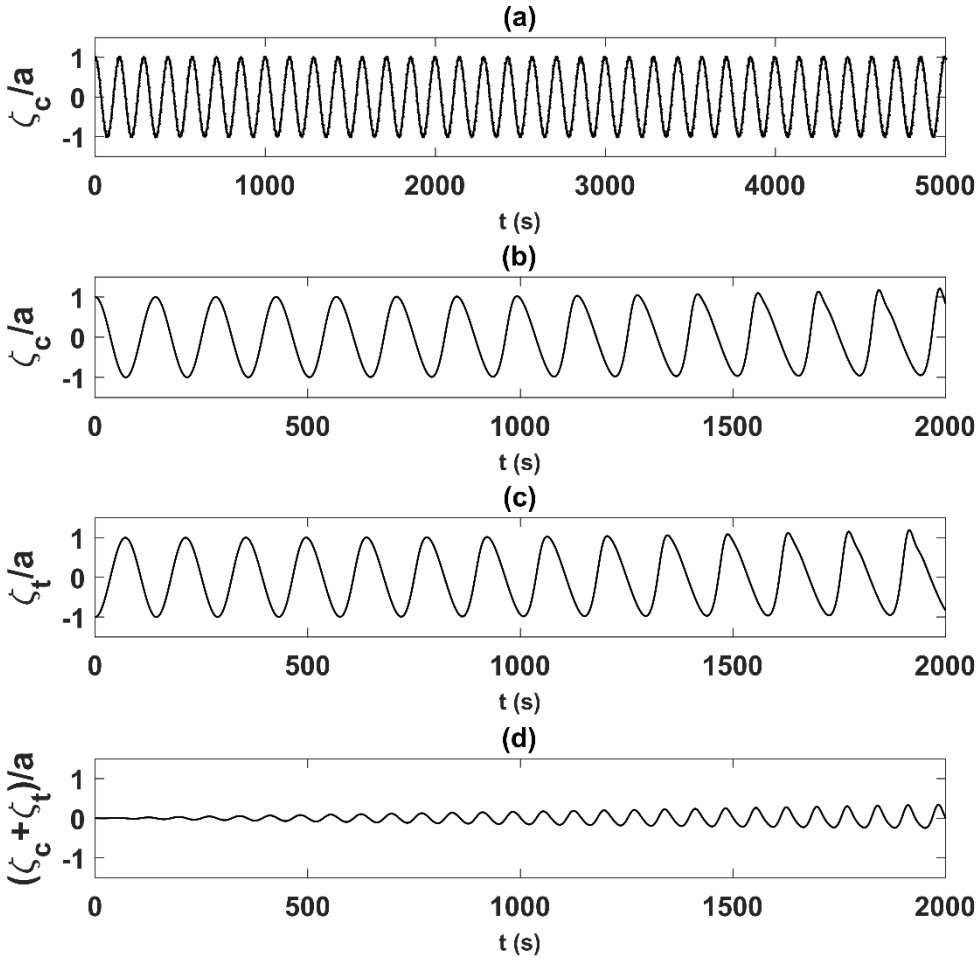

Figure 1. Sinusoidal free surface sloshing at the corner of a square tank: (a) analytical (solid line) and GN predicted (cross symbols) crest-induced free surface time histories for a = 0.005 m; (b) GN predicted crest-induced free surface time history for a = 0.05 m; (c) GN predicted trough-induced free surface time history for a = 0.05m; and (d) GN predicted even harmonics time history for a = 0.05 m.

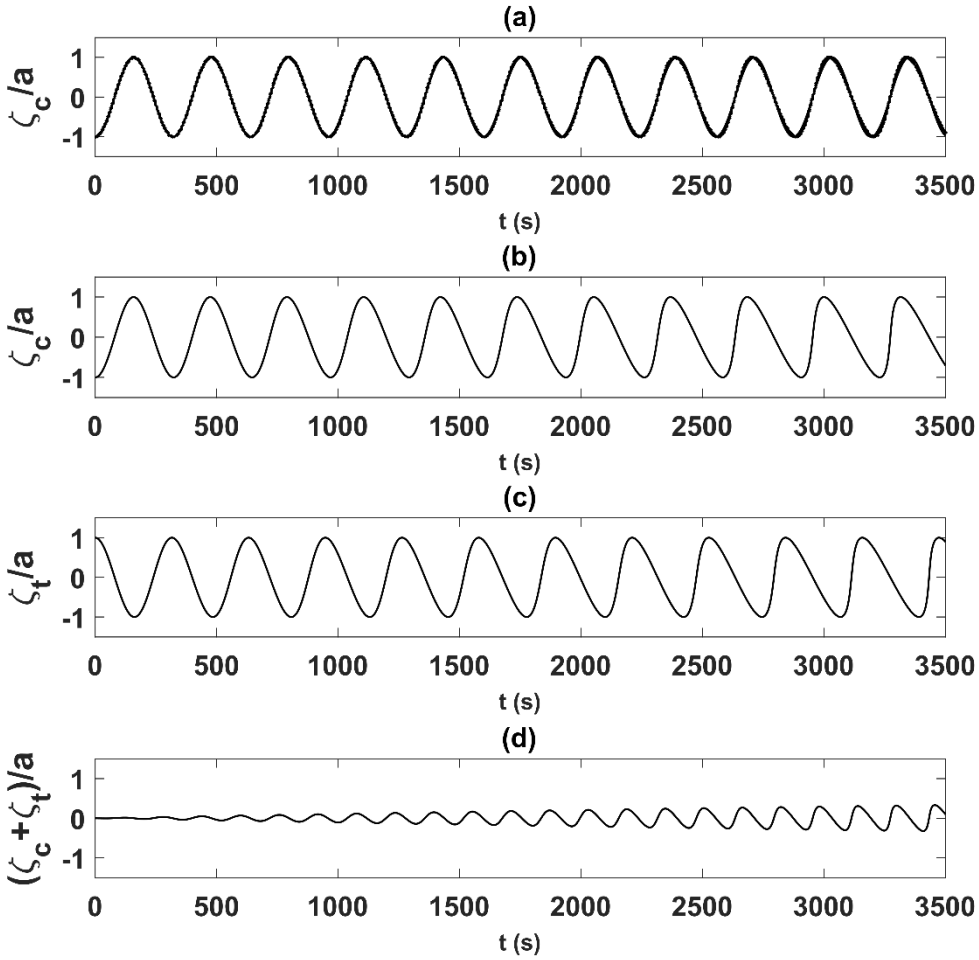

Figure 2. Sinusoidal free surface sloshing at centre of a square tank: (a) analytical (solid line) and GN predicted (cross symbols) crest-induced free surface time histories for a = 0.005 m; (b) GN predicted crest-induced free surface time history for a = 0.015 m; (c) GN predicted trough-induced free surface time history for a = 0.015 m; and (d) GN predicted even harmonics time history for a = 0.015 m.

Table 1: Initial Gaussian free surface hump in a square basin: elevation of free surface perturbation ζ_c/a at the centre of basin at time t = 0 s for different numbers of wave components (p, q) and grid size (Δx, Δy).

$\Delta x = \Delta y$ / $p=q$	0.3 m	0.075 m	0.015 m
51	0.022	1	1
101	0.022	0.355	1

Table 2: Analytical fundamental sloshing frequencies in a square basin (all values in Hz)

r / s	1	2	3	4	5
0	0.140	0.280	0.420	0.560	0. 700
1	0.198	0.313	0.442	0.577	0.714
2	0.313	0.396	0.505	0.626	0.754
3	0.442	0.505	0.594	0.700	0.816
4	0.577	0.626	0.700	0.792	0.896
5	0.714	0.754	0.816	0.896	0.990

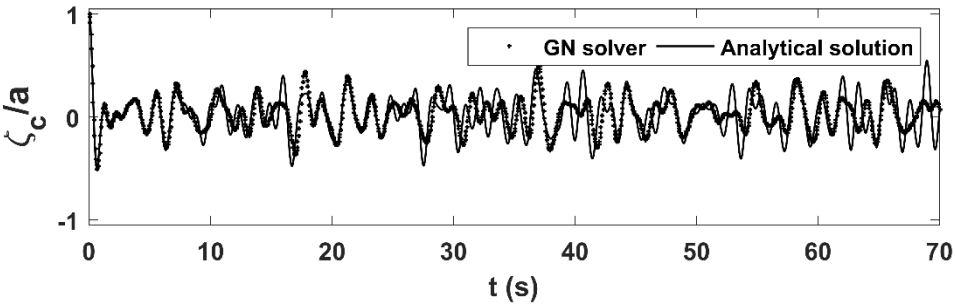

Figure 3. Analytical and predicted free surface elevation time histories at the centre of a basin for sloshing of an initial Gaussian hump in a square, flat-bottomed basin applying a = 0.045 m and b = 2 m^{-2}.

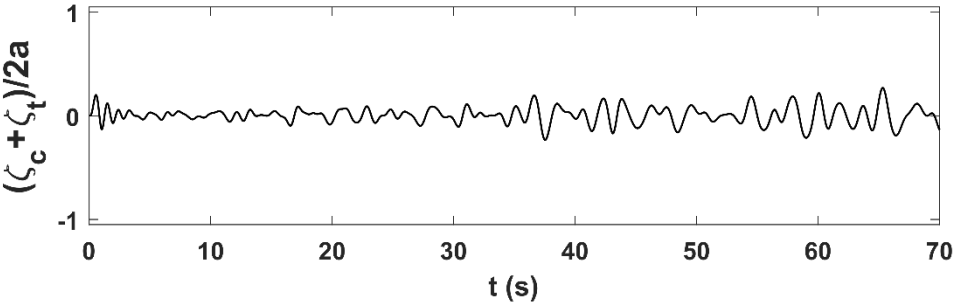

Figure 4. Free surface elevation time history of even harmonics component of an initial Gaussian hump for amplitude $a = h_0/2$ = 0.225 m at the centre of a square, flat-bottomed basin.

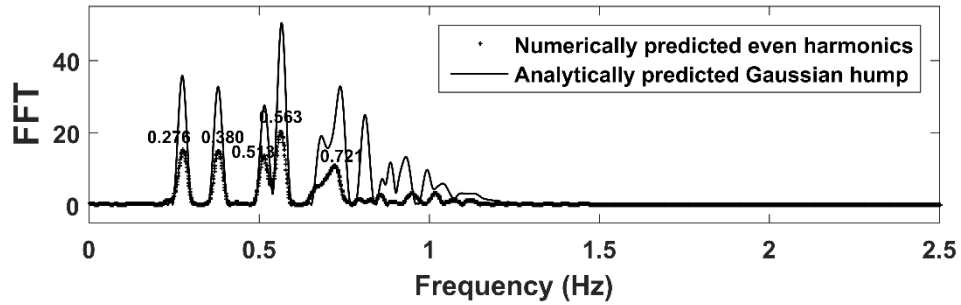

Figure 5. Comparison between analytically predicted FFT spectrum for the free surface elevation time history of the initial Gaussian hump with the numerically predicted FFT spectrum for the free surface elevation time history of even harmonics component.

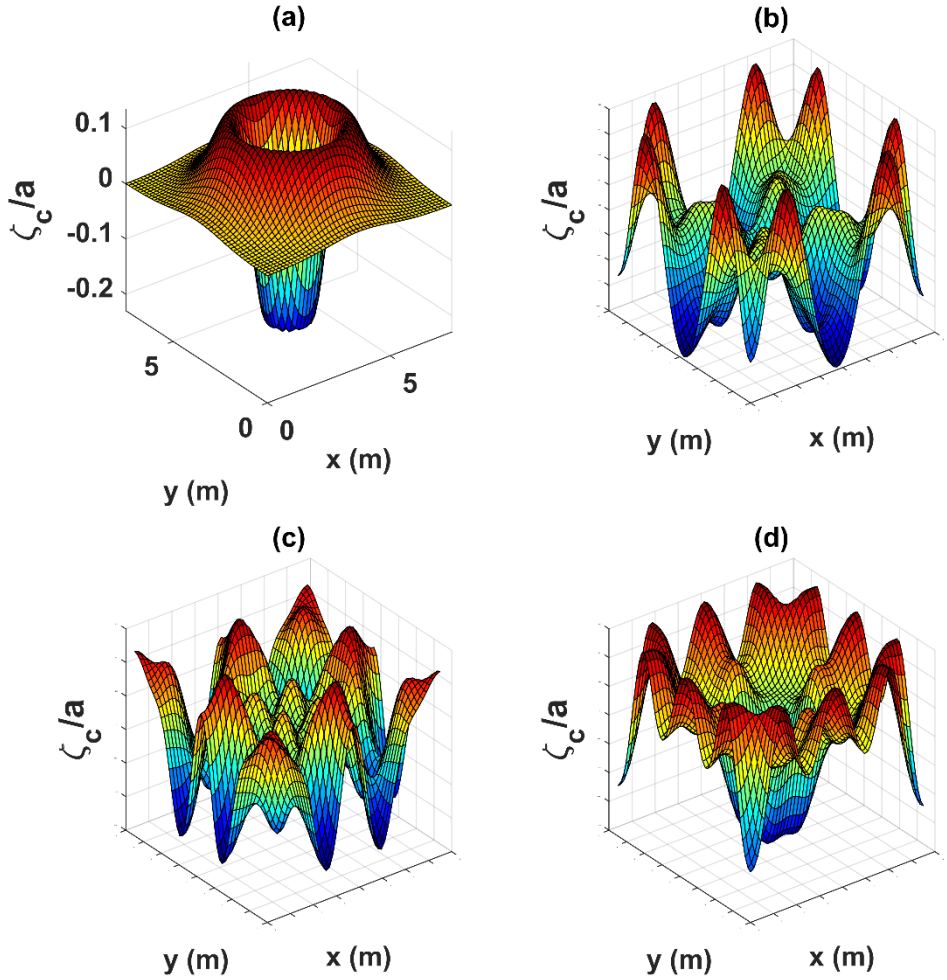

Figure 6. Predicted 3D visualisations of the sloshing of an initial Gaussian hump in a square, flat-bottomed basin: (a) $t = 1$ s; (b) $t = 5$ s; (c) $t = 10$ s; and (d) $t = 20$ s.

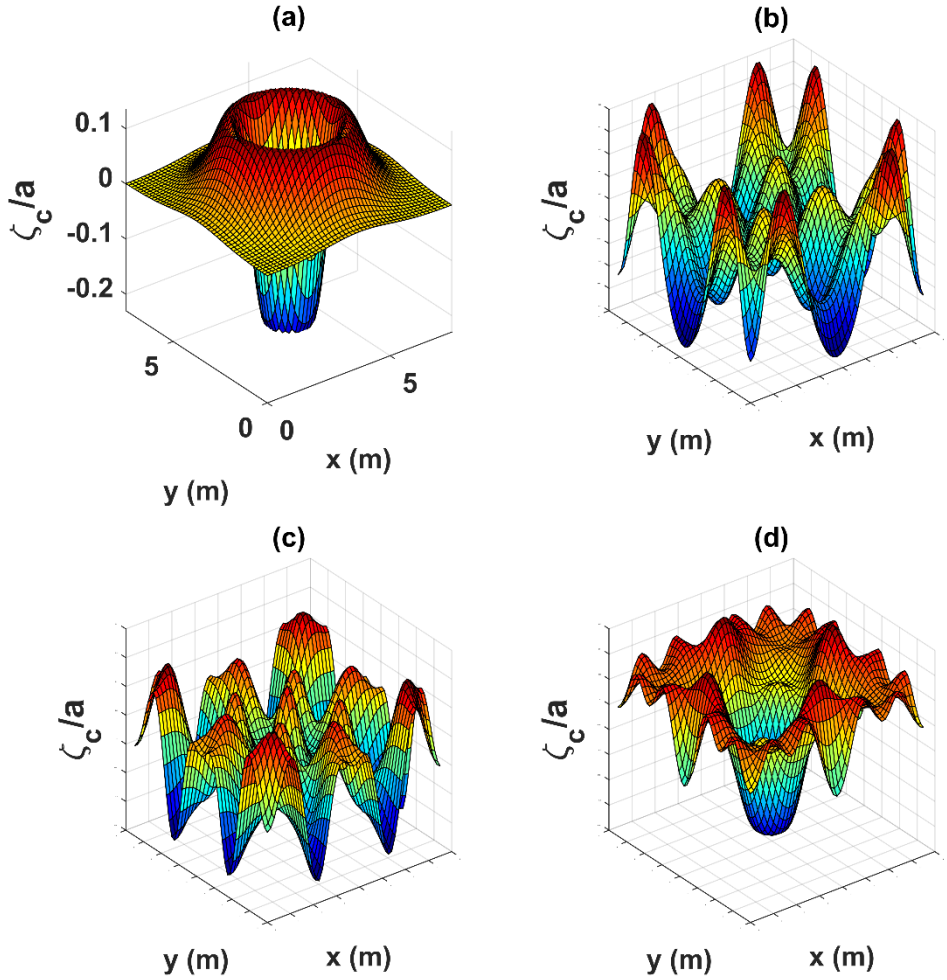

Figure 7. Analytical 3D visualisations of the sloshing of an initial Gaussian hump in a square, flat-bottomed basin: (a) $t = 1$ s; (b) $t = 5$ s; (c) $t = 10$ s; and (d) $t = 20$ s.

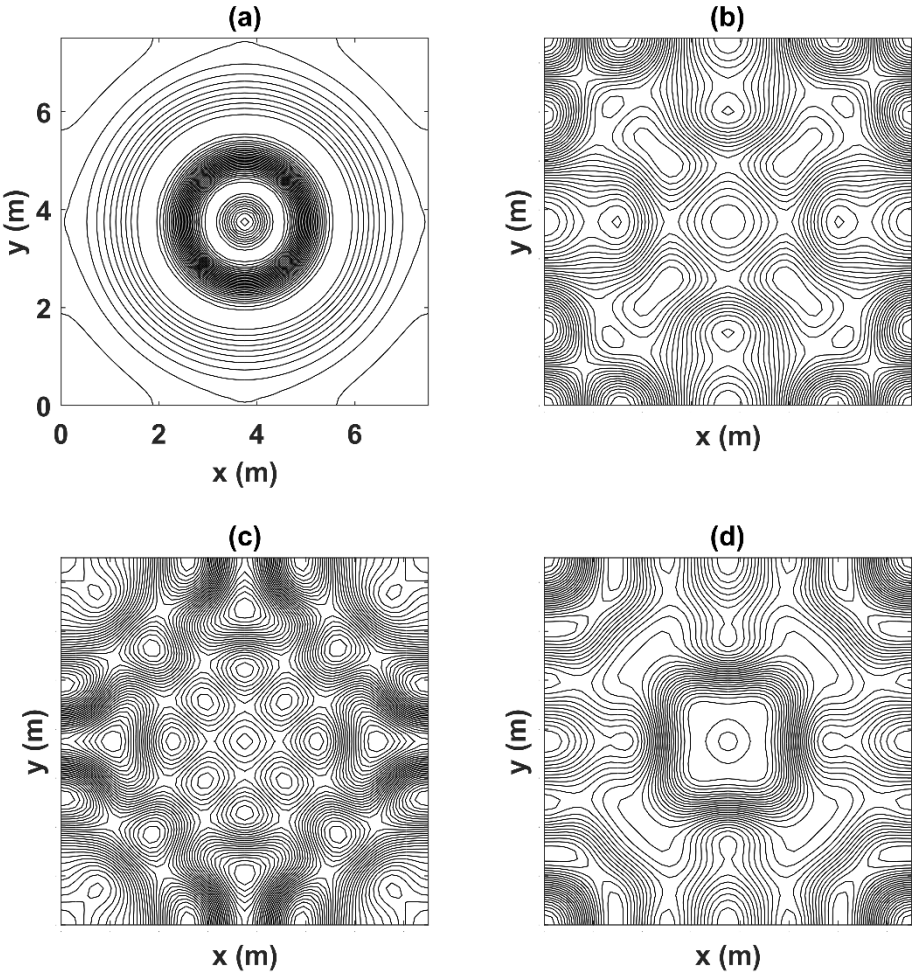

Figure 8. Predicted free surface contour maps of the sloshing of an initial Gaussian hump in a square, flat-bottomed basin: (a) t = 1 s; (b) t = 5 s; (c) t = 10 s; and (d) t = 20 s.

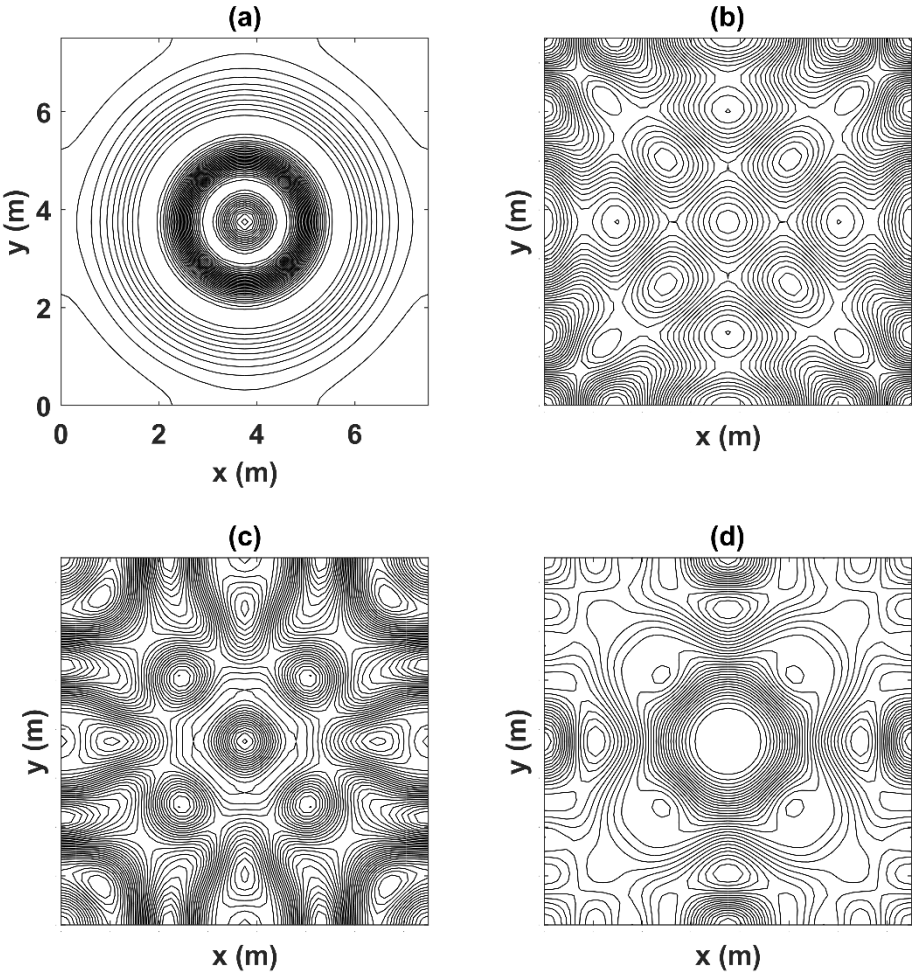

Figure 9. Analytical free surface contour maps of the sloshing of an initial Gaussian hump in a square, flat-bottomed basin: (a) t = 1 s; (b) t = 5 s; (c) t = 10 s; and (d) t = 20 s.

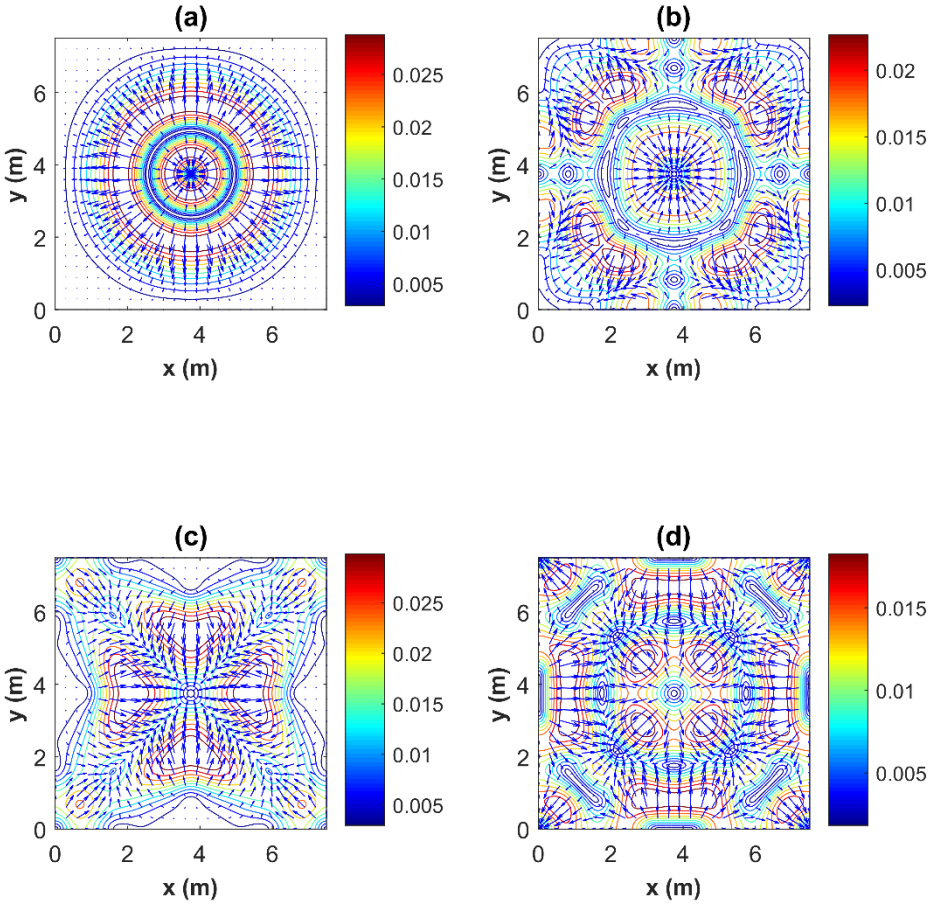

Figure 10. Numerically predicted velocity vectors and magnitude contours for the water surface in a square, flat-bottomed basin: (a) t = 1s; (b) t = 5 s; (c) t = 10 s; and (d) t = 20 s.

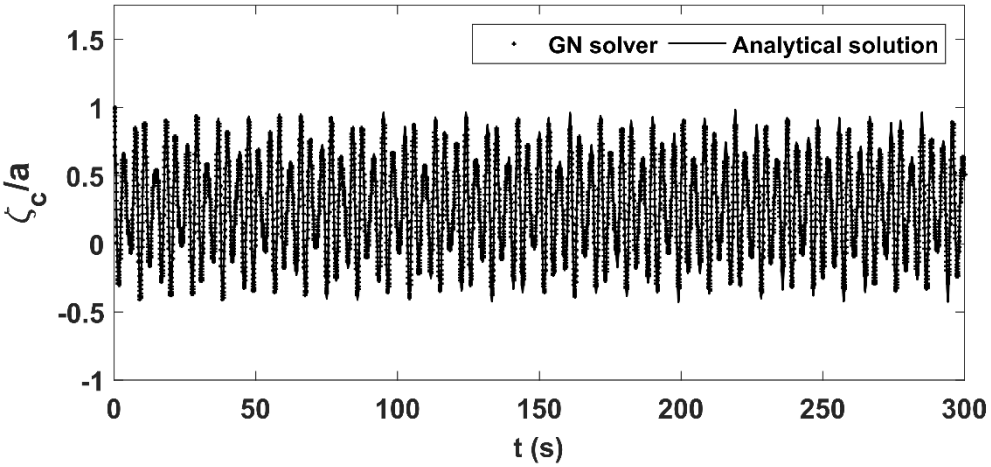

Figure 11. Analytical and predicted free surface elevation time histories at the centre of a basin for sloshing of an initial Gaussian hump in a square, flat-bottomed basin applying a = 0.001 m and b = 0.2 m^{-2}.

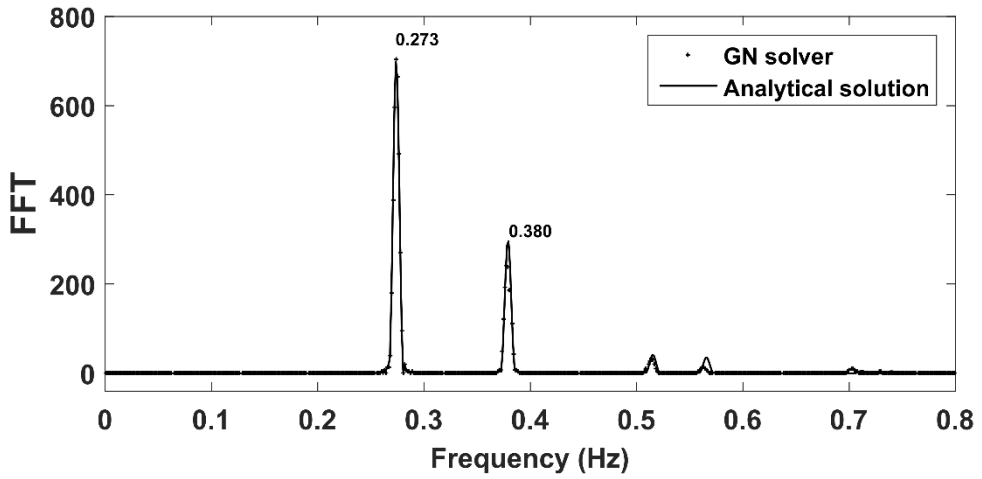

Figure 12. Comparison between analytically predicted FFT spectrum with the numerically predicted FFT spectrum for the free surface elevation time history of initial Gaussian hump applying a = 0.001m and b = 0.2m^{-2}.

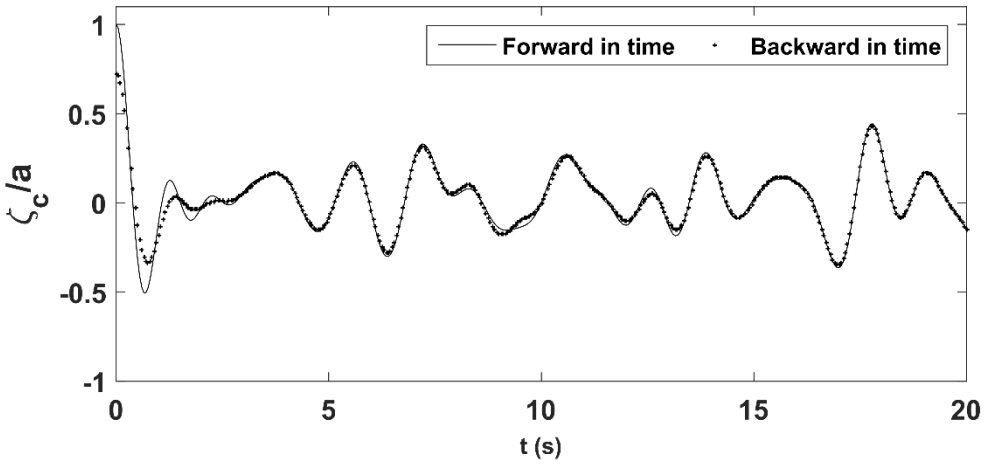

Figure 13. Reversibility test for Gaussian hump sloshing in a square, flat-bottomed basin: free surface elevation time history at the centre of basin for a = 0.045 m and b = 2 m^{-2}.

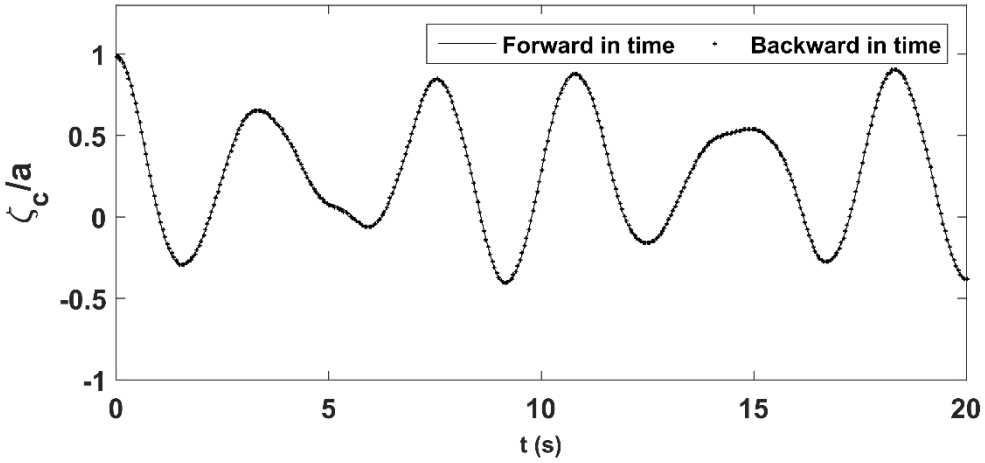

Figure 14. Reversibility test for Gaussian hump sloshing in a square, flat-bottomed basin: free surface elevation time history at the centre of basin for a = 0.001 m and b = 0.2 m^{-2}.

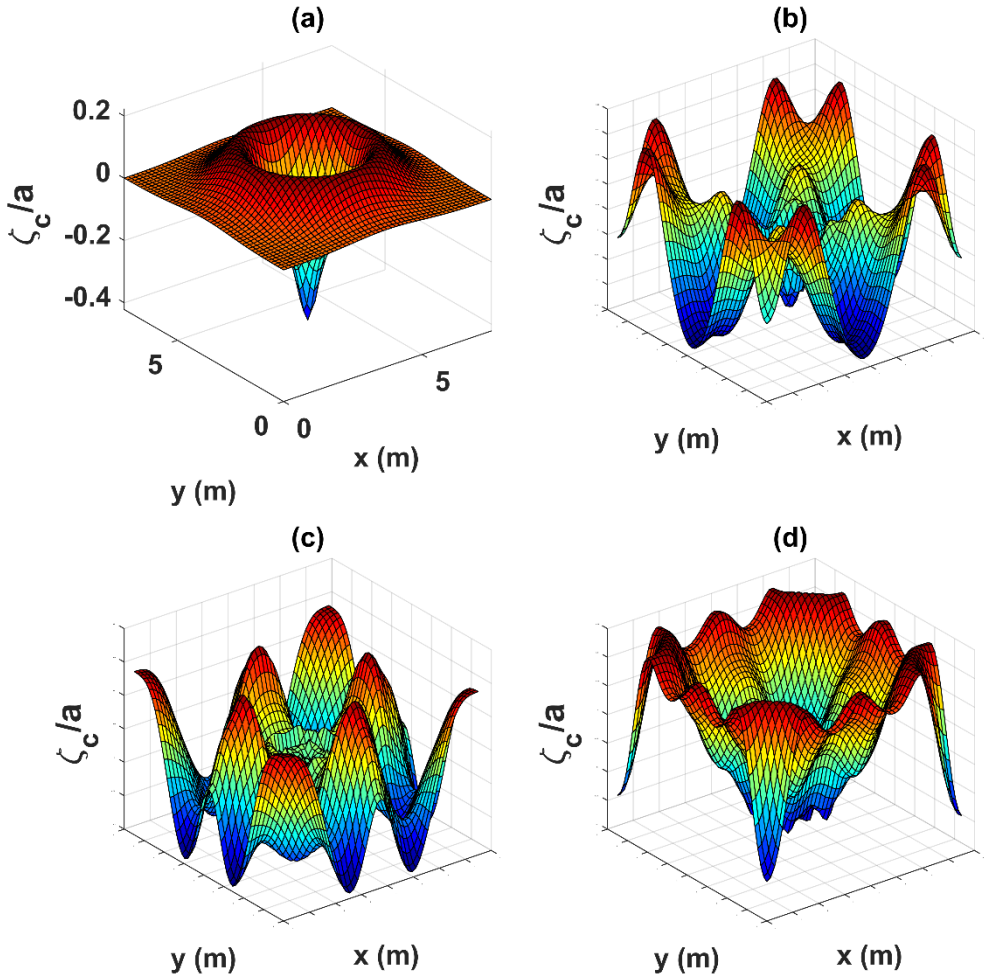

Figure 15. Predicted 3D visualisations of sloshing of an initial Gaussian hump in a square basin where the bed contains a central hump: (a) t = 1s, (b) t = 5s, (c) t = 10s; and (d) t = 20s.

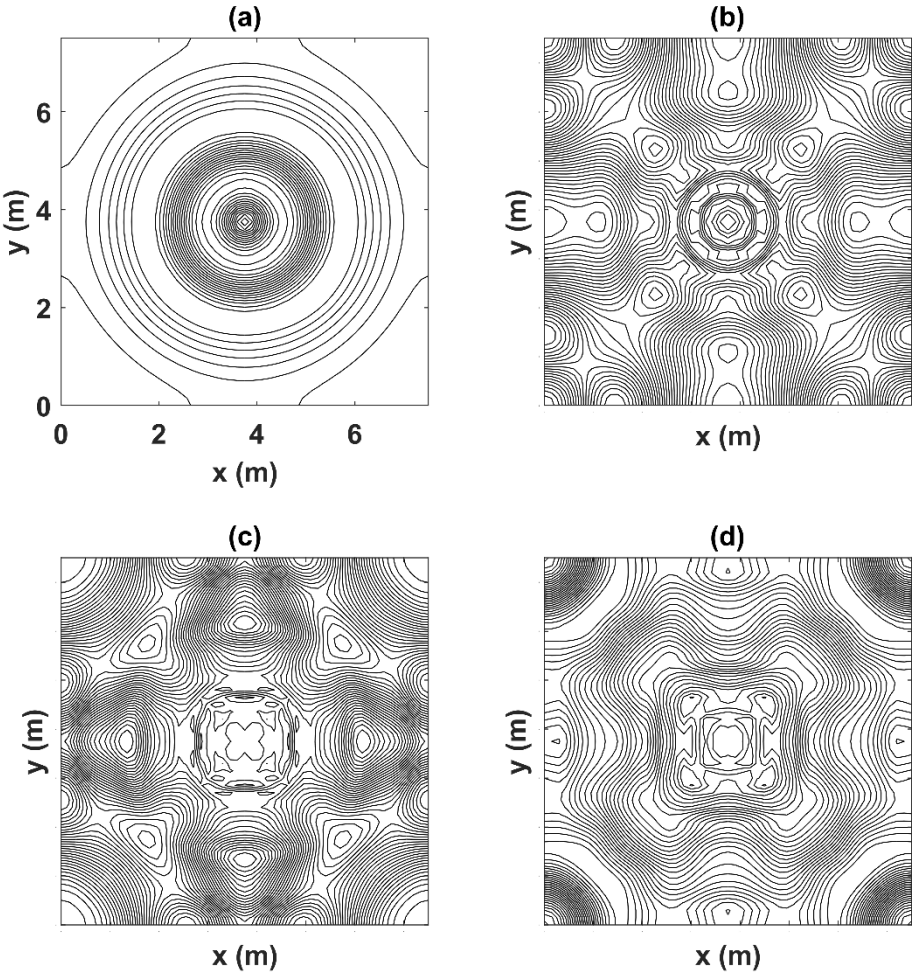

Figure 16. Predicted free surface elevation contour plots of sloshing of an initial Gaussian hump in a square basin where the bed contains a central hump: (a) t = 1 s, (b) t = 5 s, (c) t = 10 s; and (d) t = 20 s.

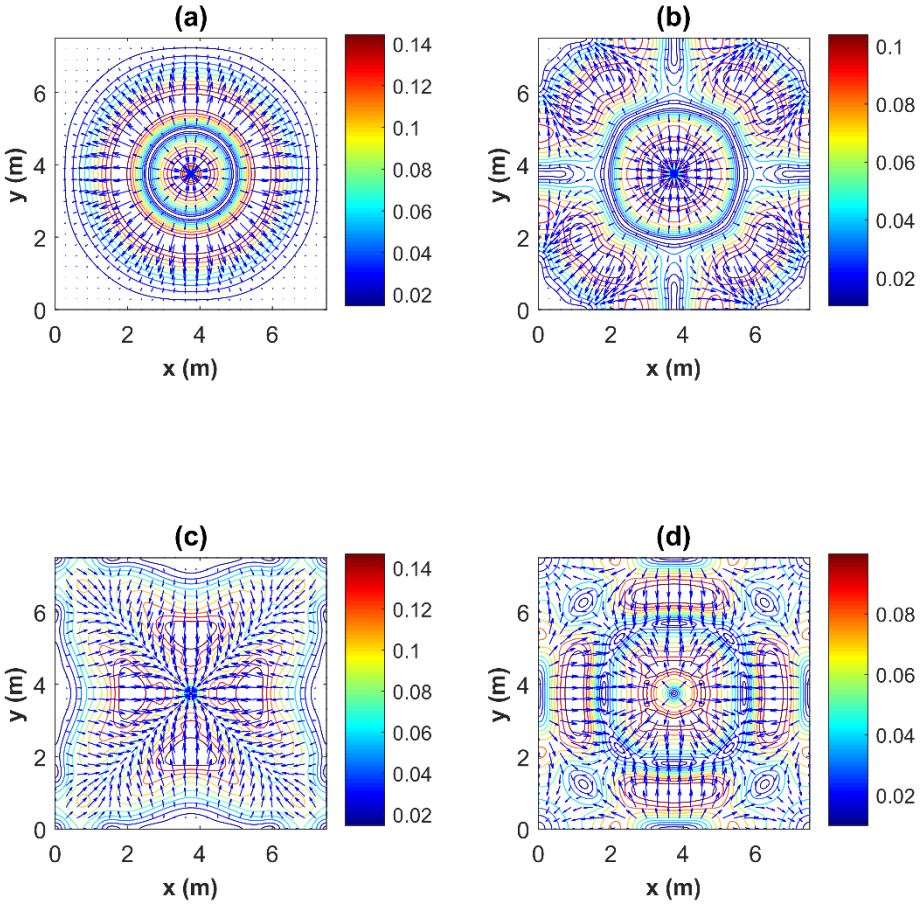

Figure 17. Predicted velocity vectors and magnitude contours for the water surface in a square basin where the bed topography contains a central hump: (a) t = 1s; (b) t = 5 s; (c) t = 10 s; and (d) t = 20 s.

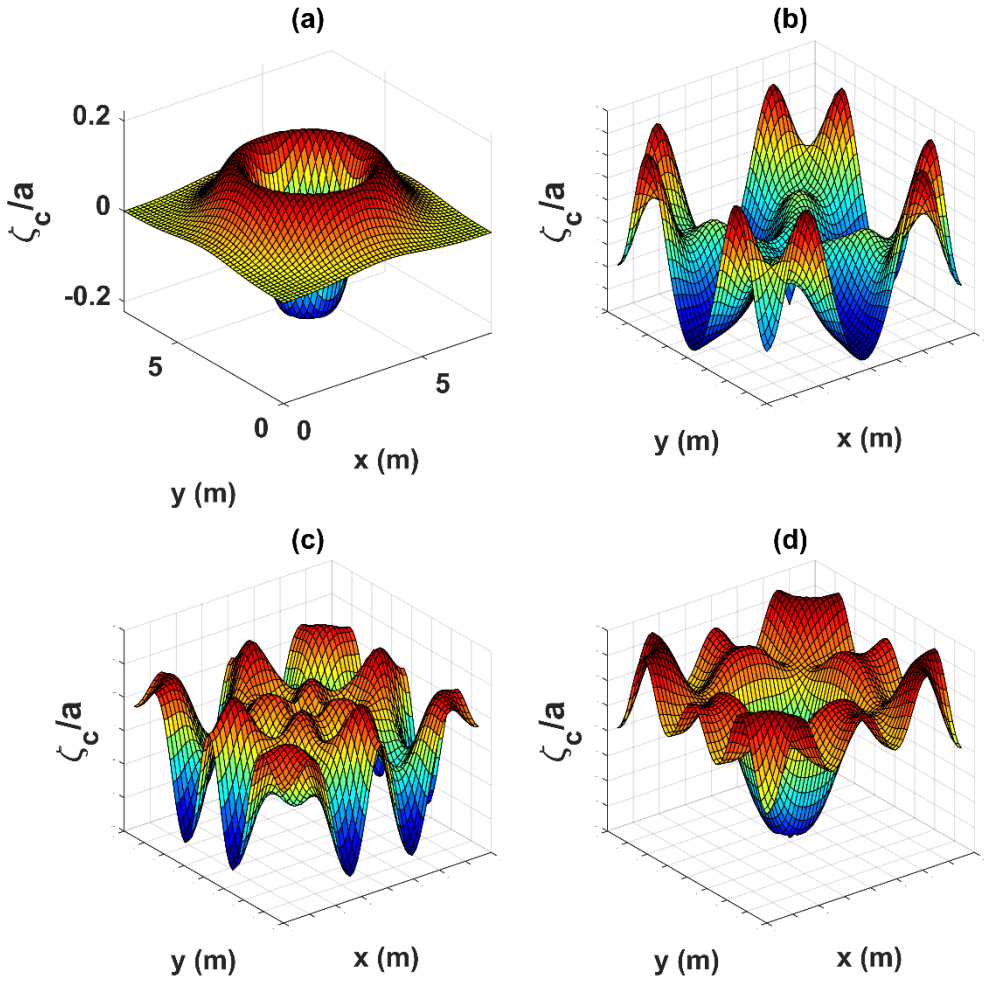

Figure 18. Predicted 3D visualisations of sloshing of an initial Gaussian hump in a square basin where the bed contains a central trough: (a) $t = 1$ s, (b) $t = 5$ s, (c) $t = 10$ s; and (d) $t = 20$ s.

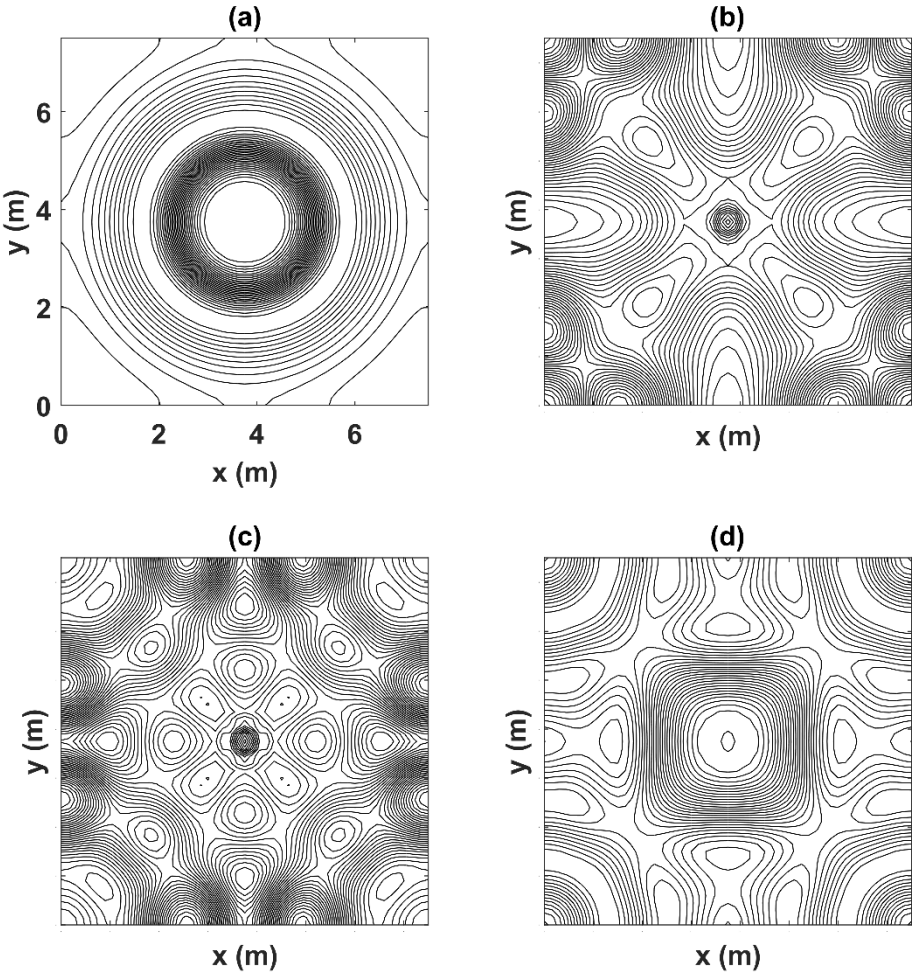

Figure 19. Predicted free surface elevation contour plots of sloshing of an initial Gaussian hump in a square basin where the bed contains a central trough: (a) t = 1 s, (b) t = 5 s, (c) t = 10 s; and (d) t = 20 s.

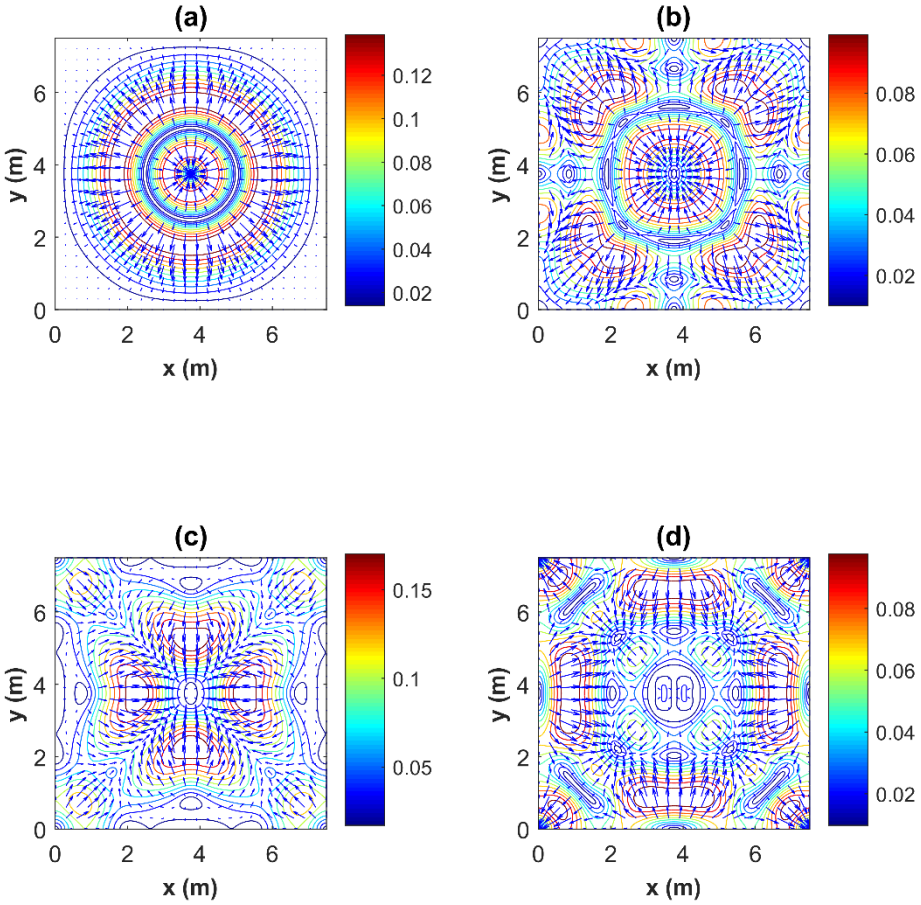

Figure 20. Predicted velocity vectors and magnitude contours for the water surface in a square basin where the bed topography contains a central trough: (a) t = 1s; (b) t = 5 s; (c) t = 10 s; and (d) t = 20 s.

Table of Contents

Nomenclature

a, amp	Amplitude
a_{z_b}	Bed amplitude
b	Inverse width in solitary wave equation
c	Solitary wave speed
a_n, b_n, c_n	Tridiagonal and pentadiagonal matrix coefficients
F, G	Vector derived from GN equations in x- and y-direction
f_{mn}	Frequencies
g	Gravity
h	Total water depth
ξ_c	Free surface elevation of the initial Gaussian hump
ξ_t	Free surface elevation of the initial Gaussian trough
h_s, h_0	Still water depth
i_{max}, j_{max}	Grid points in x- and y-directions
i_m, j_m	Integration points in Fourier analytical solution for Gaussian hump
k	Number of iteration
k_{mn}	Wave number
L_x	Basin length
L_y	Basin width
L_{xpo}, L_{ypo}	Initial position of the solitary wave crest
n, m	Wave modes and number of wave components

P	Pressure
r	number of iteration
t	Time
t_n	Specific time which is used in reversibility test
T_{mn}	Periods
u, v	Horizontal velocity components
w	Vertical velocity component
x, y	Horizontal distance and vertical distance
z_b	Bed elevation above fixed horizontal datum
$x',\ y'$	Transformed coordinate axis
Δt	Time interval
Δx	Spatial increment
ϕ	Phase
ρ	Water density
ζ, ξ	Free surface elevation above still water level
η	Free surface elevation above horizontal datum
$\eta_0(x, y)$	Elevation of initial Gaussian hump above horizontal datum
λ_n	Shape function
σ_{nm}	Kronecker's delta function
σ_η^2	Variance
∇	Gradient
ω	Angular frequency of the wave
θ	An angle θ to the x-axis

Chapter 1

Introduction and literature review

1.1. Introduction

The hydrodynamics of free surface motions in the ocean, closed tanks, and open channels are highly important in the assessment of offshore structures, sloshing in tanks, long waves in channels and rivers, etc. This chapter will consider different examples of such motions, leading to a description of different modelling strategies used to estimate free surface hydrodynamics.

1.1.1 Ocean waves

Free surface waves are formed as the gravitational response of a liquid to a disturbance, for example the wind blowing on the surface of the ocean, or a tsunami created by a submarine earthquake. Progressive waves in the ocean can be categorised according to their frequency as tides, swell, gravity waves, and capillary waves. These have oscillatory motions, and are created by gravitational attraction (tides), wind (gravity waves), etc. Waves of translation can also occur in the ocean, such as the tsunami, which is generated by a sudden displacement of the water mass. Such waves origins in seismic disturbance, volcanic action, landslides, etc. Tsunami can be simulated by numerical predictions. Tsunami wavelengths can reach hundreds of kilometres. Planetary (or Rossby) waves are another type of low amplitude, slowly propagating wave generated by oceanic density and wind-induced shear driven by the rotation of earth.

As waves enter shallow water, they refract, shoal, and break. Pre-breaking ocean waves are dispersive (i.e. waves of different wavelengths propagate with different phase speeds) whereas post-breaking waves tend to be non-dispersive and behave like hydraulic bores.

As waves approach breaking in shallow water, their behaviour becomes increasingly nonlinear until the wave becomes too steep and water particles on the surface move at a speed exceeding the celerity of the wave causing breaking to occur. Wave energy is dissipated through breaking, bed friction and turbulence. At the coast, waves can interact with the shoreline to cause edge waves and generate currents, such as the undertow, longshore current, rip current, and circulation cells. Waves diffract when they encounter large obstacles, causing energy to transfer from high energy zones to low energy zones (such as the lee of a breakwater).

Ocean waves have been responsible for many disasters in recorded history. Major coastal inundation has resulted from tsunamis, hurricane-induced storm surges on top of spring tides, extreme wave overtopping, and freak (rogue) wave interaction with maritime structures. Such disasters have caused very large numbers of fatalities and huge economic damage to certain coastal cities. Several examples follow.

Since 2000, tsunamis have caused enormous numbers of fatalities. A catastrophic example is that of the Indian Ocean tsunami which occurred on 26 December 2004 at the west coast of Sumatra. This tsunami resulted from an earthquake related to movement of the Burma Plate. The tsunami caused 230,000 fatalities and it was the deadliest tsunami in history (in terms of loss of life). The Indian Ocean tsunami also caused enormous environmental damage to mangroves, coral reefs, forests, coastal wetlands, vegetation, and groundwater [1].

Figure 1.1: Indian Ocean Tsunami (schools-wikipedia.org/images/1573/157307.jpg.htm)

[1] https://en.wikipedia.org/wiki/2004_Indian_Ocean_earthquake_and_tsunami

The Tōhoku earthquake and tsunami occurred on 11 March 2011, at 2:46 p.m. local time in Japan. The epicentre was located 373 km (231 miles) northeast of Tokyo. The seabed level off the coast of Japan dropped several metres due to the earthquake. Tsunami waves travelling towards the east coastline of the Japan and overwhelmed the 4 m sea protection walls. Tsunami wave heights reached 40.5 m in Miyako in Tōhoku's Iwate Prefecture and waves travelled 10 km inland in the Sendai. The Japanese National Police Agency reported 15,891 deaths, 6,152 injured, 2,584 people missing, and 228,863 displaced people. Vast structural damages occurred in the railways, roads and buildings. Dams collapsed and different part of city, even airports, went under the water [2]. Notably, the Tōhoku tsunami caused extensive damage to the Fukushima Daiichi nuclear plant. Equipment failures in cooling devices caused the nuclear reactors to start to melt down, and radioactive material was released into the environment. Since 2011, local residents experienced increased incidences of different types of cancer such as leukemia, thyroid cancer and breast cancer [3]. Figure 1.2 shows typical images of the Tōhoku tsunami and the destruction it wreaked on Japan.

Figure 1.2: Tōhoku tsunami's damages. Photographs of, (a) tsunami wave overtopping sea defences (telegraph.co.uk), (b) destruction at the coastal area (bulicip.comule.com), (c) destruction at the airport (telegraph.co.uk), (d) destruction at the nuclear reactor (prn.fm/tag/fukushima-daiichi-nuclear-disaster/).

[2] https://en.wikipedia.org/wiki/2011_T%C5%8Dhoku_earthquake_and_tsunami
[3] https://en.wikipedia.org/wiki/Fukushima_Daiichi_nuclear_disaster

Large-scale weather systems can cause differences in atmospheric pressure that drive surge waves. Many examples of such surges are provided by hurricanes and typhoons which are characterised by air rotating around a low pressure point. Hurricane Katrina was perhaps the deadliest hurricanes to impact the United States in recorded history. Hurricane Katrina formed from the interaction between a tropical wave and the remains of a tropical depression on 23 August 2005. The resulting storm surge inundated New Orleans. About 80% of New Orleans was inundated by water after the levees failed, with water depth reaching ~ 3m (10 ft) in some areas of the city. A total of 1,836 people lost their lives [4]. Katrina affected 90,000 square miles, causing huge economic damage to Louisiana, New Orleans and Mississippi states[5]. Katrina was one of the costliest hurricanes in the United States' history [6].

Figure 1.3: Hurricane Katrina and associated destruction in New Orleans (theguardian.com)

Hurricane Sandy developed in the Carribean in October 2012, with windspeeds reaching 500-700 m.p.h. Hurricane Sandy impacted on Haiti, killing ~54 people and making ~200,000 homeless. In Cuba, Sandy destroyed 15,000 homes and caused $2 billion economic damage. In US, Sandy created tragedy in 24 states, specifically, in New Jersey and New York[7]. Widespread disruption of the electricity network occurred in New York City and large areas of Manhattan went under water. The economic damage to the United States was about $65 billion [8].

[4] https://en.wikipedia.org/wiki/Hurricane_Katrina
[5] https://www.dosomething.org/facts/11-facts-about-hurricane-katrina
[6] http://www.cnbc.com/2015/08/30/-and-now-in-pictures.html
[7] https://en.wikipedia.org/wiki/Hurricane_Sandy
[8] http://earthobservatory.nasa.gov/Features/ClimateStorms/

Freak (rogue) waves are large waves observable in the ocean, which can be extremely hazardous to ships and maritime structures [9]. Freak waves contain enormous amounts of energy and their heights have been known to exceed 20 m, an example being the Draupner wave that occurred in the north sea on New Year's Day 1995.

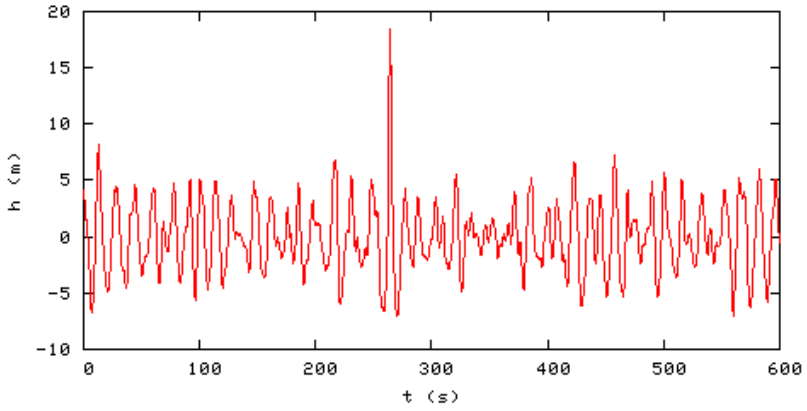

Figure 1.4: Time history of the Draupner wave (en.wikipedia.org/wiki/Rogue_wave)

1.1.2 Application of numerical modelling in prediction of oceanic disasters

As mentioned before, people's life is threatened by oceanic disasters. Therefore, a model that can predict the behaviour of gravity waves in the ocean is critical to scientists, and engineers who are in charge of understanding hazardous behaviour of extreme ocean waves, and thereby planning mitigation or evacuation strategies. To develop a numerical model, appropriate governing equations should be selected in the first place. Next, capable numerical solver should be developed to solve the governing equations. Finally, numerical predictions are compared with the experimental data in order to determine how well these two are in agreement.

The present 1D and 2D Level I GN models permit realistic simulations of the free surface hydrodynamic motions of water in tanks and channels, and can incorporate the effect of non-uniform bed topography. The model could potentially be useful in simulating the behaviour of freak waves, ship waves, tsunami waves and the interaction of such waves with marine structures, ships, oil platforms and renewable energy devices. The present GN model is not capable of simulating hurricane-induced storm surges.

[9] https://en.wikipedia.org/wiki/Rogue_wave

1.1.3 Sloshing in Tanks

When liquid with a free surface starts to move in a container, this behaviour is known as slosh. Examples of slosh occur when water in a closed tank is set in motion by a free surface displacement, or liquid natural gas in a container is vibrated by an external driving force, such as an earthquake or movement induced from transport, or the resonant seiching in a natural basin. In large tankers which carry oil and liquid gas, sloshing in the storage tanks may cause unexpected rolling motions of the tankers. The response of the liquid free surface is affected by amplitude and motion frequencies of its container; therefore, sloshing involves complex fluid-structure interactions. During sloshing, different types of motions are produced by energy exchange between the liquid and its container. In small containers, surface tension plays an important role in the behaviour of liquid as it moves up and down the tank wall, undergoing wetting and drying.

Free surface slosh motions can be categorised as simple planar, rotational, symmetric, asymmetric and chaotic (Ibrahim, 2005). In a basic sloshing problem the hydrodynamic pressure distributions, natural frequencies, and dynamic motions of the liquid free surface have to be estimated in order to evaluate the performance of the moving container. At the wall of a moving tank, the flow velocity must match the velocity of the wall, and so the hydrodynamic pressure of liquid in the vicinity of the wall is directly related to the tank velocity.

A 2-D flow tank can be classified into low and high liquid fill depths (Ibrahim, 2005). Low liquid fill depth tanks can experience the formation of hydraulic jumps and travelling waves for excitation periods around liquid resonance, when high pressures occur. In high liquid fill depth tanks, large standing waves are produced in the resonance frequency range.

In practice, civil engineers use sloshing tests to assess the likelihood of such phenomenon occurring in oil tanks, elevated water towers and large dams. For example, a water tank may be installed on the roof of a skyscraper to monitor building oscillations during an earthquake. The results of sloshing tests are also used to inform the design of stable liquefied oil containers in tankers and offshore platforms.

In the present thesis, a numerical model will be used to simulate sloshing tests in order to achieve better understanding of nonlinear even harmonic oscillations of free surface sloshing of an initial disturbance to the free surface of a liquid in a closed square basin. Figure 1.5 shows typical sloshing phenomenon that occur at different scales ranging from a cup of coffee, a moving tanker truck, and oceanic tankers transporting liquid natural gas.

(a) (b) (c)

Figure 1.5: (a) sloshing in a cup of coffee (huffingtonpost.com)

(b) tank sloshing (blog.pointwise.com/2013/10/11/this-week-in-cfd-125/)

(c) stable liquefied oil containers in tankers (mossww.com/technologies/lng.php)

1.1.4 Waves in an Open Channel

Propagation of gravity waves in an open channel is influenced by the channel geometry, in particular the bed slope. Such waves are usually created by the head differences in the channel, and may result from heavy rainfall events upstream (flood waves), tides (e.g. tidal surges and bores), the movement of ships along a canal, river flow interactions with the bed, etc.

Different types of waves including regular progressive waves, irregular progressive waves and solitary waves of displacement are formed in open channel, the type of wave depending on the mode of creation (i.e. shear or displacement mechanisms). Such waves offer interesting case studies for hydraulic and environmental engineers and researchers.

Figure 1.6 shows the River Lee in Cork, Ireland, as it experiences a flood wave, where the flow regime changes from subcritical to transcritical (Van Te Chow, 1959).

(a) (b)

Figure 1.6: Flood wave propagation along the River Lee in Cork, Ireland. Photograph (a) a hydraulic jump as the flow transitions from supercritical to subcritical as it passes a weir, taken from joanfrankham.wordpress.com (b) taken from darkroomdave.com

Solitary waves propagate along the channel without any change in their form, elevation and velocity. In 1834 John Scott Russell was the first person to discover this type of wave when he observed a solitary-type wave released by a boat as it manoeuvred in the Union Canal at Hermiston. He observed that the solitary wave moved without deformation. He estimated the wave was about 9 m long, and propagated about 2 – 3 km at a constant speed of about 14 km/h with amplitude about 0.3 – 0.45 m along the channel. Scott Russell called this solitary wave or soliton a "Wave of Translation".

Later, he built a wave tank at his residence to investigate further the behaviour of nonlinear solitons. Scott Russell reported that: (*a*) a stable solitary wave can propagate a large distance; (*b*) the wave speed is dependent on the ratios of wave amplitude and wave width with respect to the water depth; (*c*) interaction of solitary waves with each other does not change their original features and they will never merge or combine; and (*d*) in a tank of small depth, a high-amplitude wave will split into medium- and small-amplitude waves.

In 1871, Joseph Boussinesq (who developed one of the most applicable nonlinear theories of waves) utilised Scott Russell's results in his study of the nonlinear behaviour of solitons [10]. The present study will examine the use of Green-Naghdi equations to represent the behaviour of nonlinear solitary waves in an open channel and a closed basin. Figure 1.7 displays solitary wave propagation in a laboratory wave channel and the interaction between two solitary waves in the sea.

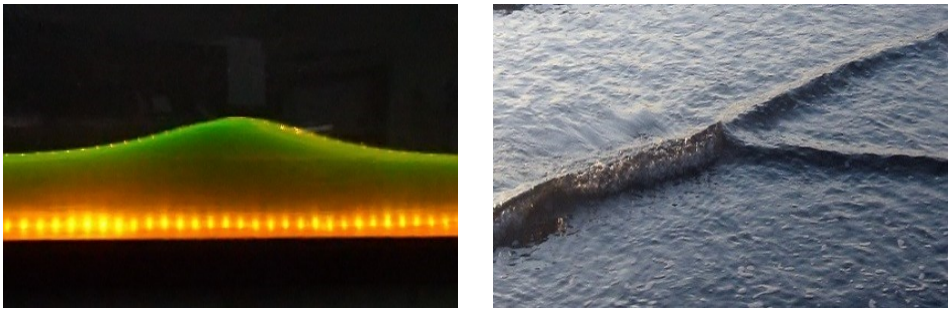

(a) (b)

Figure 1.7: Photograph (a) solitary wave in a laboratory wave channel

(en.wikipedia.org/wiki/John_Scott_Russell)

(b) interaction of a pair of solitons (scitation.aip.org)

[10] https://en.wikipedia.org/wiki/John_Scott_Russell

1.2 Review of Literature for Mathematical Models of waves

Free surface waves can be categorised as progressive, sloshing and solitary waves of displacement depending on whether they are excited as free or forced surface responses in a container, or shear driven waves in an open domain, or displacement waves (see e.g. Dean and Dalrymple (1991) for a fundamental textbook on the mechanics of such categories of waves). Gravity waves in the open ocean and in liquid containers and channels are often approximated by infinite Fourier series of sine and cosine waves which are dispersive and may travel in different directions depending on the mode of generation (Stewart, 2008). This linear representation of ocean sea states ignores inherently nonlinear pre-breaking wave behaviour (peaked crests and broad troughs) and nonlinear wave-wave interactions.

The earliest theories for progressive waves were developed by Airy (1841) and Stokes (1847, 1880), and were based on potential theory idealisations (i.e. that the fluid was inviscid, and the flow irrotational). Airy's theory was linear, in that it was strictly derived for waves of zero amplitude. Stokes extended the theory to deal with waves of finite amplitude, and he obtained series solutions that were later computed to high order by many hydrodynamicists in the late 20^{th} C (e.g. Skjelbraia and Hendrickson 1960, etc.). Nonlinear shallow water wave theories were developed from the 1800s onwards; examples being cnoidal wave theory by Korteweg and de Vries (1895) and later Fenton (1979). Turning to solitary waves, Russell (1844), Boussinesq (1871), and Rayleigh (1876) made pioneering contributions to the early understanding of such waves of displacement. By the 1970s, major advances were made in the development of high order solutions of solitary waves (see e.g. Fenton (1972,1974), Longuet-Higgins and Fenton (1974) and Byatt-Smith and Longuet-Higgins (1976)). There are several other wave theories that should be noted such as trochoidal wave theory (Gerstner 1802), linearised long wave theory (Stoker 1957), stream function wave theory (Dean 1965), and computational wave theories (e.g. Schwartz 1974). A detailed description of the different wave theories is given by Sarpkaya and Isaacson (1981).

Linearised fluid flow mass and momentum equations can be used to study the lowest modes of liquid motion for a tank undergoing forced harmonic oscillations of low amplitude. Sloshing theories originated from fluid field equations for behaviour

of free surface waves whereby mass and momentum hydrodynamics equations which are used as governing equations. Linear analytical solutions of small-amplitude sloshing behaviour have been derived that are applicable to regular geometric tanks (usually of cylindrical or rectangular shape). Relevant analytical solutions have been derived by many researchers such as Ewart (1956), Bauer (1962), Lomen (1965), Ibrahim (1969), Henrici *et al*. (1970), Kornecki (1983) and Bauer (1999).

It should be noted that the linearised solution of sloshing behaviour is not exactly realistic since not only does the position of free surface vary but also the combined free surface boundary condition is nonlinear, involving mixed kinematic and dynamic boundary conditions. The nonlinear behaviour of sloshing is particularly affected by the initial wave amplitude (which is assumed zero in linear models). Application of perturbation techniques permits approximate nonlinear solutions to the governing equations that could be helpful to obtain better understanding of rotary sloshing, nonlinear liquid interaction with elastic structures, internal resonance effects, stochastic dynamics of liquid bridges, cross-wave and spatial resonance. At high amplitudes, nonlinearity in the free surface motions can lead to amplitude jumps, chaotic motions and internal resonances (Ibrahim, 2005). Resonant excitation at the lowest frequency is extremely important, since it can change stable 2-D motions to unstable 3-D and chaotic motions (Ibrahim, 2005).

The foregoing analytical solutions are very particular to idealised situations. To extend to more realistic domains, computational methods have become widely used. These include: (1) boundary element and finite element potential flow solvers; (2) CFD – Navier-Stokes solvers with volume of fluid treatment of the free surface, Navier-Stokes solvers with level-set treatment of the free surface, Navier-Stokes solvers with mappings of the free surface; and (3) smoothed-particle-hydrodynamics. The drawback of 3D computational methods is in their inherently high computational expense, and so considerable effort has gone into depth-averaged approaches which are cheaper to compute and yet capture much of the physics. Examples include the shallow water equations (see e.g. Lamb 1879), Boussinesq-type equations (Madsen and Sørensen, 1992), and more recently the Green-Naghdi (GN) equations (1974). The nonlinear shallow water equations (SWEs) are derived as the depth-averaged form of

continuity and Navier-Stokes momentum equations, and are usually restricted to long wave behaviour because of the neglect of vertical motions and the consequent hydrostatic pressure assumption. Boussinesq equations are more complicated, and incorporate treatment of the vertical motions. GN equations are in a sense an intermediate form between SWEs and Boussinesq equations.

Figure 1.8 shows the behaviour of water particles in the shallow section, intermediate section and deep section of the ocean. In shallow depth, Figure 1.8 (a), the effect of vertical acceleration is quite small and nonlinear shallow water equations present accurate simulation of wave behaviour. However, in the intermediate depth, Figure 1.8 (b), since the effect of vertical acceleration becomes more significant the nonlinear shallow water equations are not capable of simulating wave behaviour in this section of the ocean. Green-Naghdi equations (low-level) and Boussinesq equations, both have the capability to simulate the wave behaviour in the intermediate depth section of the ocean. In deep water, Figure 1.8 (c), where the effect of vertical acceleration is much stronger than the intermediate depth, high-level of GN equations provides accurate prediction of the wave behavior (for more details see Sarpkaya and Isaacson (1981) and Nadiga et al. (1996)).

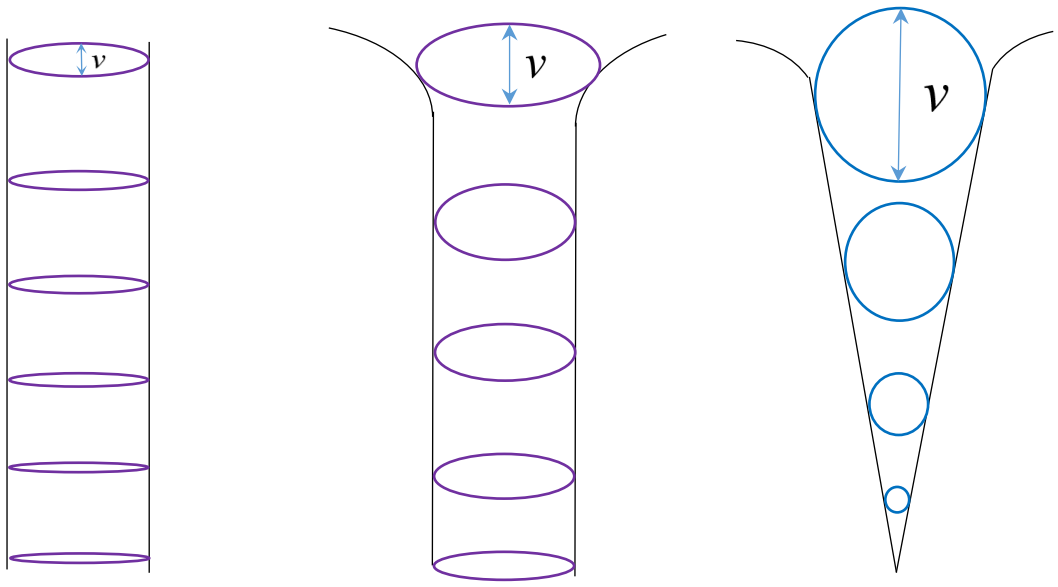

Figure 1.8: Effect of vertical acceleration in (a) shallow depth, (b) intermediate depth and (c) deep depth of ocean

1.3 Review of Literature of Green-Naghdi (GN) Theory

Green and Naghdi (1976) pioneered the development of nonlinear equations for two-dimensional incompressible inviscid fluid sheets. Green and Naghdi found that the exact solutions of a directed fluid sheets were similar to the equations obtained by Longuet-Higgins (1972). They investigated the exact time-dependent free surface flows of incompressible inviscid fluid provided that gravity and surface tension are ignored. In 1986, Green and Naghdi proposed a theory of fluid sheets known as (GN theory) to model the two dimensional continuum of unsteady inviscid three-dimensional flows. The theory facilitated prediction of unsteady, non-periodic, free surface flows. GN theory utilises some aspects of perturbation analysis in building up first-, second-, and higher-order approximations (called **levels**) to layer-averaged mass and momentum equations. According to Webster and Shields (1991) the GN approach assumes a particular flow kinematic structure in the vertical direction for shallow water problems. The fluid velocity profile is given by a finite sum of coefficients depending on space and time, multiplied by a weighting function. GN fluid sheet theory reduces the dimensions from three to two, yielding equations that can be solved efficiently. No scale is introduced and no term is deleted (Webster and Shields, 1991).

Fluid sheet theory is ideal for application to steady and unsteady two-dimensional fluid problems. The lowest level of GN theory nevertheless permits the kinematic boundary conditions to be satisfied. The theory is applicable to problems include shallow water waves, bow waves generated by marine vehicles, waterfalls, and wave reflection by obstacles (Webster and Shields, 1991). Green and Naghdi introduced a dispersive term in the momentum equation to model traveling solitary wave solutions. According to Demirbilek and Webster (1992) the difference between the classical shallow water equations and GN theory lies in the fact that since the dynamic and kinematic boundary conditions are met, GN theory is self-consistent; whereas, in Stokes and Boussinesq theories in which the dynamic and kinematic boundary conditions are not satisfied simultaneously, the equations show inconsistencies.

There are two types of GN theory: restricted and unrestricted. To draw a line between unrestricted and restricted GN theories of shallow water, it should be mentioned that the latter can successfully model an irrotational shallow water flow field.

Restricted GN theory was derived from the first level of the direct theory by means of a constrained director (Shields and Webster, 1988). Later, this procedure was extended to the k^{th} level theory (Demirbilek and Webster, 1992). In other words, in a restricted GN theory, the k components of the two-dimensional velocity components are constrained.

Demirbilek and Webster (1992) developed an unrestricted version of GN theory of shallow water by enforcing conservation of mass and momentum in the vertical direction and implementing exact boundary conditions, and demonstrated that GN theory can appropriately predict the behaviour of nonlinear numerical wave tank. Demirbilek and Webster found that the original GN theory had certain shortcomings, particularly when the crest velocity equals the wave speed.

According to Webster and Shields (1991), Green-Naghdi (GN) sheet theory lies between classical perturbation methods and pure numerical schemes. Webster and Shields note that for classical perturbation methods, there is usually no evidence that the assumed series is convergent. However, in certain flow problems, such as two-dimensional water waves in both shallow and deep water (which is addressed by GN theory), there is ample evidence of convergence. Another difference between classical perturbation methods and GN theory is that, in the former, the exact field equation is satisfied but the boundary conditions are only approximately satisfied. However, in GN theory the boundary conditions are met exactly but the field equations are approximated. GN theory simplifies free surface flow problems by reducing them from three- to two-dimensions.

Certain problems cannot be solved without using a nonlinear, time domain model of fluid flow. Examples include the shoaling of a shallow water wave as it approaches a beach, and the transition of a group of steep deep water waves when they collide with an obstacle such as a vertical wall (Webster and Shields, 1991). Unlike Boussinesq approximations, GN theories (especially, those of higher level) are more

accurate and effective modeling of shoaling waves. Furthermore, GN theories are valid for large-amplitude waves travelling over a sloping bottom (Webster and Shields, 1991).

Demirbilek and Webster (1992) categorised the one-, two-, and three-dimensional GN equations; for example, the GN equations reduce to the KdV equation assuming wave propagation is one-directional and the amplitude is finite. Demirbilek and Webster also found that 3D GN theory is superior to the 2D version in describing amplitude nonlinearity, frequency dispersion, fraction, shoaling, reflection, diffraction, seabed topography, wave-breaking and wave formation.

GN level II theory for deep water predicts linear and nonlinear waves to quite good accuracy for a wide variety of steepness (Webster and Shields (1991)), and is applicable if the spectrum of the waves remains within a narrow band. Moreover, numerical approximations by Webster and Shields confirmed the application of high level GN theory to determine the group velocity of moderately nonlinear waves for the evolution of the envelope of an incoherent wave-packet. Webster and Shields applied high level GN theory to the shoaling of water waves on a beach, and the collision of a finite group of deep water waves against a vertical wall, and found good agreement with a perturbation approximation.

Nadiga et al. (1996) compared GN, general Boussinesq (gB) and shallow water equation solvers for shallow fluid flow over a two-dimensional ridge, similar to oceanic flow over a seamount. The results demonstrated that the GN approximations were accurate for both deep and shallow water, whereas gB approximations were limited to shallow water. In addition, the GN approximations which ignored the scale of nonlinearity were also more applicable to deep water than gB approximations.

Xu et al. (1997) developed two-dimensional and three-dimensional GN models with a wave-absorbing beach for nonlinear irregular wave propagation by adding a numerical damping term into the GN equations, hence extending their applicability to unbounded flows. Kim and Ertekin (2000) developed an irrotational Green-Naghdi (IGN) model of large-amplitude nonlinear wave propagation and irregular wave-wave interactions in deep water. To this end, they transformed Lagrangian and Eulerian

variables for the water free surface. Kim and Ertekin observed that IGN Level II and GN Level III attained similarly accurate results for nonlinear regular and irregular wave simulations. Examining the IGN model from levels 1 to 12, Kim and Ertekin indicated that IGN level III can predict periodic, maximum-height waves better than the original GN model. It was found that with the increase of the level of IGN model the model converges to the exact solution. Kim and Ertekin concluded that although the IGN model could not fully reproduce freak waves, the model could be fruitfully applied to nonlinear wave-interaction in three dimensions.

Wu and Chen (2003) used the GN equations to study unsteady ship waves in shallow water of varying depth. Unlike wind and ocean waves, ship waves are hardly dissipated and may cause resonance. This increases the wave height, and the resulting energy could in turn damage ports, harbor infrastructure, and disturb ships. Wu and Chen incorporated the moving pressure disturbance to the free surface of an advancing ship in the GN equations in order to model ship-induced waves in shallow water over uneven bed topography. Hayir (2006) used GN theory to model near-field tsunami propagation.

Xia et al. (2008) extended nonlinear GN level I theory to fluid-structure interaction, and tested their model for cases involving a very large floating structure (VLFS) and solitary waves. Their results revealed that both the nonlinearity of the fluid motion and the stiffness of the structures played key roles in the hydro-elastic response of a VLFS to solitary waves.

Métayer et al. (2009) proposed a hybrid numerical method employing a Godunov-type scheme to solve the GN model for dispersive shallow water waves in transcritical flows, including dam-breaks.

Zhao and Duan (2010) found that the higher the GN level, the more accurate the simulation of fully nonlinear shallow water waves as they shoal and interact with a plane beach. By comparing level II and level III GN restricted theories, Zhao and Duan revealed that restricted level III gave results that agreed better than restricted level II with stream-function theory. Zhao et al. (2010) also conducted a study of tsunami simulation using level II GN theory. The results obtained from the three various seabed movements (impulsive, creeping and transitional) matched well with

earlier test results (Hayir (2006)). Moreover, Zhao et al. applied GN theory to examine the three-dimensional near-field tsunami amplitudes caused by submarine landslides and slumps spreading in two orthogonal directions. The GN results fully matched the linear solution.

Pearce and Esler (2010) wrote a pseudo-spectral algorithm to solve the two-dimensional GN shallow water equations for rotating flows, such as those at meso-scale in the ocean. Webster et al. (2011) applied GN equations of level > IV to shallow water waves, and found that dispersion was more accurately modelled at increasing, odd levels (i.e. V, VII, etc.).

Bonneton et al. (2011) used a shock-capturing scheme to solve the fully nonlinear, weakly dispersive GN equations for shallow water waves of large amplitude. To handle wave breaking, the Green–Naghdi equations were transformed to the NSWE, locally in time and space, by eliminating the dispersive step when the wave is ready to break. The approach was demonstrated to be highly applicable to wave transformation in coastal areas: shoaling, wave breaking and run-up. In a similar study, Chazel et al. (2011) also used a high order finite volume shock-capturing scheme to solve the Green–Naghdi equations and hence simulate strongly nonlinear, dispersive wave propagation. Recently, Zhang et al. (2012) derived Boussinesq–Green–Naghdi rotational water wave theory for nonlinear water wave transformation over different depths.

The foregoing literature review has described advances in the development and application of GN equations, the aim being to achieve more accurate simulations. The bulk of research effort has been in extending the GN equations to higher levels rather than to multi-dimensions. In certain cases, to achieve stable results with reasonable computer requirements, researchers found it necessary to eliminate certain complicated, problematic terms from the original 1-D GN equations. Most existing GN solvers are based on second-order spatial discretisations even though the order of the equations may be higher. Previous solvers tend to have been developed for shallow flow domains where the bed is horizontal. There is clearly scope for development of high order solvers of multi-dimensional GN equations incorporating all terms that apply to weakly nonlinear shallow flows over non-uniform, mild-sloped beds, such as characterise flow in many rivers, lakes, estuaries and coastal situations.

1.4 Aim and objectives

The aim of the present thesis is to develop a verified model of weakly nonlinear wave propagation in shallow flow domains by applying 1D and 2D level I GN equations. The objectives are

- To derive the 1-D and 2-D Level I GN equations for shallow flow over an uneven bed.
- To develop numerical solvers of the Level I GN equations which are stable, convergent, and accurate.
- To verify the solvers using standard benchmark tests.
- To carry out a parameter study of nonlinear sloshing in a square basin with a horizontal bed.
- To examine nonlinear sloshing in a square basin with non-uniform bathymetry.
- To examine the interaction of a solitary wave with a wall in a channel.

1.5 Applications of the developed level I GN model

The developed GN model is merely applicable to the shallow water of the ocean. However, it is recommended that the higher level of GN equations be used as governing equations for the deep water of the ocean for the future research. The present 1D and 2D level I GN equations are capable of modeling nonlinear behaviour of wave before the surf zone. In order to have correct predictions of breaking waves in the surf zone, the researcher proposes a hybrid numerical solver be developed in which GN equations are applied to the pre-breaking wave domain and the nonlinear shallow water equations are used for the post-breaking waves for further investigations. The present GN models are capable of simulating wave behaviour over uniform and non-uniform bathymetries.

1.6 Thesis outline

Chapter 2 describes the mathematical derivation of the governing 1D and 2D level I GN equations. Chapter 3 lays out the finite difference discretisation of the equations and relevant boundary conditions, and describes implicit second-order tridiagonal and fourth-order pentadiagonal matrix solvers used to solve 1D and 2D GN equations. Chapter 4 presents numerical results for sloshing in a square tank and solitary wave propagation over a flat–bed channel, these benchmark test cases being used to verify and validate the numerical schemes. Grid convergence and stability checks are undertaken. Chapter 5 presents parameter study simulations of Gaussian hump in a closed basin, and a Fast Fourier Transform (FFT) is applied to examine the nonlinear sloshing modes. Chapter 6 presents the results for solitary wave propagation in a channel, and its nonlinear behaviour of the solitary wave is also examined as it interacts with a wall. Chapter 7 lists the main conclusions and recommendations.

Chapter 2

Mathematical Formulation of 1D and 2D Level I GN Equations

2.1 Introduction and Mathematical Description

The Green-Naghdi (GN) theory provides a model for two and three dimensional steady and unsteady flows. The theory simplifies analysis of shallow and deep water problems by reducing three dimensions to two. GN theory yields governing equations that may be readily solved numerically. GN theory is potentially more capable for engineering applications than and the shallow flow equations. Nadiga et al. (1996) compared GN, general Boussinesq (gB) and shallow water equation solvers for shallow fluid flow over a two-dimensional ridge, similar to oceanic flow over a seamount. The results demonstrated that the GN approximations were accurate for both deep and shallow water, whereas gB approximations were limited to shallow water. In addition, the GN approximations which ignored the scale of nonlinearity were also more applicable to deep water than gB approximations. The GN method partially represents vertical motions, unlike the shallow water equations. Demirbilek and Webster (1992) applied GN theory to the prediction of unsteady, non-periodic, free surface problems using perturbation approximations.

Herein the general 2D level I GN equations are derived (1D GN equations derived for different levels by Demirbilek and Webster (1992)). It is assumed that water is inviscid and incompressible.

Figure 2.1 illustrates the key variables that define the flow geometry in the *x*-*z* plane. Here z_b is the elevation of the bottom surface boundary above a fixed horizontal datum, h_s is the still water depth, ξ is the free surface elevation above still water level, h is the total depth ($h = h_s + \xi$), and η is the stage, the elevation of free surface above the fixed horizontal datum ($\eta = h + z_b$).

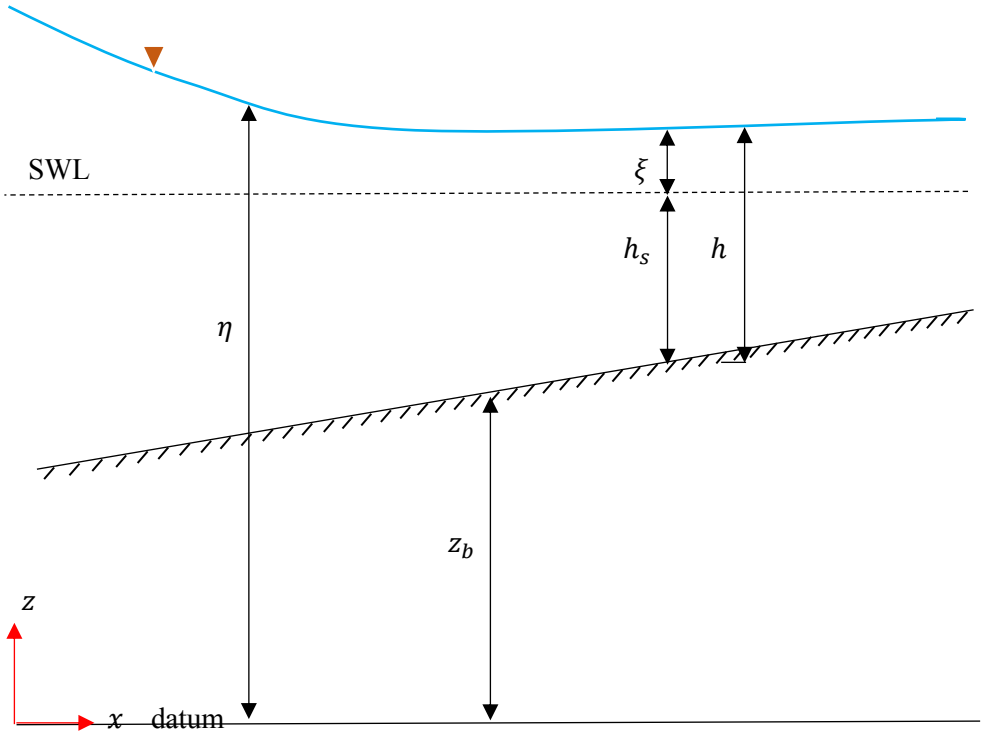

Figure 2.1: Key variables that define the flow geometry in the *x*-*z* plane

2.1.1 Derivation of 2D Level I Green-Naghdi Equations

The 2D Level I GN equations model wave propagation over non-uniform bed topography, and incorporate coupled spatial advection effects expressed as cross-derivative terms that are not modelled in one-dimensional space. The GN equations represent wave amplitude nonlinearity, frequency dispersion, refraction, shoaling, reflection, and diffraction.

2.1.2 3-D Continuity and Momentum Equations and Kinematic Boundary Condition for a Free Surface Flow of Inviscid, Incompressible Liquid

In a 3-D Cartesian system, the velocity vector $\boldsymbol{V}$ may be written as:

$$\boldsymbol{V} = (u, v, w) = \vec{\imath}\, u + \vec{\jmath}\, v + \vec{k}\, w \tag{2.1}$$

In which u, v, w are the velocity components in the *x, y, z* directions and $\vec{\imath}, \vec{\jmath}, \vec{k}$ are unit vectors in Cartesian system.

Similarly the vector of gravitational acceleration is:

$$\boldsymbol{G} = \left(g_x, g_y, g_z\right) = \vec{\imath}\, g_x + \vec{\jmath}\, g_y + \vec{k}\, g_z \tag{2.2}$$

where g_x, g_y, g_z are the Cartesian components.

In vector notation, the continuity equation is:

$$\nabla . \boldsymbol{V} = 0 \tag{2.3}$$

where $\nabla = \vec{\imath}\frac{\partial}{\partial x} + \vec{\jmath}\frac{\partial}{\partial y} + \vec{k}\frac{\partial}{\partial z}$, such that

$$\left(\vec{\imath}\,\frac{\partial}{\partial x} + \vec{\jmath}\frac{\partial}{\partial y} + \vec{k}\frac{\partial}{\partial z}\right).\left(\vec{\imath}\, u + \vec{\jmath}\, v + \vec{k}\, w\right) = 0 \tag{2.3a}$$

giving

$$\frac{\partial u}{\partial x} + \frac{\partial v}{\partial y} + \frac{\partial w}{\partial z} = 0 \tag{2.3b}$$

The momentum conservation equation is as follows:

$$\left(\frac{\partial}{\partial t} + \boldsymbol{V}.\nabla\right)\rho V = -\nabla P - \rho g \tag{2.4}$$

where P is pressure, ρ is density, and t is time.

The momentum conservation equation can be expanded in the *x*, *y* and *z* directions as follows:

(x-direction momentum) $$\frac{\partial \rho u}{\partial t} + \frac{\partial \rho u u}{\partial x} + \frac{\partial \rho u v}{\partial y} + \frac{\partial \rho u w}{\partial z} = -\frac{\partial P}{\partial x} \quad (2.4a)$$

(y-direction momentum) $$\frac{\partial \rho v}{\partial t} + \frac{\partial \rho v u}{\partial x} + \frac{\partial \rho v v}{\partial y} + \frac{\partial \rho v w}{\partial z} = -\frac{\partial P}{\partial y} \quad (2.4b)$$

(z-direction momentum) $$\frac{\partial \rho w}{\partial t} + \frac{\partial \rho w u}{\partial x} + \frac{\partial \rho w v}{\partial y} + \frac{\partial \rho w w}{\partial z} = -\rho g \quad (2.4c)$$

There is no flow through the bed, and so the kinematic bed boundary condition is as follows:

$$w\big|_b = \frac{\partial z_b}{\partial t} + \frac{dx}{dt}\frac{\partial z_b}{\partial x} + \frac{dy}{dt}\frac{\partial z_b}{\partial y} \quad (2.5)$$

where z_b is the elevation of the bottom boundary above the fixed horizontal datum.

By definition, $u_b = \frac{dx}{dt}\big|_{z_b}$ and $v_b = \frac{dy}{dt}\big|_{z_b}$. Then, at the bed,

$$w\big|_b = \frac{\partial z_b}{\partial t} + u_b\frac{\partial z_b}{\partial x} + v_b\frac{\partial z_b}{\partial y} \quad (2.6)$$

At the free surface there are two boundary conditions. The kinematic free surface boundary condition is:

$$w\big|_s = \frac{\partial \eta}{\partial t} + \frac{dx}{dt}\frac{\partial \eta}{\partial x} + \frac{dy}{dt}\frac{\partial \eta}{\partial y} \quad (2.7)$$

where η is the elevation of the top surface boundary above the fixed horizontal datum. By definition, $u_s = \frac{dx}{dt}\big|_{\eta}$ and $v_s = \frac{dy}{dt}\big|_{\eta}$, and so

$$w\big|_s = \frac{\partial \eta}{\partial t} + u_s\frac{\partial \eta}{\partial x} + v_s\frac{\partial \eta}{\partial y} \quad (2.8)$$

The dynamic free surface boundary condition is $P = P_a$ at $z = \eta$.

2.1.3 GN Continuity Equation for Free Surface Flow of Inviscid, Incompressible Liquid

In order to derive the GN continuity equation, it is assumed that the velocity vector can be written as follows:

$$\boldsymbol{V} = \vec{u}(x,y,z,t) = \sum_{n=0}^{k} \overrightarrow{W_n}\,(x,y,t)\;\lambda_n(z) \tag{2.9}$$

where $\overrightarrow{W_n} = (u_n, v_n, w_n)$ is a vector of velocity component approximations at level *n*, λ_n are assumed shape functions depending on *z,* and *k* is the level of approximation of GN theory. Expansion of Eqn. (2.9) for level I leads to the following velocity parameters:

$$\begin{cases} u(x,y,z,t) = u_0(x,y,z,t) \\ v(x,y,z,t) = v_0(x,y,z,t) \\ w(x,y,z,t) = w_0(x,y,z,t) + w_1(x,y,z,t)\;(z - z_b) \end{cases} \tag{2.10}$$

The boundary conditions (2.6) and (2.8) become

$$w_0(x,y,z,t) = \frac{\partial z_b}{\partial t} + u_0\frac{\partial z_b}{\partial x} + v_0\frac{\partial z_b}{\partial y} \tag{2.11}$$

$$w_0(x,y,z,t) + w_1(x,y,z,t)\;(\eta - z_b) = \frac{\partial \eta}{\partial t} + u_0\frac{\partial \eta}{\partial x} + v_0\frac{\partial \eta}{\partial y} \tag{2.12}$$

By inserting the velocity parameters (2.10) into (2.3b):

$$\frac{\partial u_0}{\partial x} + \frac{\partial v_0}{\partial y} + \frac{\partial [w_0(x,y,z,t) + w_1(x,y,z,t)\;(z - z_b)]}{\partial z} = 0 \tag{2.13}$$

$$w_1 = -\frac{\partial u_0}{\partial x} - \frac{\partial v_0}{\partial y}\;. \tag{2.14}$$

When Eqns. (2.11) and (2.14) are inserted into (2.12), the 2D level I GN Eqn, Eqn. (2.16), is obtained:

$$\frac{\partial z_b}{\partial t} + u_0 \frac{\partial z_b}{\partial x} + v_0 \frac{\partial z_b}{\partial y} - \frac{\partial u_0}{\partial x}(\eta - z_b) - \frac{\partial v_0}{\partial y}(\eta - z_b) = \frac{\partial \eta}{\partial t} + u_0 \frac{\partial \eta}{\partial x} + v_0 \frac{\partial \eta}{\partial y} \quad . \quad (2.15)$$

or

$$\frac{\partial \eta}{\partial t} + \frac{\partial [u_0(\eta - z_b)]}{\partial x} + \frac{\partial [v_0(\eta - z_b)]}{\partial y} = \frac{\partial z_b}{\partial t} \quad . \quad (2.16)$$

If $(\eta - z_b) = h$, then the 2D level I GN continuity equation is rewritten as:

$$\frac{\partial \eta}{\partial t} + \frac{\partial (u_0 h)}{\partial x} + \frac{\partial (v_0 h)}{\partial y} = \frac{\partial z_b}{\partial t} \quad (2.17)$$

$$\frac{\partial h}{\partial t} + \frac{\partial (u_0 h)}{\partial x} + \frac{\partial (v_0 h)}{\partial y} = 0 \quad . \quad (2.18)$$

By inserting Eqn. (2.9) into Eqn. (2.3b) the upper level of GN continuity equation becomes:

$$\sum_{n=0}^{k} \left(\frac{\partial u_n}{\partial x} + \frac{\partial v_n}{\partial y}\right) \lambda_n(z) + \sum_{n=0}^{k} w_n \frac{\partial \lambda_n(z)}{\partial z} = 0 \quad . \quad (2.19)$$

Similarly inserting Eqn. (2.9) into the kinematic boundary conditions Eqns. (2.6) and (2.8) gives:

$$\sum_{n=0}^{k} w_n \lambda_n(z_b) = \frac{\partial z_b}{\partial t} + \sum_{n=0}^{k} u_n \lambda_n \frac{\partial z_b}{\partial x} + \sum_{n=0}^{k} v_n \lambda_n \frac{\partial z_b}{\partial y} \quad (2.20)$$

$$\sum_{n=0}^{k} w_n \lambda_n(\eta) = \frac{\partial \eta}{\partial t} + \sum_{n=0}^{k} u_n \lambda_n \frac{\partial \eta}{\partial x} + \sum_{n=0}^{k} v_n \lambda_n \frac{\partial \eta}{\partial y} \quad . \quad (2.21)$$

Eqn. (2.20) is the bottom boundary condition and Eqn. (2.21) is the free surface kinematic boundary condition.

2.1.4 GN Momentum Equations for Free Surface Flow of Inviscid, Incompressible Liquid

Consider the general momentum conservation equations Eqn. (2.4). Integrating (2.4a), gives:

$$\int_{z_b}^{\eta}\left(\frac{\partial \rho u}{\partial t}+\frac{\partial \rho uu}{\partial x}+\frac{\partial \rho uv}{\partial y}+\frac{\partial \rho uw}{\partial z}\right)\lambda_n dz=-\int_{z_b}^{\eta}\left(\frac{\partial P}{\partial x}\right)\lambda_n dz\ . \tag{2.22}$$

The left hand side of the Eqn. (2.22) can be rewritten as:

$$\int_{z_b}^{\eta}\left(\frac{\partial \rho u}{\partial t}\lambda_n+\frac{\partial \rho uu}{\partial x}\lambda_n+\frac{\partial \rho uv}{\partial y}\lambda_n+\frac{\partial \rho uw}{\partial z}\lambda_n\right)dz \tag{2.23}$$

Using the chain rule for fourth term gives

$$\int_{z_b}^{\eta}\left(\frac{\partial \rho u}{\partial t}\lambda_n\right)dz+\int_{z_b}^{\eta}\left(\frac{\partial \rho uu}{\partial x}\lambda_n\right)dz+\int_{z_b}^{\eta}\left(\frac{\partial \rho uv}{\partial y}\lambda_n\right)dz+\rho uw\,\lambda_n\big|_{z_b}^{\eta}$$
$$-\int_{z_b}^{\eta}(\rho uw\lambda_n')\,dz \tag{2.24}$$

where $\lambda_n'=\frac{d\lambda_n}{dz}$.

Then, the Leibnitz Rule is applied to the right hand side of Eqn. (2.22), giving

$$-\int_{z_b}^{\eta}\left(\frac{\partial P}{\partial x}\right)\lambda_n dz=-\frac{\partial\left(\int_{z_b}^{\eta}\rho\lambda_n\,dz\right)}{\partial x}+[P\lambda_n]\big|_{\eta}\frac{\partial \eta}{\partial x}-[P\lambda_n]\big|_{z_b}\frac{\partial z_b}{\partial x} \tag{2.25}$$

Eqns. (2.24) and (2.25) are combined to give

$$\int_{z_b}^{\eta}\left(\frac{\partial \rho u}{\partial t}\lambda_n\right)dz+\int_{z_b}^{\eta}\left(\frac{\partial \rho uu}{\partial x}\lambda_n\right)dz+\int_{z_b}^{\eta}\left(\frac{\partial \rho uv}{\partial y}\lambda_n\right)dz+\rho uw\,\lambda_n\big|_{z_b}^{\eta}$$
$$-\int_{z_b}^{\eta}(\rho uw\lambda_n')dz=-\frac{\partial P_n}{\partial x}+\hat{P}\lambda_n\big|_{\eta}\frac{\partial \eta}{\partial x}-\bar{P}\lambda_n\big|_{z_b}\frac{\partial z_b}{\partial x} \tag{2.26}$$

where $P_n = \left(\int_{z_b}^{\eta} P\lambda_n \, dz\right)$, $\hat{P}$ is pressure at the free surface, and $\bar{P}$ is pressure at the bottom. Inclusion of the kinematic assumed parameters, Eqn. (2.10), on the left hand side of Eqn. (2.26) leads to

$$\int_{z_b}^{\eta}\left(\frac{\partial \rho \sum_{m=0}^{k} u_m \lambda_m \lambda_n}{\partial t}\right) dz + \int_{z_b}^{\eta}\left(\frac{\partial \rho \sum_{m=0}^{k} u_m \lambda_m \sum_{r=0}^{k} u_r \lambda_r \lambda_n}{\partial x}\right) dz$$

$$+ \int_{z_b}^{\eta}\left(\frac{\partial \rho \sum_{m=0}^{k} u_m \lambda_m \sum_{r=0}^{k} v_r \lambda_r \lambda_n}{\partial y}\right) dz + \rho \sum_{m=0}^{k} u_m \lambda_m \sum_{r=0}^{k} w_r \lambda_r \lambda_n \Big|_{z_b}^{\eta}$$

$$- \int_{z=z_b}^{\eta} \left(\rho \sum_{m=0}^{k} u_m \lambda_m \sum_{r=0}^{k} w_r \lambda_r \lambda_n'\right) dz$$

$$= \sum_{m=0}^{k} \rho \frac{\partial u_m}{\partial t} \int_{z_b}^{\eta} \lambda_m \lambda_n \, dz + \sum_{m=0}^{k}\sum_{r=0}^{k} \rho \frac{\partial u_m u_r}{\partial x} \int_{z_b}^{\eta} \lambda_m \lambda_r \lambda_n \, dz$$

$$+ \sum_{m=0}^{k}\sum_{r=0}^{k} \rho \frac{\partial u_m v_r}{\partial y} \int_{z_b}^{\eta} \lambda_m \lambda_r \lambda_n dz + \sum_{m=0}^{k}\sum_{r=0}^{k} \rho u_m w_r \lambda_m \lambda_r \lambda_n \Big|_{z_b}^{\eta}$$

$$- \sum_{m=0}^{k}\sum_{r=0}^{k} \rho u_m w_r \int_{z_b}^{\eta} \lambda_m \lambda_r \lambda_n' \, dz$$

$$= \sum_{m=0}^{k} \rho \frac{\partial u_m}{\partial t} \, y_{mn} + \sum_{m=0}^{k}\sum_{r=0}^{k} \rho \frac{\partial u_m u_r}{\partial x} \, y_{mrn} + \sum_{m=0}^{k}\sum_{r=0}^{k} \rho \frac{\partial u_m v_r}{\partial y} \, y_{mrn}$$

$$+ \sum_{m=0}^{k}\sum_{r=0}^{k} \rho u_m w_r \lambda_m \lambda_r \lambda_n \Big|_{z=z_b}^{\eta} - \sum_{m=0}^{k}\sum_{r=0}^{k} \rho u_m w_r \, y_{mr}^{n} \qquad (2.27)$$

where

$y_{mn} = \int_{z=z_b}^{\eta} (\lambda_m \lambda_n) dz$, $y_{mrn} = \int_{z=z_b}^{\eta} (\lambda_m \lambda_r \lambda_n) dz$ and $y_{mr}^{n} = \int_{z=z_b}^{\eta} (\lambda_m \lambda_r \lambda_n') dz$.

Rewriting Eqn. (2.26) gives,

$$\sum_{m=0}^{k} \rho \frac{\partial u_m}{\partial t}\, y_{mn} + \sum_{m=0}^{k}\sum_{r=0}^{k} \rho\, \frac{\partial u_m u_r}{\partial x}\, y_{mrn} + \sum_{m=0}^{k}\sum_{r=0}^{k} \rho\, \frac{\partial u_m v_r}{\partial y}\, y_{mrn}$$
$$+ \sum_{m=0}^{k}\sum_{r=0}^{k} \rho u_m w_r\, \lambda_m \lambda_r\, \lambda_n \Big|_{z=z_b}^{\eta} - \sum_{m=0}^{k}\sum_{r=0}^{k} \rho u_m w_r\, y_{mr}^{n}$$
$$= -\frac{\partial P_n}{\partial x} + \hat{P}\lambda_n \Big|_{\eta} \frac{\partial \eta}{\partial x} - \bar{P}\lambda_n \Big|_{z_b} \frac{\partial z_b}{\partial x} \qquad (2.28)$$

Eqn. (2.28) is simplified using the Krylov-Kantorovich method to give the continuity equation Eqn. (2.19). If the index *n* is changed to *r*, Eqn. (2.19) becomes

$$\sum_{r=0}^{k} \frac{\partial u_r}{\partial x} \lambda_r + \sum_{r=0}^{k} \frac{\partial v_r}{\partial y} \lambda_r + \sum_{r=0}^{k} w_r\, \lambda_r' = 0 \qquad (2.29)$$

Multiplying Eqn. (2.29) by λ_n , λ_m and summing over *m* and then depth integrating gives

$$\int_{z_b}^{\eta} \left(\sum_{m=0}^{k}\sum_{r=0}^{k} \frac{\partial u_r}{\partial x} \lambda_r \lambda_m \lambda_n \right) dz + \int_{z_b}^{\eta} \left(\sum_{m=0}^{k}\sum_{r=0}^{k} \frac{\partial v_r}{\partial y} \lambda_r \lambda_m \lambda_n \right) dz$$

$$+ \int_{z_b}^{\eta} \left(\sum_{m=0}^{k}\sum_{r=0}^{k} w_r\, \lambda_r' \lambda_m \lambda_n \right) dz = 0$$

or

$$\sum_{m=0}^{k}\sum_{r=0}^{k} \frac{\partial u_r}{\partial x} \left[\int_{z_b}^{\eta} (\lambda_r \lambda_m \lambda_n)\, dz \right] + \sum_{m=0}^{k}\sum_{r=0}^{k} \frac{\partial v_r}{\partial y} \left[\int_{z_b}^{\eta} (\lambda_r \lambda_m \lambda_n)\, dz \right]$$

$$+ \sum_{m=0}^{k}\sum_{r=0}^{k} w_r \left[\int_{z_b}^{\eta} (\lambda_m \lambda_n \lambda_r')\, dz \right] = 0 \quad . \qquad (2.30)$$

Next, the order of summation and integration is interchanged.

$$\begin{cases} \sum_{m=0}^{k}\sum_{r=0}^{k}\frac{\partial u_r}{\partial x}\,y_{mrn}+\sum_{m=0}^{k}\sum_{r=0}^{k}\frac{\partial v_r}{\partial y}\,y_{mrn}+\sum_{m=0}^{k}\sum_{r=0}^{k}w_r y_{mn}^{r}=0 \quad , \\ \text{or} \\ \sum_{m=0}^{k}\sum_{r=0}^{k}\frac{\partial u_r}{\partial x}\,y_{mrn}=-\sum_{m=0}^{k}\sum_{r=0}^{k}\frac{\partial v_r}{\partial y}\,y_{mrn}-\sum_{m=0}^{k}\sum_{r=0}^{k}w_r y_{mn}^{r} \end{cases} \tag{2.31}$$

where

$$y_{mn}^{r}=\int_{z=z_b}^{\eta}(\lambda_m\lambda_n\lambda_r')\,dz\,.$$

Implementing the chain rule, the second and third terms on the left hand side of Eqn. (2.28) are expanded and then the second term replaced by Eqn. (2.31)

$$\begin{aligned} &\sum_{m=0}^{k}\rho\frac{\partial u_m}{\partial t}\,y_{mn}+\sum_{m=0}^{k}\sum_{r=0}^{k}\rho\frac{\partial u_m}{\partial x}u_r\,y_{mrn}+\sum_{m=0}^{k}\sum_{r=0}^{k}\rho\frac{\partial u_r}{\partial x}u_m\,y_{mrn}+ \\ &\sum_{m=0}^{k}\sum_{r=0}^{k}\rho\frac{\partial u_m}{\partial y}v_r\,y_{mrn}+\sum_{m=0}^{k}\sum_{r=0}^{k}\rho\frac{\partial v_r}{\partial y}u_m\,y_{mrn}+\sum_{m=0}^{k}\sum_{r=0}^{k}\rho u_m w_r\,\lambda_m\lambda_r\,\lambda_n\Big|_{z_b}^{\eta} \\ &-\sum_{m=0}^{k}\sum_{r=0}^{k}\rho u_m w_r\,y_{mr}^{n} \\ &=\sum_{m=0}^{k}\rho\frac{\partial u_m}{\partial t}\,y_{mn}+\sum_{m=0}^{k}\sum_{r=0}^{k}\rho\frac{\partial u_m}{\partial x}u_r\,y_{mrn}-\sum_{m=0}^{k}\sum_{r=0}^{k}\rho\frac{\partial v_r}{\partial y}u_m\,y_{mrn}- \\ &\sum_{m=0}^{k}\sum_{r=0}^{k}\rho\,w_r u_m\,y_{mn}^{r}+\sum_{m=0}^{k}\sum_{r=0}^{k}\rho\frac{\partial u_m}{\partial y}v_r\,y_{mrn}+\sum_{m=0}^{k}\sum_{r=0}^{k}\rho\frac{\partial v_r}{\partial y}u_m\,y_{mrn}+ \\ &\sum_{m=0}^{k}\sum_{r=0}^{k}\rho u_m w_r\,\lambda_m\lambda_r\,\lambda_n\Big|_{z_b}^{\eta}-\sum_{m=0}^{k}\sum_{r=0}^{k}\rho\,u_m\,w_r\,y_{mr}^{n} \end{aligned} \tag{2.32}$$

$$= \sum_{m=0}^{k} \rho \frac{\partial u_m}{\partial t}\, y_{mn} + \sum_{m=0}^{k}\sum_{r=0}^{k} \rho \frac{\partial u_m}{\partial x} u_r\, y_{mrn} + \sum_{m=0}^{k}\sum_{r=0}^{k} \rho \frac{\partial u_m}{\partial y} v_r\, y_{mrn} +$$

$$- \sum_{m=0}^{k}\sum_{r=0}^{k} \rho\, u_m\, w_r\, (y_{mn}^{r} + y_{mr}^{n}) + \sum_{m=0}^{k}\sum_{r=0}^{k} \rho u_m w_r\, \lambda_m \lambda_r\, \lambda_n \Big|_{z_b}^{\eta} \qquad (2.33)$$

Integration by parts leads to the determination of $(y_{mn}^{r} + y_{mr}^{n})$

$$(y_{mn}^{r} + y_{mr}^{n}) = \int_{z_b}^{\eta} (\lambda_m \lambda_n \lambda_r')\, dz + \int_{z_b}^{\eta} (\lambda_m \lambda_r \lambda_n')\, dz = \int_{z_b}^{\eta} \lambda_m (\lambda_n \lambda_r)'\, dz$$

$$= \lambda_m \lambda_n \lambda_r \Big|_{z_b}^{\eta} - \int_{z_b}^{\eta} (\lambda_n \lambda_r \lambda_m')\, dz = \lambda_m \lambda_n \lambda_r \Big|_{z_b}^{\eta} - y_{rn}^{m} \qquad (2.34)$$

The *x*-direction momentum equation is obtained by inserting Eqn. (2.34) into Eqn. (2.33) and combining it with right hand side as in Eqn. (2.28)

$$\sum_{m=0}^{k} \rho \frac{\partial u_m}{\partial t}\, y_{mn} + \sum_{m=0}^{k}\sum_{r=0}^{k} \rho \frac{\partial u_m}{\partial x} u_r\, y_{mrn} + \sum_{m=0}^{k}\sum_{r=0}^{k} \rho \frac{\partial u_m}{\partial y} v_r\, y_{mrn}$$

$$- \sum_{m=0}^{k}\sum_{r=0}^{k} \rho u_m w_r\, \lambda_m \lambda_r\, \lambda_n \Big|_{z_b}^{\eta} + \sum_{m=0}^{k}\sum_{r=0}^{k} \rho\, u_m\, w_r\, y_{rn}^{m}$$

$$+ \sum_{m=0}^{k}\sum_{r=0}^{k} \rho u_m w_r\, \lambda_m \lambda_r\, \lambda_n \Big|_{z_b}^{\eta}$$

$$= \sum_{m=0}^{k} \rho \frac{\partial u_m}{\partial t}\, y_{mn} + \sum_{m=0}^{k}\sum_{r=0}^{k} \rho \frac{\partial u_m}{\partial x} u_r\, y_{mrn} + \sum_{m=0}^{k}\sum_{r=0}^{k} \rho \frac{\partial u_m}{\partial y} v_r\, y_{mrn}$$

$$+ \sum_{m=0}^{k}\sum_{r=0}^{k} \rho\, u_m\, w_r\, y_{rn}^{m} = -\frac{\partial P_n}{\partial x} + \hat{P} \lambda_n \Big|_{\eta} \frac{\partial \eta}{\partial x} - \bar{P} \lambda_n \Big|_{z_b} \frac{\partial z_b}{\partial x} \qquad (2.35)$$

2.1.5 2D level I GN Momentum equation in vertical (z) direction

By multiplying Eqn. (2.4c) in λ_n and then depth-integrating from the bottom to the free surface, the z-direction GN Momentum equation is obtained

$$\int_{z_b}^{\eta}\left(\frac{\partial \rho w}{\partial t}+\frac{\partial \rho w u}{\partial x}+\frac{\partial \rho w v}{\partial y}+\frac{\partial \rho w w}{\partial z}\right)\lambda_n dz=-\int_{z_b}^{\eta}\left(\frac{\partial P}{\partial z}+\rho g_z\right)\lambda_n dz \tag{2.36}$$

The left hand side of the Eqn. (2.36) can be rewritten as:

$$\int_{z_b}^{\eta}\left(\frac{\partial \rho w}{\partial t}\lambda_n+\frac{\partial \rho w u}{\partial x}\lambda_n+\frac{\partial \rho w v}{\partial y}\lambda_n+\frac{\partial \rho w w}{\partial z}\lambda_n\right)dz \tag{2.37}$$

Using the chain rule for fourth term gives

$$\int_{z_b}^{\eta}\left(\frac{\partial \rho w}{\partial t}\lambda_n\right)dz+\int_{z_b}^{\eta}\left(\frac{\partial \rho w u}{\partial x}\lambda_n\right)dz+\int_{z_b}^{\eta}\left(\frac{\partial \rho w v}{\partial y}\lambda_n\right)dz+\rho w w\,\lambda_n\Big|_{z_b}^{\eta}$$
$$-\int_{z_b}^{\eta}(\rho w w\lambda_n')\,dz \tag{2.38}$$

Then, Leibnitz Rule is applied to the right hand side of Eqn. (2.36), giving

$$-\int_{z_b}^{\eta}\frac{\partial P}{\partial z}\lambda_n dz-\int_{z_b}^{\eta}\rho g_z\lambda_n dz=-\left(P\lambda_n-\int_{z_b}^{\eta}P\lambda_n'\,dz\right)-\int_{z_b}^{\eta}\rho g_z\lambda_n\,dz$$
$$=-[P\lambda_n]\Big|_{z_b}^{\eta}+\int_{z_b}^{\eta}P\lambda_n'\,dz-\rho g_z\int_{z_b}^{\eta}\lambda_n\,dz \tag{2.39}$$

Eqn. (2.38) and (2.39) are combined to give

$$\int_{z_b}^{\eta}\left(\frac{\partial \rho w}{\partial t}\lambda_n\right)dz+\int_{z_b}^{\eta}\left(\frac{\partial \rho w u}{\partial x}\lambda_n\right)dz+\int_{z_b}^{\eta}\left(\frac{\partial \rho w v}{\partial y}\lambda_n\right)dz+\rho w w\,\lambda_n\Big|_{z_b}^{\eta}$$
$$-\int_{z_b}^{\eta}\rho w w\lambda_n'\,dz=-\hat{P}\lambda_n\Big|_{\eta}+\bar{P}\lambda_n\Big|_{z_b}+P_n'-\rho g_z\int_{z_b}^{\eta}\lambda_n\,dz \tag{2.40}$$

where $P_n'=\int_{z_b}^{\eta}P\lambda_n'\,dz$.

Insertion of the kinematic assumed parameters Eqn. (2.10) on the left hand side of Eqn. (2.40) leads to

$$\int_{z_b}^{\eta}\left(\frac{\partial\rho\sum_{m=0}^{k} w_m\lambda_m\lambda_n}{\partial t}\right)dz+\int_{z_b}^{\eta}\left(\frac{\partial\rho\ \sum_{r=0}^{k} u_r\lambda_r\lambda_n\ \sum_{m=0}^{k} w_m\lambda_m}{\partial x}\right)dz$$

$$+\int_{z_b}^{\eta}\left(\frac{\partial\rho\ \sum_{r=0}^{k} v_r\lambda_r\lambda_n\ \sum_{m=0}^{k} w_m\lambda_m}{\partial y}\right)dz+\rho\sum_{m=0}^{k} w_m\lambda_m\sum_{r=0}^{k} w_r\lambda_r\lambda_n\Big|_{z_b}^{\eta}$$

$$-\int_{z_b}^{\eta}\left(\rho\sum_{m=0}^{k} w_m\lambda_m\sum_{r=0}^{k} w_r\lambda_r\lambda_n'\right)dz$$

$$=\sum_{m=0}^{k}\rho\frac{\partial w_m}{\partial t}\int_{z_b}^{\eta}(\lambda_m\lambda_n)dz+\sum_{m=0}^{k}\sum_{r=0}^{k}\rho\frac{\partial w_m u_r}{\partial x}\int_{z_b}^{\eta}(\lambda_m\lambda_r\lambda_n)dz$$

$$+\sum_{m=0}^{k}\sum_{r=0}^{k}\rho\frac{\partial w_m v_r}{\partial y}\int_{z_b}^{\eta}\lambda_m\lambda_r\lambda_n\,dz+\sum_{m=0}^{k}\sum_{r=0}^{k}\rho w_m w_r\ \lambda_m\lambda_r\lambda_n\Big|_{z_b}^{\eta}$$

$$-\sum_{m=0}^{k}\sum_{r=0}^{k}\rho w_m w_r\int_{z_b}^{\eta}\lambda_m\lambda_r\lambda_n'\,dz$$

$$=\sum_{m=0}^{k}\rho\frac{\partial w_m}{\partial t}\,y_{mn}+\sum_{m=0}^{k}\sum_{r=0}^{k}\rho\frac{\partial w_m u_r}{\partial x}\,y_{mrn}+\sum_{m=0}^{k}\sum_{r=0}^{k}\rho\frac{\partial w_m v_r}{\partial y}\,y_{mrn}$$

$$+\sum_{m=0}^{k}\sum_{r=0}^{k}\rho w_m w_r\ \lambda_m\lambda_r\lambda_n\Big|_{z_b}^{\eta}-\sum_{m=0}^{k}\sum_{r=0}^{k}\rho w_m w_r\,y_{mr}^{n} \tag{2.41}$$

Rewriting Eqn. (2.40) gives,

$$\sum_{m=0}^{k}\rho\frac{\partial w_m}{\partial t}\,y_{mn}+\sum_{m=0}^{k}\sum_{r=0}^{k}\rho\frac{\partial w_m u_r}{\partial x}\,y_{mrn}+\sum_{m=0}^{k}\sum_{r=0}^{k}\rho\frac{\partial w_m v_r}{\partial y}\,y_{mrn}$$

$$+\sum_{m=0}^{k}\sum_{r=0}^{k}\rho w_m w_r\ \lambda_m\lambda_r\lambda_n\Big|_{z_b}^{\eta}-\sum_{m=0}^{k}\sum_{r=0}^{k}\rho w_m w_r\,y_{mr}^{n}$$

$$=-\hat{P}\lambda_n\Big|_{\eta}+\bar{P}\lambda_n\Big|_{z_b}+P_n'-\rho g_z y_n \tag{2.42}$$

where $y_{mn}=\int_{z_b}^{\eta}(\lambda_m\lambda_n)dz$.

Implementing the chain rule, the second and third terms on the left hand side of Eqn. (2.42) are expanded and then the second term replaced by Eqn. (2.31)

$$\sum_{m=0}^{k} \rho \frac{\partial w_m}{\partial t}\, y_{mn} + \sum_{m=0}^{k}\sum_{r=0}^{k} \rho \frac{\partial w_m}{\partial x} u_r\, y_{mrn} + \sum_{m=0}^{k}\sum_{r=0}^{k} \rho \frac{\partial u_r}{\partial x} w_m\, y_{mrn} +$$

$$\sum_{m=0}^{k}\sum_{r=0}^{k} \rho \frac{\partial w_m}{\partial y} v_r\, y_{mrn} + \sum_{m=0}^{k}\sum_{r=0}^{k} \rho \frac{\partial v_r}{\partial y} w_m\, y_{mrn} + \sum_{m=0}^{k}\sum_{r=0}^{k} \rho w_m w_r\, \lambda_m \lambda_r\, \lambda_n \Big|_{z_b}^{\eta}$$

$$- \sum_{m=0}^{k}\sum_{r=0}^{k} \rho w_m w_r\, y_{mr}^{n}$$

$$= \sum_{m=0}^{k} \rho \frac{\partial w_m}{\partial t}\, y_{mn} + \sum_{m=0}^{k}\sum_{r=0}^{k} \rho \frac{\partial w_m}{\partial x} u_r\, y_{mrn} - \sum_{m=0}^{k}\sum_{r=0}^{k} \rho \frac{\partial v_r}{\partial y} w_m\, y_{mrn} -$$

$$\sum_{m=0}^{k}\sum_{r=0}^{k} \rho\, w_m\, w_r y_{mn}^{r} + \sum_{m=0}^{k}\sum_{r=0}^{k} \rho \frac{\partial w_m}{\partial y} v_r\, y_{mrn} + \sum_{m=0}^{k}\sum_{r=0}^{k} \rho \frac{\partial v_r}{\partial y} w_m\, y_{mrn} +$$

$$\sum_{m=0}^{k}\sum_{r=0}^{k} \rho w_m w_r\, \lambda_m \lambda_r\, \lambda_n \Big|_{z_b}^{\eta} - \sum_{m=0}^{k}\sum_{r=0}^{k} \rho\, w_m\, w_r\, y_{mr}^{n}$$

$$= \sum_{m=0}^{k} \rho \frac{\partial w_m}{\partial t}\, y_{mn} + \sum_{m=0}^{k}\sum_{r=0}^{k} \rho \frac{\partial w_m}{\partial x} u_r\, y_{mrn} + \sum_{m=0}^{k}\sum_{r=0}^{k} \rho \frac{\partial w_m}{\partial y} v_r\, y_{mrn}$$

$$- \sum_{m=0}^{k}\sum_{r=0}^{k} \rho\, w_m\, w_r\, (y_{mn}^{r} + y_{mr}^{n}) + \sum_{m=0}^{k}\sum_{r=0}^{k} \rho w_m w_r\, \lambda_m \lambda_r\, \lambda_n \Big|_{z_b}^{\eta} \qquad (2.43)$$

Integration by parts leads to the determination of $(y_{mn}^{r} + y_{mr}^{n})$

$$(y_{mn}^{r} + y_{mr}^{n}) = \int_{z_b}^{\eta} (\lambda_m \lambda_n \lambda_r')\, dz + \int_{z_b}^{\eta} (\lambda_m \lambda_r \lambda_n')\, dz = \int_{z_b}^{\eta} \lambda_m (\lambda_n \lambda_r)'\, dz$$

$$= \lambda_m \lambda_n \lambda_r \Big|_{z_b}^{\eta} - \int_{z_b}^{\eta} (\lambda_n \lambda_r \lambda_m')\, dz = \lambda_m \lambda_n \lambda_r \Big|_{z_b}^{\eta} - y_{rn}^{m} \qquad (2.44)$$

The z-direction momentum equation is obtained by inserting Eqn. (2.44) into Eqn. (2.43) and combining it with right hand side as in Eqn. (2.42)

$$\sum_{m=0}^{k} \rho \frac{\partial w_m}{\partial t}\, y_{mn} + \sum_{m=0}^{k}\sum_{r=0}^{k} \rho \frac{\partial w_m}{\partial x} u_r\, y_{mrn} + \sum_{m=0}^{k}\sum_{r=0}^{k} \rho \frac{\partial w_m}{\partial y} v_r\, y_{mrn} -$$

$$\sum_{m=0}^{k}\sum_{r=0}^{k} \rho w_m w_r\, \lambda_m \lambda_r\, \lambda_n \Big|_{z_b}^{\eta} + \sum_{m=0}^{k}\sum_{r=0}^{k} \rho\, w_m\, w_r\, y_{rn}^{m}$$

$$+ \sum_{m=0}^{k}\sum_{r=0}^{k} \rho w_m w_r\, \lambda_m \lambda_r\, \lambda_n \Big|_{z_b}^{\eta}$$

$$= \sum_{m=0}^{k} \rho \frac{\partial w_m}{\partial t}\, y_{mn} + \sum_{m=0}^{k}\sum_{r=0}^{k} \rho \frac{\partial w_m}{\partial x} u_r\, y_{mrn} + \sum_{m=0}^{k}\sum_{r=0}^{k} \rho \frac{\partial w_m}{\partial y} v_r\, y_{mrn}$$

$$+ \sum_{m=0}^{k}\sum_{r=0}^{k} \rho\, w_m\, w_r\, y_{rn}^{m} = -\hat{P}\lambda_n \big|_{\eta} + \bar{P}\lambda_n \big|_{z_b} + P_n' - \rho g_z y_n \qquad (2.45)$$

Writing out in full for Level I, the following parameters are defined (noting their presence in the GN continuity equation):

$$\begin{cases} u(x,y,z,t) = u_0(x,y,z,t)\, \lambda_{0\,x} + u_1(x,y,z,t)\, \lambda_{1\,x} \\ v(x,y,z,t) = v_0(x,y,z,t)\, \lambda_{0\,y} + v_1(x,y,z,t)\, \lambda_{1\,y} \\ w(x,y,z,t) = w_0(x,y,z,t)\, \lambda_{0\,z} + w_1(x,y,z,t)\, \lambda_{1\,z} \end{cases} \qquad (2.46)$$

where, in this case:

$\lambda_{0\,x} = \lambda_{0\,y} = \lambda_{0\,z} = 1$, $\lambda_{1\,x} = \lambda_{1\,y} = \lambda_{1\,z} = (z - z_b)$, $u_1(x,y,z,t) = v_1(x,y,z,t) = 0$

as in Eqn. (2.10).

For $n = 0, 1, 2 \ldots k$

$$\begin{cases} y_{mn} = \int_{z_b}^{\eta} (\lambda_m \lambda_n) dz \,, \quad y_{mrn} = \int_{z_b}^{\eta} (\lambda_m \lambda_r \lambda_n) dz \,, \quad y_{mr}^{n} = \int_{z_b}^{\eta} \lambda_m \lambda_r (\frac{\partial \lambda_n}{\partial z}) dz \,, \\ y_n = \displaystyle\int_{z=z_b}^{\eta} (\lambda_n) dz \,, \quad P_n = \int_{z=z_b}^{\eta} (P \lambda_n) dz \quad \text{and} \quad P_n' = \int_{z=z_b}^{\eta} \left(P \frac{\partial \lambda_n}{\partial z} \right) dz \end{cases} \quad (2.47)$$

When shape functions of $\lambda_0 = 1$ and $\lambda_1 = z$ are incorporated into the above,

$$\begin{cases} y_{000} = y_{00} = y_0 = \displaystyle\int_{z_b}^{\eta} 1 \, dz = \eta - z_b = h \,, \\ y_{100} = y_{001} = y_{10} = y_{01} = y_1 = \displaystyle\int_{z_b}^{\eta} (z - z_b) dz = \frac{(\eta - z_b)^2}{2} = \frac{h^2}{2} \,, \\ y_{110} = y_{101} = y_{011} = y_{11} = \displaystyle\int_{z_b}^{\eta} (z - z_b)^2 dz = \frac{(\eta - z_b)^3}{3} = \frac{h^3}{3} \,, \\ y_{mr}^{0} = \displaystyle\int_{z_b}^{\eta} \lambda_m \lambda_r \frac{\partial 1}{\partial z} \, dz = 0 \,, \quad y_{00}^{1} = \int_{z_b}^{\eta} 1 \, \frac{\partial (z - z_b)}{\partial z} \, dz = \int_{z_b}^{\eta} 1 \, dz = h \\ y_{10}^{1} = y_{01}^{1} = \displaystyle\int_{z_b}^{\eta} (z - z_b) \frac{\partial (z - z_b)}{\partial z} \, dz = \frac{(\eta - z_b)^2}{2} = \frac{h^2}{2} \,, \\ y_{11}^{1} = \displaystyle\int_{z_b}^{\eta} (z - z_b)^2 \frac{\partial (z - z_b)}{\partial z} \, dz = \frac{(\eta - z_b)^3}{3} = \frac{h^3}{3} \,, \\ P_0 = \displaystyle\int_{z_b}^{\eta} P \, \lambda_0 \, dz = \int_{z_b}^{\eta} P \, dz \,, \quad P_1 = \int_{z_b}^{\eta} P \, \lambda_1 \, dz = \int_{z_b}^{\eta} P (z - z_b) \, dz \,, \end{cases} \quad (2.48a)$$

and

$$P_0' = \int_{z_b}^{\eta} P \, \frac{\partial \lambda_0}{\partial z} \, dz = 0 \,, \quad P_1' = \int_{z_b}^{\eta} P \, \frac{\partial \lambda_1}{\partial z} \, dz = \int_{z_b}^{\eta} P \, dz = P_0 \,. \quad (2.48b)$$

If the *x*-momentum equation, Eqn. (2.35), is considered for $n = 0$ and $n = 1$

***n* = 0:**

$$\rho \frac{\partial u_0}{\partial t} y_{00} + \rho \frac{\partial u_0}{\partial x} u_0 \, y_{000} + \rho \frac{\partial u_0}{\partial y} v_0 \, y_{000} + \rho \, u_0 \, w_0 \, y_{00}^{0} + \rho \, u_0 \, w_1 \, y_{10}^{0}$$

$$= -\frac{\partial P_0}{\partial x} + \hat{P} \lambda_0 \big|_{\eta} \frac{\partial \eta}{\partial x} - \bar{P} \lambda_0 \big|_{z_b} \frac{\partial z_b}{\partial x} \,, \quad (2.49a)$$

and

***n* = 1:**

$$\rho \frac{\partial u_0}{\partial t} y_{01} + \rho \frac{\partial u_0}{\partial x} u_0\, y_{001} + \rho \frac{\partial u_0}{\partial y} v_0\, y_{001} + \rho\, u_0\, w_0\, y_{01}^0 + \rho\, u_0\, w_1\, y_{11}^0$$

$$= -\frac{\partial P_1}{\partial x} + \hat{P}\lambda_1 \big|_\eta \frac{\partial \eta}{\partial x} - \bar{P}\lambda_1 \big|_{z_b} \frac{\partial z_b}{\partial x} \quad . \tag{2.49b}$$

The *y*-momentum equation and *z*-momentum equation (Eqn. (2.45)) undergo the same expansions for $n = 0$ and $n = 1$.

In the *y*-direction,

***n* = 0:**

$$\rho \frac{\partial v_0}{\partial t} y_{00} + \rho \frac{\partial v_0}{\partial x} u_0\, y_{000} + \rho \frac{\partial v_0}{\partial y} v_0\, y_{000} + \rho\, v_0\, w_0\, y_{00}^0 + \rho\, v_0\, w_1\, y_{10}^0$$

$$= -\frac{\partial P_0}{\partial y} + \hat{P}\lambda_0 \big|_\eta \frac{\partial \eta}{\partial y} - \bar{P}\lambda_0 \big|_{z_b} \frac{\partial z_b}{\partial y} \quad . \tag{2.50a}$$

and

***n* = 1:**

$$\rho \frac{\partial v_0}{\partial t} y_{01} + \rho \frac{\partial v_0}{\partial x} u_0\, y_{001} + \rho \frac{\partial v_0}{\partial y} v_0\, y_{001} + \rho\, v_0\, w_0\, y_{01}^0 + \rho\, v_0\, w_1\, y_{11}^0$$

$$= -\frac{\partial P_1}{\partial y} + \hat{P}\lambda_1 \big|_\eta \frac{\partial \eta}{\partial y} - \bar{P}\lambda_1 \big|_{z_b} \frac{\partial z_b}{\partial y} \quad . \tag{2.50b}$$

In the *z*-direction,

***n* = 0:**

$$\rho \frac{\partial w_0}{\partial t} y_{00} + \rho \frac{\partial w_1}{\partial t} y_{10} + \rho \frac{\partial w_0}{\partial x} u_0\, y_{000} + \rho \frac{\partial w_1}{\partial x} u_0\, y_{100} + \rho \frac{\partial w_0}{\partial y} v_0\, y_{000}$$

$$+ \rho \frac{\partial w_1}{\partial y} v_0\, y_{100} + \rho\, w_0\, w_0\, y_{00}^0 + \rho\, w_0\, w_1\, y_{10}^0 + \rho\, w_1\, w_0\, y_{00}^1 +$$

$$\rho\, w_1\, w_1\, y_{10}^1 = -\hat{P}\lambda_0 \big|_\eta + \bar{P}\lambda_0 \big|_{z_b} + P_0' - \rho g y_0 \tag{2.51a}$$

and

***n* = 1:**

$$\rho\frac{\partial w_0}{\partial t}y_{01}+\rho\frac{\partial w_1}{\partial t}y_{11}+\rho\frac{\partial w_0}{\partial x}u_0\,y_{001}+\rho\frac{\partial w_1}{\partial x}u_0\,y_{101}+\rho\frac{\partial w_0}{\partial y}v_0\,y_{001}$$

$$+\rho\frac{\partial w_1}{\partial y}v_0\,y_{101}+\rho\,w_0\,w_0\,y_{01}^0+\rho\,w_0\,w_1\,y_{11}^0+\rho\,w_1\,w_0\,y_{01}^1+$$

$$\rho\,w_1\,w_1\,y_{11}^1=-\hat{P}\lambda_1\big|_\eta+\bar{P}\lambda_1\big|_{z_b}+P_1'-\rho g y_1 \qquad (2.51b)$$

Substituting for y_{000}, and so on; gives:

x-momentum equations,

$$n=0:\quad \rho\frac{\partial u_0}{\partial t}h+\rho\frac{\partial u_0}{\partial x}u_0\,h+\rho\frac{\partial u_0}{\partial y}v_0\,h=-\frac{\partial P_0}{\partial x}+\hat{P}\frac{\partial \eta}{\partial x}-\bar{P}\frac{\partial z_b}{\partial x}\quad , \quad (2.52a)$$

$$n=1:\quad \rho\frac{\partial u_0}{\partial t}\frac{h^2}{2}+\rho\frac{\partial u_0}{\partial x}u_0\,\frac{h^2}{2}+\rho\frac{\partial u_0}{\partial y}v_0\,\frac{h^2}{2}=-\frac{\partial P_1}{\partial x}+\hat{P}h\frac{\partial \eta}{\partial x}\quad , \quad (2.52b)$$

y-momentum equations,

$$n=0:\quad \rho\frac{\partial v_0}{\partial t}h+\rho\frac{\partial v_0}{\partial x}u_0\,h+\rho\frac{\partial v_0}{\partial y}v_0\,h=-\frac{\partial P_0}{\partial y}+\hat{P}\frac{\partial \eta}{\partial y}-\bar{P}\frac{\partial z_b}{\partial y}\quad , \quad (2.53a)$$

$$n=1:\quad \rho\frac{\partial v_0}{\partial t}\frac{h^2}{2}+\rho\frac{\partial v_0}{\partial x}u_0\,\frac{h^2}{2}+\rho\frac{\partial v_0}{\partial y}v_0\,\frac{h^2}{2}=-\frac{\partial P_1}{\partial y}+\hat{P}h\frac{\partial \eta}{\partial y}\quad , \quad (2.53b)$$

z-momentum equations,

$$n=0:\quad \rho\frac{\partial w_0}{\partial t}h+\rho\frac{\partial w_1}{\partial t}\frac{h^2}{2}+\rho\frac{\partial w_0}{\partial x}u_0\,h+\rho\frac{\partial w_1}{\partial x}u_0\,\frac{h^2}{2}+\rho\frac{\partial w_0}{\partial y}v_0\,h$$

$$+\rho\frac{\partial w_1}{\partial y}v_0\,\frac{h^2}{2}+\rho\,w_1\,w_0\,h+\rho\,w_1\,w_1\,\frac{h^2}{2}=-\hat{P}+\bar{P}-\rho g h\quad , \qquad (2.54a)$$

$$n=1:\quad \rho\frac{\partial w_0}{\partial t}\frac{h^2}{2}+\rho\frac{\partial w_1}{\partial t}\frac{h^3}{3}+\rho\frac{\partial w_0}{\partial x}u_0\,\frac{h^2}{2}+\rho\frac{\partial w_1}{\partial x}u_0\,\frac{h^3}{3}+\rho\frac{\partial w_0}{\partial y}v_0\,\frac{h^2}{2}$$

$$+\rho\frac{\partial w_1}{\partial y}v_0\,\frac{h^3}{3}+\rho\,w_1\,w_0\,\frac{h^2}{2}+\rho\,w_1\,w_1\,\frac{h^3}{3}=-\hat{P}h+P_0-\rho g\frac{h^2}{2}\quad . \quad (2.54b)$$

Let the surface pressure $\hat{P} = 0$ everywhere (i.e. no storm surges). Note that $P_1' = P_0$. Then $\frac{\partial P_0}{\partial x}$ and $\frac{\partial P_0}{\partial y}$ are eliminated from the equation along with $\bar{P}$.

Thus Eqn. (2.52), (2.53) and (2.54) become

x-momentum equations,

$$n = 0: \qquad \rho \frac{\partial u_0}{\partial t} h + \rho \frac{\partial u_0}{\partial x} u_0\, h + \rho \frac{\partial u_0}{\partial y} v_0\, h = -\frac{\partial P_0}{\partial x} - \bar{P} \frac{\partial z_b}{\partial x} \quad , \qquad (2.55a)$$

$$n = 1: \qquad \rho \frac{\partial u_0}{\partial t} \frac{h^2}{2} + \rho \frac{\partial u_0}{\partial x} u_0\, \frac{h^2}{2} + \rho \frac{\partial u_0}{\partial y} v_0\, \frac{h^2}{2} = -\frac{\partial P_1}{\partial x} \quad , \qquad (2.55b)$$

y-momentum equations,

$$n = 0: \qquad \rho \frac{\partial v_0}{\partial t} h + \rho \frac{\partial v_0}{\partial x} u_0\, h + \rho \frac{\partial v_0}{\partial y} v_0\, h = -\frac{\partial P_0}{\partial y} - \bar{P} \frac{\partial z_b}{\partial y} \quad , \qquad (2.56a)$$

$$n = 1: \qquad \rho \frac{\partial v_0}{\partial t} \frac{h^2}{2} + \rho \frac{\partial v_0}{\partial x} u_0\, \frac{h^2}{2} + \rho \frac{\partial v_0}{\partial y} v_0\, \frac{h^2}{2} = -\frac{\partial P_1}{\partial y} \quad , \qquad (2.56b)$$

z-momentum equations,

$$n = 0: \qquad \rho \frac{\partial w_0}{\partial t} h + \rho \frac{\partial w_1}{\partial t} \frac{h^2}{2} + \rho \frac{\partial w_0}{\partial x} u_0\, h + \rho \frac{\partial w_1}{\partial x} u_0\, \frac{h^2}{2} + \rho \frac{\partial w_0}{\partial y} v_0\, h$$
$$+ \rho \frac{\partial w_1}{\partial y} v_0\, \frac{h^2}{2} + \rho\, w_1\, w_0\, h + \rho\, w_1\, w_1\, \frac{h^2}{2} = \bar{P} - \rho g h \quad , \qquad (2.57a)$$

$$n = 1: \qquad \rho \frac{\partial w_0}{\partial t} \frac{h^2}{2} + \rho \frac{\partial w_1}{\partial t} \frac{h^3}{3} + \rho \frac{\partial w_0}{\partial x} u_0\, \frac{h^2}{2} + \rho \frac{\partial w_1}{\partial x} u_0\, \frac{h^3}{3} + \rho \frac{\partial w_0}{\partial y} v_0\, \frac{h^2}{2}$$
$$+ \rho \frac{\partial w_1}{\partial y} v_0\, \frac{h^3}{3} + \rho\, w_1\, w_0\, \frac{h^2}{2} + \rho\, w_1\, w_1\, \frac{h^3}{3} = P_0 - \rho g \frac{h^2}{2} \quad . \qquad (2.57b)$$

Substituting for w_0 and w_1:

$$\begin{cases} W_0 = \dfrac{\partial z_b}{\partial t} + u_0 \dfrac{\partial z_b}{\partial x} + v_0 \dfrac{\partial z_b}{\partial y} \\ w_1 = -\dfrac{\partial u_0}{\partial_x} - \dfrac{\partial v_0}{\partial_y} \end{cases} \tag{2.58}$$

Thus, the *z*-momentum equations become

***n* = 0:**

$$\rho h\left(\frac{\partial^2 z_b}{\partial t^2} + \frac{\partial u_0}{\partial t}\frac{\partial z_b}{\partial x} + u_0\frac{\partial^2 z_b}{\partial x \partial t} + \frac{\partial v_0}{\partial t}\frac{\partial z_b}{\partial y} + v_0\frac{\partial^2 z_b}{\partial y \partial t}\right)$$

$$+\frac{\rho h^2}{2}\left(-\frac{\partial^2 u_0}{\partial x \partial t} - \frac{\partial^2 v_0}{\partial y \partial t}\right) + \rho u_0 h\left(\frac{\partial^2 z_b}{\partial x \partial t} + \frac{\partial u_0}{\partial x}\frac{\partial z_b}{\partial x} + u_0\frac{\partial^2 z_b}{\partial x^2} + \frac{\partial v_0}{\partial x}\frac{\partial z_b}{\partial y} + v_0\frac{\partial^2 z_b}{\partial x \partial y}\right)$$

$$+\rho u_0\frac{h^2}{2}\left(-\frac{\partial^2 u_0}{\partial x^2} - \frac{\partial^2 v_0}{\partial x \partial y}\right) + \rho v_0 h\left(\frac{\partial^2 z_b}{\partial y \partial t} + \frac{\partial u_0}{\partial y}\frac{\partial z_b}{\partial x} + u_0\frac{\partial^2 z_b}{\partial x \partial y} + \frac{\partial v_0}{\partial y}\frac{\partial z_b}{\partial y} + v_0\frac{\partial^2 z_b}{\partial y^2}\right)$$

$$+\rho v_0\frac{h^2}{2}\left(-\frac{\partial^2 v_0}{\partial y^2} - \frac{\partial^2 u_0}{\partial x \partial y}\right) - \rho h\left(\frac{\partial u_0}{\partial x} + \frac{\partial v_0}{\partial y}\right)\left(\frac{\partial z_b}{\partial t} + u_0\frac{\partial z_b}{\partial x} + v_0\frac{\partial z_b}{\partial y}\right)$$

$$+\frac{\rho h^2}{2}\left(\frac{\partial u_0}{\partial x} + \frac{\partial v_0}{\partial y}\right)^2 = \overline{P} - \rho g h \tag{2.59a}$$

and

***n* = 1:**

$$\frac{\rho h^2}{2}\left(\frac{\partial^2 z_b}{\partial t^2} + \frac{\partial u_0}{\partial t}\frac{\partial z_b}{\partial x} + u_0\frac{\partial^2 z_b}{\partial x \partial t} + \frac{\partial v_0}{\partial t}\frac{\partial z_b}{\partial y} + v_0\frac{\partial^2 z_b}{\partial y \partial t}\right) + \frac{\rho h^3}{3}\left(-\frac{\partial^2 u_0}{\partial x \partial t} - \frac{\partial^2 v_0}{\partial y \partial t}\right)$$

$$+\rho u_0\frac{h^2}{2}\left(\frac{\partial^2 z_b}{\partial x \partial t} + \frac{\partial u_0}{\partial x}\frac{\partial z_b}{\partial x} + u_0\frac{\partial^2 z_b}{\partial x^2} + \frac{\partial v_0}{\partial x}\frac{\partial z_b}{\partial y} + v_0\frac{\partial^2 z_b}{\partial x \partial y}\right)$$

$$+\rho u_0\frac{h^3}{3}\left(-\frac{\partial^2 u_0}{\partial x^2} - \frac{\partial^2 v_0}{\partial x \partial y}\right) + \frac{\rho h^3}{3}\left(\frac{\partial u_0}{\partial x}\frac{\partial u_0}{\partial x} + 2\frac{\partial u_0}{\partial x}\frac{\partial v_0}{\partial y} + \frac{\partial v_0}{\partial y}\frac{\partial v_0}{\partial y}\right)$$

$$+\rho v_0\frac{h^2}{2}\left(\frac{\partial^2 z_b}{\partial y \partial t} + \frac{\partial u_0}{\partial y}\frac{\partial z_b}{\partial x} + u_0\frac{\partial^2 z_b}{\partial x \partial y} + \frac{\partial v_0}{\partial y}\frac{\partial z_b}{\partial y} + v_0\frac{\partial^2 z_b}{\partial y^2}\right)$$

$$-\frac{\rho h^2}{2}\left(\frac{\partial u_0}{\partial x}\frac{\partial z_b}{\partial t} + u_0\frac{\partial u_0}{\partial x}\frac{\partial z_b}{\partial x} + v_0\frac{\partial u_0}{\partial x}\frac{\partial z_b}{\partial y} + \frac{\partial v_0}{\partial y}\frac{\partial z_b}{\partial t} + u_0\frac{\partial v_0}{\partial y}\frac{\partial z_b}{\partial x} + v_0\frac{\partial v_0}{\partial y}\frac{\partial z_b}{\partial y}\right)$$

$$+\rho v_0\frac{h^3}{3}\left(-\frac{\partial^2 v_0}{\partial y^2} - \frac{\partial^2 u_0}{\partial x \partial y}\right) = P_0 - \rho g\frac{h^2}{2} \quad . \tag{2.59b}$$

When Eqn. (2.59b) is differentiated with respect to x and added to Eqn. (2.55a), then

$$\rho h\left(\frac{\partial h}{\partial x}\right)\left(\frac{\partial^2 z_b}{\partial t^2}+\frac{\partial u_0}{\partial t}\frac{\partial z_b}{\partial x}+u_0\frac{\partial^2 z_b}{\partial x\partial t}+\frac{\partial v_0}{\partial t}\frac{\partial z_b}{\partial y}+v_0\frac{\partial^2 z_b}{\partial y\partial t}\right)+$$

$$\frac{\rho h^2}{2}\left(\frac{\partial^3 z_b}{\partial x\partial t^2}+\frac{\partial^2 u_0}{\partial x\partial t}\frac{\partial z_b}{\partial x}+\frac{\partial u_0}{\partial t}\frac{\partial^2 z_b}{\partial x^2}+\frac{\partial u_0}{\partial x}\frac{\partial^2 z_b}{\partial x\partial t}+u_0\frac{\partial^3 z_b}{\partial x^2\partial t}+\frac{\partial^2 v_0}{\partial x\partial t}\frac{\partial z_b}{\partial y}+\frac{\partial v_0}{\partial t}\frac{\partial^2 z_b}{\partial x\partial y}\right.$$

$$\left.+\frac{\partial v_0}{\partial x}\frac{\partial^2 z_b}{\partial y\partial t}+v_0\frac{\partial^3 z_b}{\partial x\partial y\partial t}\right)+\rho h^2\left(\frac{\partial h}{\partial x}\right)\left(-\frac{\partial^2 u_0}{\partial x\partial t}-\frac{\partial^2 v_0}{\partial y\partial t}\right)+\frac{\rho h^3}{3}\left(-\frac{\partial^3 u_0}{\partial x^2\partial t}-\frac{\partial^3 v_0}{\partial x\partial y\partial t}\right)$$

$$+\rho u_0 h\left(\frac{\partial h}{\partial x}\right)\left(\frac{\partial^2 z_b}{\partial x\partial t}+\frac{\partial u_0}{\partial x}\frac{\partial z_b}{\partial x}+u_0\frac{\partial^2 z_b}{\partial x^2}+\frac{\partial v_0}{\partial x}\frac{\partial z_b}{\partial y}+v_0\frac{\partial^2 z_b}{\partial x\partial y}\right)+$$

$$\frac{\rho h^2}{2}\left(u_0\frac{\partial^3 z_b}{\partial x^2\partial t}+\frac{\partial u_0}{\partial x}\frac{\partial^2 z_b}{\partial x\partial t}+\frac{\partial u_0}{\partial x}\frac{\partial u_0}{\partial x}\frac{\partial z_b}{\partial x}+u_0\frac{\partial^2 u_0}{\partial x^2}\frac{\partial z_b}{\partial x}+u_0\frac{\partial u_0}{\partial x}\frac{\partial^2 z_b}{\partial x^2}+2u_0\frac{\partial u_0}{\partial x}\frac{\partial^2 z_b}{\partial x^2}\right.$$

$$+u_0^2\frac{\partial^3 z_b}{\partial x^3}+\frac{\partial u_0}{\partial x}\frac{\partial v_0}{\partial x}\frac{\partial z_b}{\partial y}+u_0\frac{\partial^2 v_0}{\partial x^2}\frac{\partial z_b}{\partial y}+u_0\frac{\partial v_0}{\partial x}\frac{\partial^2 z_b}{\partial x\partial y}+v_0\frac{\partial u_0}{\partial x}\frac{\partial^2 z_b}{\partial x\partial y}+u_0 v_0\frac{\partial^3 z_b}{\partial x^2\partial y}$$

$$\left.+u_0\frac{\partial v_0}{\partial x}\frac{\partial^2 z_b}{\partial x\partial y}\right)+\frac{\rho h^3}{3}\left(-\frac{\partial u_0}{\partial x}\frac{\partial^2 u_0}{\partial x^2}-u_0\frac{\partial^3 u_0}{\partial x^3}-\frac{\partial u_0}{\partial x}\frac{\partial^2 v_0}{\partial x\partial y}-u_0\frac{\partial^3 v_0}{\partial x^2\partial y}\right)$$

$$+\rho v_0 h\left(\frac{\partial h}{\partial x}\right)\left(\frac{\partial^2 z_b}{\partial y\partial t}+\frac{\partial u_0}{\partial y}\frac{\partial z_b}{\partial x}+u_0\frac{\partial^2 z_b}{\partial x\partial y}+\frac{\partial v_0}{\partial y}\frac{\partial z_b}{\partial y}+v_0\frac{\partial^2 z_b}{\partial y^2}\right)+$$

$$\frac{\rho h^2}{2}\left(\frac{\partial v_0}{\partial x}\frac{\partial^2 z_b}{\partial y\partial t}+v_0\frac{\partial^3 z_b}{\partial x\partial y\partial t}+\frac{\partial v_0}{\partial x}\frac{\partial u_0}{\partial y}\frac{\partial z_b}{\partial x}+v_0\frac{\partial^2 u_0}{\partial x\partial y}\frac{\partial z_b}{\partial x}+v_0\frac{\partial u_0}{\partial y}\frac{\partial^2 z_b}{\partial x^2}\right.$$

$$+u_0\frac{\partial v_0}{\partial x}\frac{\partial^2 z_b}{\partial x\partial y}+v_0\frac{\partial u_0}{\partial x}\frac{\partial^2 z_b}{\partial x\partial y}+u_0 v_0\frac{\partial^3 z_b}{\partial x^2\partial y}+\frac{\partial v_0}{\partial x}\frac{\partial v_0}{\partial y}\frac{\partial z_b}{\partial y}+v_0\frac{\partial^2 v_0}{\partial x\partial y}\frac{\partial z_b}{\partial y}$$

$$\left.+v_0\frac{\partial v_0}{\partial y}\frac{\partial^2 z_b}{\partial x\partial y}+2v_0\frac{\partial v_0}{\partial x}\frac{\partial^2 z_b}{\partial y^2}+v_0^2\frac{\partial^3 z_b}{\partial x\partial y^2}\right)+\rho u_0 h^2\left(\frac{\partial h}{\partial x}\right)\left(-\frac{\partial^2 u_0}{\partial x^2}-\frac{\partial^2 v_0}{\partial x\partial y}\right)$$

$$+\frac{\rho h^3}{3}\left(-\frac{\partial v_0}{\partial x}\frac{\partial^2 u_0}{\partial x\partial y}-v_0\frac{\partial^3 u_0}{\partial x^2\partial y}-\frac{\partial v_0}{\partial x}\frac{\partial^2 v_0}{\partial y^2}-v_0\frac{\partial^3 v_0}{\partial x\partial y^2}\right)-$$

$$\rho h\left(\frac{\partial h}{\partial x}\right)\left(\frac{\partial u_0}{\partial x}\frac{\partial z_b}{\partial t}+u_0\frac{\partial u_0}{\partial x}\frac{\partial z_b}{\partial x}+v_0\frac{\partial u_0}{\partial x}\frac{\partial z_b}{\partial y}+\frac{\partial v_0}{\partial y}\frac{\partial z_b}{\partial t}+u_0\frac{\partial v_0}{\partial y}\frac{\partial z_b}{\partial x}+v_0\frac{\partial v_0}{\partial y}\frac{\partial z_b}{\partial y}\right)$$

$$-\frac{\rho h^2}{2}\left(\frac{\partial^2 u_0}{\partial x^2}\frac{\partial z_b}{\partial t}+\frac{\partial u_0}{\partial x}\frac{\partial^2 z_b}{\partial x\partial t}+\frac{\partial u_0}{\partial x}\frac{\partial u_0}{\partial x}\frac{\partial z_b}{\partial x}+u_0\frac{\partial^2 u_0}{\partial x^2}\frac{\partial z_b}{\partial x}+u_0\frac{\partial u_0}{\partial x}\frac{\partial^2 z_b}{\partial x^2}\right.$$

$$+\frac{\partial v_0}{\partial x}\frac{\partial u_0}{\partial x}\frac{\partial z_b}{\partial y}+v_0\frac{\partial^2 u_0}{\partial x^2}\frac{\partial z_b}{\partial y}+v_0\frac{\partial u_0}{\partial x}\frac{\partial^2 z_b}{\partial x\partial y}+\frac{\partial^2 v_0}{\partial x\partial y}\frac{\partial z_b}{\partial t}+\frac{\partial v_0}{\partial y}\frac{\partial^2 z_b}{\partial x\partial t}$$

$$+\frac{\partial u_0}{\partial x}\frac{\partial v_0}{\partial y}\frac{\partial z_b}{\partial x}+u_0\frac{\partial^2 v_0}{\partial x\partial y}\frac{\partial z_b}{\partial x}+u_0\frac{\partial v_0}{\partial y}\frac{\partial^2 z_b}{\partial x^2}+\frac{\partial v_0}{\partial x}\frac{\partial v_0}{\partial y}\frac{\partial z_b}{\partial y}+v_0\frac{\partial^2 v_0}{\partial x\partial y}\frac{\partial z_b}{\partial y}$$

$$+v_0\frac{\partial v_0}{\partial y}\frac{\partial^2 z_b}{\partial x\partial y}\Big)+\frac{\rho h^3}{3}\Big(2\frac{\partial^2 u_0}{\partial x^2}\frac{\partial u_0}{\partial x}+2\frac{\partial^2 u_0}{\partial x^2}\frac{\partial v_0}{\partial y}+2\frac{\partial u_0}{\partial x}\frac{\partial^2 v_0}{\partial x\partial y}+2\frac{\partial v_0}{\partial y}\frac{\partial^2 v_0}{\partial x\partial y}\Big)$$

$$+\rho h^2\Big(\frac{\partial h}{\partial x}\Big)\Big(\frac{\partial u_0}{\partial x}\frac{\partial u_0}{\partial x}+2\frac{\partial u_0}{\partial x}\frac{\partial v_0}{\partial y}+\frac{\partial v_0}{\partial y}\frac{\partial v_0}{\partial y}\Big)+\rho h\Big(\frac{\partial u_0}{\partial t}+u_0\frac{\partial u_0}{\partial x}+v_0\frac{\partial u_0}{\partial y}\Big)$$

$$+\rho v_0 h^2\Big(\frac{\partial h}{\partial x}\Big)\Big(-\frac{\partial^2 v_0}{\partial y^2}-\frac{\partial^2 u_0}{\partial x\partial y}\Big)=-\rho g h\Big(\frac{\partial h}{\partial x}\Big)-\bar{P}\frac{\partial z_b}{\partial x} \qquad (2.60)$$

The pressure $\bar{P}$ is now eliminated by using Eqn. (2.59a) $\times \frac{\partial z_b}{\partial x}$ and adding it to (2.60)

$$\rho h\frac{\partial h}{\partial x}\begin{pmatrix}\frac{\partial u_0}{\partial t}\frac{\partial z_b}{\partial x}+2u_0\frac{\partial^2 z_b}{\partial x\partial t}+\frac{\partial v_0}{\partial t}\frac{\partial z_b}{\partial y}+2v_0\frac{\partial^2 z_b}{\partial y\partial t}+u_0^2\frac{\partial^2 z_b}{\partial x^2}+u_0\frac{\partial v_0}{\partial x}\frac{\partial z_b}{\partial y}+2u_0v_0\frac{\partial^2 z_b}{\partial x\partial y}\\ \frac{\partial^2 z_b}{\partial t^2}+v_0\frac{\partial u_0}{\partial y}\frac{\partial z_b}{\partial x}+v_0^2\frac{\partial^2 z_b}{\partial y^2}-\frac{\partial u_0}{\partial x}\frac{\partial z_b}{\partial t}-v_0\frac{\partial u_0}{\partial x}\frac{\partial z_b}{\partial y}-\frac{\partial v_0}{\partial y}\frac{\partial z_b}{\partial t}-u_0\frac{\partial v_0}{\partial y}\frac{\partial z_b}{\partial x}\end{pmatrix}$$

$+$

$$\rho h\frac{\partial z_b}{\partial x}\begin{pmatrix}\frac{\partial u_0}{\partial t}\frac{\partial z_b}{\partial x}+2u_0\frac{\partial^2 z_b}{\partial x\partial t}+\frac{\partial v_0}{\partial t}\frac{\partial z_b}{\partial y}+2v_0\frac{\partial^2 z_b}{\partial y\partial t}+u_0^2\frac{\partial^2 z_b}{\partial x^2}+u_0\frac{\partial v_0}{\partial x}\frac{\partial z_b}{\partial y}+2u_0v_0\frac{\partial^2 z_b}{\partial x\partial y}\\ \frac{\partial^2 z_b}{\partial t^2}+v_0\frac{\partial u_0}{\partial y}\frac{\partial z_b}{\partial x}+v_0^2\frac{\partial^2 z_b}{\partial y^2}-\frac{\partial u_0}{\partial x}\frac{\partial z_b}{\partial t}-v_0\frac{\partial u_0}{\partial x}\frac{\partial z_b}{\partial y}-\frac{\partial v_0}{\partial y}\frac{\partial z_b}{\partial t}-u_0\frac{\partial v_0}{\partial y}\frac{\partial z_b}{\partial x}\end{pmatrix}$$

$+$

$$\frac{\rho h^2}{2}\Big(\frac{\partial^3 z_b}{\partial x\partial t^2}+\frac{\partial^2 u_0}{\partial x\partial t}\frac{\partial z_b}{\partial x}+\frac{\partial u_0}{\partial t}\frac{\partial^2 z_b}{\partial x^2}+\frac{\partial u_0}{\partial x}\frac{\partial^2 z_b}{\partial x\partial t}+2u_0\frac{\partial^3 z_b}{\partial x^2\partial t}+\frac{\partial^2 v_0}{\partial x\partial t}\frac{\partial z_b}{\partial y}+\frac{\partial v_0}{\partial t}\frac{\partial^2 z_b}{\partial x\partial y}$$

$$+2\frac{\partial v_0}{\partial x}\frac{\partial^2 z_b}{\partial y\partial t}+2v_0\frac{\partial^3 z_b}{\partial x\partial y\partial t}+2u_0\frac{\partial u_0}{\partial x}\frac{\partial^2 z_b}{\partial x^2}+u_0^2\frac{\partial^3 z_b}{\partial x^3}+u_0\frac{\partial^2 v_0}{\partial x^2}\frac{\partial z_b}{\partial y}+v_0^2\frac{\partial^3 z_b}{\partial x\partial y^2}$$

$$+3u_0\frac{\partial v_0}{\partial x}\frac{\partial^2 z_b}{\partial x\partial y}+2u_0v_0\frac{\partial^3 z_b}{\partial x^2\partial y}+\frac{\partial v_0}{\partial x}\frac{\partial u_0}{\partial y}\frac{\partial z_b}{\partial x}+v_0\frac{\partial^2 u_0}{\partial x\partial y}\frac{\partial z_b}{\partial x}+v_0\frac{\partial u_0}{\partial y}\frac{\partial^2 z_b}{\partial x^2}$$

$$+v_0\frac{\partial u_0}{\partial x}\frac{\partial^2 z_b}{\partial x\partial y}+2v_0\frac{\partial v_0}{\partial x}\frac{\partial^2 z_b}{\partial y^2}-\frac{\partial^2 u_0}{\partial x^2}\frac{\partial z_b}{\partial t}-v_0\frac{\partial^2 u_0}{\partial x^2}\frac{\partial z_b}{\partial y}-\frac{\partial^2 v_0}{\partial x\partial y}\frac{\partial z_b}{\partial t}-\frac{\partial v_0}{\partial y}\frac{\partial^2 z_b}{\partial x\partial t}$$

$$-\frac{\partial u_0}{\partial x}\frac{\partial v_0}{\partial y}\frac{\partial z_b}{\partial x}-u_0\frac{\partial^2 v_0}{\partial x\partial y}\frac{\partial z_b}{\partial x}-u_0\frac{\partial v_0}{\partial y}\frac{\partial^2 z_b}{\partial x^2}\Big)$$

$+$

$$\rho h^2\Big(\frac{\partial h}{\partial x}\Big)\Big(-\frac{\partial^2 u_0}{\partial x\partial t}-\frac{\partial^2 v_0}{\partial y\partial t}-u_0\frac{\partial^2 u_0}{\partial x^2}-u_0\frac{\partial^2 v_0}{\partial x\partial y}-v_0\frac{\partial^2 u_0}{\partial x\partial y}-v_0\frac{\partial^2 v_0}{\partial y^2}+\frac{\partial u_0}{\partial x}\frac{\partial u_0}{\partial x}$$
$$+2\frac{\partial u_0}{\partial x}\frac{\partial v_0}{\partial y}+\frac{\partial v_0}{\partial y}\frac{\partial v_0}{\partial y}\Big)$$

+

$$\frac{\rho h^2}{2}\left(\frac{\partial z_b}{\partial x}\right)\left(-\frac{\partial^2 u_0}{\partial x \partial t}-\frac{\partial^2 v_0}{\partial y \partial t}-u_0\,\frac{\partial^2 u_0}{\partial x^2}-u_0\,\frac{\partial^2 v_0}{\partial x \partial y}-v_0\,\frac{\partial^2 u_0}{\partial x \partial y}-v_0\,\frac{\partial^2 v_0}{\partial y^2}+\frac{\partial u_0}{\partial x}\,\frac{\partial u_0}{\partial x}\right.$$
$$\left.+2\frac{\partial u_0}{\partial x}\,\frac{\partial v_0}{\partial y}+\frac{\partial v_0}{\partial y}\,\frac{\partial v_0}{\partial y}\right)$$

+

$$\frac{\rho h^3}{3}\left(-\frac{\partial^3 u_0}{\partial x^2 \partial t}-\frac{\partial^3 v_0}{\partial x \partial y \partial t}-u_0\,\frac{\partial^3 u_0}{\partial x^3}-u_0\,\frac{\partial^3 v_0}{\partial x^2 \partial y}-\frac{\partial v_0}{\partial x}\,\frac{\partial^2 u_0}{\partial x \partial y}-v_0\,\frac{\partial^3 u_0}{\partial x^2 \partial y}-\frac{\partial v_0}{\partial x}\,\frac{\partial^2 v_0}{\partial y^2}\right.$$
$$\left.-v_0\,\frac{\partial^3 v_0}{\partial x \partial y^2}+\frac{\partial^2 u_0}{\partial x^2}\,\frac{\partial u_0}{\partial x}+2\frac{\partial^2 u_0}{\partial x^2}\,\frac{\partial v_0}{\partial y}+\frac{\partial u_0}{\partial x}\,\frac{\partial^2 v_0}{\partial x \partial y}+2\frac{\partial v_0}{\partial y}\,\frac{\partial^2 v_0}{\partial x \partial y}\right)$$

+

$$\rho h\left(\frac{\partial u_0}{\partial t}+u_0\,\frac{\partial u_0}{\partial x}+v_0\,\frac{\partial u_0}{\partial y}\right)=-\rho g h\left(\frac{\partial h}{\partial x}\right)-\rho g h\left(\frac{\partial z_b}{\partial x}\right) \quad . \qquad (2.61)$$

Simplifying the above equation,

$$\rho h\frac{\partial \eta}{\partial x}\begin{pmatrix}\frac{\partial u_0}{\partial t}\,\frac{\partial z_b}{\partial x}+2u_0\,\frac{\partial^2 z_b}{\partial x \partial t}+\frac{\partial v_0}{\partial t}\,\frac{\partial z_b}{\partial y}+2v_0\,\frac{\partial^2 z_b}{\partial y \partial t}+u_0^2\,\frac{\partial^2 z_b}{\partial x^2}+u_0\,\frac{\partial v_0}{\partial x}\,\frac{\partial z_b}{\partial y}+2u_0 v_0\,\frac{\partial^2 z_b}{\partial x \partial y}\\ \frac{\partial^2 z_b}{\partial t^2}+v_0\,\frac{\partial u_0}{\partial y}\,\frac{\partial z_b}{\partial x}+v_0^2\,\frac{\partial^2 z_b}{\partial y^2}-\frac{\partial u_0}{\partial x}\,\frac{\partial z_b}{\partial t}-v_0\,\frac{\partial u_0}{\partial x}\,\frac{\partial z_b}{\partial y}-\frac{\partial v_0}{\partial y}\,\frac{\partial z_b}{\partial t}-u_0\,\frac{\partial v_0}{\partial y}\,\frac{\partial z_b}{\partial x}+g\end{pmatrix}$$

$$+\frac{\rho h^2}{2}\left(\frac{\partial^3 z_b}{\partial x \partial t^2}+\frac{\partial^2 u_0}{\partial x \partial t}\,\frac{\partial z_b}{\partial x}+\frac{\partial u_0}{\partial t}\,\frac{\partial^2 z_b}{\partial x^2}+\frac{\partial u_0}{\partial x}\,\frac{\partial^2 z_b}{\partial x \partial t}+2u_0\frac{\partial^3 z_b}{\partial x^2 \partial t}+\frac{\partial^2 v_0}{\partial x \partial t}\,\frac{\partial z_b}{\partial y}+u_0^2\,\frac{\partial^3 z_b}{\partial x^3}\right.$$
$$+\frac{\partial v_0}{\partial t}\,\frac{\partial^2 z_b}{\partial x \partial y}+2\,\frac{\partial v_0}{\partial x}\,\frac{\partial^2 z_b}{\partial y \partial t}+2v_0\,\frac{\partial^3 z_b}{\partial x \partial y \partial t}+2u_0\,\frac{\partial u_0}{\partial x}\,\frac{\partial^2 z_b}{\partial x^2}+u_0\,\frac{\partial^2 v_0}{\partial x^2}\,\frac{\partial z_b}{\partial y}+v_0^2\,\frac{\partial^3 z_b}{\partial x \partial y^2}$$
$$+3u_0\,\frac{\partial v_0}{\partial x}\,\frac{\partial^2 z_b}{\partial x \partial y}+2u_0 v_0\,\frac{\partial^3 z_b}{\partial x^2 \partial y}+\frac{\partial v_0}{\partial x}\,\frac{\partial u_0}{\partial y}\,\frac{\partial z_b}{\partial x}+v_0\,\frac{\partial^2 u_0}{\partial x \partial y}\,\frac{\partial z_b}{\partial x}+v_0\,\frac{\partial u_0}{\partial y}\,\frac{\partial^2 z_b}{\partial x^2}$$
$$+v_0\,\frac{\partial u_0}{\partial x}\,\frac{\partial^2 z_b}{\partial x \partial y}+2v_0\,\frac{\partial v_0}{\partial x}\,\frac{\partial^2 z_b}{\partial y^2}-\frac{\partial^2 u_0}{\partial x^2}\,\frac{\partial z_b}{\partial t}-v_0\,\frac{\partial^2 u_0}{\partial x^2}\,\frac{\partial z_b}{\partial y}-\frac{\partial^2 v_0}{\partial x \partial y}\,\frac{\partial z_b}{\partial t}-\frac{\partial v_0}{\partial y}\,\frac{\partial^2 z_b}{\partial x \partial t}$$
$$\left.-\frac{\partial u_0}{\partial x}\,\frac{\partial v_0}{\partial y}\,\frac{\partial z_b}{\partial x}-u_0\,\frac{\partial^2 v_0}{\partial x \partial y}\,\frac{\partial z_b}{\partial x}-u_0\frac{\partial v_0}{\partial y}\,\frac{\partial^2 z_b}{\partial x^2}\right)$$

+

$$\rho h^2\,\frac{\partial\left(h+\frac{z_b}{2}\right)}{\partial x}\left(-\frac{\partial^2 u_0}{\partial x \partial t}-\frac{\partial^2 v_0}{\partial y \partial t}-u_0\,\frac{\partial^2 u_0}{\partial x^2}-u_0\,\frac{\partial^2 v_0}{\partial x \partial y}-v_0\,\frac{\partial^2 u_0}{\partial x \partial y}-v_0\,\frac{\partial^2 v_0}{\partial y^2}\right.$$

$$+2\frac{\partial u_0}{\partial x}\frac{\partial v_0}{\partial y}+\frac{\partial v_0}{\partial y}\frac{\partial v_0}{\partial y}\Big)$$

$$+$$

$$\frac{\rho h^3}{3}\Big(-\frac{\partial^3 u_0}{\partial x^2\partial t}-\frac{\partial^3 v_0}{\partial x\partial y\partial t}-u_0\frac{\partial^3 u_0}{\partial x^3}-u_0\frac{\partial^3 v_0}{\partial x^2\partial y}-\frac{\partial v_0}{\partial x}\frac{\partial^2 u_0}{\partial x\partial y}-v_0\frac{\partial^3 u_0}{\partial x^2\partial y}-\frac{\partial v_0}{\partial x}\frac{\partial^2 v_0}{\partial y^2}$$

$$-v_0\frac{\partial^3 v_0}{\partial x\partial y^2}+\frac{\partial^2 u_0}{\partial x^2}\frac{\partial u_0}{\partial x}+2\frac{\partial^2 u_0}{\partial x^2}\frac{\partial v_0}{\partial y}+\frac{\partial u_0}{\partial x}\frac{\partial^2 v_0}{\partial x\partial y}+2\frac{\partial v_0}{\partial y}\frac{\partial^2 v_0}{\partial x\partial y}\Big)$$

$$+\rho h\Big(\frac{\partial u_0}{\partial t}+u_0\frac{\partial u_0}{\partial x}+v_0\frac{\partial u_0}{\partial y}\Big)=0 \qquad . \tag{2.62}$$

By factoring similar terms, the following simpler equation results,

$$\rho h\left(\frac{\partial \eta}{\partial x}\right)\Big[\frac{\partial^2 z_b}{\partial t^2}+\frac{\partial z_b}{\partial x}\Big(\frac{\partial u_0}{\partial t}+v_0\frac{\partial u_0}{\partial y}-u_0\frac{\partial v_0}{\partial y}\Big)+2u_0\frac{\partial^2 z_b}{\partial x\partial t}+2v_0\frac{\partial^2 z_b}{\partial y\partial t}$$
$$+\frac{\partial z_b}{\partial y}\Big(\frac{\partial v_0}{\partial t}+u_0\frac{\partial v_0}{\partial x}-v_0\frac{\partial u_0}{\partial x}\Big)+u_0^2\frac{\partial^2 z_b}{\partial x^2}+2u_0v_0\frac{\partial^2 z_b}{\partial x\partial y}+v_0^2\frac{\partial^2 z_b}{\partial y^2}$$
$$-\frac{\partial z_b}{\partial t}\Big(\frac{\partial u_0}{\partial x}+\frac{\partial v_0}{\partial y}\Big)+g\Big]$$

$$+$$

$$\frac{\rho h^2}{2}\Big[\frac{\partial^3 z_b}{\partial x\partial t^2}+\frac{\partial z_b}{\partial x}\Big(\frac{\partial^2 u_0}{\partial x\partial t}+\frac{\partial v_0}{\partial x}\frac{\partial u_0}{\partial y}+v_0\frac{\partial^2 u_0}{\partial x\partial y}-\frac{\partial u_0}{\partial x}\frac{\partial v_0}{\partial y}-u_0\frac{\partial^2 v_0}{\partial x\partial y}\Big)$$
$$+\frac{\partial^2 z_b}{\partial x^2}\Big(\frac{\partial u_0}{\partial t}+2u_0\frac{\partial u_0}{\partial x}+v_0\frac{\partial u_0}{\partial y}-u_0\frac{\partial v_0}{\partial y}\Big)+\frac{\partial^2 z_b}{\partial x\partial t}\Big(\frac{\partial u_0}{\partial x}-\frac{\partial v_0}{\partial y}\Big)+2u_0\frac{\partial^3 z_b}{\partial x^2\partial t}$$
$$+\frac{\partial z_b}{\partial y}\Big(\frac{\partial^2 v_0}{\partial x\partial t}+u_0\frac{\partial^2 v_0}{\partial x^2}-v_0\frac{\partial^2 u_0}{\partial x^2}\Big)+\frac{\partial^2 z_b}{\partial x\partial y}\Big(\frac{\partial v_0}{\partial t}+3u_0\frac{\partial v_0}{\partial x}+v_0\frac{\partial u_0}{\partial x}\Big)$$
$$+2\frac{\partial v_0}{\partial x}\frac{\partial^2 z_b}{\partial y\partial t}+2v_0\frac{\partial^3 z_b}{\partial x\partial y\partial t}+u_0^2\frac{\partial^3 z_b}{\partial x^3}+2u_0v_0\frac{\partial^3 z_b}{\partial x^2\partial y}+2v_0\frac{\partial v_0}{\partial x}\frac{\partial^2 z_b}{\partial y^2}$$
$$+v_0^2\frac{\partial^3 z_b}{\partial x\partial y^2}-\frac{\partial z_b}{\partial t}\Big(\frac{\partial^2 u_0}{\partial x^2}+\frac{\partial^2 v_0}{\partial x\partial y}\Big)\Big]$$

$$+$$

$$\rho h^2\frac{\partial\left(h+\frac{z_b}{2}\right)}{\partial x}\Big[-\frac{\partial^2 u_0}{\partial x\partial t}-\frac{\partial^2 v_0}{\partial y\partial t}-u_0\frac{\partial^2 u_0}{\partial x^2}-\frac{\partial^2(u_0v_0)}{\partial x\partial y}-v_0\frac{\partial^2 v_0}{\partial y^2}+\Big(\frac{\partial u_0}{\partial x}+\frac{\partial v_0}{\partial y}\Big)^2\Big]$$

$$+$$

$$\frac{\rho h^3}{3}\left[-\frac{\partial^3 u_0}{\partial x^2 \partial t}-\frac{\partial^3 v_0}{\partial x \partial y \partial t}-u_0\,\frac{\partial^3 u_0}{\partial x^3}-\frac{\partial^3 (u_0 v_0)}{\partial x^2 \partial y}-\frac{\partial v_0}{\partial x}\left(\frac{\partial^2 u_0}{\partial x \partial y}+\frac{\partial^2 v_0}{\partial y^2}\right)-v_0\,\frac{\partial^3 v_0}{\partial x \partial y^2}\right.$$
$$\left.+\left(\frac{\partial u_0}{\partial x}+2\frac{\partial v_0}{\partial y}\right)\left(\frac{\partial^2 v_0}{\partial x \partial y}+\frac{\partial^2 u_0}{\partial x^2}\right)\right]$$

+

$$\rho h\left(\frac{\partial u_0}{\partial t}+u_0\,\frac{\partial u_0}{\partial x}+v_0\,\frac{\partial u_0}{\partial y}\right)=0 \qquad . \tag{2.63}$$

2D level I x-momentum GN equation for a fixed bed ($\frac{\partial z_b}{\partial t}=\frac{\partial^2 z_b}{\partial x \partial t}=\frac{\partial^2 z_b}{\partial y \partial t}=0$) is

$$\rho h\left(\frac{\partial \eta}{\partial x}\right)\left[\frac{\partial z_b}{\partial x}\left(\frac{\partial u_0}{\partial t}+v_0\,\frac{\partial u_0}{\partial y}-u_0\frac{\partial v_0}{\partial y}\right)+\frac{\partial z_b}{\partial y}\left(\frac{\partial v_0}{\partial t}+u_0\,\frac{\partial v_0}{\partial x}-v_0\,\frac{\partial u_0}{\partial x}\right)+u_0^2\,\frac{\partial^2 z_b}{\partial x^2}\right.$$
$$\left.+2u_0 v_0\,\frac{\partial^2 z_b}{\partial x \partial y}+v_0^2\,\frac{\partial^2 z_b}{\partial y^2}+g\right]$$

+

$$\frac{\rho h^2}{2}\left[\frac{\partial z_b}{\partial x}\left(\frac{\partial^2 u_0}{\partial x \partial t}+\frac{\partial v_0}{\partial x}\,\frac{\partial u_0}{\partial y}+v_0\,\frac{\partial^2 u_0}{\partial x \partial y}-\frac{\partial u_0}{\partial x}\,\frac{\partial v_0}{\partial y}-u_0\,\frac{\partial^2 v_0}{\partial x \partial y}\right)+u_0^2\,\frac{\partial^3 z_b}{\partial x^3}+v_0^2\,\frac{\partial^3 z_b}{\partial x \partial y^2}\right.$$
$$+\frac{\partial^2 z_b}{\partial x^2}\left(\frac{\partial u_0}{\partial t}+2u_0\,\frac{\partial u_0}{\partial x}+v_0\,\frac{\partial u_0}{\partial y}-u_0\frac{\partial v_0}{\partial y}\right)+\frac{\partial z_b}{\partial y}\left(\frac{\partial^2 v_0}{\partial x \partial t}+u_0\,\frac{\partial^2 v_0}{\partial x^2}-v_0\,\frac{\partial^2 u_0}{\partial x^2}\right)$$
$$\left.+\frac{\partial^2 z_b}{\partial x \partial y}\left(\frac{\partial v_0}{\partial t}+3u_0\,\frac{\partial v_0}{\partial x}+v_0\,\frac{\partial u_0}{\partial x}\right)+2u_0 v_0\,\frac{\partial^3 z_b}{\partial x^2 \partial y}+2v_0\,\frac{\partial v_0}{\partial x}\,\frac{\partial^2 z_b}{\partial y^2}\right]$$

+

$$\rho h^2\,\frac{\partial\left(h+\frac{z_b}{2}\right)}{\partial x}\left[-\frac{\partial^2 u_0}{\partial x \partial t}-\frac{\partial^2 v_0}{\partial y \partial t}-u_0\,\frac{\partial^2 u_0}{\partial x^2}-\frac{\partial^2 (u_0 v_0)}{\partial x \partial y}-v_0\,\frac{\partial^2 v_0}{\partial y^2}+\left(\frac{\partial u_0}{\partial x}+\frac{\partial v_0}{\partial y}\right)^2\right]$$

+

$$\frac{\rho h^3}{3}\left[-\frac{\partial^3 u_0}{\partial x^2 \partial t}-\frac{\partial^3 v_0}{\partial x \partial y \partial t}-u_0\,\frac{\partial^3 u_0}{\partial x^3}-\frac{\partial^3 (u_0 v_0)}{\partial x^2 \partial y}-\frac{\partial v_0}{\partial x}\left(\frac{\partial^2 u_0}{\partial x \partial y}+\frac{\partial^2 v_0}{\partial y^2}\right)-v_0\,\frac{\partial^3 v_0}{\partial x \partial y^2}\right.$$
$$\left.+\left(\frac{\partial u_0}{\partial x}+2\frac{\partial v_0}{\partial y}\right)\left(\frac{\partial^2 v_0}{\partial x \partial y}+\frac{\partial^2 u_0}{\partial x^2}\right)\right]$$

+

$$\rho h\left(\frac{\partial u_0}{\partial t}+u_0\,\frac{\partial u_0}{\partial x}+v_0\,\frac{\partial u_0}{\partial y}\right)=0 \quad . \tag{2.64}$$

For a flat horizontal bed,

$$\frac{\partial z_b}{\partial x}=\frac{\partial^2 z_b}{\partial x^2}=\frac{\partial^3 z_b}{\partial x^3}=\frac{\partial z_b}{\partial y}=\frac{\partial^2 z_b}{\partial y^2}=\frac{\partial^3 z_b}{\partial y^3}=\frac{\partial z_b}{\partial x\partial y}=\frac{\partial^3 z_b}{\partial x^2\partial y}=0 \ ,$$

Then we have

$$\rho h\left(\frac{\partial \eta}{\partial x}\right)g+\rho h^2\left(\frac{\partial h}{\partial x}\right)\left[-\frac{\partial^2 u_0}{\partial x\partial t}-\frac{\partial^2 v_0}{\partial y\partial t}-u_0\frac{\partial^2 u_0}{\partial x^2}-\frac{\partial^2(u_0v_0)}{\partial x\partial y}-v_0\frac{\partial^2 v_0}{\partial y^2}+\left(\frac{\partial u_0}{\partial x}+\frac{\partial v_0}{\partial y}\right)^2\right]$$

+

$$\frac{\rho h^3}{3}\left[-\frac{\partial^3 u_0}{\partial x^2\partial t}-\frac{\partial^3 v_0}{\partial x\partial y\partial t}-u_0\frac{\partial^3 u_0}{\partial x^3}-\frac{\partial^3(u_0v_0)}{\partial x^2\partial y}-\frac{\partial v_0}{\partial x}\left(\frac{\partial^2 u_0}{\partial x\partial y}+\frac{\partial^2 v_0}{\partial y^2}\right)-v_0\frac{\partial^3 v_0}{\partial x\partial y^2}+\left(\frac{\partial u_0}{\partial x}+2\frac{\partial v_0}{\partial y}\right)\left(\frac{\partial^2 v_0}{\partial x\partial y}+\frac{\partial^2 u_0}{\partial x^2}\right)\right]+\rho h\left(\frac{\partial u_0}{\partial t}+u_0\frac{\partial u_0}{\partial x}+v_0\frac{\partial u_0}{\partial y}\right)=0 \quad . \tag{2.65}$$

By simplifying the above equation, the two-dimensional level I GN momentum equation for fixed-flat horizontal bed in *x*-direction is achieved:

$$\frac{\partial u_0}{\partial t}+u_0\frac{\partial u_0}{\partial x}+v_0\frac{\partial u_0}{\partial y}=$$

$$-g\frac{\partial \eta}{\partial x}+h\left(\frac{\partial h}{\partial x}\right)\left[\frac{\partial^2 u_0}{\partial x\partial t}+\frac{\partial^2 v_0}{\partial y\partial t}+u_0\frac{\partial^2 u_0}{\partial x^2}+\frac{\partial^2(u_0v_0)}{\partial x\partial y}+v_0\frac{\partial^2 v_0}{\partial y^2}-\left(\frac{\partial u_0}{\partial x}+\frac{\partial v_0}{\partial y}\right)^2\right]$$

$$+\frac{h^2}{3}\left[\frac{\partial^3 u_0}{\partial x^2\partial t}+\frac{\partial^3 v_0}{\partial x\partial y\partial t}+u_0\frac{\partial^3 u_0}{\partial x^3}+\frac{\partial^3(u_0v_0)}{\partial x^2\partial y}+\frac{\partial v_0}{\partial x}\left(\frac{\partial^2 u_0}{\partial x\partial y}+\frac{\partial^2 v_0}{\partial y^2}\right)+v_0\frac{\partial^3 v_0}{\partial x\partial y^2}-\left(\frac{\partial u_0}{\partial x}+2\frac{\partial v_0}{\partial y}\right)\left(\frac{\partial^2 v_0}{\partial x\partial y}+\frac{\partial^2 u_0}{\partial x^2}\right)\right] \quad . \tag{2.66}$$

Similar to the momentum equation for *x*-direction, the momentum equation for *y*-direction is as follows (The derivation of the 2D level I GN momentum equation in *y*-direction is essentially the same as for the *x*-direction and so the final equations are summarized):

$$\rho h\left(\frac{\partial \eta}{\partial y}\right)\left[\frac{\partial^2 z_b}{\partial t^2}+\frac{\partial z_b}{\partial x}\left(\frac{\partial u_0}{\partial t}+v_0\frac{\partial u_0}{\partial y}-u_0\frac{\partial v_0}{\partial y}\right)+2u_0\frac{\partial^2 z_b}{\partial x\partial t}+2v_0\frac{\partial^2 z_b}{\partial y\partial t}\right.$$
$$\left.+\frac{\partial z_b}{\partial y}\left(\frac{\partial v_0}{\partial t}+u_0\frac{\partial v_0}{\partial x}-v_0\frac{\partial u_0}{\partial x}\right)+u_0^2\frac{\partial^2 z_b}{\partial x^2}+2u_0v_0\frac{\partial^2 z_b}{\partial x\partial y}+v_0^2\frac{\partial^2 z_b}{\partial y^2}\right.$$
$$\left.-\frac{\partial z_b}{\partial t}\left(\frac{\partial u_0}{\partial x}+\frac{\partial v_0}{\partial y}\right)+g\right]$$

+

$$\frac{\rho h^2}{2}\left[\frac{\partial^3 z_b}{\partial y\partial t^2}+\frac{\partial z_b}{\partial x}\left(\frac{\partial^2 u_0}{\partial y\partial t}+v_0\frac{\partial^2 u_0}{\partial y^2}-u_0\frac{\partial^2 v_0}{\partial y^2}\right)+2\frac{\partial u_0}{\partial y}\frac{\partial^2 z_b}{\partial x\partial t}+2u_0\frac{\partial^3 z_b}{\partial x\partial y\partial t}\right.$$

$$+\frac{\partial z_b}{\partial y}\left(\frac{\partial^2 v_0}{\partial y\partial t}+\frac{\partial u_0}{\partial y}\frac{\partial v_0}{\partial x}+u_0\frac{\partial^2 v_0}{\partial x\partial y}-\frac{\partial v_0}{\partial y}\frac{\partial u_0}{\partial x}-v_0\frac{\partial^2 u_0}{\partial x\partial y}\right)+v_0^2\frac{\partial^3 z_b}{\partial y^3}+2v_0\frac{\partial^3 z_b}{\partial y^2\partial t}$$

$$+\frac{\partial^2 z_b}{\partial x\partial y}\left(\frac{\partial u_0}{\partial t}+3v_0\frac{\partial u_0}{\partial y}+u_0\frac{\partial v_0}{\partial y}\right)+\frac{\partial^2 z_b}{\partial y^2}\left(\frac{\partial v_0}{\partial t}+u_0\frac{\partial v_0}{\partial x}+2v_0\frac{\partial v_0}{\partial y}-v_0\frac{\partial u_0}{\partial x}\right)+$$

$$\left.2u_0\frac{\partial u_0}{\partial y}\frac{\partial^2 z_b}{\partial x^2}+u_0^2\frac{\partial^3 z_b}{\partial x^2\partial y}+2u_0v_0\frac{\partial^3 z_b}{\partial x\partial y^2}+\frac{\partial^2 z_b}{\partial y\partial t}\left(\frac{\partial v_0}{\partial y}-\frac{\partial u_0}{\partial x}\right)-\frac{\partial z_b}{\partial t}\left(\frac{\partial^2 u_0}{\partial x\partial y}+\frac{\partial^2 v_0}{\partial y^2}\right)\right]$$

+

$$\rho h^2\frac{\partial\left(h+\frac{z_b}{2}\right)}{\partial y}\left[-\frac{\partial^2 u_0}{\partial x\partial t}-\frac{\partial^2 v_0}{\partial y\partial t}-u_0\frac{\partial^2 u_0}{\partial x^2}-\frac{\partial^2(u_0v_0)}{\partial x\partial y}-v_0\frac{\partial^2 v_0}{\partial y^2}+\left(\frac{\partial u_0}{\partial x}+\frac{\partial v_0}{\partial y}\right)^2\right]$$

$$+\frac{\rho h^3}{3}\left[-\frac{\partial^3 u_0}{\partial x\partial y\partial t}-\frac{\partial^3 v_0}{\partial y^2\partial t}-\frac{\partial u_0}{\partial y}\frac{\partial^2 u_0}{\partial x^2}-u_0\frac{\partial^3 u_0}{\partial x^2\partial y}-\frac{\partial u_0}{\partial y}\frac{\partial^2 v_0}{\partial x\partial y}-\frac{\partial^3(u_0v_0)}{\partial x\partial y^2}-v_0\frac{\partial^3 v_0}{\partial y^3}\right.$$
$$\left.+\left(2\frac{\partial u_0}{\partial x}+\frac{\partial v_0}{\partial y}\right)\left(\frac{\partial^2 u_0}{\partial x\partial y}+\frac{\partial^2 v_0}{\partial y^2}\right)\right]$$

$$+\rho h\left(\frac{\partial v_0}{\partial t}+u_0\frac{\partial v_0}{\partial x}+v_0\frac{\partial v_0}{\partial y}\right)=0 \qquad . \tag{2.67}$$

The 2D level I y-momentum GN equation for a fixed bed ($\frac{\partial^2 z_b}{\partial t^2} = \frac{\partial^2 z_b}{\partial x \partial t} = \frac{\partial^2 z_b}{\partial y \partial t} = 0$) is

$$\rho h \left(\frac{\partial \eta}{\partial y}\right)\left[\frac{\partial z_b}{\partial x}\left(\frac{\partial u_0}{\partial t} + v_0 \frac{\partial u_0}{\partial y} - u_0 \frac{\partial v_0}{\partial y}\right) + \frac{\partial z_b}{\partial y}\left(\frac{\partial v_0}{\partial t} + u_0 \frac{\partial v_0}{\partial x} - v_0 \frac{\partial u_0}{\partial x}\right) + u_0^2 \frac{\partial^2 z_b}{\partial x^2} + 2u_0 v_0 \frac{\partial^2 z_b}{\partial x \partial y} + v_0^2 \frac{\partial^2 z_b}{\partial y^2} + g\right]$$

$+$

$$\frac{\rho h^2}{2}\left[\frac{\partial z_b}{\partial x}\left(\frac{\partial^2 u_0}{\partial y \partial t} + v_0 \frac{\partial^2 u_0}{\partial y^2} - u_0 \frac{\partial^2 v_0}{\partial y^2}\right) + \frac{\partial^2 z_b}{\partial x \partial y}\left(\frac{\partial u_0}{\partial t} + 3v_0 \frac{\partial u_0}{\partial y} + u_0 \frac{\partial v_0}{\partial y}\right) + v_0^2 \frac{\partial^3 z_b}{\partial y^3}\right.$$

$$+ \frac{\partial z_b}{\partial y}\left(\frac{\partial^2 v_0}{\partial y \partial t} + \frac{\partial u_0}{\partial y}\frac{\partial v_0}{\partial x} + u_0 \frac{\partial^2 v_0}{\partial x \partial y} - \frac{\partial v_0}{\partial y}\frac{\partial u_0}{\partial x} - v_0 \frac{\partial^2 u_0}{\partial x \partial y}\right) + 2u_0 \frac{\partial u_0}{\partial y}\frac{\partial^2 z_b}{\partial x^2}$$

$$\left. + \frac{\partial^2 z_b}{\partial y^2}\left(\frac{\partial v_0}{\partial t} + u_0 \frac{\partial v_0}{\partial x} + 2v_0 \frac{\partial v_0}{\partial y} - v_0 \frac{\partial u_0}{\partial x}\right) + u_0^2 \frac{\partial^3 z_b}{\partial x^2 \partial y} + 2u_0 v_0 \frac{\partial^3 z_b}{\partial x \partial y^2}\right]$$

$+$

$$\rho h^2 \frac{\partial\left(h + \frac{z_b}{2}\right)}{\partial y}\left[-\frac{\partial^2 u_0}{\partial x \partial t} - \frac{\partial^2 v_0}{\partial y \partial t} - u_0 \frac{\partial^2 u_0}{\partial x^2} - \frac{\partial^2 (u_0 v_0)}{\partial x \partial y} - v_0 \frac{\partial^2 v_0}{\partial y^2} + \left(\frac{\partial u_0}{\partial x} + \frac{\partial v_0}{\partial y}\right)^2\right]$$

$+$

$$\frac{\rho h^3}{3}\left[-\frac{\partial^3 u_0}{\partial x \partial y \partial t} - \frac{\partial^3 v_0}{\partial y^2 \partial t} - \frac{\partial u_0}{\partial y}\frac{\partial^2 u_0}{\partial x^2} - u_0 \frac{\partial^3 u_0}{\partial x^2 \partial y} - \frac{\partial u_0}{\partial y}\frac{\partial^2 v_0}{\partial x \partial y} - \frac{\partial^3 (u_0 v_0)}{\partial x \partial y^2} - v_0 \frac{\partial^3 v_0}{\partial y^3}\right.$$

$$\left. + \left(2\frac{\partial u_0}{\partial x} + \frac{\partial v_0}{\partial y}\right)\left(\frac{\partial^2 u_0}{\partial x \partial y} + \frac{\partial^2 v_0}{\partial y^2}\right)\right]$$

$$+ \rho h\left(\frac{\partial v_0}{\partial t} + u_0 \frac{\partial v_0}{\partial x} + v_0 \frac{\partial v_0}{\partial y}\right) = 0 \qquad . \qquad (2.68)$$

For a flat horizontal bed,

$$\frac{\partial z_b}{\partial x}=\frac{\partial^2 z_b}{\partial x^2}=\frac{\partial^3 z_b}{\partial x^3}=\frac{\partial z_b}{\partial y}=\frac{\partial^2 z_b}{\partial y^2}=\frac{\partial^3 z_b}{\partial y^3}=\frac{\partial z_b}{\partial x\partial y}=\frac{\partial^3 z_b}{\partial x^2\partial y}=0 \ :$$

$$\rho h\ \frac{\partial \eta}{\partial y}g+\rho h^2\left(\frac{\partial h}{\partial y}\right)\left[-\frac{\partial^2 u_0}{\partial x\partial t}-\frac{\partial^2 v_0}{\partial y\partial t}-u_0\ \frac{\partial^2 u_0}{\partial x^2}-\frac{\partial^2(u_0v_0)}{\partial x\partial y}-v_0\ \frac{\partial^2 v_0}{\partial y^2}+\left(\frac{\partial u_0}{\partial x}+\frac{\partial v_0}{\partial y}\right)^2\right]$$

$$+\frac{\rho h^3}{3}\left[-\frac{\partial^3 u_0}{\partial x\partial y\partial t}-\frac{\partial^3 v_0}{\partial y^2\partial t}-\frac{\partial u_0}{\partial y}\ \frac{\partial^2 u_0}{\partial x^2}-u_0\ \frac{\partial^3 u_0}{\partial x^2\partial y}-\frac{\partial u_0}{\partial y}\ \frac{\partial^2 v_0}{\partial x\partial y}-\frac{\partial^3(u_0v_0)}{\partial x\partial y^2}-v_0\ \frac{\partial^3 v_0}{\partial y^3}\right.$$
$$\left.+\left(2\frac{\partial u_0}{\partial x}+\frac{\partial v_0}{\partial y}\right)\left(\frac{\partial^2 u_0}{\partial x\partial y}+\frac{\partial^2 v_0}{\partial y^2}\right)\right]$$

$$+\rho h\left(\frac{\partial v_0}{\partial t}+u_0\ \frac{\partial v_0}{\partial x}+v_0\ \frac{\partial v_0}{\partial y}\right)=0 \quad . \tag{2.69}$$

By simplifying the above, the two-dimensional level I GN momentum equation for fixed-flat horizontal bed in *y*-direction is derived:

$$\frac{\partial v_0}{\partial t}+u_0\ \frac{\partial v_0}{\partial x}+v_0\ \frac{\partial v_0}{\partial y}=$$

$$-g\frac{\partial \eta}{\partial y}+h\left(\frac{\partial h}{\partial y}\right)\left[\frac{\partial^2 u_0}{\partial x\partial t}+\frac{\partial^2 v_0}{\partial y\partial t}+u_0\ \frac{\partial^2 u_0}{\partial x^2}+\frac{\partial^2(u_0v_0)}{\partial x\partial y}+v_0\ \frac{\partial^2 v_0}{\partial y^2}-\left(\frac{\partial u_0}{\partial x}+\frac{\partial v_0}{\partial y}\right)^2\right]$$

$$+\frac{h^2}{3}\left[\frac{\partial^3 u_0}{\partial x\partial y\partial t}+\frac{\partial^3 v_0}{\partial y^2\partial t}+\frac{\partial u_0}{\partial y}\ \frac{\partial^2 u_0}{\partial x^2}+u_0\ \frac{\partial^3 u_0}{\partial x^2\partial y}+\frac{\partial u_0}{\partial y}\ \frac{\partial^2 v_0}{\partial x\partial y}+\frac{\partial^3(u_0v_0)}{\partial x\partial y^2}+v_0\ \frac{\partial^3 v_0}{\partial y^3}\right.$$
$$\left.-\left(2\frac{\partial u_0}{\partial x}+\frac{\partial v_0}{\partial y}\right)\left(\frac{\partial^2 u_0}{\partial x\partial y}+\frac{\partial^2 v_0}{\partial y^2}\right)\right] \quad . \tag{2.70}$$

Then by applying Eqn. (2.64) in 1-D we have:

$$\rho h\ \left(\frac{\partial \eta}{\partial x}\right)\left[\frac{\partial u_0}{\partial t}\ \frac{\partial z_b}{\partial x}+u_0^2\ \frac{\partial^2 z_b}{\partial x^2}+g\right]+\frac{\rho h^3}{3}\left[-\frac{\partial^3 u_0}{\partial x^2\partial t}-u_0\ \frac{\partial^3 u_0}{\partial x^3}+\frac{\partial u_0}{\partial x}\ \frac{\partial^2 u_0}{\partial x^2}\right]$$

$$+\rho h^2\ \frac{\partial\left(h+\frac{z_b}{2}\right)}{\partial x}\left[-\frac{\partial^2 u_0}{\partial x\partial t}-u_0\ \frac{\partial^2 u_0}{\partial x^2}+\left(\frac{\partial u_0}{\partial x}\right)^2\right]+\rho h\left[\frac{\partial u_0}{\partial t}+u_0\ \frac{\partial u_0}{\partial x}\right]$$

$$+\frac{\rho h^2}{2}\left[\frac{\partial^2 u_0}{\partial x\partial t}\ \frac{\partial z_b}{\partial x}+\frac{\partial^2 z_b}{\partial x^2}\left(\frac{\partial u_0}{\partial t}+2u_0\ \frac{\partial u_0}{\partial x}\right)+u_0^2\ \frac{\partial^3 z_b}{\partial x^3}\right]=0 \quad . \tag{2.71}$$

For a flat horizontal bed,

$$\frac{\partial z_b}{\partial x} = \frac{\partial^2 z_b}{\partial x^2} = 0 \ ,$$

and so the, 1D level I GN momentum equation for fixed-flat horizontal bed in *x*-direction is obtained as:

$$\frac{\partial u_0}{\partial t} + u_0 \frac{\partial u_0}{\partial x} = -g\frac{\partial \eta}{\partial x} + h\left(\frac{\partial h}{\partial x}\right)\left[\frac{\partial^2 u_0}{\partial x \partial t} + u_0 \frac{\partial^2 u_0}{\partial x^2} - \left(\frac{\partial u_0}{\partial x}\right)^2\right]$$

$$+\frac{h^2}{3}\left[\frac{\partial^3 u_0}{\partial x^2 \partial t} + u_0 \frac{\partial^3 u_0}{\partial x^3} - \frac{\partial u_0}{\partial x}\frac{\partial^2 u_0}{\partial x^2}\right] \quad . \tag{2.72}$$

Here, The 1D level I GN continuity equation is:

$$\frac{\partial h}{\partial t} + \frac{\partial (u_0 h)}{\partial x} = 0 \tag{2.73}$$

By applying Eqn. (2.68) in 1-D we have:

$$\rho h \left(\frac{\partial \eta}{\partial y}\right)\left[\frac{\partial v_0}{\partial t}\frac{\partial z_b}{\partial y} + v_0^2 \frac{\partial^2 z_b}{\partial y^2} + g\right] + \frac{\rho h^3}{3}\left[-\frac{\partial^3 v_0}{\partial y^2 \partial t} - v_0 \frac{\partial^3 v_0}{\partial y^3} + \frac{\partial v_0}{\partial y}\frac{\partial^2 v_0}{\partial y^2}\right]$$

$$+\rho h^2 \frac{\partial\left(h + \frac{z_b}{2}\right)}{\partial y}\left[-\frac{\partial^2 v_0}{\partial y \partial t} - v_0 \frac{\partial^2 v_0}{\partial y^2} + \left(\frac{\partial v_0}{\partial y}\right)^2\right] + \rho h\left[\frac{\partial v_0}{\partial t} + v_0 \frac{\partial v_0}{\partial y}\right]$$

$$+\frac{\rho h^2}{2}\left[\frac{\partial^2 v_0}{\partial y \partial t}\frac{\partial z_b}{\partial y} + \frac{\partial^2 z_b}{\partial y^2}\left(\frac{\partial v_0}{\partial t} + 2v_0 \frac{\partial v_0}{\partial y}\right) + v_0^2 \frac{\partial^3 z_b}{\partial y^3}\right] = 0 \quad . \tag{2.74}$$

For a flat horizontal bed,

$$\frac{\partial z_b}{\partial y} = \frac{\partial^2 z_b}{\partial y^2} = 0 \ ,$$

1D level I GN momentum equation for fixed-flat horizontal bed in *y*-direction is:

$$\frac{\partial v_0}{\partial t} + v_0 \frac{\partial v_0}{\partial y} = -g\frac{\partial \eta}{\partial y} + h\left(\frac{\partial h}{\partial y}\right)\left[\frac{\partial^2 v_0}{\partial y \partial t} + v_0 \frac{\partial^2 v_0}{\partial y^2} - \left(\frac{\partial v_0}{\partial y}\right)^2\right]$$

$$+\frac{h^2}{3}\left[\frac{\partial^3 v_0}{\partial y^2 \partial t} + v_0 \frac{\partial^3 v_0}{\partial y^3} - \frac{\partial v_0}{\partial y}\frac{\partial^2 v_0}{\partial y^2}\right] \tag{2.75}$$

Here, the 1D level I GN continuity equation is:

$$\frac{\partial h}{\partial t} + \frac{\partial (v_0 h)}{\partial y} = 0 \tag{2.76}$$

2.2 Summery

- 2D and 1D level I GN equations were derived in this chapter. A mathematical Level I GN model has been formulated based on the 3-D continuity and momentum equations and kinematic boundary condition applicable to the free surface flow of inviscid, incompressible liquid over a fixed bed.

- For the first time, to the author's knowledge, the GN Level I mass and momentum equations have been derived in two horizontal dimensions for non-uniform beds. These equations are summarised by Eqn. (2.18) for mass conservation and Eqns. (2.64) and (2.68) for momentum conservation. The 2D level I GN equations for a horizontal bed were also obtained as a reduced version of the non-uniform bed equations, and are summarised as Eqns. (2.18), (2.66) and (2.70). 1D level I GN equations of a horizontal bed were obtained as Eqns. (2.72) and (2.73).

- 1D level I GN equations are solved numerically. The details of discretisations are presented in chapter 3 (section 3.2). 2D level I GN numerical discretisations are presented in sections 3.3 and 3.4 of chapter 3. Wave predictions of 1D and 2D level I GN numerical solvers are presented in chapter 4 and chapters 5, respectively.

Chapter 3

Numerical Implementation of 1D and 2D Level I GN Equations

3.1 Finite Difference Solvers of Green-Naghdi Equations

3.1.1 Introduction

This chapter presents the implicit numerical schemes used for spatial discretisation of the level I GN equations. Two matrix solvers, second-order tridiagonal and fourth-order pentadiagonal matrix, will be introduced. A Runge-Kutta fourth-order scheme is used for time integration. The boundary conditions are outlined. The numerical procedure used to solve the 1D and 2D level I GN equations is explained.

Flowchart 1 presents the steps of developing numerical solver of GN equations:

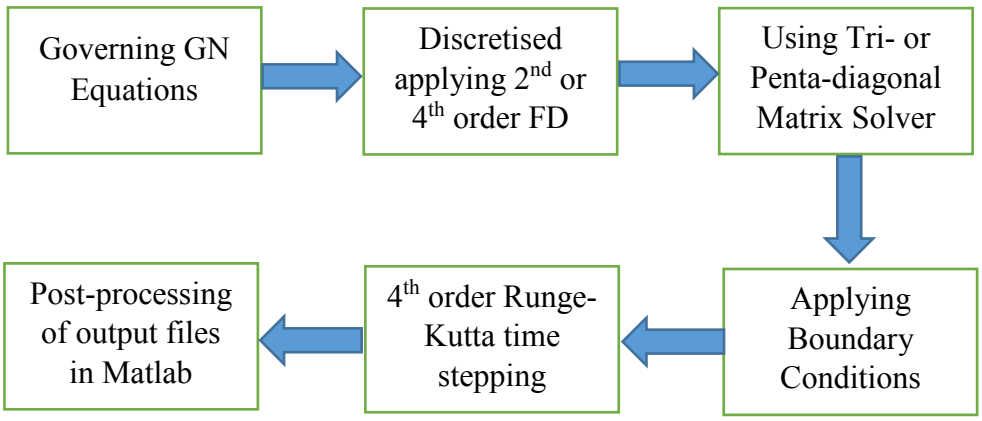

Flowchart 1: Steps of developing numerical solvers

3.2 Finite Difference Solver of 1-D Green-Naghdi Equations

Herein, the nonlinear Green-Naghdi equations are discretised using finite differences and solved on a uniform Cartesian grid for specific initial and boundary conditions. The Finite Difference method (FDM) involves approximation of the derivatives within the PDEs by algebraic differences using Taylor series. Figure 3.1 is a definition sketch showing the node indexing system for the one-dimensional finite difference grid used.

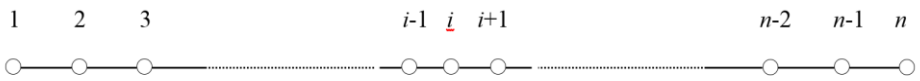

Figure 3.1: Finite Difference Grid

By Taylor Series expansions, finite differences are obtained. Second-order central differences of the first, second, and third derivatives are respectively as follows:

$$\frac{\partial f}{\partial x}|_i^k = \frac{f_{i+1}^k - f_{i-1}^k}{2\Delta x} \tag{3.1a}$$

$$\frac{\partial^2 f}{\partial x^2}|_i^k = \frac{f_{i+1}^k - 2\,f_i^k + f_{i-1}^k}{\Delta x^2} \tag{3.1b}$$

$$\frac{\partial^3 f}{\partial x^3}|_i^k = \frac{f_{i+2}^k - 2\,f_{i+1}^k + 2\,f_{i-1}^k - f_{i-2}^k}{2\Delta x^3} \tag{3.1c}$$

where $X = (i-1)\Delta x,\ t = k\Delta t$, Δx is the spatial increment, and Δt is the time step. Fourth-order central difference approximations to the first, second, and third derivatives are respectively:

$$\frac{\partial f}{\partial x}|_i^k = \frac{1}{12\Delta x}\left(f_{i-2}^k - 8f_{i-1}^k + 8f_{i+1}^k - f_{i+2}^k\right) \tag{3.2a}$$

$$\frac{\partial^2 f}{\partial x^2}|_i^k = \frac{1}{12\Delta x^2}\left(-f_{i-2}^k + 16\,f_{i-1}^k - 30\,f_i^k + 16\,f_{i+1}^k - f_{i+2}^k\right) \tag{3.2b}$$

$$\frac{\partial^3 f}{\partial x^3}|_i^k = \frac{1}{8\Delta x^3}\left(f_{i-3}^k - 8\ f_{i-2}^k + 13\,f_{i-1}^k - 13\,f_{i+1}^k + 8\,f_{i+2}^k - f_{i+3}^k\right) \tag{3.2c}$$

It is demonstrated later that both the second-order and the fourth-order central difference approximations are sufficient to represent accurately the derivative terms in the Green-Naghdi equations. From before, the GN equations for 1-D flow over a flat, horizontal, non-erodible bed are given by:

continuity:

$$\frac{\partial h}{\partial t} + \frac{\partial (u_0 h)}{\partial x} = 0 \qquad (3.3a)$$

in which h is the total depth and u_0 is horizontal velocity component.

momentum:

$$\frac{\partial u_0}{\partial t} + u_0 \frac{\partial u_0}{\partial x} = -g\frac{\partial \eta}{\partial x} + h\left(\frac{\partial h}{\partial x}\right)\left[\frac{\partial^2 u_0}{\partial x \partial t} + u_0 \frac{\partial^2 u_0}{\partial x^2} - \left(\frac{\partial u_0}{\partial x}\right)^2\right] + \frac{h^2}{3}\left[\frac{\partial^3 u_0}{\partial x^2 \partial t} + u_0 \frac{\partial^3 u_0}{\partial x^3} - \frac{\partial u_0}{\partial x}\frac{\partial^2 u_0}{\partial x^2}\right] \qquad (3.3b)$$

where η is the free surface elevation above a fixed horizontal datum, z_b is the bed elevation above the same datum, and g is the acceleration due to gravity.

Rearranging these equations gives,

$$\frac{\partial h}{\partial t} = -\frac{\partial (u_0 h)}{\partial x} \qquad (3.4a)$$

and

$$\frac{\partial u_0}{\partial t} = -u_0 \frac{\partial u_0}{\partial x} - g\frac{\partial \eta}{\partial x} + h\left(\frac{\partial h}{\partial x}\right)\left[\frac{\partial^2 u_0}{\partial x \partial t} + u_0 \frac{\partial^2 u_0}{\partial x^2} - \left(\frac{\partial u_0}{\partial x}\right)^2\right] + \frac{h^2}{3}\left[\frac{\partial^3 u_0}{\partial x^2 \partial t} + u_0 \frac{\partial^3 u_0}{\partial x^3} - \frac{\partial u_0}{\partial x}\frac{\partial^2 u_0}{\partial x^2}\right] \qquad (3.4b)$$

Eqn. (3.4*b*) contains two terms ($\frac{\partial^2 u_0}{\partial x \partial t}$ and $\frac{\partial^3 u_0}{\partial x^2 \partial t}$) that are cross-derivatives involving space and time. An explicit predictor-corrector scheme is incapable of solving this kind of equation, and so an implicit finite difference scheme is used to solve the 1-D GN momentum equation (Eqn. 3.4*b*). Herein, both implicit tridiagonal and pentadiagonal matrix inversion schemes are utilised to solve Eqn. (3.4*b*) using second-order and fourth-order differences, respectively.

3.2.1 Second-order tridiagonal scheme for 1D GN equations

Rearranging Equation (3.4*b*), we have

$$\frac{\partial u_0}{\partial t} - h\frac{\partial h}{\partial x}\frac{\partial}{\partial x}\left(\frac{\partial u_0}{\partial t}\right) - \frac{h^2}{3}\frac{\partial^2}{\partial x^2}\left(\frac{\partial u_0}{\partial t}\right)$$

$$= -u_0\,\frac{\partial u_0}{\partial x} - g\frac{\partial \eta}{\partial x} + h\left(\frac{\partial h}{\partial x}\right)\left[u_0\,\frac{\partial^2 u_0}{\partial x^2} - \left(\frac{\partial u_0}{\partial x}\right)^2\right] + \frac{h^2}{3}\left[u_0\,\frac{\partial^3 u_0}{\partial x^3} - \frac{\partial u_0}{\partial x}\,\frac{\partial^2 u_0}{\partial x^2}\right] \qquad (3.4c)$$

Now let

$$F = -u_0\,\frac{\partial u_0}{\partial x} - g\frac{\partial \eta}{\partial x} + h\left(\frac{\partial h}{\partial x}\right)\left[u_0\,\frac{\partial^2 u_0}{\partial x^2} - \left(\frac{\partial u_0}{\partial x}\right)^2\right] + \frac{h^2}{3}\left[u_0\,\frac{\partial^3 u_0}{\partial x^3} - \frac{\partial u_0}{\partial x}\,\frac{\partial^2 u_0}{\partial x^2}\right] \qquad (3.4d)$$

Then, Eqn. (3.4*c*) becomes:

$$F = \frac{\partial u_0}{\partial t} - h\frac{\partial h}{\partial x}\frac{\partial}{\partial x}\left(\frac{\partial u_0}{\partial t}\right) - \frac{h^2}{3}\frac{\partial^2}{\partial x^2}\left(\frac{\partial u_0}{\partial t}\right) \qquad (3.4e)$$

Discretising this equation using second-order central differences leads to:

$$\begin{cases} F_i^k = \dfrac{\partial u_0}{\partial t}\Big|_i^k - h_i^k\,\dfrac{h_{i+1}^k - h_{i-1}^k}{4\Delta x^2}\left(\dfrac{\partial u_0}{\partial t}\Big|_{i+1}^k - \dfrac{\partial u_0}{\partial t}\Big|_{i-1}^k\right) - \dfrac{(h_i^k)^2}{3\Delta x^2}\left(\dfrac{\partial u_0}{\partial t}\Big|_{i+1}^k - 2\dfrac{\partial u_0}{\partial t}\Big|_i^k + \dfrac{\partial u_0}{\partial t}\Big|_{i-1}^k\right) \\ \text{or} \\ F_i^k = \left[h_i^k\,\dfrac{h_{i+1}^k - h_{i-1}^k}{4\Delta x^2} - \dfrac{(h_i^k)^2}{3\Delta x^2}\right]\hat{u}_{i-1}^k + \left[1 + \dfrac{2(h_i^k)^2}{3\Delta x^2}\right]\hat{u}_i^k - \left[h_i^k\,\dfrac{h_{i+1}^k - h_{i-1}^k}{4\Delta x^2} + \dfrac{(h_i^k)^2}{3\Delta x^2}\right]\hat{u}_{i+1}^k \end{cases} \qquad (3.5)$$

where $\hat{u} = \frac{\partial u_0}{\partial t}$. The discretised equation is rewritten as

$$F_i^k = a_i\,\hat{u}_{i-1}^k + b_i\,\hat{u}_i^k + c_i\,\hat{u}_{i+1}^k \qquad (3.6)$$

in which

$$a_i = \left[h_i^k\,\frac{h_{i+1}^k - h_{i-1}^k}{4\Delta x^2} - \frac{(h_i^k)^2}{3\Delta x^2}\right], b_i = \left[1 + \frac{2(h_i^k)^2}{3\Delta x^2}\right], c_i = -\left[h_i^k\,\frac{h_{i+1}^k - h_{i-1}^k}{4\Delta x^2} + \frac{(h_i^k)^2}{3\Delta x^2}\right] \qquad (3.7)$$

The right hand side of Eqn. (3.4*c*) is also discretised using second-order central differences, giving:

$$F_i = -u_{0_i}\,\frac{\partial u_0}{\partial x}\Big|_i - g\frac{\partial \eta}{\partial x}\Big|_i + h_i\,\frac{\partial h}{\partial x}\Big|_i\left[u_{0_i}\,\frac{\partial^2 u_0}{\partial x^2}\Big|_i - \left(\frac{\partial u_0}{\partial x}\right)^2\Big|_i\right]$$
$$+\frac{h_i^2}{3}\left[u_{0_i}\,\frac{\partial^3 u_0}{\partial x^3}\Big|_i - \frac{\partial u_0}{\partial x}\Big|_i\frac{\partial^2 u_0}{\partial x^2}\Big|_i\right] \qquad (3.8)$$

The above set of discretised equations form the following tridiagonal matrix system:

$$\begin{bmatrix} b_2 & c_2 & & & \cdots \\ a_3 & b_3 & c_3 & & \cdots \\ & \ddots & & & \\ & a_i & b_i & c_i & \\ & & \ddots & & \\ & & & \ddots & \\ & & & \ddots & \\ & a_{i_{max}-2} & b_{i_{max}-2} & c_{i_{max}-2} & \\ & & a_{i_{max}-1} & b_{i_{max}-1} & \end{bmatrix} \cdot \begin{bmatrix} \hat{u}_2 \\ \hat{u}_3 \\ \vdots \\ \vdots \\ \hat{u}_i \\ \vdots \\ \vdots \\ \hat{u}_{i_{max}-2} \\ \hat{u}_{i_{max}-1} \end{bmatrix} = \begin{bmatrix} \hat{F}_2 - a_2\,\hat{u}_1 \\ \hat{F}_3 \\ \vdots \\ \vdots \\ \hat{F}_i \\ \vdots \\ \vdots \\ \hat{F}_{i_{max}-2} \\ \hat{F}_{i_{max}-1} - c_{i_{max}-1}\,\hat{u}_{i_{max}} \end{bmatrix}$$

The unknown values $\hat{u}_i^k = \frac{\partial u_0}{\partial t}\Big|_i^k$ are obtained by for $i = 2, \ldots, i_{max}\text{-}1$ using the Thomas algorithm (Press *et al*. 2007).

3.2.2 Fourth-order pentadiagonal scheme for 1D GN equations

Applying fourth order central differences to Eqn. (3.4*e*) leads to:

$$F_i^k = \frac{\partial u_0}{\partial t}\Big|_i^k - \frac{(h_i^k)^2}{36\Delta x^2}\left(-\frac{\partial u_0}{\partial t}\Big|_{i-2}^k + 16\,\frac{\partial u_0}{\partial t}\Big|_{i-1}^k - 30\,\frac{\partial u_0}{\partial t}\Big|_i^k + 16\,\frac{\partial u_0}{\partial t}\Big|_{i+1}^k - \frac{\partial u_0}{\partial t}\Big|_{i+2}^k\right)$$

$$-h_i^k\,\frac{h_{i-2}^k - 8\,h_{i-1}^k + 8\,h_{i+1}^k - h_{i+2}^k}{144\Delta x^2}\left(\frac{\partial u_0}{\partial t}\Big|_{i-2}^k - 8\,\frac{\partial u_0}{\partial t}\Big|_{i-1}^k + 8\,\frac{\partial u_0}{\partial t}\Big|_{i+1}^k - \frac{\partial u_0}{\partial t}\Big|_{i+2}^k\right) \quad (3.9)$$

or

$$F_i^k = \left[\frac{(h_i^k)^2}{36\,\Delta x^2} + \frac{h_i^k}{12\,\Delta x}\left(\frac{-h_{i-2}^k + 8\,h_{i-1}^k - 8\,h_{i+1}^k + h_{i+2}^k}{12\,\Delta x}\right)\right]\,\hat{u}_{i-2}^k$$

$$+\left[\frac{-16\,(h_i^k)^2}{36\,\Delta x^2} + \frac{8\,h_i^k}{12\,\Delta x}\left(\frac{h_{i-2}^k - 8\,h_{i-1}^k + 8\,h_{i+1}^k - h_{i+2}^k}{12\,\Delta x}\right)\right]\,\hat{u}_{i-1}^k$$

$$+\left[1 + \frac{30\,(h_i^k)^2}{36\,\Delta x^2}\right]\hat{u}_i^k \quad (3.10)$$

$$+\left[\frac{-16\,(h_i^k)^2}{36\,\Delta x^2} + \frac{8\,h_i^k}{12\,\Delta x}\left(\frac{-h_{i-2}^k + 8\,h_{i-1}^k - 8\,h_{i+1}^k + h_{i+2}^k}{12\,\Delta x}\right)\right]\,\hat{u}_{i+1}^k$$

$$+\left[\frac{(h_i^k)^2}{36\,\Delta x^2} + \frac{h_i^k}{12\,\Delta x}\left(\frac{h_{i-2}^k - 8\,h_{i-1}^k + 8\,h_{i+1}^k - h_{i+2}^k}{12\,\Delta x}\right)\right]\,\hat{u}_{i+2}^k$$

where $\hat{u}_i^k = \frac{\partial u_0}{\partial t}$ hence,

$$F_i^k = a_i\,\hat{u}_{i-2}^k + b_i\,\hat{u}_{i-1}^k + c_i\,\hat{u}_i^k + d_i\,\hat{u}_{i+1}^k + e_i\,\hat{u}_{i+2}^k \tag{3.11}$$

where

$$\begin{cases} a_i = \left[\dfrac{(h_i^k)^2}{36\,\Delta x^2} + \dfrac{h_i^k}{144\,\Delta x^2}\left(-h_{i-2}^k + 8\,h_{i-1}^k - 8\,h_{i+1}^k + h_{i+2}^k\right)\right] \\ b_i = \left[\dfrac{-4\,(h_i^k)^2}{9\,\Delta x^2} + \dfrac{h_i^k}{18\,\Delta x^2}\left(h_{i-2}^k - 8\,h_{i-1}^k + 8\,h_{i+1}^k - h_{i+2}^k\right)\right] \\ c_i = \left[1 + \dfrac{5\,(h_i^k)^2}{6\,\Delta x^2}\right] \\ d_i = \left[\dfrac{-4\,(h_i^k)^2}{9\,\Delta x^2} + \dfrac{h_i^k}{18\,\Delta x^2}\left(-h_{i-2}^k + 8\,h_{i-1}^k - 8\,h_{i+1}^k + h_{i+2}^k\right)\right] \\ e_i = \left[\dfrac{(h_i^k)^2}{36\,\Delta x^2} + \dfrac{h_i^k}{144\,\Delta x^2}\left(h_{i-2}^k - 8\,h_{i-1}^k + 8\,h_{i+1}^k - h_{i+2}^k\right)\right] \end{cases} \tag{3.12}$$

The right hand side of Eqn. (3.4*c*) is discretised using fourth-order central difference:

$$F_i = -u_{0_i}\,\frac{\partial u_0}{\partial x}\Big|_i - g\,\frac{\partial \eta}{\partial x}\Big|_i + h_i\,\frac{\partial h}{\partial x}\Big|_i \left[u_{0_i}\,\frac{\partial^2 u_0}{\partial x^2}\Big|_i - \left(\frac{\partial u_0}{\partial x}\right)^2\Big|_i\right] + \frac{h_i^2}{3}\left[u_{0_i}\,\frac{\partial^3 u_0}{\partial x^3}\Big|_i - \frac{\partial u_0}{\partial x}\Big|_i \frac{\partial^2 u_0}{\partial x^2}\Big|_i\right] \tag{3.13}$$

The resulting pentadiagonal matrix equation is as follows:

$$\begin{bmatrix} c_2 & d_2 & e_2 & & & \cdots \\ b_3 & c_3 & d_3 & e_3 & & \cdots \\ & & \ddots & & & \\ & & a_i & b_i & c_i & d_i & e_i \\ & & & & \ddots & & \\ & & & & & \ddots & \\ & & & & & & \ddots \\ & & a_{i_{max}-2} & b_{i_{max}-2} & c_{i_{max}-2} & d_{i_{max}-2} & e_{i_{max}-2} \\ & & & a_{i_{max}-1} & b_{i_{max}-1} & c_{i_{max}-1} & d_{i_{max}-1} \end{bmatrix} \cdot \begin{bmatrix} \hat{u}_2 \\ \hat{u}_3 \\ \vdots \\ \vdots \\ \hat{u}_i \\ \vdots \\ \vdots \\ \hat{u}_{i_{max}-2} \\ \hat{u}_{i_{max}-1} \end{bmatrix} = \begin{bmatrix} \hat{F}_2 - a_2\,\hat{u}_0 - b_2\,\hat{u}_1 \\ \hat{F}_3 - a_3\,\hat{u}_1 - b_3\,\hat{u}_2 \\ \vdots \\ \vdots \\ \hat{F}_i \\ \vdots \\ \vdots \\ \hat{F}_{i_{max}-2} - a_{i_{max}-2}\,\hat{u}_{imax-4} - b_{i_{max}-2}\,\hat{u}_{imax-3} \\ \hat{F}_{i_{max}-1} - b_{i_{max}-1}\,\hat{u}_{imax-3} \end{bmatrix}$$

$\hat{u}_i^k = \frac{\partial u_0}{\partial t}\Big|_i^k$ is obtained by using matrix inversion (Press *et al*. 2007).

Runge-Kutta fourth-order time-integration is used for time integration where total depth and horizontal velocity are updated each times.

$$h_i^{k+1} = h_i^k + \frac{1}{6}\Delta t(k_{11} + 2\,k_{12} + 2\,k_{13} + k_{14}) \qquad (3.14a)$$

$$u_i^{k+1} = u_i^k + \frac{1}{6}\Delta t(k_{21} + 2\,k_{22} + 2\,k_{23} + k_{24}) \qquad (3.14b)$$

where

$$\begin{cases} k_{11} = \left[\frac{dh}{dt}(t_i, h_i)\right] & , \quad k_{21} = \left[\frac{du}{dt}(t_i, u_i)\right] \\ k_{12} = \left[\frac{dh}{dt}\left(t_i + \frac{\Delta t}{2}, h_i + \frac{k_{11}}{2}\right)\right] & , \quad k_{22} = \left[\frac{du}{dt}\left(t_i + \frac{\Delta t}{2}, u_i + \frac{k_{21}}{2}\right)\right] \\ k_{13} = \left[\frac{dh}{dt}\left(t_i + \frac{\Delta t}{2}, h_i + \frac{k_{12}}{2}\right)\right] & , \quad k_{23} = \left[\frac{du}{dt}\left(t_i + \frac{\Delta t}{2}, u_i + \frac{k_{22}}{2}\right)\right] \\ k_{14} = \left[\frac{dh}{dt}(t_i + \Delta t, h_i + k_{13})\right] & , \quad k_{24} = \left[\frac{du}{dt}(t_i + \Delta t, u_i + k_{23})\right] \end{cases} \qquad (3.15)$$

The fourth-order pentadiagonal matrix scheme is inherently more accurate than the second-order tridiagonal matrix scheme. However, the tridiagonal approach involves less complicated formulae and leads to better computational performance than the pentadiagonal matrix scheme. In order to assess the relative merits and drawbacks of both matrix approaches, the present study implements both the tridiagonal and pentadiagonal schemes and compares results obtained from the different schemes for standard benchmark tests in Chapters four, five and six.

3.3 Finite Difference Solver of 2D GN Equations for uniform bed

3.3.1 Second-order tridiagonal scheme for 2G GN equation

Rearranging the 2D level I GN momentum equation for a uniform bed in *x*-direction, Eqn. (2.66), we have:

$$\frac{\partial u_0}{\partial t} - h\frac{\partial h}{\partial x}\frac{\partial}{\partial x}\left(\frac{\partial u_0}{\partial t}\right) - \frac{h^2}{3}\frac{\partial^2}{\partial x^2}\left(\frac{\partial u_0}{\partial t}\right) = -u_0\,\frac{\partial u_0}{\partial x} - v_0\,\frac{\partial u_0}{\partial y} - g\frac{\partial \eta}{\partial x} + h\frac{\partial h}{\partial x}\frac{\partial}{\partial y}\left(\frac{\partial v_0}{\partial t}\right)$$

$$+\frac{h^2}{3}\,\frac{\partial^2}{\partial x \partial y}\left(\frac{\partial v_0}{\partial t}\right) + h\left(\frac{\partial h}{\partial x}\right)\left[u_0\,\frac{\partial^2 u_0}{\partial x^2} + \frac{\partial^2 (u_0 v_0)}{\partial x \partial y} + v_0\,\frac{\partial^2 v_0}{\partial y^2} - \left(\frac{\partial u_0}{\partial x} + \frac{\partial v_0}{\partial y}\right)^2\right]$$

$$+\frac{h^2}{3}\left[u_0\,\frac{\partial^3 u_0}{\partial x^3} + \frac{\partial^3 (u_0 v_0)}{\partial x^2 \partial y} + \frac{\partial v_0}{\partial x}\left(\frac{\partial^2 u_0}{\partial x \partial y} + \frac{\partial^2 v_0}{\partial y^2}\right) + v_0\,\frac{\partial^3 v_0}{\partial x \partial y^2}\right.$$

$$\left. - \left(\frac{\partial u_0}{\partial x} + 2\frac{\partial v_0}{\partial y}\right)\left(\frac{\partial^2 v_0}{\partial x \partial y} + \frac{\partial^2 u_0}{\partial x^2}\right)\right] \tag{3.16}$$

Now let

$$F = -\left[u_0\frac{\partial u_0}{\partial x} + v_0\frac{\partial u_0}{\partial y} + g\frac{\partial \eta}{\partial x}\right] + h\frac{\partial h}{\partial x}\left[u_0\frac{\partial^2 u_0}{\partial x^2} + \frac{\partial^2 u_0 v_0}{\partial x \partial y} + v_0\frac{\partial^2 v_0}{\partial y^2} - \left(\frac{\partial u_0}{\partial x} + \frac{\partial v_0}{\partial y}\right)^2\right]$$

$$+\frac{h^2}{3}\left[u_0\frac{\partial^3 u_0}{\partial x^3} + \frac{\partial^3 u_0 v_0}{\partial x^2 \partial y} + \frac{\partial v_0}{\partial x}\left(\frac{\partial^2 u_0}{\partial x \partial y} + \frac{\partial^2 v_0}{\partial y^2}\right) + v_0\frac{\partial^3 v_0}{\partial x \partial y^2} - \left(\frac{\partial u_0}{\partial x} + 2\frac{\partial v_0}{\partial y}\right)\left(\frac{\partial^2 v_0}{\partial x \partial y} + \frac{\partial^2 u_0}{\partial x^2}\right)\right]$$

$$+h\frac{\partial h}{\partial x}\frac{\partial}{\partial y}\left(\frac{\partial v_0}{\partial t}\right) + \frac{h^2}{3}\,\frac{\partial^2}{\partial x \partial y}\left(\frac{\partial v_0}{\partial t}\right) \tag{3.17}$$

Then, Eqn. (3.16) becomes:

$$F = \frac{\partial u_0}{\partial t} - h\frac{\partial h}{\partial x}\frac{\partial}{\partial x}\left(\frac{\partial u_0}{\partial t}\right) - \frac{h^2}{3}\frac{\partial^2}{\partial x^2}\left(\frac{\partial u_0}{\partial t}\right) \tag{3.18}$$

Discretising this equation using second-order central differences leads to:

$$\begin{cases} F_{ij}^k = \dfrac{\partial u_0}{\partial t}\Big|_{ij}^k - h_{ij}^k\dfrac{h_{i+1j}^k - h_{i-1j}^k}{4\Delta x^2}\left(\dfrac{\partial u_0}{\partial t}\Big|_{i+1j}^k - \dfrac{\partial u_0}{\partial t}\Big|_{i-1j}^k\right) - \dfrac{(h_{ij}^k)^2}{3\Delta x^2}\left(\dfrac{\partial u_0}{\partial t}\Big|_{i+1j}^k - 2\dfrac{\partial u_0}{\partial t}\Big|_{ij}^k + \dfrac{\partial u_0}{\partial t}\Big|_{i-1j}^k\right) \\ \text{or} \\ F_{ij}^k = \left[h_{ij}^k\dfrac{h_{i+1\,j}^k - h_{i-1\,j}^k}{4\Delta x^2} - \dfrac{(h_{ij}^k)^2}{3\Delta x^2}\right]\hat{u}_{i-1\,j}^k + \left[1 + \dfrac{2(h_{ij}^k)^2}{3\Delta x^2}\right]\hat{u}_{ij}^k - \left[h_{ij}^k\dfrac{h_{i+1\,j}^k - h_{i-1\,j}^k}{4\Delta x^2} + \dfrac{(h_{ij}^k)^2}{3\Delta x^2}\right]\hat{u}_{i+1\,j}^k \end{cases} \tag{3.19}$$

where $\hat{u}_{ij}^k = \dfrac{\partial u_0}{\partial t}\Big|_{ij}^k$. The discretised equation is rewritten as

$$F_{ij}^k = a_i\,\hat{u}_{i-1\,j}^k + b_i\,\hat{u}_{i\,j}^k + c_i\,\hat{u}_{i+1\,j}^k \tag{3.20}$$

in which

$$a_i = \left[h_{ij}^k \frac{h_{i+1\,j}^k - h_{i-1\,j}^k}{4\Delta x^2} - \frac{(h_{ij}^k)^2}{3\Delta x^2}\right], b_i = \left[1 + \frac{2(h_{ij}^k)^2}{3\Delta x^2}\right], c_i = -\left[h_{ij}^k \frac{h_{i+1\,j}^k - h_{i-1\,j}^k}{4\Delta x^2} + \frac{(h_{ij}^k)^2}{3\Delta x^2}\right] \quad (3.21)$$

The right hand side of Eqn. (3.16) is also discretised using second-order central differences, giving:

$$\begin{aligned} F_{ij} = &-\left[u_{0_{ij}} \frac{\partial u_0}{\partial x}\Big|_{ij} + v_{0_{ij}} \frac{\partial u_0}{\partial y}\Big|_{ij} + g\frac{\partial \eta}{\partial x}\Big|_{ij}\right] + h_{ij}\frac{\partial h}{\partial x}\Big|_{ij} \frac{\partial}{\partial y}\left(\frac{\partial v_0}{\partial t}\right)\Big|_{ij} \\ &+h_{ij}\frac{\partial h}{\partial x}\Big|_{ij}\left[u_{0_{ij}}\frac{\partial^2 u_0}{\partial x^2}\Big|_{ij} + \frac{\partial^2(u_0 v_0)}{\partial x \partial y}\Big|_{ij} + v_{0_{ij}}\frac{\partial^2 v_0}{\partial y^2}\Big|_{ij} - \left(\frac{\partial u_0}{\partial x}\Big|_{ij} + \frac{\partial v_0}{\partial y}\Big|_{ij}\right)^2\right] \\ &+\frac{h_{ij}^2}{3}\left[u_{0_{ij}}\frac{\partial^3 u_0}{\partial x^3}\Big|_{ij} + \frac{\partial^3(u_0 v_0)}{\partial x^2 \partial y}\Big|_{ij} + \frac{\partial v_0}{\partial x}\Big|_{ij}\left(\frac{\partial^2 u_0}{\partial x \partial y}\Big|_{ij} + \frac{\partial^2 v_0}{\partial y^2}\Big|_{ij}\right) + v_{0_{ij}}\frac{\partial^3 v_0}{\partial x \partial y^2}\Big|_{ij}\right. \\ &\left.-\left(\frac{\partial u_0}{\partial x}\Big|_{ij} + 2\frac{\partial v_0}{\partial y}\Big|_{ij}\right)\left(\frac{\partial^2 v_0}{\partial x \partial y}\Big|_{ij} + \frac{\partial^2 u_0}{\partial x^2}\Big|_{ij}\right)\right] + \frac{h_{ij}^2}{3}\frac{\partial^2}{\partial x \partial y}\left(\frac{\partial v_0}{\partial t}\right)\Big|_{ij} \end{aligned} \quad (3.22)$$

The above set of discretised equations forms the following tridiagonal matrix system:

$$\begin{bmatrix} b_2 & c_2 & & & \cdots \\ a_3 & b_3 & c_3 & & \cdots \\ & & \ddots & & \\ & & a_i & b_i & c_i \\ & & & \ddots & \\ & & & & \ddots \\ & & a_{i_{max}-2} & b_{i_{max}-2} & c_{i_{max}-2} \\ & & & a_{i_{max}-1} & b_{i_{max}-1} \end{bmatrix} \cdot \begin{bmatrix} \hat{u}_{2\,j} \\ \hat{u}_{3\,j} \\ \vdots \\ \vdots \\ \hat{u}_{ij} \\ \vdots \\ \hat{u}_{i_{max}-2\,j} \\ \hat{u}_{i_{max}-1\,j} \end{bmatrix} = \begin{bmatrix} \hat{F}_2 - a_2\,\hat{u}_{1\,j} \\ \hat{F}_3 \\ \vdots \\ \vdots \\ \hat{F}_i \\ \vdots \\ \vdots \\ \hat{F}_{i_{max}-2} \\ \hat{F}_{i_{max}-1} - c_{i_{max}-1}\,\hat{u}_{i_{max}\,j} \end{bmatrix}$$

The unknown values $\hat{u}_{ij}^k = \frac{\partial u_0}{\partial t}\Big|_{ij}^k$ are obtained for $j = 2, \ldots, j_{\max}\text{-}1$ and $i = 1, \ldots, i_{\max}$ using the Thomas algorithm (Press *et al*. 2007). The 2D level I GN momentum equation for a uniform bed in y-direction is as follows:

$$\begin{aligned} &\frac{\partial v_0}{\partial t} + u_0\frac{\partial v_0}{\partial x} + v_0\frac{\partial v_0}{\partial y} = \\ &-g\frac{\partial \eta}{\partial y} + h\left(\frac{\partial h}{\partial y}\right)\left[\frac{\partial^2 u_0}{\partial x \partial t} + \frac{\partial^2 v_0}{\partial y \partial t} + u_0\frac{\partial^2 u_0}{\partial x^2} + \frac{\partial^2(u_0 v_0)}{\partial x \partial y} + v_0\frac{\partial^2 v_0}{\partial y^2} - \left(\frac{\partial u_0}{\partial x} + \frac{\partial v_0}{\partial y}\right)^2\right] \\ &+\frac{h^2}{3}\left[\frac{\partial^3 u_0}{\partial x \partial y \partial t} + \frac{\partial^3 v_0}{\partial y^2 \partial t} + \frac{\partial u_0}{\partial y}\frac{\partial^2 u_0}{\partial x^2} + u_0\frac{\partial^3 u_0}{\partial x^2 \partial y} + \frac{\partial u_0}{\partial y}\frac{\partial^2 v_0}{\partial x \partial y} + \frac{\partial^3(u_0 v_0)}{\partial x \partial y^2} + v_0\frac{\partial^3 v_0}{\partial y^3}\right. \\ &\left.-\left(2\frac{\partial u_0}{\partial x} + \frac{\partial v_0}{\partial y}\right)\left(\frac{\partial^2 u_0}{\partial x \partial y} + \frac{\partial^2 v_0}{\partial y^2}\right)\right] \end{aligned} \quad (3.23)$$

Similarly, rearranging the 2D level I GN momentum equation for a uniform bed in y-direction, Eqn. (3.23), gives:

$$\frac{\partial v_0}{\partial t} - h\left(\frac{\partial h}{\partial y}\right)\frac{\partial}{\partial y}\left(\frac{\partial v_0}{\partial t}\right) - \frac{h^2}{3}\frac{\partial^2}{\partial y^2}\left(\frac{\partial v_0}{\partial t}\right)$$
$$= -u_0\,\frac{\partial v_0}{\partial x} - v_0\,\frac{\partial v_0}{\partial y} - g\frac{\partial \eta}{\partial y} + h\left(\frac{\partial h}{\partial y}\right)\left[u_0\,\frac{\partial^2 u_0}{\partial x^2} + \frac{\partial^2 (u_0 v_0)}{\partial x \partial y} + v_0\,\frac{\partial^2 v_0}{\partial y^2} - \left(\frac{\partial u_0}{\partial x} + \frac{\partial v_0}{\partial y}\right)^2\right]$$

$$+\frac{h^2}{3}\left[\frac{\partial u_0}{\partial y}\,\frac{\partial^2 u_0}{\partial x^2} + u_0\,\frac{\partial^3 u_0}{\partial x^2 \partial y} + \frac{\partial u_0}{\partial y}\,\frac{\partial^2 v_0}{\partial x \partial y} + \frac{\partial^3 (u_0 v_0)}{\partial x \partial y^2} + v_0\,\frac{\partial^3 v_0}{\partial y^3}\right.$$
$$\left. -\left(2\frac{\partial u_0}{\partial x} + \frac{\partial v_0}{\partial y}\right)\left(\frac{\partial^2 u_0}{\partial x \partial y} + \frac{\partial^2 v_0}{\partial y^2}\right)\right] + h\left(\frac{\partial h}{\partial y}\right)\frac{\partial}{\partial x}\left(\frac{\partial u_0}{\partial t}\right) + \frac{h^2}{3}\frac{\partial^2}{\partial x \partial y}\left(\frac{\partial u_0}{\partial t}\right) \quad (3.24)$$

Now let

$$G = -\left[u_0\,\frac{\partial v_0}{\partial x} + v_0\,\frac{\partial v_0}{\partial y} + g\frac{\partial \eta}{\partial y}\right] + h\frac{\partial h}{\partial y}\left[u_0\,\frac{\partial^2 u_0}{\partial x^2} + \frac{\partial^2 u_0 v_0}{\partial x \partial y} + v_0\frac{\partial^2 v_0}{\partial y^2} - \left(\frac{\partial u_0}{\partial x} + \frac{\partial v_0}{\partial y}\right)^2\right]$$
$$+\frac{h^2}{3}\left[\frac{\partial u_0}{\partial y}\,\frac{\partial^2 u_0}{\partial x^2} + u_0\,\frac{\partial^3 u_0}{\partial x^2 \partial y} + \frac{\partial u_0}{\partial y}\,\frac{\partial^2 v_0}{\partial x \partial y} + \frac{\partial^3 (u_0 v_0)}{\partial x \partial y^2} + v_0\,\frac{\partial^3 v_0}{\partial y^3}\right.$$
$$\left. -\left(2\frac{\partial u_0}{\partial x} + \frac{\partial v_0}{\partial y}\right)\left(\frac{\partial^2 u_0}{\partial x \partial y} + \frac{\partial^2 v_0}{\partial y^2}\right)\right] + h\left(\frac{\partial h}{\partial y}\right)\frac{\partial}{\partial x}\left(\frac{\partial u_0}{\partial t}\right) + \frac{h^2}{3}\frac{\partial^2}{\partial x \partial y}\left(\frac{\partial u_0}{\partial t}\right) \quad (3.25)$$

Then, Eqn. (3.24) becomes:

$$G = \frac{\partial v_0}{\partial t} - h\left(\frac{\partial h}{\partial y}\right)\frac{\partial}{\partial y}\left(\frac{\partial v_0}{\partial t}\right) - \frac{h^2}{3}\frac{\partial^2}{\partial y^2}\left(\frac{\partial v_0}{\partial t}\right) \quad (3.26)$$

Discretising this equation using second-order central differences results in:

$$\begin{cases} G_{ij}^k = \frac{\partial v_0}{\partial t}\Big|_{ij}^k - h_{ij}^k \frac{h_{i\,j+1}^k - h_{ij-1}^k}{4\Delta y^2}\left(\frac{\partial v_0}{\partial t}\Big|_{ij+1}^k - \frac{\partial v_0}{\partial t}\Big|_{ij-1}^k\right) - \frac{(h_{ij}^k)^2}{3\Delta y^2}\left(\frac{\partial v_0}{\partial t}\Big|_{ij+1}^k - 2\frac{\partial v_0}{\partial t}\Big|_{ij}^k + \frac{\partial v_0}{\partial t}\Big|_{ij-1}^k\right) \\ \text{or} \\ G_{ij}^k = \left[h_{ij}^k \frac{h_{i\,j+1}^k - h_{i\,j-1}^k}{4\Delta y^2} - \frac{(h_{ij}^k)^2}{3\Delta y^2}\right]\hat{v}_{i\,j-1}^k + \left[1 + \frac{2(h_{ij}^k)^2}{3\Delta y^2}\right]\hat{v}_{ij}^k - \left[h_{ij}^k \frac{h_{i\,j+1}^k - h_{i\,j-1}^k}{4\Delta y^2} + \frac{(h_{ij}^k)^2}{3\Delta y^2}\right]\hat{v}_{i\,j+1}^k \end{cases} \quad (3.27)$$

where $\hat{v}_{ij}^k = \frac{\partial v_0}{\partial t}\Big|_{ij}^k$. The discretised equation is rewritten as:

$$G_{ij}^k = aa_j\,\hat{v}_{i\,j-1}^k + bb_j\,\hat{v}_{i\,j}^k + cc_j\,\hat{v}_{i\,j+1}^k \quad (3.28)$$

in which

$$aa_j = \left[h_{ij}^k \frac{h_{ij+1}^k - h_{ij-1}^k}{4\Delta y^2} - \frac{(h_{ij}^k)^2}{3\Delta y^2}\right], bb_j = \left[1 + \frac{2(h_{ij}^k)^2}{3\Delta y^2}\right], cc_j = -\left[h_{ij}^k \frac{h_{ij+1}^k - h_{ij-1}^k}{4\Delta y^2} + \frac{(h_{ij}^k)^2}{3\Delta y^2}\right] \quad (3.29)$$

The right hand side of Eqn. (3.24) is also discretised using second-order central differences,

$$G_{ij} = -\left[u_{0_{ij}} \left.\frac{\partial v_0}{\partial x}\right|_{ij} + v_{0_{ij}} \left.\frac{\partial v_0}{\partial y}\right|_{ij} + g \left.\frac{\partial \eta}{\partial y}\right|_{ij}\right] + h_{ij} \left.\frac{\partial h}{\partial y}\right|_{ij} \left.\frac{\partial}{\partial x}\left(\frac{\partial u_0}{\partial t}\right)\right|_{ij}$$

$$+ h_{ij} \left(\left.\frac{\partial h}{\partial y}\right|_{ij}\right) \left[u_{0_{ij}} \left.\frac{\partial^2 u_0}{\partial x^2}\right|_{ij} + \left.\frac{\partial^2 u_0 v_0}{\partial x \partial y}\right|_{ij} + v_{0_{ij}} \left.\frac{\partial^2 v_0}{\partial y^2}\right|_{ij} - \left(\left.\frac{\partial u_0}{\partial x}\right|_{ij} + \left.\frac{\partial v_0}{\partial y}\right|_{ij}\right)^2\right]$$

$$+ \frac{h_{ij}^2}{3}\left[\left.\frac{\partial u_0}{\partial y}\right|_{ij} \left.\frac{\partial^2 u_0}{\partial x^2}\right|_{ij} + u_{0_{ij}} \left.\frac{\partial^3 u_0}{\partial x^2 \partial y}\right|_{ij} + \left.\frac{\partial u_0}{\partial y}\right|_{ij} \left.\frac{\partial^2 v_0}{\partial x \partial y}\right|_{ij} + \left.\frac{\partial^3 u_0 v_0}{\partial x \partial y^2}\right|_{ij} + v_{0_{ij}} \left.\frac{\partial^3 v_0}{\partial y^3}\right|_{ij}\right.$$

$$\left. - \left(2\left.\frac{\partial u_0}{\partial x}\right|_{ij} + \left.\frac{\partial v_0}{\partial y}\right|_{ij}\right)\left(\left.\frac{\partial^2 u_0}{\partial x \partial y}\right|_{ij} + \left.\frac{\partial^2 v_0}{\partial y^2}\right|_{ij}\right)\right] + \frac{h_{ij}^2}{3} \frac{\partial^2}{\partial x \partial y}\left(\frac{\partial u_0}{\partial t}\right)\Big|_{ij} \qquad (3.30)$$

The above set of discretised equations forms the following tridiagonal matrix system:

$$\begin{bmatrix} bb_2 & cc_2 & & & \cdots \\ aa_3 & bb_3 & cc_3 & & \cdots \\ & & \ddots & & \\ & & aa_i & bb_i & cc_i \\ & & & \ddots & \\ & & & \ddots & \\ & & aa_{j_{max}-2} & bb_{j_{max}-2} & cc_{j_{max}-2} \\ & & & aa_{j_{max}-1} & bb_{j_{max}-1} \end{bmatrix} \cdot \begin{bmatrix} \hat{v}_{i\,2} \\ \hat{v}_{i\,3} \\ \vdots \\ \vdots \\ \hat{v}_{ij} \\ \vdots \\ \hat{v}_{i\,j_{max}-2} \\ \hat{v}_{i\,j_{max}-1} \end{bmatrix} = \begin{bmatrix} \hat{G}_2 - aa_2\,\hat{v}_{i\,1} \\ \hat{G}_3 \\ \vdots \\ \vdots \\ \hat{G}_j \\ \vdots \\ \vdots \\ \hat{G}_{j_{max}-2} \\ \hat{G}_{j_{max}-1} - cc_{j_{max}-1}\,\hat{v}_{i\,j_{max}} \end{bmatrix}$$

The unknown values $\hat{v}_{ij}^k = \left.\frac{\partial v_0}{\partial t}\right|_{ij}^k$ are obtained for $i = 2, \ldots, i_{\max}\text{-}1$ and $j = 1, \ldots, j_{\max}$ by means of the Thomas algorithm. Iteration is used to centre correctly (in space and time) the cross-derivative terms that appear in both the *x*- and *y*- momentum equations.

3.3.2 Fourth-order pentadiagonal scheme for 2G GN equation

Pentadiagonal matrix solvers for *x*- and *y*-direction are:

$$\begin{bmatrix} c_2 & d_2 & e_2 & & & \cdots \\ b_3 & c_3 & d_3 & e_3 & & \cdots \\ & & \ddots & & & \\ & & a_i & b_i & c_i & d_i & e_i \\ & & & & \ddots & & \\ & & & & \ddots & & \\ & & a_{i_{max}-2} & b_{i_{max}-2} & c_{i_{max}-2} & d_{i_{max}-2} & e_{i_{max}-2} \\ & & & a_{i_{max}-1} & b_{i_{max}-1} & c_{i_{max}-1} & d_{i_{max}-1} \end{bmatrix} \cdot \begin{bmatrix} \hat{u}_{2\,j} \\ \hat{u}_{3\,j} \\ \vdots \\ \vdots \\ \hat{u}_{ij} \\ \vdots \\ \hat{u}_{i_{max}-2\,j} \\ \hat{u}_{i_{max}-1\,j} \end{bmatrix} = \begin{bmatrix} \hat{F}_2 - a_2\,\hat{u}_{0\,j} - b_2\,\hat{u}_{1\,j} \\ \hat{F}_3 - a_3\,\hat{u}_{1\,j} - b_3\,\hat{u}_{2\,j} \\ \vdots \\ \vdots \\ \hat{F}_i \\ \vdots \\ \hat{F}_{i_{max}-2} - a_{i_{max}-2}\,\hat{u}_{i_{max}-4\,j} - b_{i_{max}-2}\,\hat{u}_{i_{max}-3\,j} \\ \hat{F}_{i_{max}-1} - b_{i_{max}-1}\,\hat{u}_{i_{max}-3\,j} \end{bmatrix}$$

$$\begin{bmatrix} cc_2 & dd_2 & ee_2 & & & \cdots \\ bb_3 & cc_3 & dd_3 & ee_3 & & \cdots \\ & & \ddots & & & \\ & & aa_j & bb_j & cc_j & dd_j & ee_j \\ & & & & \ddots & & \\ & & & & \ddots & & \\ & & aa_{j_{max}-2} & bb_{j_{max}-2} & cc_{j_{max}-2} & dd_{j_{max}-2} & ee_{j_{max}-2} \\ & & & aa_{j_{max}-1} & bb_{j_{max}-1} & cc_{j_{max}-1} & dd_{j_{max}-1} \end{bmatrix} \cdot \begin{bmatrix} \hat{v}_{i\,2} \\ \hat{v}_{i\,3} \\ \vdots \\ \vdots \\ \hat{v}_{ij} \\ \vdots \\ \hat{v}_{i\,j_{max}-2} \\ \hat{v}_{i\,j_{max}-1} \end{bmatrix} = \begin{bmatrix} \hat{G}_2 - aa_2\,\hat{v}_{i\,0} - bb_2\,\hat{v}_{i\,1} \\ \hat{G}_3 - aa_3\,\hat{v}_{i\,1} - bb_3\,\hat{v}_{i\,2} \\ \vdots \\ \vdots \\ \hat{G}_j \\ \vdots \\ \vdots \\ \hat{G}_{j_{max}-2} - aa_{j_{max}-2}\,\hat{v}_{i\,j_{max}-4} - bb_{j_{max}-2}\,\hat{v}_{i\,j_{max}-3} \\ \hat{G}_{j_{max}-1} - bb_{j_{max}-1}\,\hat{v}_{i\,j_{max}-3} \end{bmatrix}$$

3.4 Finite Difference Solver of 2D GN Equations for non-uniform bed

2D level I x-momentum GN equation for a non-uniform bed is

$$\left(\frac{\partial \eta}{\partial x}\right)\left[\frac{\partial z_b}{\partial x}\left(\frac{\partial u_0}{\partial t}+v_0\,\frac{\partial u_0}{\partial y}-u_0\frac{\partial v_0}{\partial y}\right)+\frac{\partial z_b}{\partial y}\left(\frac{\partial v_0}{\partial t}+u_0\,\frac{\partial v_0}{\partial x}-v_0\,\frac{\partial u_0}{\partial x}\right)+u_0^2\,\frac{\partial^2 z_b}{\partial x^2}\right.$$

$$\left.+2u_0v_0\,\frac{\partial^2 z_b}{\partial x\partial y}+v_0^2\,\frac{\partial^2 z_b}{\partial y^2}+g\right]+\left[\frac{\partial u_0}{\partial t}+u_0\,\frac{\partial u_0}{\partial x}+v_0\,\frac{\partial u_0}{\partial y}\right]$$

$$+\,\frac{h}{2}\left[\frac{\partial z_b}{\partial x}\left(\frac{\partial^2 u_0}{\partial x\partial t}+\frac{\partial v_0}{\partial x}\,\frac{\partial u_0}{\partial y}+v_0\,\frac{\partial^2 u_0}{\partial x\partial y}-\frac{\partial u_0}{\partial x}\,\frac{\partial v_0}{\partial y}-u_0\,\frac{\partial^2 v_0}{\partial x\partial y}\right)+u_0^2\,\frac{\partial^3 z_b}{\partial x^3}\right.$$

$$+\frac{\partial^2 z_b}{\partial x^2}\left(\frac{\partial u_0}{\partial t}+2u_0\,\frac{\partial u_0}{\partial x}+v_0\,\frac{\partial u_0}{\partial y}-u_0\frac{\partial v_0}{\partial y}\right)+\frac{\partial z_b}{\partial y}\left(\frac{\partial^2 v_0}{\partial x\partial t}+u_0\,\frac{\partial^2 v_0}{\partial x^2}-v_0\,\frac{\partial^2 u_0}{\partial x^2}\right)$$

$$\left.+\frac{\partial^2 z_b}{\partial x\partial y}\left(\frac{\partial v_0}{\partial t}+3u_0\,\frac{\partial v_0}{\partial x}+v_0\,\frac{\partial u_0}{\partial x}\right)+2u_0v_0\,\frac{\partial^3 z_b}{\partial x^2\partial y}+2v_0\,\frac{\partial v_0}{\partial x}\,\frac{\partial^2 z_b}{\partial y^2}+v_0^2\,\frac{\partial^3 z_b}{\partial x\partial y^2}\right]$$

$$+h\,\frac{\partial\left(h+\frac{z_b}{2}\right)}{\partial x}\left[-\frac{\partial^2 u_0}{\partial x\partial t}-\frac{\partial^2 v_0}{\partial y\partial t}-u_0\,\frac{\partial^2 u_0}{\partial x^2}-\frac{\partial^2 (u_0v_0)}{\partial x\partial y}-v_0\,\frac{\partial^2 v_0}{\partial y^2}+\left(\frac{\partial u_0}{\partial x}+\frac{\partial v_0}{\partial y}\right)^2\right]$$

$$+\frac{h^2}{3}\left[-\frac{\partial^3 u_0}{\partial x^2\partial t}-\frac{\partial^3 v_0}{\partial x\partial y\partial t}-u_0\,\frac{\partial^3 u_0}{\partial x^3}-\frac{\partial^3 (u_0v_0)}{\partial x^2\partial y}-\frac{\partial v_0}{\partial x}\left(\frac{\partial^2 u_0}{\partial x\partial y}+\frac{\partial^2 v_0}{\partial y^2}\right)-v_0\,\frac{\partial^3 v_0}{\partial x\partial y^2}\right.$$

$$\left.+\left(\frac{\partial u_0}{\partial x}+2\frac{\partial v_0}{\partial y}\right)\left(\frac{\partial^2 v_0}{\partial x\partial y}+\frac{\partial^2 u_0}{\partial x^2}\right)\right]=0\quad . \tag{3.31}$$

Discretising this equation using second-order central differences leads to:

$$\begin{cases} a_i=\left[h_{ij}^k\left(\dfrac{h_{i+1\,j}^k-h_{i-1\,j}^k}{4\Delta x^2}+\dfrac{{z_b}_{i+1\,j}^{\,k}-{z_b}_{i-1\,j}^{\,k}}{8\Delta x^2}\right)-\dfrac{h_{ij}^k}{\Delta x^2}\left(\dfrac{h_{ij}^k}{3}+\dfrac{{z_b}_{i+1\,j}^{\,k}-{z_b}_{i-1\,j}^{\,k}}{8}\right)\right] \\ b_i=\left[1+\dfrac{2(h_{ij}^k)^2}{3\Delta x^2}+h_{ij}^k\dfrac{{z_b}_{i+1\,j}^{\,k}-2{z_b}_{ij}^{\,k}+{z_b}_{i-1\,j}^{\,k}}{2\Delta x^2}+\dfrac{(\eta_{i+1\,j}^k-\eta_{i-1\,j}^k)({z_b}_{i+1\,j}^{\,k}-{z_b}_{i-1\,j}^{\,k})}{4\Delta x^2}\right] \\ c_i=\left[-h_{ij}^k\left(\dfrac{h_{i+1\,j}^k-h_{i-1\,j}^k}{4\Delta x^2}+\dfrac{{z_b}_{i+1\,j}^{\,k}-{z_b}_{i-1\,j}^{\,k}}{8\Delta x^2}\right)+\dfrac{h_{ij}^k}{\Delta x^2}\left(-\dfrac{h_{ij}^k}{3}+\dfrac{{z_b}_{i+1\,j}^{\,k}-{z_b}_{i-1\,j}^{\,k}}{8}\right)\right] \end{cases} \tag{3.32}$$

The 2D level I y-momentum GN equation for a non-uniform bed is

$$\left(\frac{\partial \eta}{\partial y}\right)\left[\frac{\partial z_b}{\partial x}\left(\frac{\partial u_0}{\partial t}+v_0\,\frac{\partial u_0}{\partial y}-u_0\frac{\partial v_0}{\partial y}\right)+\frac{\partial z_b}{\partial y}\left(\frac{\partial v_0}{\partial t}+u_0\,\frac{\partial v_0}{\partial x}-v_0\,\frac{\partial u_0}{\partial x}\right)+u_0^2\,\frac{\partial^2 z_b}{\partial x^2}\right.$$
$$\left.+2u_0v_0\,\frac{\partial^2 z_b}{\partial x\partial y}+v_0^2\,\frac{\partial^2 z_b}{\partial y^2}+g\right]+\left[\frac{\partial v_0}{\partial t}+u_0\,\frac{\partial v_0}{\partial x}+v_0\,\frac{\partial v_0}{\partial y}\right]$$

$$+\frac{h}{2}\left[\frac{\partial z_b}{\partial x}\left(\frac{\partial^2 u_0}{\partial y\partial t}+v_0\,\frac{\partial^2 u_0}{\partial y^2}-u_0\,\frac{\partial^2 v_0}{\partial y^2}\right)+\frac{\partial^2 z_b}{\partial x\partial y}\left(\frac{\partial u_0}{\partial t}+3v_0\frac{\partial u_0}{\partial y}+u_0\frac{\partial v_0}{\partial y}\right)+u_0^2\,\frac{\partial^3 z_b}{\partial x^2\partial y}\right.$$
$$+\frac{\partial z_b}{\partial y}\left(\frac{\partial^2 v_0}{\partial y\partial t}+\frac{\partial u_0}{\partial y}\,\frac{\partial v_0}{\partial x}+u_0\,\frac{\partial^2 v_0}{\partial x\partial y}-\frac{\partial v_0}{\partial y}\,\frac{\partial u_0}{\partial x}-v_0\,\frac{\partial^2 u_0}{\partial x\partial y}\right)+2u_0\,\frac{\partial u_0}{\partial y}\frac{\partial^2 z_b}{\partial x^2}+v_0^2\,\frac{\partial^3 z_b}{\partial y^3}$$
$$\left.+\frac{\partial^2 z_b}{\partial y^2}\left(\frac{\partial v_0}{\partial t}+u_0\,\frac{\partial v_0}{\partial x}+2v_0\,\frac{\partial v_0}{\partial y}-v_0\,\frac{\partial u_0}{\partial x}\right)+2u_0v_0\,\frac{\partial^3 z_b}{\partial x\partial y^2}\right]$$

$$+h\,\frac{\partial\left(h+\frac{z_b}{2}\right)}{\partial y}\left[-\frac{\partial^2 u_0}{\partial x\partial t}-\frac{\partial^2 v_0}{\partial y\partial t}-u_0\,\frac{\partial^2 u_0}{\partial x^2}-\frac{\partial^2(u_0v_0)}{\partial x\partial y}-v_0\,\frac{\partial^2 v_0}{\partial y^2}+\left(\frac{\partial u_0}{\partial x}+\frac{\partial v_0}{\partial y}\right)^2\right]$$

$$+\frac{h^2}{3}\left[-\frac{\partial^3 u_0}{\partial x\partial y\partial t}-\frac{\partial^3 v_0}{\partial y^2\partial t}-\frac{\partial u_0}{\partial y}\,\frac{\partial^2 u_0}{\partial x^2}-u_0\,\frac{\partial^3 u_0}{\partial x^2\partial y}-\frac{\partial u_0}{\partial y}\frac{\partial^2 v_0}{\partial x\partial y}-\frac{\partial^3(u_0v_0)}{\partial x\partial y^2}-v_0\,\frac{\partial^3 v_0}{\partial y^3}\right.$$
$$\left.+\left(2\frac{\partial u_0}{\partial x}+\frac{\partial v_0}{\partial y}\right)\left(\frac{\partial^2 u_0}{\partial x\partial y}+\frac{\partial^2 v_0}{\partial y^2}\right)\right]=0 \qquad (3.33)$$

Discretising this equation using second-order central differences leads to:

$$\begin{cases} aa_j=\left[h_{ij}^k\left(\dfrac{h_{i\,j+1}^k-h_{i\,j-1}^k}{4\Delta y^2}+\dfrac{{z_b}_{i\,j+1}^k-{z_b}_{i\,j-1}^k}{8\Delta y^2}\right)-\dfrac{h_{ij}^k}{\Delta y^2}\left(\dfrac{h_{ij}^k}{3}+\dfrac{{z_b}_{i\,j+1}^k-{z_b}_{i\,j-1}^k}{8}\right)\right] \\ bb_j=\left[1+\dfrac{2(h_{ij}^k)^2}{3\Delta y^2}+h_{ij}^k\dfrac{{z_b}_{i\,j+1}^k-2{z_b}_{ij}^k+{z_b}_{i\,j-1}^k}{2\Delta y^2}+\dfrac{(\eta_{i\,j+1}^k-\eta_{i\,j-1}^k)({z_b}_{i\,j+1}^k-{z_b}_{i\,j-1}^k)}{4\Delta y^2}\right] \\ cc_j=\left[-h_{ij}^k\left(\dfrac{h_{i\,j+1}^k-h_{i\,j-1}^k}{4\Delta y^2}+\dfrac{{z_b}_{i\,j+1}^k-{z_b}_{i\,j-1}^k}{8\Delta y^2}\right)+\dfrac{h_{ij}^k}{\Delta y^2}\left(-\dfrac{h_{ij}^k}{3}+\dfrac{{z_b}_{i\,j+1}^k-{z_b}_{i\,j-1}^k}{8}\right)\right] \end{cases} (2.34)$$

Similar to 2D GN momentum equations for uniform bed, the foregoing results in two matrix equations in the x- and y-directions. As above, the matrix equations are solved using the Thomas algorithm in each case, with iteration used to centre the discretised cross-derivative terms. The 1D tests show (see Chapter 4) that second-order differences are sufficient to obtain satisfactory results, and so the 2-D solver was restricted to second-order differences.

3.5 Boundary conditions

To solve the 2D GN equations accurately, it is necessary to impose flexible and compatible boundary conditions (see figure 3.2). For instance, solid wall boundaries are located at the ends of the domain when simulating sloshing of waves in a tank. The surface elevation at the boundary is obtained by cubic Lagrange interpolation of interior values, following Haniffah (2013). The velocity is set to zero at solid wall boundaries. Additional ghost grid points are located outside the boundaries, with anti-symmetry imposed for horizontal velocity (u) on y-direction and symmetry on x-direction.

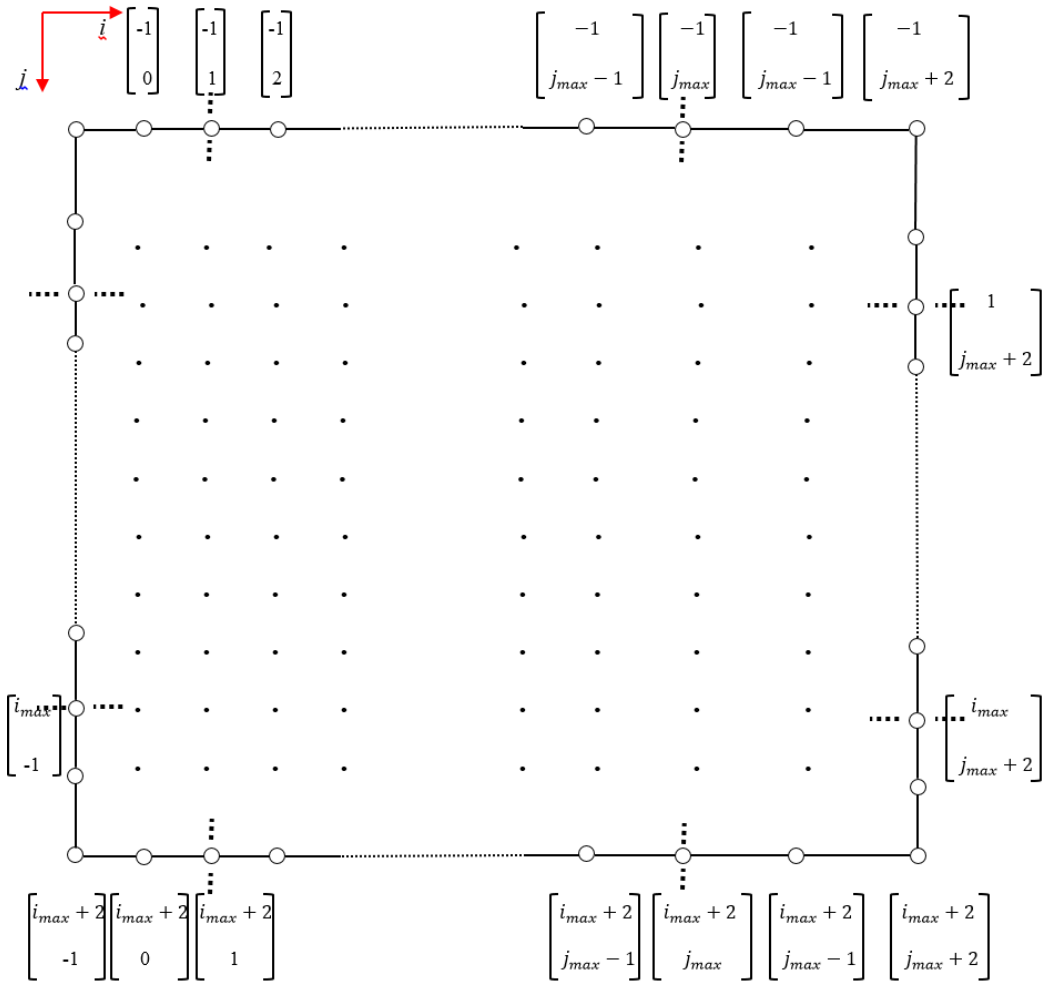

Figure 3.2: Boundary conditions for 2-D GN equations

The boundary conditions for *u* are:

$$\begin{cases} \dfrac{\partial u_0}{\partial t}\Big|_{1,j}=0\,, \quad \dfrac{\partial u_0}{\partial t}\Big|_{0,j}=-\dfrac{\partial u_0}{\partial t}\Big|_{2,j}\,, \quad \dfrac{\partial u_0}{\partial t}\Big|_{-1,j}=-\dfrac{\partial u_0}{\partial t}\Big|_{3,j} \\ \dfrac{\partial u_0}{\partial t}\Big|_{i_{max},j}=0\,, \quad \dfrac{\partial u_0}{\partial t}\Big|_{i_{max}+1,j}=-\dfrac{\partial u_0}{\partial t}\Big|_{i_{max}-1,j}\,, \quad \dfrac{\partial u_0}{\partial t}\Big|_{i_{max}+2,j}=-\dfrac{\partial u_0}{\partial t}\Big|_{i_{max}-2,j} \\ \dfrac{\partial u_0}{\partial t}\Big|_{i,1}=0\,, \quad \dfrac{\partial u_0}{\partial t}\Big|_{i,0}=\dfrac{\partial u_0}{\partial t}\Big|_{i,2}\,, \quad \dfrac{\partial u_0}{\partial t}\Big|_{i,-1}=\dfrac{\partial u_0}{\partial t}\Big|_{i,3} \\ \dfrac{\partial u_0}{\partial t}\Big|_{i,j_{max}}=0\,, \quad \dfrac{\partial u_0}{\partial t}\Big|_{i,j_{max}+1}=\dfrac{\partial u_0}{\partial t}\Big|_{i,j_{max}-1}\,, \quad \dfrac{\partial u_0}{\partial t}\Big|_{i,j_{max}+2}=\dfrac{\partial u_0}{\partial t}\Big|_{i,j_{max}-2} \end{cases} \tag{2.35}$$

Anti-symmetry boundary imposed for horizontal velocity (*v*) on *x*-direction and symmetry on *y*-direction. The boundary conditions for *v* are:

$$\begin{cases} \dfrac{\partial v_0}{\partial t}\Big|_{i,1}=0\,, \quad \dfrac{\partial v_0}{\partial t}\Big|_{i,0}=-\dfrac{\partial v_0}{\partial t}\Big|_{i,2}\,, \quad \dfrac{\partial v_0}{\partial t}\Big|_{i,-1}=-\dfrac{\partial v_0}{\partial t}\Big|_{i,3} \\ \dfrac{\partial v_0}{\partial t}\Big|_{i,j_{max}}=0\,, \quad \dfrac{\partial v_0}{\partial t}\Big|_{i,j_{max}+1}=-\dfrac{\partial v_0}{\partial t}\Big|_{i,j_{max}-1}\,, \quad \dfrac{\partial v_0}{\partial t}\Big|_{i,j_{max}+2}=-\dfrac{\partial v_0}{\partial t}\Big|_{i,j_{max}-2} \\ \dfrac{\partial v_0}{\partial t}\Big|_{1,j}=0\,, \quad \dfrac{\partial v_0}{\partial t}\Big|_{0,j}=\dfrac{\partial v_0}{\partial t}\Big|_{2,j}\,, \quad \dfrac{\partial v_0}{\partial t}\Big|_{-1,j}=\dfrac{\partial v_0}{\partial t}\Big|_{3,j} \\ \dfrac{\partial v_0}{\partial t}\Big|_{i_{max},j}=0\,, \quad \dfrac{\partial v_0}{\partial t}\Big|_{i_{max}+1,j}=\dfrac{\partial v_0}{\partial t}\Big|_{i_{max}-1,j}\,, \quad \dfrac{\partial v_0}{\partial t}\Big|_{i_{max}+2,j}=\dfrac{\partial v_0}{\partial t}\Big|_{i_{max}-2,j} \end{cases} \tag{2.36}$$

The symmetry boundaries imposed for surface elevation are:

$$\begin{cases} \dfrac{\partial h}{\partial t}\Big|_{0,j}=\dfrac{\partial h}{\partial t}\Big|_{2,j}\,, \quad \dfrac{\partial h}{\partial t}\Big|_{1,j}=4\dfrac{\partial h}{\partial t}\Big|_{2,j}-6\dfrac{\partial h}{\partial t}\Big|_{3,j}+4\dfrac{\partial h}{\partial t}\Big|_{4,j}-\dfrac{\partial h}{\partial t}\Big|_{5,j} \\ \dfrac{\partial h}{\partial t}\Big|_{i_{max},j}=4\dfrac{\partial h}{\partial t}\Big|_{i_{max}-1,j}-6\dfrac{\partial h}{\partial t}\Big|_{i_{max}-2,j}+4\dfrac{\partial h}{\partial t}\Big|_{i_{max}-3,j}-\dfrac{\partial h}{\partial t}\Big|_{i_{max}-4,j} \\ \dfrac{\partial h}{\partial t}\Big|_{i_{max}+1,j}=\dfrac{\partial h}{\partial t}\Big|_{i_{max}-1,j} \\ \dfrac{\partial h}{\partial t}\Big|_{i,0}=\dfrac{\partial h}{\partial t}\Big|_{i,2}\,, \quad \dfrac{\partial h}{\partial t}\Big|_{i,1}=4\dfrac{\partial h}{\partial t}\Big|_{i,2}-6\dfrac{\partial h}{\partial t}\Big|_{i,3}+4\dfrac{\partial h}{\partial t}\Big|_{i,4}-\dfrac{\partial h}{\partial t}\Big|_{i,5} \\ \dfrac{\partial h}{\partial t}\Big|_{i,j_{max}}=4\dfrac{\partial h}{\partial t}\Big|_{i,j_{max}-1}-6\dfrac{\partial h}{\partial t}\Big|_{i,j_{max}-2}+4\dfrac{\partial h}{\partial t}\Big|_{i,j_{max}-3}-\dfrac{\partial h}{\partial t}\Big|_{i,j_{max}-4} \\ \dfrac{\partial h}{\partial t}\Big|_{i,j_{max}+1}=\dfrac{\partial h}{\partial t}\Big|_{i,j_{max}-1} \end{cases} \tag{2.37}$$

In 1D GN equations boundaries with symmetry imposed for surface elevation, and anti-symmetry for velocity are taken into consideration (see figure 3.3).

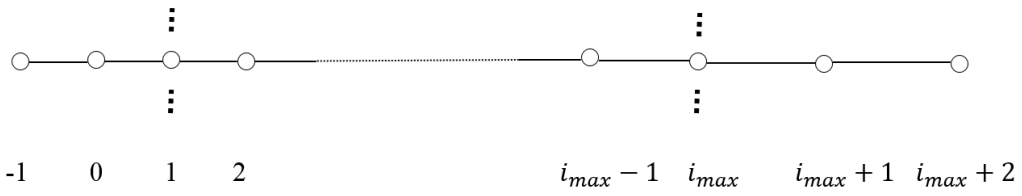

Figure 3.3: Boundary conditions for 1-D GN equation

The boundary conditions for 1D GN equations are:

$$\begin{cases} \frac{\partial u_0}{\partial t}\Big|_1 = 0 \quad , \quad \frac{\partial u_0}{\partial t}\Big|_0 = -\frac{\partial u_0}{\partial t}\Big|_2 \quad , \quad \frac{\partial u_0}{\partial t}\Big|_{-1} = -\frac{\partial u_0}{\partial t}\Big|_3 \\ \frac{\partial u_0}{\partial t}\Big|_{i_{max}} = 0 \quad , \quad \frac{\partial u_0}{\partial t}\Big|_{i_{max}+1} = -\frac{\partial u_0}{\partial t}\Big|_{i_{max}-1} \quad , \quad \frac{\partial u_0}{\partial t}\Big|_{i_{max}+2} = -\frac{\partial u_0}{\partial t}\Big|_{i_{max}-2} \\ \frac{\partial h}{\partial t}\Big|_0 = \frac{\partial h}{\partial t}\Big|_2 \quad , \quad \frac{\partial h}{\partial t}\Big|_1 = 4\frac{\partial h}{\partial t}\Big|_2 - 6\frac{\partial h}{\partial t}\Big|_3 + 4\frac{\partial h}{\partial t}\Big|_4 - \frac{\partial h}{\partial t}\Big|_5 \\ \frac{\partial h}{\partial t}\Big|_{i_{max}} = 4\frac{\partial h}{\partial t}\Big|_{i_{max}-1} - 6\frac{\partial h}{\partial t}\Big|_{i_{max}-2} + 4\frac{\partial h}{\partial t}\Big|_{i_{max}-3} - \frac{\partial h}{\partial t}\Big|_{i_{max}-4} \\ \frac{\partial h}{\partial t}\Big|_{i_{max}+1} = \frac{\partial h}{\partial t}\Big|_{i_{max}-1} \end{cases} \tag{2.38}$$

3.6 Limitations of the present numerical solver

The present finite difference solver is not capable of simulating dam-break. Thus, the finite volume method could be applied for simulating this phenomenon. Moreover, the developed numerical scheme cannot capture the behaviour of hydraulic bore after the breaking wave in the surf zone. Godunov-type shock-capturing scheme can address this problem in the future studies.

3.7 Numerical Procedure

The 2D GN program comprises four main subroutines: input, calculation, update and output. For each test case the following initial values are input to the program: bed elevation, initial water depth, amplitude, length and width of the study basin, number of grid points, time step, and duration of simulation time. Initial conditions are supplied for the bed elevation above fixed horizontal datum, local depth, and local horizontal velocity components throughout the tank. The three benchmark tests comprise: sloshing in a square tank, solitary wave propagation, and free surface sloshing of an initial Gaussian hump in a square basin. These test cases provide adequate evidence to indicate that the predictions of the developed numerical solver are in good agreement with the linear theory of wave.

The calculation steps are as follows. The discretised continuity equation is solved to provide new water depth values throughout the grid. The discretised x-momentum and y-momentum equations are solved using either a second-order tridiagonal scheme or a fourth-order pentadiagonal scheme, as prescribed. Iteration is used to solve for the cross-derivative velocity terms in the momentum equation. Boundary conditions are then invoked.

The values of u, v, h and η are updated after each time integration, time advanced one time step, and the calculation process repeated until the simulation is completed.

The output comprises: channel geometry of channel, and time histories of free surface elevation, and horizontal velocity components.

3.8 Summery

- In this chapter 1D and 2D Level I GN equations were discretised using second-order and fourth-order finite differences in space and time integration through applying a Runge-Kutta fourth-order scheme. The numerical model utilised a tridiagonal matrix solver and a pentadiagonal matrix solver, the former for the second-order space discretisation, the latter for the fourth order. A detailed explanation of the numerical procedure and the boundary conditions required to close the model is provided.

Chapter 4

1D Model Verification and Parameter Tests

4.1 Introduction

In this chapter the numerical schemes for 1D level I GN equations are validated for two benchmark problems: sloshing in a tank and propagation of solitary wave over a flat-bed. For sloshing in a tank, the effect of grid convergence and time step on the accuracy and stability of simulations is studied, and the results compared against analytical solutions of the linearised shallow water equations (originally proposed by Lamb, 1916). Nonlinear behaviour is investigated through spectral analysis of the even and odd harmonics components of the sloshing motions. Grid convergence and time step stability tests are also conducted for propagation of solitary wave over a flat bed, and results compared against a published analytical solution (Metayer *et al*. 2010).

4.2 1D GN equations numerical solver validation test cases

4.2.1 Sinusoidal sloshing in a tank

In order to examine the capability of the spatially second-order tridiagonal and fourth-order pentadiagonal matrix solvers of the 1D GN equations, we first consider the benchmark test of sinusoidal free surface sloshing in a square tank. The wavelength L is 1000 m and the still water depth h_0 is 5 m. The first order analytical solution for the depth profile evolution in space and time of a standing wave in a channel (see e.g. Dean and Dalrymple, 2002) is

$$h = h_0 + a\ \cos(kx + \phi)\cos(\omega t + \phi) \tag{4.1}$$

where a is the amplitude of the standing wave, k is the wave number, ω is the angular frequency of the wave, x is distance along the tank, t is time, and ϕ is the phase. The wave number k and the wave angular frequency ω are given by

$$k = \frac{2\pi}{L} \qquad \text{and} \qquad \omega = \frac{2\pi}{T} \tag{4.2}$$

in which L is the wavelength and T is the period of oscillation of the wave in the tank. The wavelength L is the distance between two successive wave crests or troughs at particular time. The wave period T is the time it takes for the two successive wave crests or troughs to pass a particular point.

At time $t = 0$ the initial depth at the i-th computational node along the tank is given by

$$h_i^0 = h_0 + a\ \cos(kx_i + \phi) \tag{4.3}$$

Figure 4.1 shows numerically predicted sloshing wave profile at $t = 0$ s.
Wave frequency ω is related to wave number k by the dispersion relation

$$\omega^2 = gk\ \tanh(kh_0) \tag{4.4}$$

where g is the acceleration due to gravity and h_0 is the still water depth. For this case:

$$\omega = \sqrt{9.81\left(\frac{2\pi}{1000}\right)\tanh\left(\frac{\pi}{100}\right)} = 0.044\ \frac{\text{rad}}{\text{s}} \tag{4.5}$$

$$T = \frac{2\pi}{\omega} = 142.8\ \text{s} \quad \text{and} \quad f(\text{frequency}) = \frac{1}{T} = 0.007\ \text{Hz} \tag{4.6}$$

To test for grid independence, simulations were performed using the second-order tridiagonal and fourth-order pentadiagonal schemes on different numbers of grid nodes. Results are presented here for the tridiagonal solver, for brevity because of the very close similarity to the pentadiagonal grid results.

Figure 4.2 shows the time histories of wave elevation at the corner of the tank (in positive x-direction) for an initially small-amplitude disturbance $a = 0.0005$ m obtained on grids of increasingly fine resolution ($i_{max} = 41$, 101, 201 and 1001) with phase $\phi = 0$ and a fixed time step $\Delta t = 0.25$ s. The results presented in Figure 4.2 demonstrate that $i_{max} = 101$ is sufficient to achieve a converged solution of the 1D GN equations.

Next, we consider the effect of altering the time step on the converged grid. Figures 4.3 depicts the sloshing wave time histories at the corner of the tank for different time steps ($\Delta t = 0.25$, 1.0 and 2.0 s) on the converged grid with $i_{max} = 101$. It is obvious that the time step does not have significant effect on the results for a small-amplitude disturbance $a = 0.0005$ m. As a result, $\Delta t = 1$ s is adequate for accurate simulation.

Figure 4.4 reveals the corresponding water level time histories obtained for an initially medium-amplitude disturbance $a = 0.005$ m. Once again it is observed that $i_{max} = 101$ is sufficient, for a time step $\Delta t = 0.25$ s. Figure 4.5 shows the close agreement between the results obtained using the second-order scheme for three values of time step ($\Delta t = 0.25$, 1.0 and 2.0 s) on the grid with $i_{max} = 101$.

Figure 4.6 presents the sloshing motions obtained for an even larger amplitude disturbance a= 0.05 m. In this case, the grid resolution is such that i_{max} = 201, and results are presented for $\Delta t = 0.1$ s and $\Delta t = 1$ s. It is clear that the numerical solver is unable to simulate the long term sloshing behaviour of such steep waves, with high-order even harmonic oscillations appearing after 2200 s. The corresponding results on a finer grid with i_{max} = 1001 and smaller time steps of $\Delta t = 0.2$ and 0.02 s did not lead to any significant change in the sloshing behaviour, indicating that this finding is grid independent.

Figure 4.7 presents a direct comparison of the sloshing motions of waves of increasing initial amplitude (and hence nonlinearity) on a relatively coarse grid with $i_{max} = 201$ and relatively large time step of $\Delta t =$ 1 s. All the time histories follow essentially the same trend with increasing initial wave amplitude. The smallest waves a = 0.0005 m and 0.005 m retain almost linear behaviour. The results for larger amplitude a = 0.05 m showed a breakdown into higher order components of increasing amplitude with time.

These simulations, figures 4.1 to 4.7, indicated that relatively coarse grid, $i_{max} = 101$, and relatively large time step of $\Delta t = 1$ s are adequate for GN numerical solver to produce accurate simulations of time histories of wave elevation for an initially small-amplitude ($a = 0.0005$ m) and medium-amplitude disturbance ($a =$ 0.0005 m) at the corner of the tank.

Figure 4.8 depicts the excellent agreement in free surface motions at corner of the tank obtained for medium-amplitude (a = 0.005 m) using the first-order analytical solution, the second-order tridiagonal scheme, and the fourth-order pentadiagonal scheme. In this case, i_{max} = 101 and Δt = 1 s. This case verifies that the numerical schemes give a correct representation of the underlying mathematical description, provided the waves are nearly linear.

4.2.2 Spectral analysis for the sinusoidal sloshing in a tank

To understand better the resonant free surface sloshing in the tank, it is useful to carry out spectral analysis using a Fast Fourier Transform (FFT) of the free surface elevation components of time series. Peaks in the spectra indicate important frequencies and wavelengths where resonant behaviour may be occurring. The free surface motion time series are now interpreted using Fast Fourier Transforms for medium and large amplitude initially sinusoidal sloshing events in a 1000 m x 1000 m square tank with still water depth of 5 m. The code for spectrum analysis developed as M-file of Matlab softeware and FFT analysis is performed by using FFT toolbox of Matlab.

The 2D GN solver is applied on a grid ($i_{max} = j_{max} = 101$) with time step 0.5 s. Figure 4.9 shows the numerical prediction of the free surface elevation time history at the corner of the tank and the corresponding FFT plot obtained for medium amplitude ($a=h_0/1000=0.005$ m) sloshing. In Figure 4.9 two peaks appear at 0.007 and 0.014 Hz. It is worth mentioning that the smaller peak results from the effect of reflection of waves from the tank wall. Here, ξ_c refers to the free surface elevation time series of the hump-induced sloshing. Figure 4.10 shows the corresponding plots for large amplitude ($a = h_0/100 = 0.05$ m) sloshing. The first peak in both medium and large amplitude simulations appears at 0.007 Hz which is the same as that obtained analytically using linearised shallow water theory (Lamb 1879).

It can be seen by comparing Figure 4.10 (b) with Figure 4.9 (b) that an increase in the value of amplitude increases the effect of nonlinearity. The free surface elevation time history displayed in Figure 4.10 (a) is shorter than that in Figure 4.9 (a) because the nonlinear effects eventually caused shock-like steepening of the wave profiles (becoming visible at about $t = 1425$ s) in the larger amplitude case leading to the numerical model becoming unstable. A shock-capturing scheme would be needed to overcome this problem, and is recommended for future work. For the large amplitude, $a = 0.05$ m, case in Figure 4.10 (b), three peaks can be seen at 0.007, 0.014 and 0.021 Hz.

Figures 4.11 (a) and 4.11 (b), respectively, show the numerically predicted free surface elevation time histories of the trough-induced sloshing at the corner of the tank and the corresponding FFT spectrum for the medium amplitude initial condition ($a = h_0/1000 = 0.005$ m). Here, ξ_t refers to the free surface elevation time series of the trough-induced sloshing. The results are qualitatively almost the same as for the crest-induced case (i.e. Figure 4.9). Figure 4.12 shows the time evolution of large amplitude ($a = h_0/100 = 0.05$ m) sloshing in the tank, and the corresponding FFT spectrum. The slosh motions sharpen up into a saw-tooth profile more quickly than for the medium slosh case.

Figures 4.13 and 4.14 show the numerically predicted free surface elevation time histories of the even harmonic components (obtained by $\left[\frac{\xi_c+\xi_t}{2a}\right]$ taking the average of results obtained for $\phi = 0$ and π) and the corresponding FFT spectrum for the medium amplitude ($a = h_0/1000 = 0.005$ m) and large amplitude ($a = h_0/100 = 0.05$ m) slosh cases, respectively. The effect of nonlinearity increases as the initial slosh amplitude increases, as would be expected. Furthermore, an even harmonic peak appears at the same frequency of the second peak in the hump-induced FFT plot at 0.014 Hz (compare figure 4.9 (b) with 4.13 (b) and figure 4.10 (b) with 4.14 (b)).

Figures 4.15 plots the numerically predicted free surface elevation time history of the odd harmonic components (obtained by $\left[\frac{\xi_c-\xi_t}{2a}\right]$) at the corner of the tank and the corresponding FFT plot for the medium amplitude ($a = h_0/1000 = 0.005$ m) case. The odd harmonics are dominated by a single peak corresponding to the linear sloshing mode at 0.007 Hz (compare figure 4.9 (b) with 4.15 (b)). Figure 4.16 presents the equivalent plots for large amplitude ($a = h_0/100 = 0.05$ m) sloshing; the spectrum contains two peaks corresponding to the first and third peaks in the hump-induced sloshing spectrum at 0.007 and 0.021 Hz (compare figure 4.10 (b) with 4.16 (b)).

4.2.3 Solitary Wave Propagation over a Flat Bed

The second verification case concerns the propagation of a solitary wave in a 1D channel over a horizontal, frictionless bed. In this case, the solitary wave is nonlinear, uniform, and at steady state, such that its form does not change with time. Figure 4.17 shows key variables that define the solitary wave flow geometry. The free surface profile of the solitary wave is given by Drazin and Johnson, 1989:

$$\xi(x,t) = a\,\mathrm{sech}^2\big(b\,(x-ct)\big) \tag{4.7}$$

where ξ is the free surface elevation above still water level, a is amplitude, b is the inverse width, and c is the solitary wave speed. Metayer *et al*. (2010) derive the following definition of b and c for a GN solitary wave:

$$b = \frac{1}{2}\sqrt{\left(\frac{3a}{{h_0}^2(h_0+a)}\right)} \quad , \tag{4.8}$$

$$c = \sqrt{g(h_0+a)} \quad , \tag{4.9}$$

and

$$h = h_0 + \xi \tag{4.10}$$

where h_0 is the still water depth and h is the total water depth. Metayer *et al*. (2010) also derive the following expression for horizontal fluid velocity component:

$$u(x,t) = c\left(1 - \frac{h_0}{\xi+h_0}\right) \tag{4.11}$$

To examine grid convergence, the second-order and fourth-order solvers were used to simulate the propagation of a solitary wave of 2 m initial amplitude in otherwise still water of depth 10 m along the 10000 m channel on increasingly fine grids with i_{max} = 1001, 2001, 5001 and 10001 and a fixed time step $\Delta t = 0.5$ s. The position of the initial wave crest is set to be 1000 m away from the west wall ($L_{xpo} =$ 1000 m). Figures 4.18 and 4.19, respectively, show the free surface profiles simulated by second-order and fourth-order solvers at time t = 480 s corresponding to the different grids. In second-order simulations, on the coarser grids, the solitary wave loses amplitude as it dissipates energy into the production of trailing waves (connected to numerical error from lack of spatial resolution). The trailing waves almost disappear and the solitary wave retains its amplitude on the finer grids with i_{max} = 5001 and

10001. As a result, i_{max} = 10001 appears to satisfy grid convergence when simulating the solitary wave using the second-order solver. On the other hand, in the fourth-order simulations using coarser grids the solitary wave does not lose amplitude as it does in second-order simulations. Thus, trailing waves are not produced (figure 4.19).

Figures 4.20 and 4.21, respectively, present the evolved profiles of the solitary wave on the converged grid using second-order tridiagonal and fourth-order pentadiagonal solvers for time steps Δt = 0.01, 0.05, 0.1, 0.5 and 1.0 s. The results for Δt = 0.5 s are in agreement with the results for the smaller time steps, and so is selected for the remainder of the solitary wave study.

Figures 4.22 shows the excellent agreement obtained between the second-order solver predictions and the analytical solution of the solitary wave profile at t = 480 s on the converged grid with i_{max} = 10001 for $\Delta t = 0.1$ s and $\Delta t = 0.5$ s. To illustrate again the effect of grid convergence, figure 4.23 shows the corresponding profiles of increasing accuracy obtained at t = 480 s for i_{max} = 1001, 2001, 5001 and 10001 and $\Delta t = 0.1$ s. Figures 4.24 and 4.25 depict the solitary wave profiles obtained on the same grids of increasing fineness for Δt = 0.5 s and 1.0 s. The results confirm that increasing the number of grid nodes for Δt = 0.5 s improves the accuracy of the tridiagonal solver results. For Δt = 1.0 s, however, the accuracy of the second-order simulation does not increase beyond a certain point by increasing the number of grids. The value of time step should be selected carefully, since using big time steps in the numerical model may lead to inaccurate simulations.

Similar tests were performed using fourth-order pentadiagonal solver, the results of which are reported in figures 4.26, 4.27 and 4.28. The fourth-order simulations are in complete agreement with the analytical solution of the solitary wave profile at t = 480 s on the converged grid with i_{max} = 10001 for $\Delta t = 0.1$ s and $\Delta t = 0.5$ s (figures 4.26). To demonstrate the effect of grid convergence, figure 4.27 shows the corresponding profiles of increasing accuracy obtained at t = 480 s for i_{max} = 1001, 2001, 5001 and 10001 and $\Delta t = 0.1$ s. Figures 4.28 depicts the solitary wave profiles obtained on the same grids of increasing fineness for Δt = 0.5 s. The results indicate that increasing the number of grid nodes for Δt = 0.5 s improves the accuracy of the fourth-order solver results.

Figure 4.29 and Figure 4.30 show the evolution in space and time of the solitary wave of initial amplitude 2 m on otherwise still water of depth 10 m as predicted by the spatially fourth-order pentadiagonal solver on a fine grid with i_{max}= 10001 and $\Delta t = 0.5$ s. Figure 4.29 provides an *x*-*t* plot of the free surface evolution. Figure 4.30 depicts the propagation of the solitary wave profile as it moves along the channel at times *t* = 0, 80, 160, 240, 320,400, and 480 s. It is obvious that the wave shape does not change with time, in accordance with the analytical solution, thus providing further verification of the fourth-order solver of the GN equations.

The same simulation was performed using second-order solver on a coarser grid with i_{max}= 1001 and time step of $\Delta t = 0.5$ s. Figure 4.31 again shows snapshots of the solitary wave profile at different times. However, the results are not as accurate as those in Figure 4.30, due to the coarse grid being used.

Figure 4.32 and Figure 4.33 taken together offer a comparison between the results obtained using the second-order tridiagonal and fourth-order pentadiagonal solvers on a grid with i_{max}= 10001 and time step $\Delta t = 0.01$ s. Both figures present the solitary wave profiles simulated at times *t* = 0 and *t* = 480 s, and focus on the trailing oscillatory waves that occur behind the solitary wave (and are a measure as to how accurate the solver is at representing the analytical solution which is without trailing waves). In both cases, the trailing waves are very small, though those obtained using the tridiagonal scheme are rather larger than by the pentadiagonal scheme (as would be expected given that the former is second-order accurate and the latter is fourth-order).

Figures 4.34 shows the free surface profiles of the solitary wave, respectively, simulated by linear analytical solution (black line), second-order tridiagonal solver (blue line) and fourth-order pentadiagonal solver (cross symbols) at time *t* = 480 s on the converged grid with i_{max} = 10001 for $\Delta t = 0.1$ s. An excellent and in complete agreement respectively obtained for second-order and fourth-order numerical predictions against the linear analytical solution of the solitary wave profile in which the cross symbols essentially overlay the black line.

4.3 Summery

- In this chapter, the verification tests undertaken for the 1D level I GN equations comprised of free surface sloshing of an initial sinusoidal wave in a tank and the propagation of solitary wave over a flat-bed.

- For sloshing in a tank, excellent agreement was obtained between the model predictions using both second-order and fourth-order schemes and the standard first-order analytical solution for relatively small initial wave amplitude ($a \leq$ 0.005 m). At larger amplitudes of initial disturbance, the free surface elevation time history developed saw-tooth profiles. A shock-capturing scheme would be needed to overcome this problem, and is recommended for future work. By means of the FFT analysis, it was found that nonlinear behaviour was particularly pronounced in the even harmonic slosh components.

- In the second verification test, it was found that both second- and fourth-order solvers produced accurate simulations of solitary wave propagation when the results were compared against a standard solution.

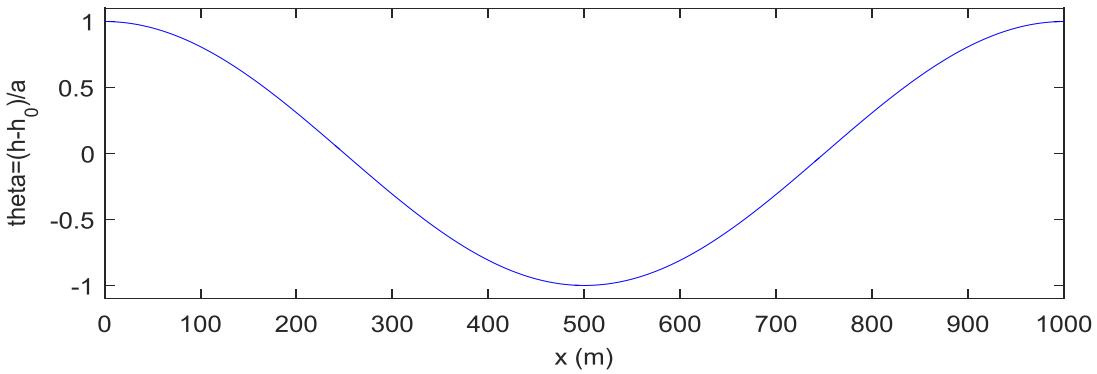

Figure 4.1: Predicted sloshing wave profile at t = 0 s.

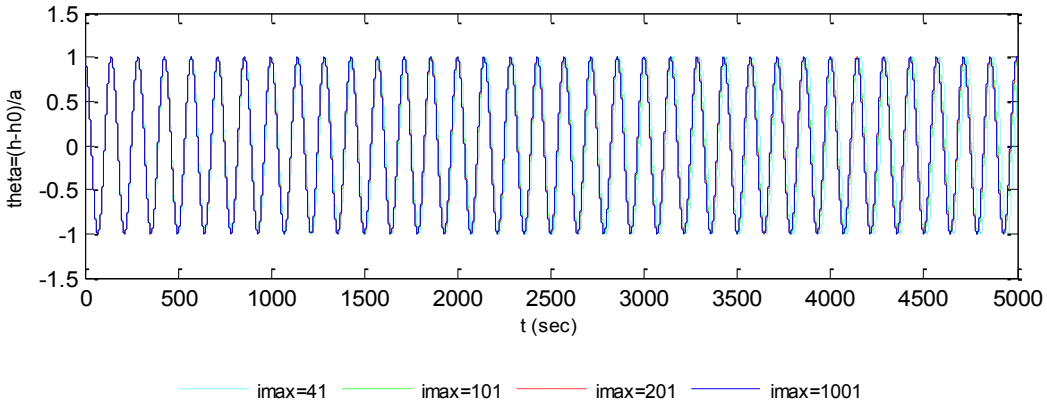

Figure 4.2: Predicted free surface elevation time history for a small-amplitude disturbance (a = 0.0005 m) at the corner of the tank: i_{max} = 41, 101, 201, and 1001.

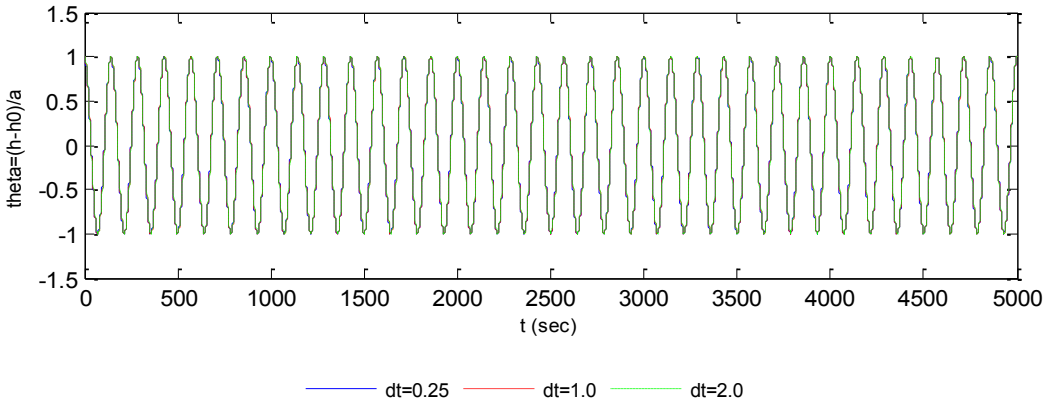

Figure 4.3: Predicted free surface elevation time history for a small-amplitude disturbance (a = 0.0005 m) at the corner of the tank: i_{max} = 101 for Δt = 0.25, 1, and 2 s.

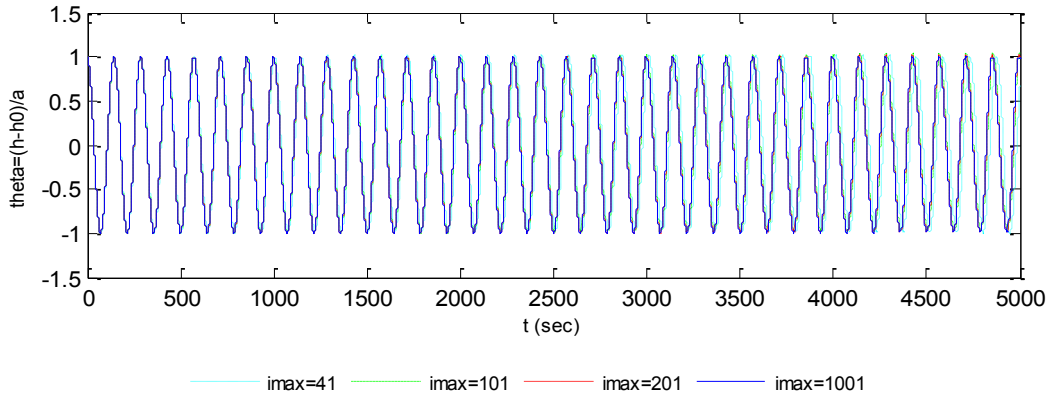

Figure 4.4: Predicted free surface elevation time history for a medium-amplitude disturbance (a = 0.005 m) at the corner of the tank: i_{max} = 41, 101, 201, and 1001.

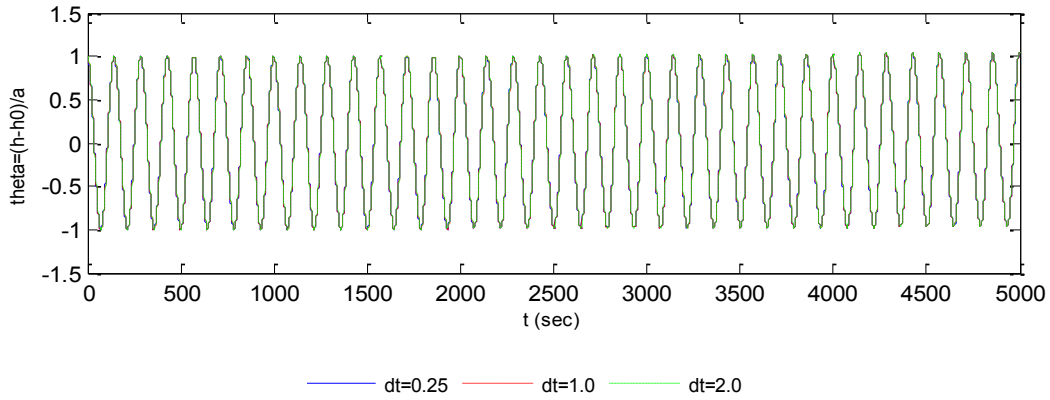

Figure 4.5: Predicted free surface elevation time history for a medium-amplitude disturbance (a = 0.005 m) at the corner of the tank: i_{max} = 101 for Δt = 0.25 s, 1 s, and 2 s.

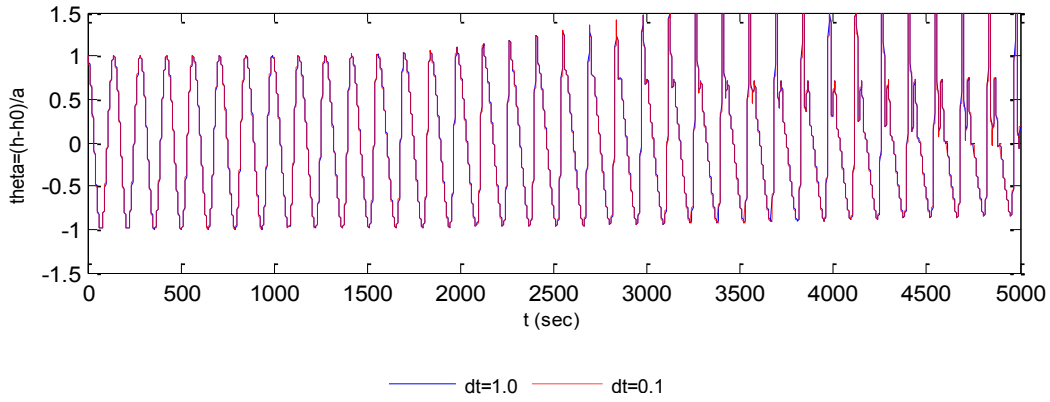

Figure 4.6: Predicted free surface elevation time history for a large-amplitude disturbance (a = 0.05 m) at the corner of the tank: i_{max} = 201 for Δt = 0.1 and 1 s.

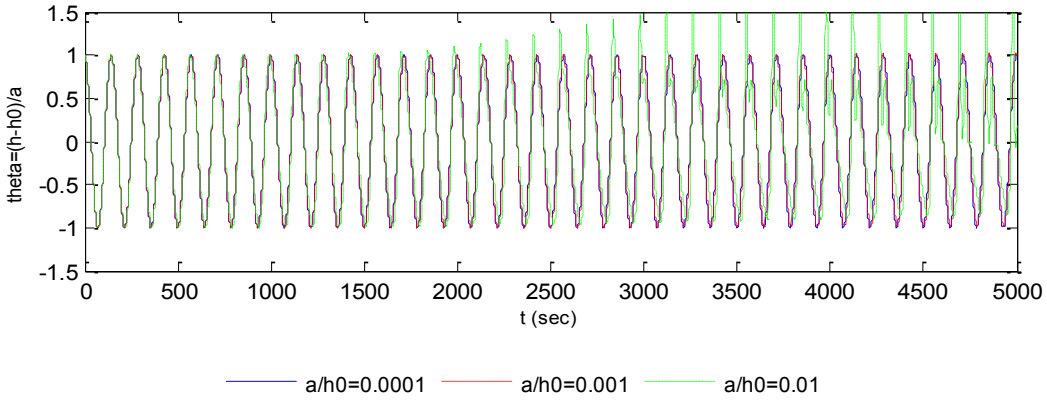

Figure 4.7: Predicted free surface elevation time history for different initial disturbance amplitude (a = 0.0005, 0.005, and 0.05 m) at the corner of the tank: i_{max}= 201, Δt=1 s.

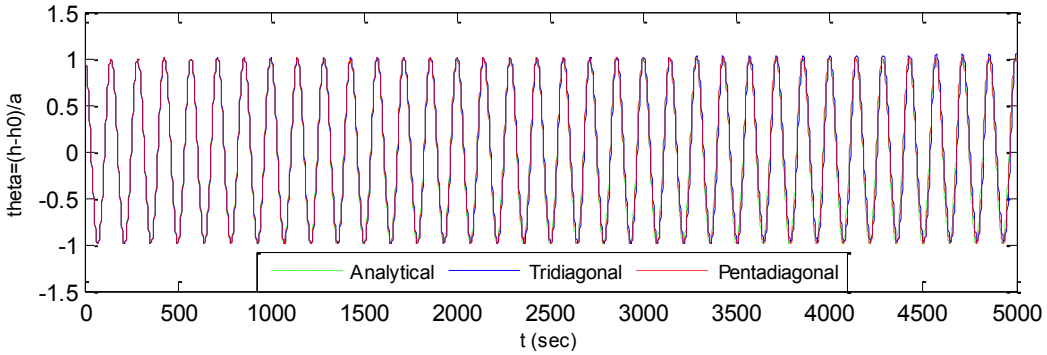

Figure 4.8: Predicted free surface elevation time histories for a medium-amplitude disturbance (a = 0.005 m) at the corner of the tank: i_{max} = 101, Δt = 1 s; analytical solution for i_m= 101.

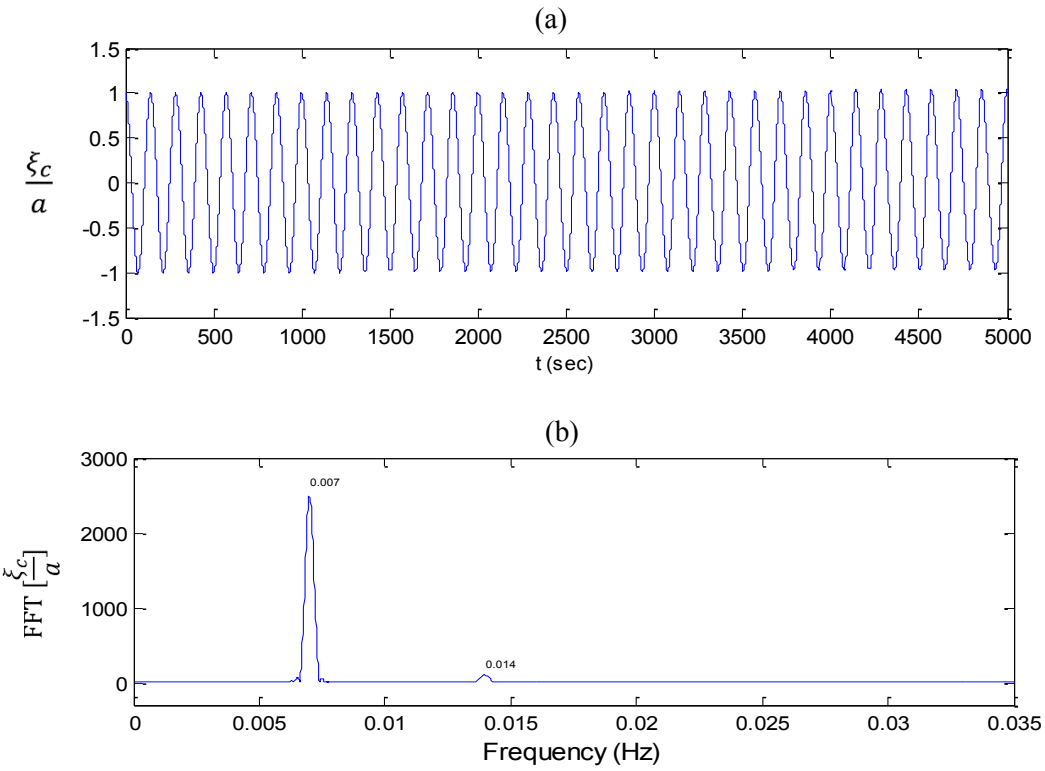

Figure 4.9: Prediction of hump-induced sloshing in the tank for a = 0.005 m: (a) free surface elevation time history at the corner of the tank; and (b) FFT spectrum.

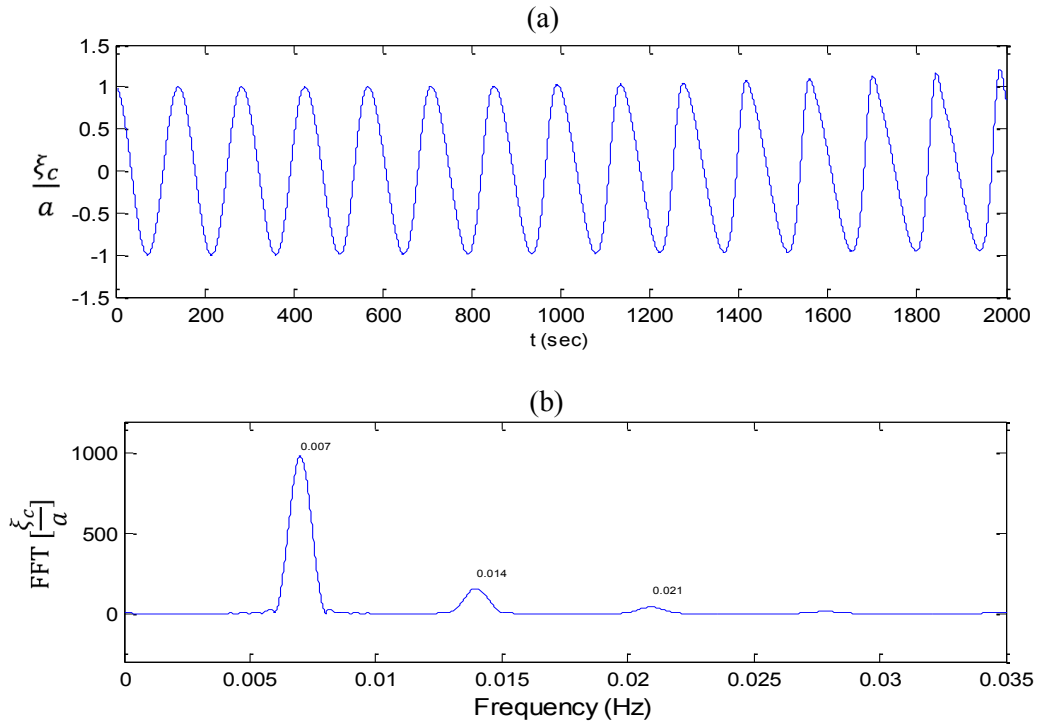

Figure 4.10: Prediction of hump-induced sloshing in the tank for a = 0.05 m: (a) free surface elevation time history at the corner of the tank; and (b) FFT spectrum.

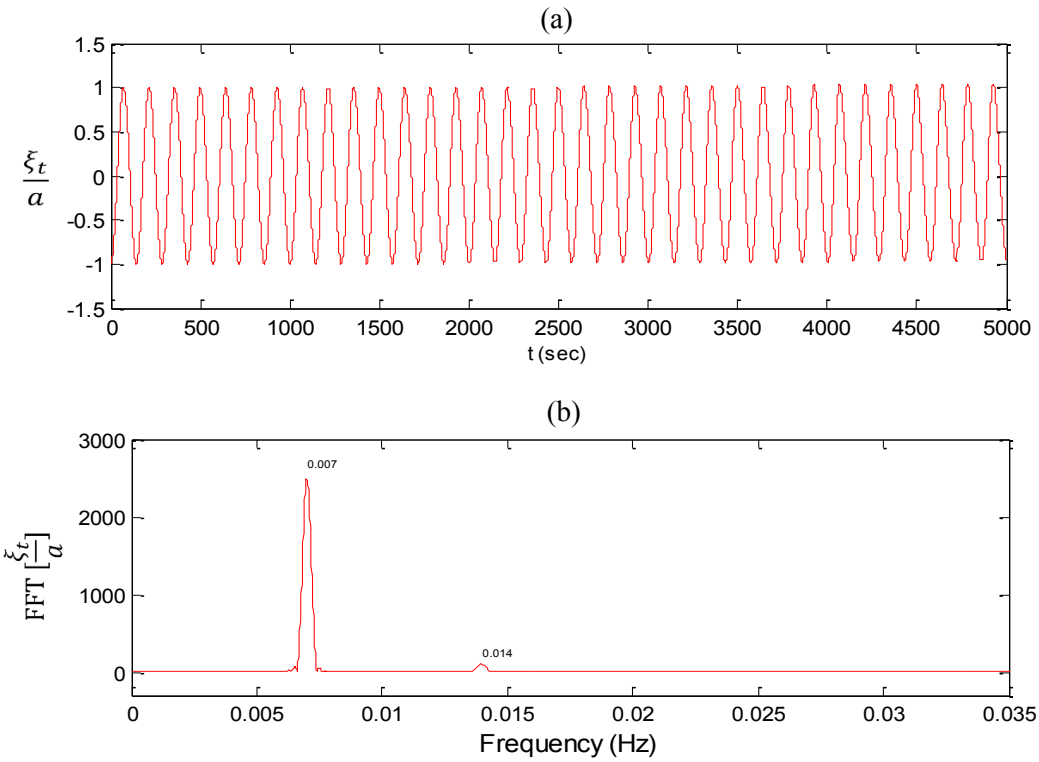

Figure 4.11: Prediction of trough-induced sloshing in the tank for a = 0.005 m: (a) free surface elevation time history at the corner of the tank; and (b) FFT spectrum.

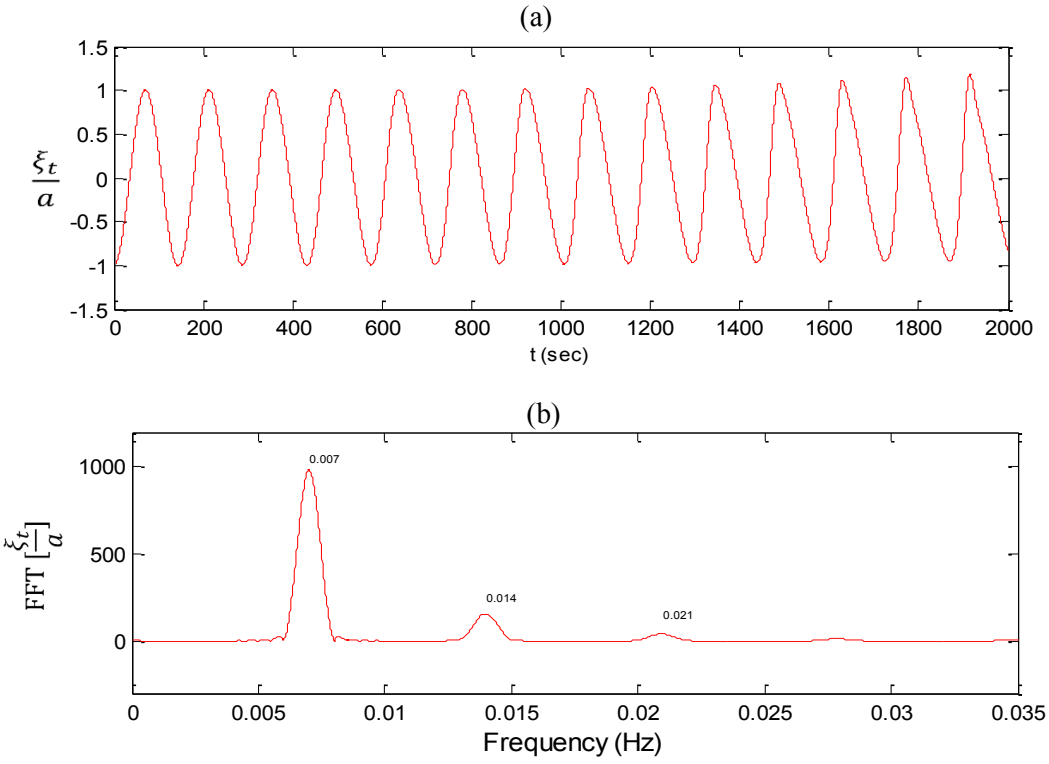

Figure 4.12: Prediction of trough-induced sloshing in the tank for a = 0.05 m: (a) free surface elevation time history at the corner of the tank; and (b) FFT spectrum.

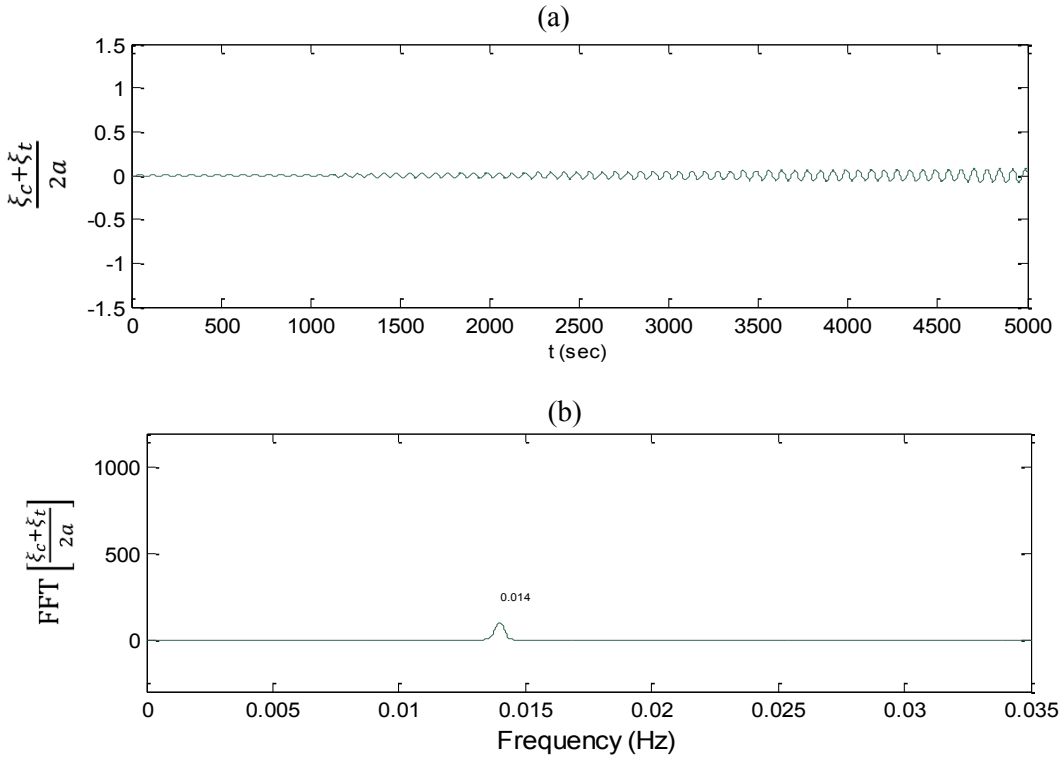

Figure 4.13: Predicted even harmonics for sloshing of initial a = 0.005 m: (a) free surface elevation time history at the corner of the tank; and (b) FFT spectrum.

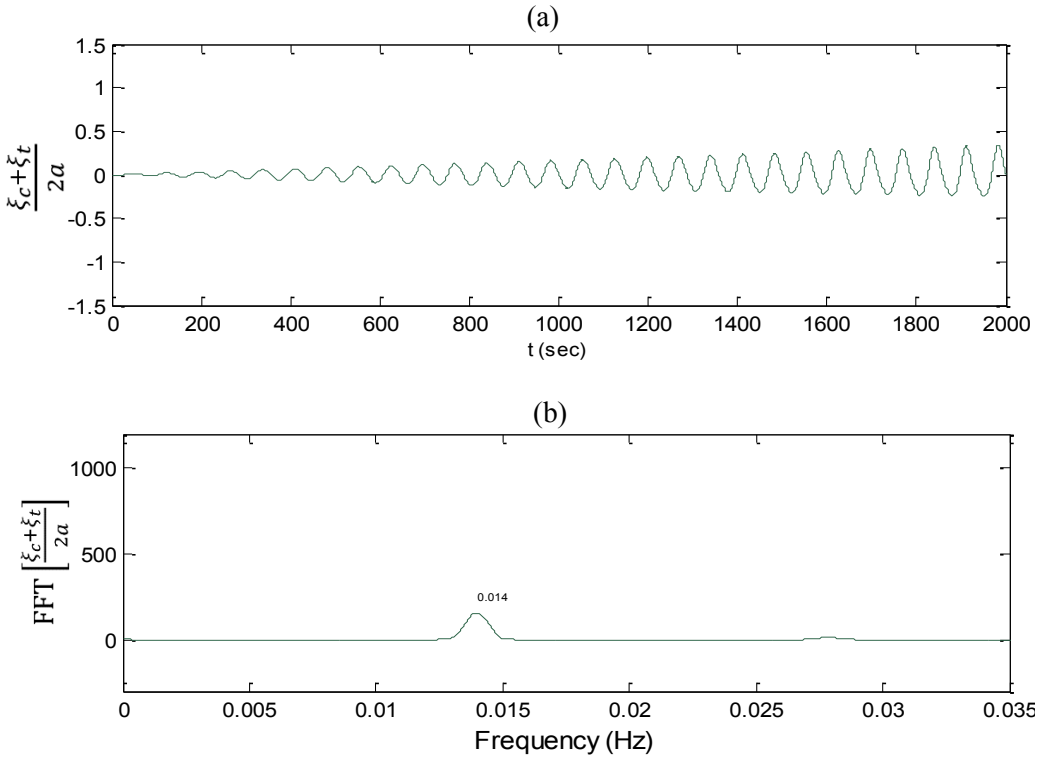

Figure 4.14: Predicted even harmonics for sloshing of initial a = 0.05 m: (a) free surface elevation time history at the corner of the tank; and (b) FFT spectrum.

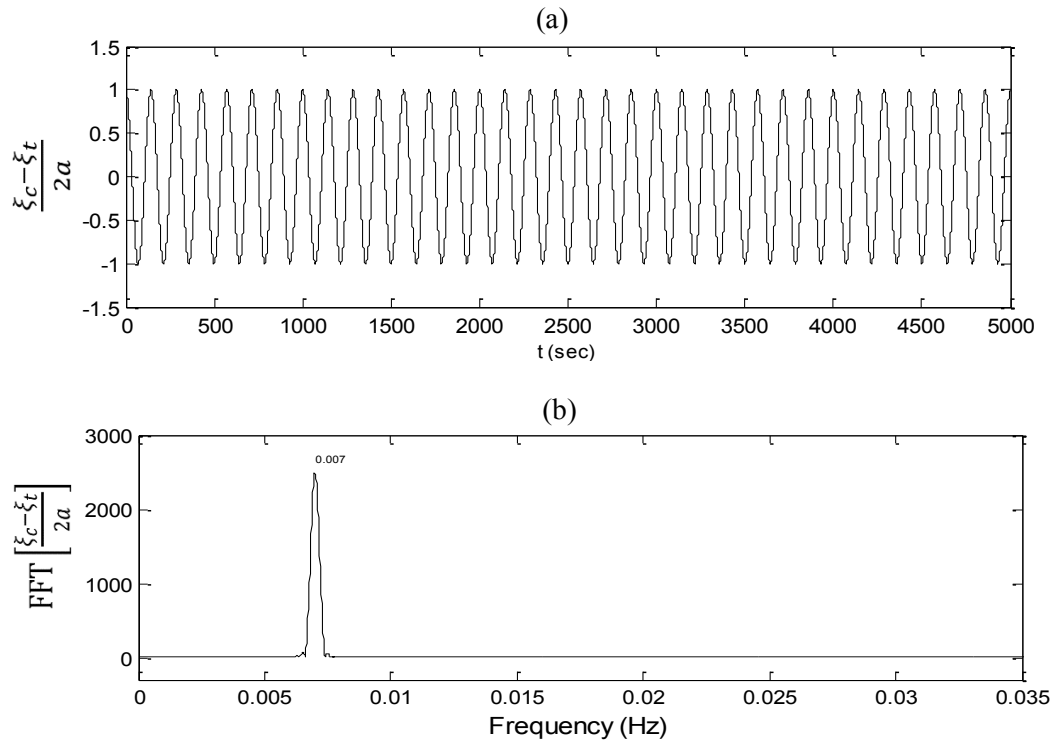

Figure 4.15: Predicted odd harmonics for sloshing of initial a = 0.005 m: (a) free surface elevation time history at the corner of the tank; and (b) FFT spectrum.

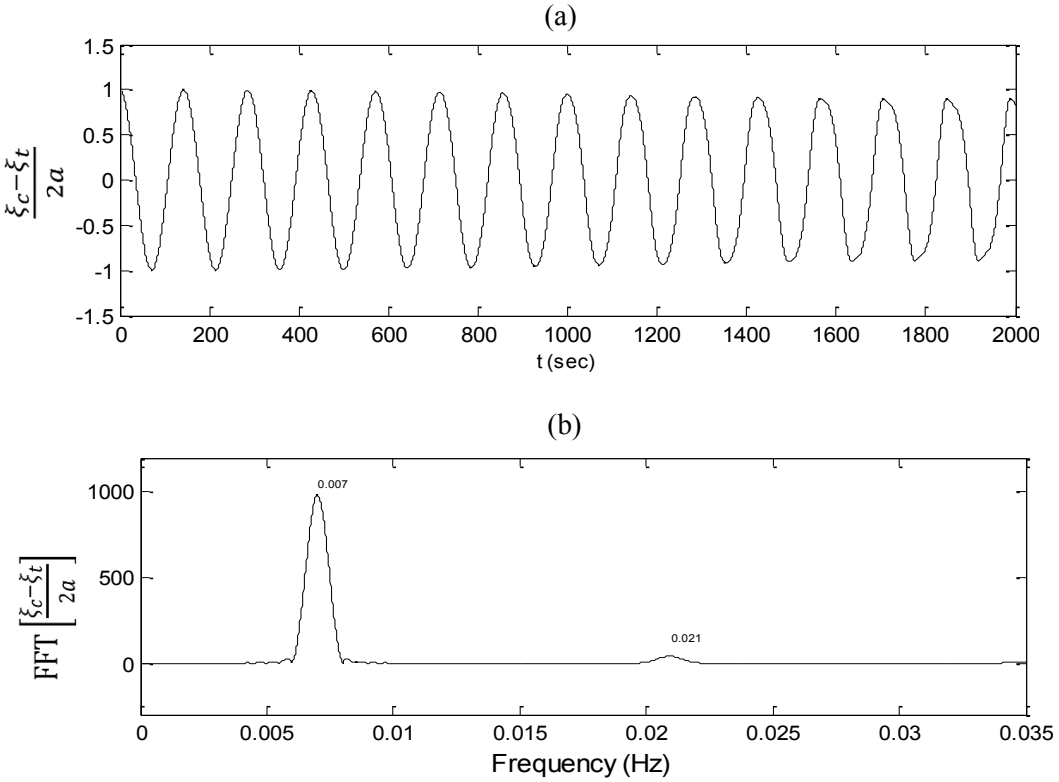

Figure 4.16: Predicted odd harmonics for sloshing of initial a = 0.05 m: (a) free surface elevation time history at the corner of the tank; and (b) FFT spectrum.

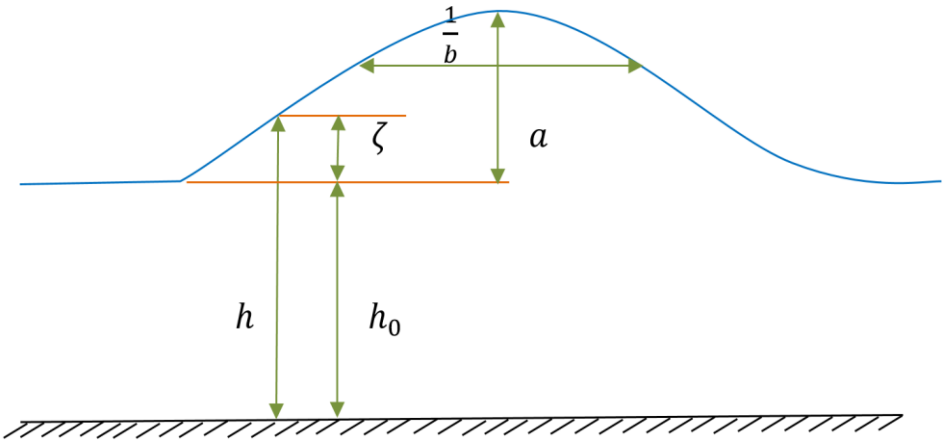

Figure 4.17: Key variables that define the solitary wave flow geometry

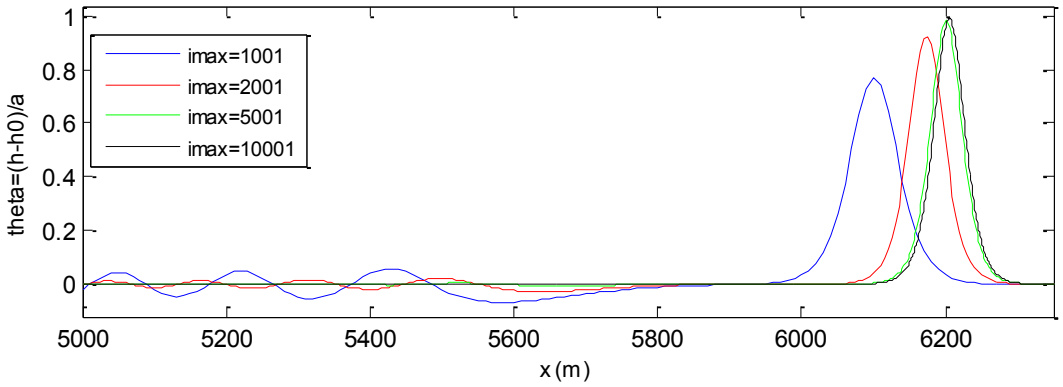

Figure 4.18: Solitary wave propagation over a flat-bed: predicted free surface elevation profiles at t=480 s using second-order solver for i_{max}=1001, 2001, 5001, and 10001, Δt=0.5 s.

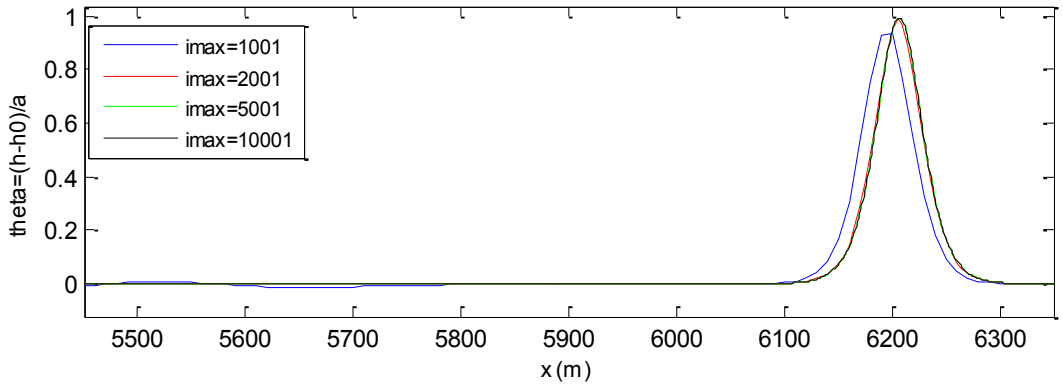

Figure 4.19: Solitary wave propagation over a flat-bed: predicted free surface elevation profiles at t= 480 s using fourth-order solver for i_{max}= 1001, 2001, 5001, and 10001, Δt=0.5 s.

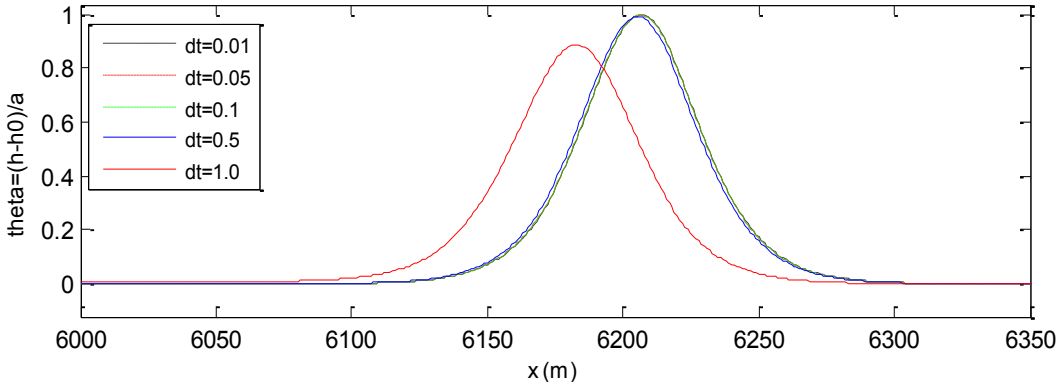

Figure 4.20: Solitary wave propagation over a flat-bed: predicted free surface elevation profiles at t=480 s using second-order solver for i_{max}= 10001, Δt= 0.01, 0.05, 0.1, 0.5 and 1 s.

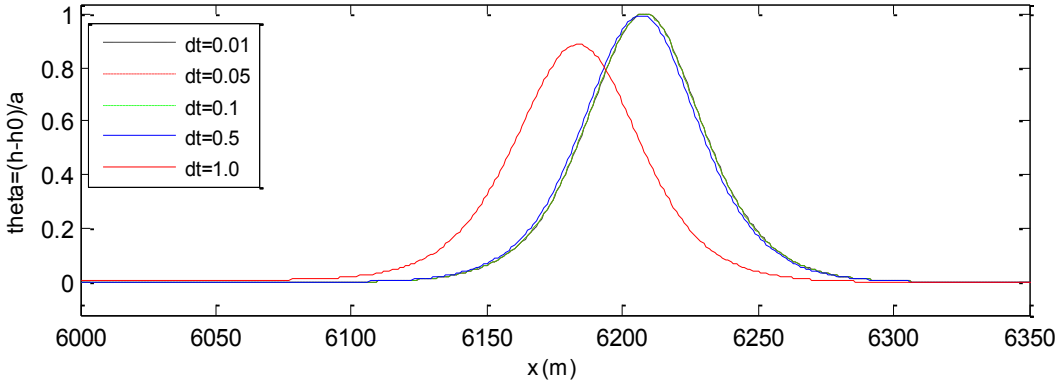

Figure 4.21: Solitary wave propagation over a flat-bed: predicted free surface elevation profiles at t= 480 s using fourth-order solver for i_{max}= 10001, Δt = 0.01, 0.05, 0.1, 0.5 and 1 s.

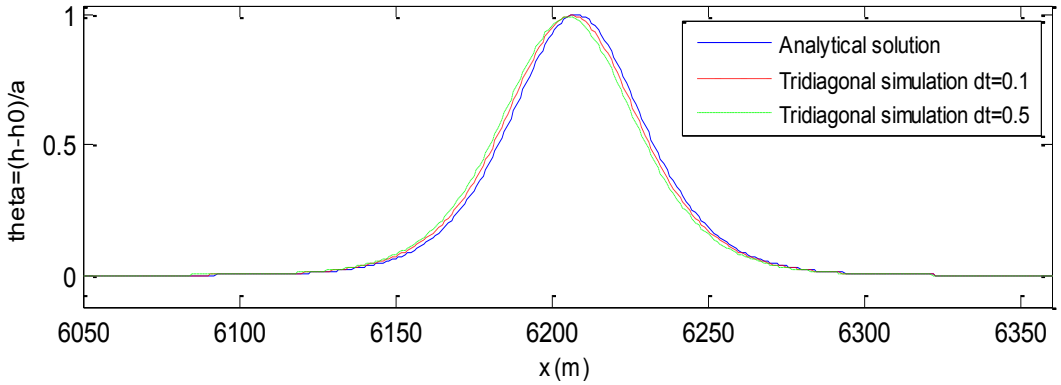

Figure 4.22: Solitary wave propagation over a flat-bed: predicted free surface elevation profiles at t = 480 s using linear analytical solution, second-order solver for i_{max} = 10001, Δt = 0.1 s, and second-order solver for i_{max} = 10001, Δt = 0.5 s.

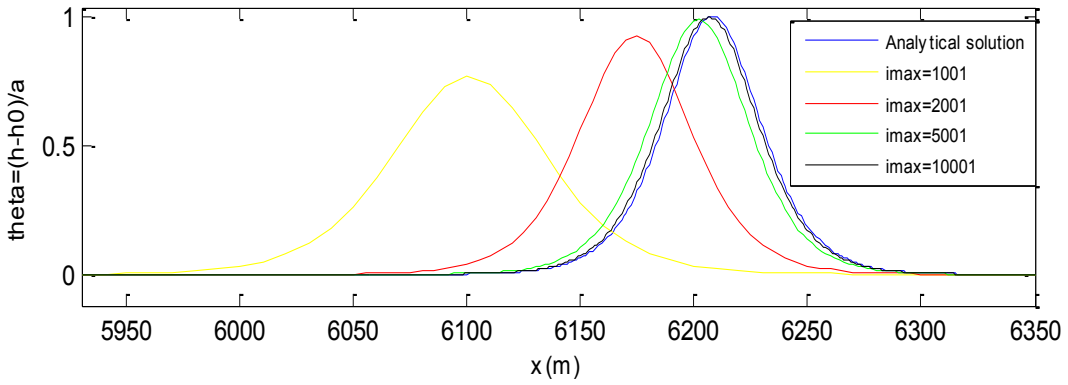

Figure 4.23: Solitary wave propagation over a flat-bed: predicted free surface elevation profiles at t = 480 s using linear analytical solution (blue solid line), second-order solver for i_{max} = 1001 (yellow), 2001 (red), 5001 (green), and 10001 (black), all with Δt = 0.1 s.

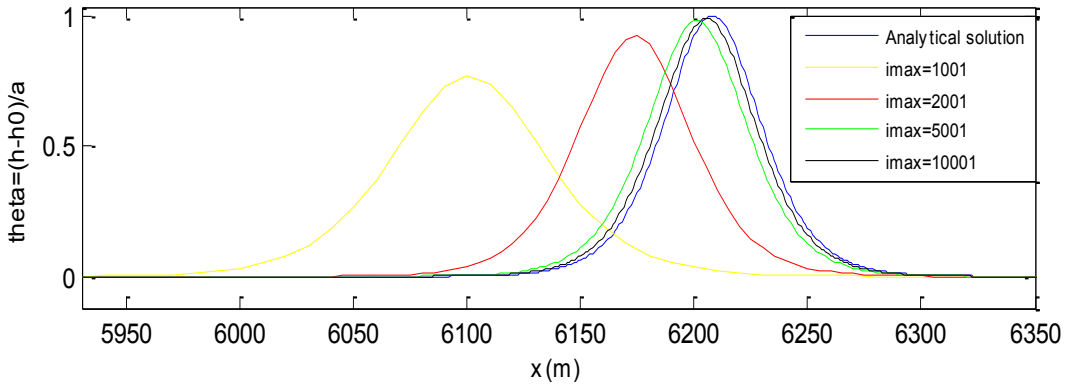

Figure 4.24: Solitary wave propagation over a flat-bed: predicted free surface elevation profiles at t = 480 s using linear analytical solution (blue solid line), second-order solver for i_{max} = 1001 (yellow), 2001 (red), 5001 (green), and 10001 (black), all with Δt = 0.5 s.

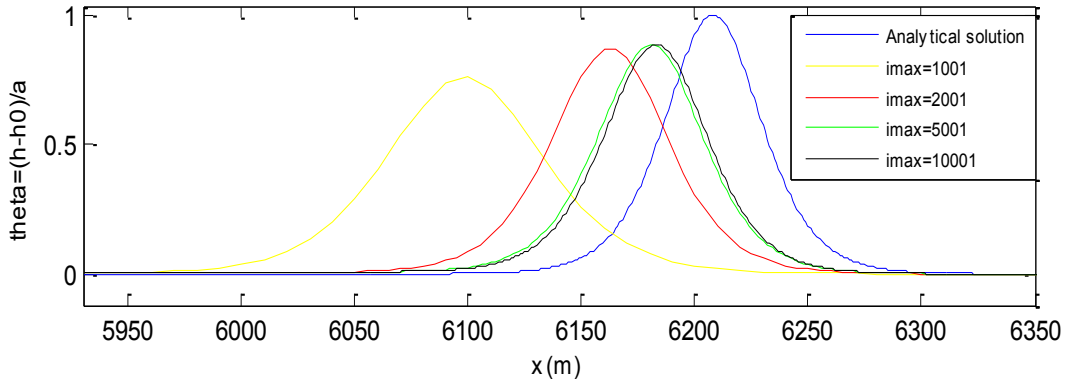

Figure 4.25: Solitary wave propagation over a flat-bed: predicted free surface elevation profiles at t = 480 s using linear analytical solution (blue solid line), second-order solver for i_{max} = 1001 (yellow), 2001 (red), 5001 (green), and 10001 (black), all with Δt = 1.0 s.

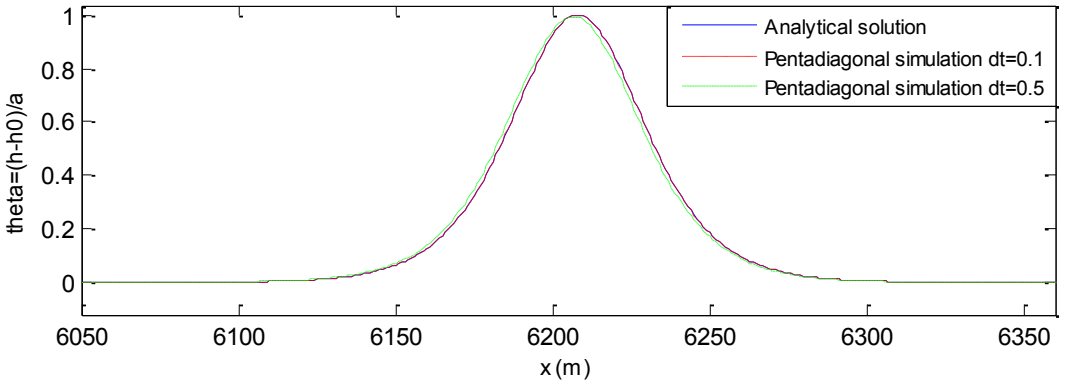

Figure 4.26: Solitary wave propagation over a flat-bed: predicted free surface elevation profiles at t = 480 s using linear analytical solution, fourth-order solver for i_{max} = 10001, Δt = 0.1 s, and fourth-order solver for i_{max} = 10001, Δt = 0.5 s.

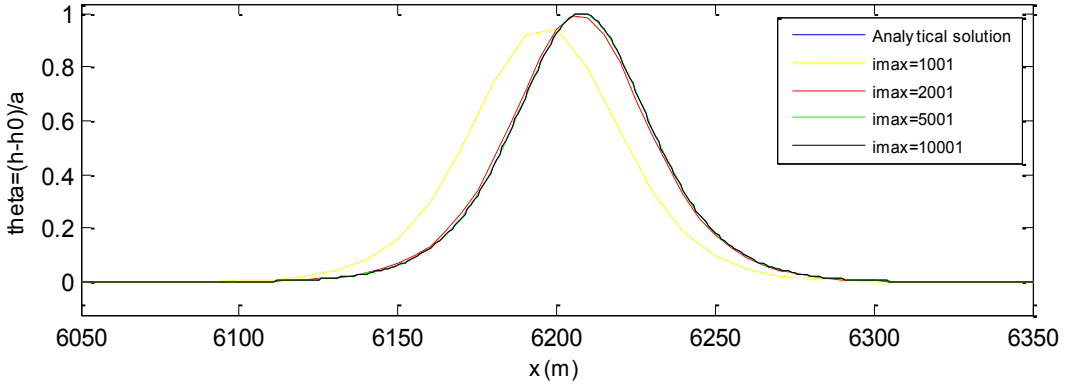

Figure 4.27: Solitary wave propagation over a flat-bed: predicted free surface elevation profiles at t = 480 s using linear analytical solution (blue solid line), fourth-order solver for i_{max} = 1001 (yellow), 2001 (red), 5001 (green), and 10001 (black), all with Δt = 0.1 s.

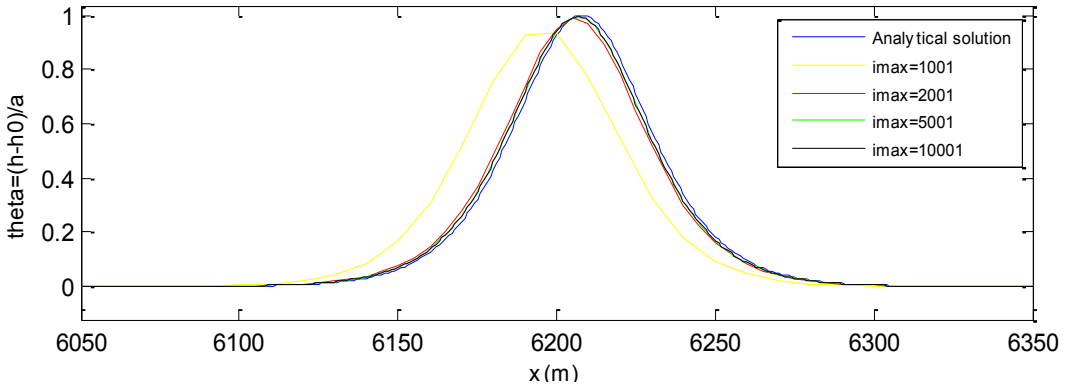

Figure 4.28: Solitary wave propagation over a flat-bed: predicted free surface elevation profiles at t = 480 s using linear analytical solution (blue solid line), fourth-order solver for i_{max} = 1001 (yellow), 2001 (red), 5001 (green), and 10001 (black), all with Δt = 0.5 s.

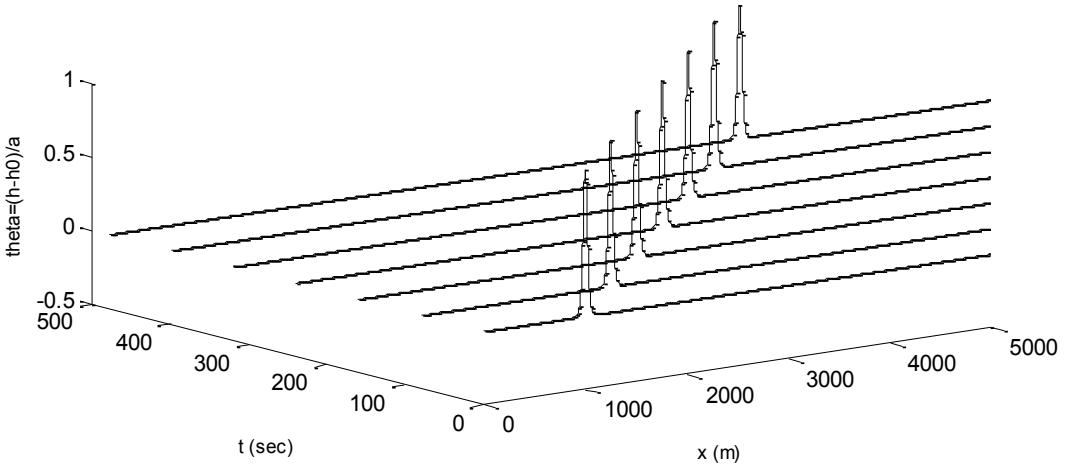

Figure 4.29: Solitary wave propagation: *x-t* plot of free surface profiles at t = 0, 80, 160, 240, 320,400, and 480 s predicted using the fourth-order solver for i_{max} = 10001, Δt = 0.5 s.

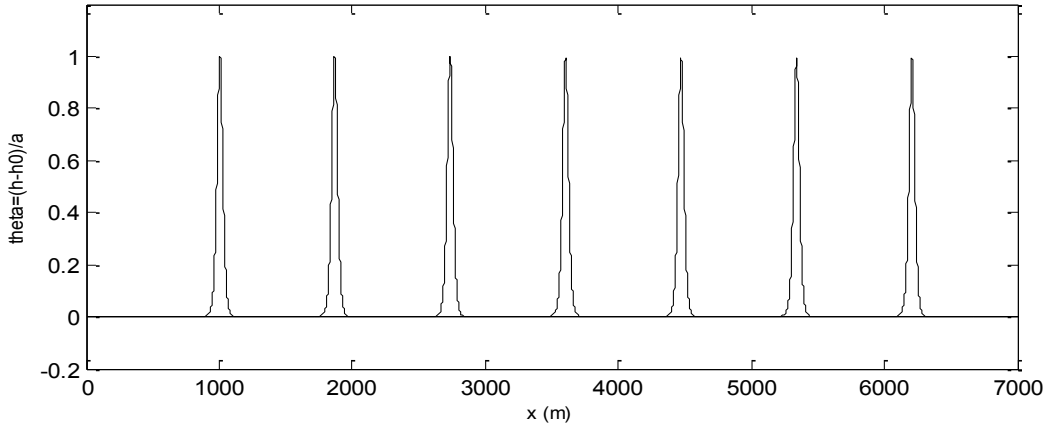

Figure 4.30: Solitary wave propagation over a flat-bed: free surface profiles at t = 0, 80, 160, 240, 320,400, and 480 s predicted using the fourth-order solver for i_{max} = 10001, Δt = 0.5 s.

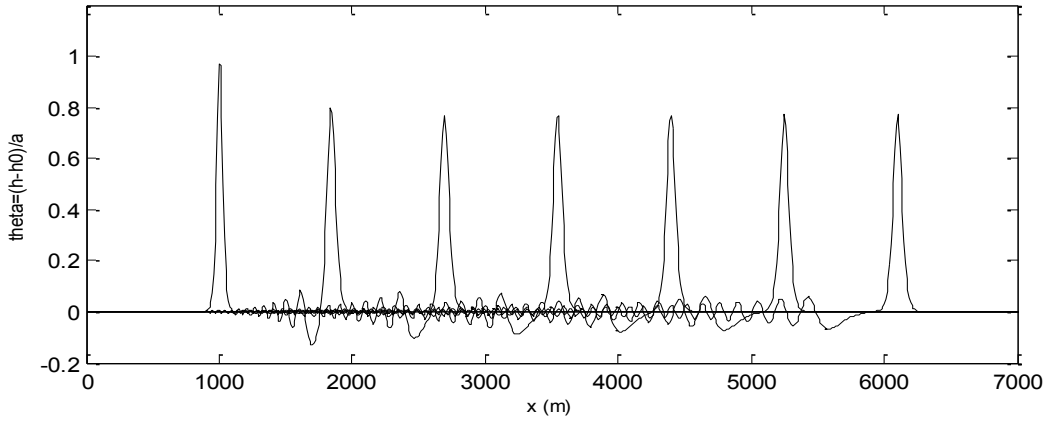

Figure 4.31: Solitary wave propagation over a flat-bed: free surface profiles at t = 0, 80, 160, 240, 320, 400, and 480 s predicted using the second-order solver for i_{max} = 1001, Δt = 0.5 s.

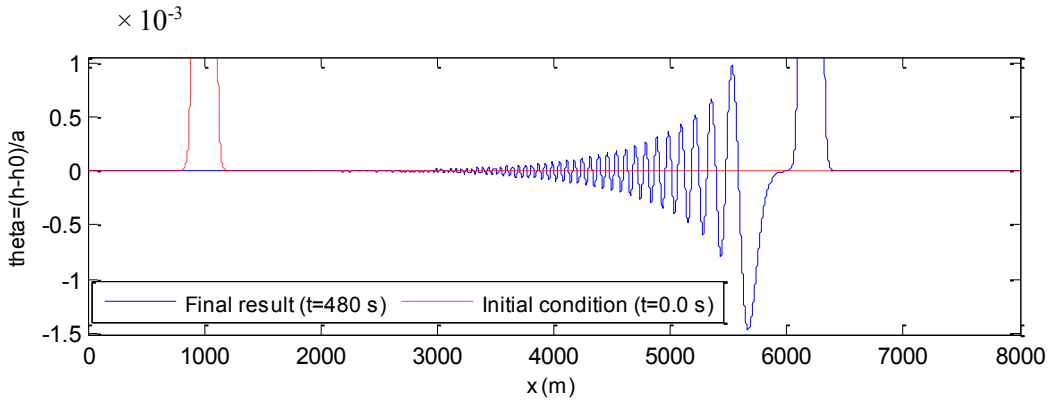

Figure 4.32: Trailing oscillatory waves behind the solitary wave at t = 480 s predicted using the second-order scheme: i_{max} = 10001, Δt = 0.01 s.

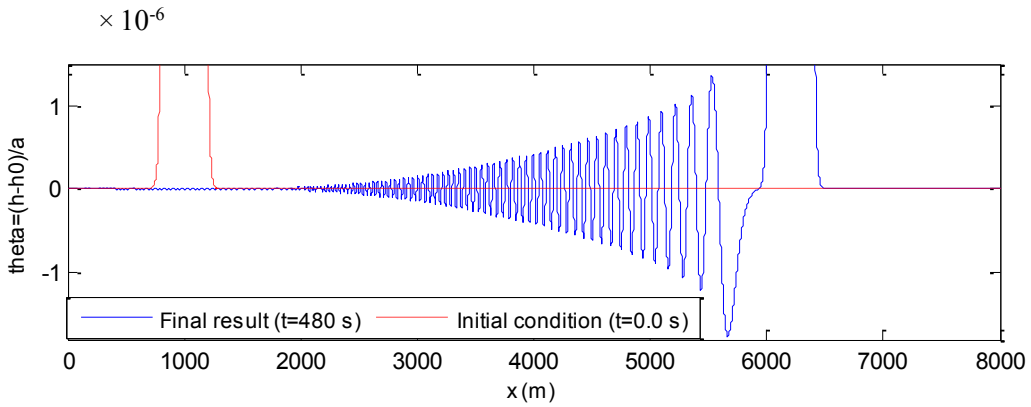

Figure 4.33: Trailing oscillatory waves behind the solitary wave at t = 480 s predicted using the fourth-order scheme: i_{max} = 10001, Δt = 0.01 s.

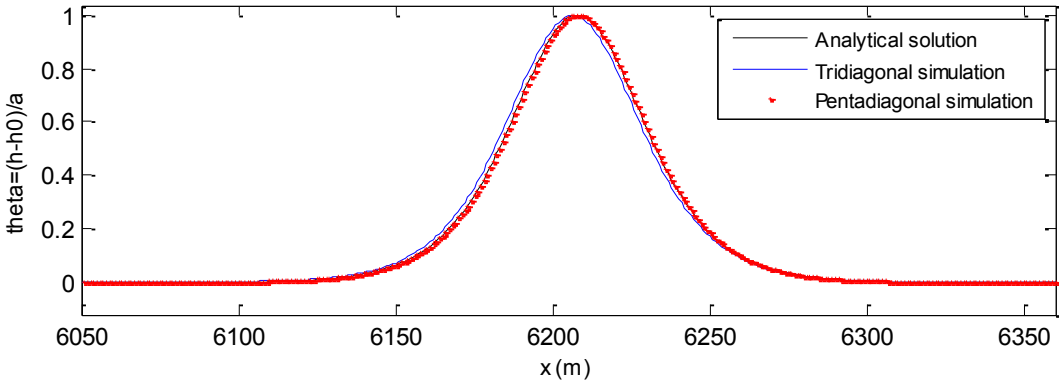

Figure 4.34: Solitary wave propagation over a flat-bed: predicted free surface elevation profiles at t = 480 s using linear analytical solution (black solid line), second-order solver for i_{max} = 10001, Δt = 0.1 s (blue solid line), and fourth-order solver for i_{max} = 10001, Δt = 0.1 s (cross symbols).

Chapter 5

2D Model Verification and Parameter Tests Simulation of Free Surface Sloshing of an Initial Gaussian Hump

5.1 Introduction

In this chapter, free surface sloshing of an initial Gaussian hump in wall-bounded basin are selected as benchmark test cases to validate the developed numerical schemes for 2D level I GN equations. Double Fourier series semi-analytical solutions for the evolution of the Gaussian hump are applied against numerical scheme simulations to indicate the capability of the developed 2D GN model in simulating nonlinear behaviour of waves. Reverse simulations of the Gaussian hump as well as the even and odd harmonics of forward simulations reveal the nonlinear behaviour of the developed 2D GN numerical model. Moreover, the Fast Fourier Transform (FFT) is applied for spectral analysis of Gaussian hump simulations.

5.2 Verification tests for numerical solver of 2D GN equations

5.2.1 Free surface sloshing of an initial Gaussian hump in a closed square, flat-bottomed basin

The 2-D numerical solver is first verified for nonlinear free surface sloshing motions arising from an initial Gaussian hump in a closed square, flat-bottomed basin (for which an analytical solution is available). The sloshing of free surface waves is commonly used as a verification test for numerical models, given that there is a well-established analytical solution to this problem (see e.g. Lamb 1879). Figure 5.1 depicts a square basin of plan dimensions, $0 \leq x \leq L_x$ and $0 \leq y \leq L_y$, which is bounded by solid walls at $x = L_x$ and, $y = L_y$. Figure 5.2 illustrates the computational mesh

plotted in physical domain. The basin contains water of still depth (in the absence of the hump), h_0, and an initial free surface profile above still water level given by $\zeta(x, y, t = 0)$. From the linearised shallow water equations we have:

$$\frac{\partial \zeta}{\partial t} + \frac{\partial (uh)}{\partial x} + \frac{\partial (vh)}{\partial y} = 0 \tag{5.1}$$

Here ζ is the free surface elevation above still water level, h is the total depth ($h = h_s + \zeta$), u is the horizontal velocity component in the x-direction, and v is the horizontal velocity component in the y-direction. Assuming $\ll h$, then we can approximate (5.1) by

$$\frac{\partial \zeta}{\partial t} + \frac{\partial (uh_s)}{\partial x} + \frac{\partial (vh_s)}{\partial y} = 0 \tag{5.2}$$

Considering the flat horizontal bed (i.e. uniform still water depth) then,

$$\frac{\partial \zeta}{\partial t} + h_s \left(\frac{\partial u}{\partial x} + \frac{\partial v}{\partial y} \right) = 0 \tag{5.3}$$

When the above equation is differentiated with respect to t:

$$\frac{\partial^2 \zeta}{\partial t^2} + h_s \left(\frac{\partial^2 u}{\partial x \partial t} + \frac{\partial^2 v}{\partial y \partial t} \right) = 0 \tag{5.4}$$

From the linearised momentum equation (without second order term), we have:

$$\frac{\partial u}{\partial t} = -g \frac{\partial \zeta}{\partial x} \quad \text{and} \quad \frac{\partial v}{\partial t} = -g \frac{\partial \zeta}{\partial y} \tag{5.5}$$

Hence, eliminating u and v from Eqn. (5.4),

$$\frac{\partial^2 \zeta}{\partial t^2} + c^2 \left(\frac{\partial^2 \zeta}{\partial x^2} + \frac{\partial^2 \zeta}{\partial y^2} \right) = 0 \tag{5.6}$$

where $c^2 = gh$. Letting $\zeta(x, y, z, t) = \eta(x, y)\, e^{i\omega t}$, then:

$$\begin{cases} \dfrac{\partial \zeta}{\partial x} = \dfrac{\partial \eta}{\partial x}\, e^{i\omega t} \implies \dfrac{\partial^2 \zeta}{\partial x^2} = \dfrac{\partial^2 \eta}{\partial x^2}\, e^{i\omega t} \quad , \quad \dfrac{\partial \zeta}{\partial y} = \dfrac{\partial \eta}{\partial y}\, e^{i\omega t} \implies \dfrac{\partial^2 \zeta}{\partial y^2} = \dfrac{\partial^2 \eta}{\partial y^2}\, e^{i\omega t} \\ \text{and} \quad \dfrac{\partial \zeta}{\partial t} = \eta\, i\omega e^{i\omega t} \implies \dfrac{\partial^2 \zeta}{\partial t^2} = -\omega^2 \eta\, e^{i\omega t} \end{cases} \tag{5.7}$$

By replacing the above parameters (5.7) in Eqn. (5.6) and then dividing both sides of Eqn. (5.6) by $e^{i\omega t}$ we obtain:

$$-\omega^2 \eta = c^2 \left(\frac{\partial^2 \eta}{\partial x^2} + \frac{\partial^2 \eta}{\partial y^2}\right) \quad \text{or} \quad \frac{\partial^2 \eta}{\partial x^2} + \frac{\partial^2 \eta}{\partial y^2} + \frac{\omega^2}{c^2}\eta = 0 \tag{5.8}$$

As a result, the basic equation that governs the behaviour of the hump is as follows:

$$\begin{cases} \left(\dfrac{\partial^2}{\partial x^2} + \dfrac{\partial^2}{\partial y^2} + k^2\right)\eta = 0 \\ \text{or} \\ (\nabla^2 + k^2)\,\eta = 0 \end{cases} \tag{5.9}$$

where $k = \frac{\omega}{c} = \frac{2\pi}{T}$.

To solve Eqn. (5.9), the following boundary conditions are taken into consideration (No flux condition at lateral walls):

$$\begin{cases} \dfrac{\partial \eta}{\partial x} = 0 \quad \text{at} \quad x = 0 \quad \text{and} \quad x = L_x \\ \dfrac{\partial \eta}{\partial y} = 0 \quad \text{at} \quad y = 0 \quad \text{and} \quad y = L_y \end{cases} \tag{5.10}$$

Separation of variables is applied to solve Eqn. (5.9), giving:

$$\eta_{mn}(x, y, t) = \sum_{m=0}^{k=\infty} \sum_{n=0}^{k=\infty} \tilde{\eta}_{mn}\, \bar{\eta}_{mn} \tag{5.11}$$

where

$$\bar{\eta}_{mn} = \left(\cos n\lambda x \;\; \cos m\lambda y \;\; e^{-i\omega t}\right) \tag{5.12}$$

and

$$\tilde{\eta}_{mn} = \frac{4}{(1+\sigma_{m0})(1+\sigma_{n0})L_x L_y} \int_{-L_x}^{L_x} \int_{-L_y}^{L_y} \eta_0(x, y) \cos(n\lambda x) \cos(m\lambda y) dx dy \tag{5.13}$$

Here λ is wavelength ($\lambda = \frac{\pi}{L_x} = \frac{\pi}{L_y}$), σ_{mn} is Kronecker's delta function of m and n (Kronecker's delta represents 1 if $m = n$ and 0 if $m \neq n$).

Each of the (m, n) modes has a corresponding natural frequency that is given by:

$$\omega^2{}_{mn} = gk_{mn}\ \tanh(k_{mn}h_0) \tag{5.14}$$

where h_0 is still water depth in the basin.

The wave numbers are given by:

$$k^2{}_{mn} = \left(\frac{\pi}{L_x}\right)^2 (m^2 + n^2) \tag{5.15}$$

The initial surface elevation is of a Gaussian shape $\eta_0(x, y)$ as follows:

$$\eta_0(x, y) = h_0 + a\exp\left\{-b\left[\left(x - \frac{L_x}{2}\right)^2 + \left(y - \frac{L_y}{2}\right)^2\right]\right\} \tag{5.16}$$

where a is the wave amplitude and b is spreading parameter.

Thus, the analytical solution for hump in the closed square basin is:

$$\eta(x, y, t) = \sum_{m=0}^{k=\infty}\sum_{n=0}^{k=\infty} \tilde{\eta}_{mn} e^{-i\omega t}\cos(n\lambda x)\ \cos(m\lambda y) \tag{5.17}$$

Consider a basin of 7.5 m length and 7.5 m width. The mean depth of the water without the hump, h_0 is 0.45 m. The initial amplitude of the hump a is 0.045 m and the spreading parameter in (5.16) is b = 2 m. The analytical solution is derived by first extending the domain using method of images in both x and y directions. Thus, a waveform is developed which is periodic over $2L_x$, $2L_y$ and even about any image of reflecting walls.

In order to obtain an accurate estimate of the analytical solution, different numbers of wave components (n and m) and integration points (i_m and j_m) are selected to solve the double Fourier series. Table (5.1) reveals that use of 51 components ($n = m = 51$) and 201 integration points ($i_m = j_m = 201$) is sufficient to obtain a converged solution. Application of higher numbers of integration points ($i_m = j_m = 401$ and 1001) does not have any significant effect on the estimates of the analytical solution (see figure 5.3 a). When a higher number of components ($n = m = 101$) is examined for $i_m = j_m = 401$ and 1001, similar results are again achieved (see figure 5.3 b). Therefore, 51 components ($n = m = 51$) and 201 integration points ($i_m = j_m = 201$) are selected for the remaining estimates of the analytical solution.

The second-order solver of the two-dimensional GN equations is applied at different times (t = 0, 0.05, 0.1, 015, 0.2, 0.25, …, 19 s) and animations of these simulations are presented in a video file as supplementary material. To determine which number of iterations are required for the numerical solver to obtain converged results, different values of r (number of iteration) are selected. Figure 5.4 compares the numerical model predictions with the analytical estimates of the water free surface in the basin 4 s after release of the hump. It is obvious that a r value of 4 is sufficient for the numerical predictions to be in complete agreement with the analytical result.

Furthermore, to identify how many grid points are required to produce an accurate simulation (using the second-order solver), a grid convergence test has been performed for different numbers of grid points. To this end, 3D plots and contour maps of the free surface elevation patterns in the basin obtained using the tridiagonal solver for fixed numbers of iteration r = 4 and 10 on increasingly grid points with i_{max} = $j_{\max}$ = 51, 201, and 1001 at t = 4.0 and 10.0 s are simulated. Figures 5.5 and 5.6 illustrate how the results converge at t = 4 s as the grid becomes finer for r = 4 and 10, respectively. It is evident that the medium grid i_{max} = $j_{\max}$ = 201 is sufficient to convergence. Figures 5.7 and 5.8, respectively, show the corresponding results at t = 10 s. Again, there is no difference between the free surface distributions for r = 4 and r = 10 iterations, and grid convergence is achieved for i_{max} = $j_{\max}$ = 201. Therefore, r = 4 and i_{max} = $j_{\max}$ = 201 are chosen for the rest of numerical simulations.

To compare the second-order numerical simulations with the analytical solutions, Figures 5.9 to 5.14 plot the water surface using 3D visualisations and contour maps at times t = 0, 1, 2, 4, 6, 8, 10, 12, and 14 s. As can be seen in Figures 5.9 and 5.10, there the numerical and analytical results at t = 0, 1 and 2 s are in excellent agreement. Figures 5.11 and 5.12, show the corresponding results at t = 4, 6 and 8 s. Discrepancies between the numerical and analytical simulations become evident at t = 6 and 8 s, and grow with simulation time as can be seen in Figures 5.13 and 5.14 at t=10, 12 and 14 s where phase differences can be observed. It is likely that these discrepancies are largely due to nonlinear (second- and higher-order) wave interactions which are modelled by the GN equations, but neglected in the analytical solution of the linearised shallow water equations.

Slosh motions evolve in the basin from the initial hump as it rapidly drops under its own weight, causing a deep trough at the centre of the basin with an associated circular wave front. The very initial free surface motions are remarkably similar to those generated by the collapse of a liquid column, as modelled by Toro (2001) amongst others, except that the central oscillations do not die away as quickly. The balance between potential and kinetic energy drives repeated up and down motions at the centre of the basin, driving circular waves that propagate radially away from the centre of the basin and reflect with the basin walls. The repeated reflections between the waves with each other and the walls promote increasingly complicated sloshing modes dominated by waves whose wavelength is half the length of the basin.

Figure 5.15 depicts the numerical free surface elevation time history for $r = 4$ at the centre of the basin for an initial Gaussian hump of amplitude $a = 0.045$ m obtained on grids of increasingly fine resolution ($i_{max} = j_{max} = 51$, 101, 201, 401 and 1001) and a fixed time step $\Delta t = 0.05$ s. This figure confirms that $i_{max} = j_{max} = 201$ is sufficient to obtain a converged solution of the 2D GN equations. Figure 5.16 shows the numerical free surface elevation time history for $r = 4$ iterations and $i_{max} = j_{max} = 201$ for different time steps (Δt = 0.05, 0.1 and 0.2 s), where it can be seen that Δt = 0.05 s is sufficient for accurate results.

Figure 5.17*a* and figure 5.17*b*, respectively, compare the numerical free surface elevation time history for $r = 4$ ($i_{max} = j_{max} = 201$) with the analytical solution ($n = m = 51$ and $i_m = j_m = 201$) at the centre and corner of the basin for a total simulation of 70 s after release of the hump. Excellent agreement exists between the numerical simulation and the analytical solution for the first 10 s after release of the elevation, after which differences are discernible between the numerical predictions and analytical solution, due in part to nonlinear wave interaction effects which are not described by the analytical theory.

5.2.2 Reverse simulations of free surface sloshing of an initial Gaussian hump

We now turn to the reversibility of the simulations. In order to carry out the reverse simulation, the Gaussian hump is released and the water surface propagated forward in time until a prescribed time is reached, after which the time step is made negative and the numerical scheme allowed to simulate the backward propagation of the water surface until time zero is again reached. The results should be in almost identical agreement, given that the problem is thermodynamically reversible. There is no viscosity present, no turbulence, no surface tension, and no sources of friction (e.g. from the basin walls or bed).

Figure 5.18 depicts the 3D plot and contour map when the simulation travelled 5 s, 10 s and 20 s forward then backward in time. The results are generally similar, with the shape of the original hump being largely recovered, though as the amount of time spent travelling forward and backward increases, there is an increasing amount of spurious error evident in the plots, particularly in the vicinity of the basin corners.

Figures 5.19 and 5.20 indicate effect of reversibility on free surface elevation time history simulations at two locations: the centre and corner of the basin. The total duration of the simulated time is 40 s, of which 20 s is forward in time (blue line) and 20 s is backward in time (red dots). It is evident that by travelling forward and backward in time, the accumulated dissipative error causes the recovered hump to experience loss of amplitude compared to its original value at $t = 0$ s. Increasing the number of iterations to $r = 10$ did not reduce the magnitude of this accumulated dissipative error.

5.2.3 Even and odd harmonics component of an initial Gaussian hump

A second group of simulations was undertaken in order to separate out the even and odd harmonics Gaussian hump. To achieve this, the harmonics are treated as orthogonal functions. Hence, the even harmonics are obtained additively from $\left(\frac{\xi_c+\xi_t}{2}\right)$ in which ξ_c refers to the free surface elevation time series of the initial Gaussian hump and ξ_t to the equivalent time series for the initial Gaussian trough. The odd harmonics are determined by subtraction from $\left(\frac{\xi_c-\xi_t}{2}\right)$. It is worth noting that the (linear) analytical solution is not capable to show the nonlinear behaviour of even harmonics.

Figure 5.21 (a) depicts the time history of even harmonic components of free surface elevation at the centre of basin for a small-amplitude initial hump/trough (*amp* = h_0/10 m). Figure 5.21 (b) shows the even harmonic free surface profiles along the basin at times t = 59, 60, 62 and 65 s. The deviations from zero in all the subplots of Figure 5.21 indicate that nonlinear effects are quite small in this case, which is to be expected given the small-amplitude of the initial disturbance.

Figure 5.22 depicts (a) the odd harmonic free surface elevation time history at the centre of the basin, and (b) odd harmonic profiles along the basin at different times t= 0, 0.65, 6.45 and 17.8 s for the initial small-amplitude disturbance (*amp* = h_0/10 m). The results are very similar to free surface motions of the linear solution.

Figure 5.23 shows the equivalent even harmonic results obtained for a larger-amplitude initial disturbance (*amp*=h_0/2 m). Now, the effect of nonlinearity is more evident, as can be seen by the wave motions in the even harmonics. The results for odd harmonics are very similar to those for the small-amplitude case, and so are not plotted here.

Figures 5.24 and 5.25 present 3D plots and contour maps of even harmonics, showing their evolution at different times (selected to coincide with the largest crests and troughs observed in figure 5.23 (a)). Figures 5.26 and 5.27 show the corresponding patterns obtained for the odd harmonics (again at times when the crests and troughs are largest in Figure 5.22 (a)).

5.2.4 Spectral analysis for sloshing of an initial Gaussian hump

To understand better the resonant free surface motions driven by an initial Gaussian disturbance in the square flat-bottomed basin, it is useful to carry out spectral analysis using a Fast Fourier Transform (FFT) of the free surface elevation component time series and spatial profiles. The FFT reveals the variance of the signal within a given frequency or wave number bandwidth. The area of the overall spectrum is therefore equal to the variance of the input signal in time or space (depending on which signal is selected). Peaks in the spectra indicate important frequencies and wavelengths where resonant behaviour may be occurring.

The fundamental frequencies can be determined from the free surface elevation time histories. Each FFT plot includes a series of magnitude peaks, each associated with a particular frequency. From the analytical solution for free surface sloshing in a closed square flat-bottomed basin, the mode corresponding to a given peak can be determined. Each mode (*m*, *n*) has a corresponding natural frequency.

$$k_{mn} = \sqrt{\left(\frac{\pi}{L_x}\right)^2 (m^2 + n^2)} \quad \text{and} \quad \omega_{mn} = \sqrt{g h_0}\, k_{mn} \tag{5.18}$$

The natural periods and frequencies are: $T_{mn} = \frac{2\pi}{\omega_{mn}}$ and $f_{mn} = \frac{1}{T_{mn}}$ (5.19)

Table 5.2 lists the resonant frequencies associated with different modes for the basin of interest (*n* and *m*). The frequency at the lowest fundamental mode is 0.140 Hz. The predicted frequency (0.571 Hz) obtained from free surface elevation time histories data coincides with the fundamental frequency at $m = 4$ and $n = 0$.

Figure 5.28 (a) shows the analytical predictions of the free surface elevation time histories of the initial hump at the centre of the basin where the initial amplitude $amp = h_0/2 = 0.225$ m. Figure 5.28 (b) is the corresponding FFT plot obtained from the analytical hump time series, and contains 7 significant peaks. The first peak at 0.273 Hz occurs at almost half the fundamental frequency at $m = 4$ and $n = 0$. Figure 5.29 (a) and figure 5.29 (b), respectively, reveal the numerically predicted free surface elevation time history and the FFT plot of the free surface motions at the centre of the

basin driven by the initial hump of amplitude $amp = h_0/2$ =0.225 m. In figure 5.29 (a) 5 major peaks are observable, the first four of which are similar to those in the analytical spectrum. The magnitudes of the first, second and fifth peaks of the analytical spectrum are less than the numerical ones; however, the magnitudes of the third and fourth peaks of the analytical spectrum are larger than the corresponding numerical peaks. Looking at Table 5.2, it can be seen that for both analytical and numerical results: the first peak occurs at mode $m = 2$ and $n = 0$; the second peak at mode $m = 2$ and $n = 2$, the third peak at mode $m = 3$ and $n = 2$; and the fourth peak at mode $m = 4$ and $n = 0$. The fifth peak of the numerical spectrum at mode $m = 5$ and $n = 1$, whereas that in the analytical spectrum occurs at mode $m = 4$ and $n = 3$. The sixth and seventh peaks in the analytical spectrum occur at mode $m = 5$ and $n = 2$, and mode $m = 5$ and $n = 3$, respectively.

Figure 5.30 shows the analytical free surface elevation time history and FFT spectrum for the initial troughs of amplitude $amp = h_0/2 = 0.225$ m. Figure 5.31 show the corresponding results obtained using the numerical model. The first four peaks in the analytical and numerically predicted trough spectra occur at almost the same frequencies. However, the first four peaks predicted numerically have lower magnitudes than the corresponding analytical peaks.

The effect of even harmonics is not visible in the analytical time series (Figure 5.32). Figure 5.33 reveals that for a relatively large amplitude hump ($amp = h_0/2 = 0.225$ m), it is possible to see evidence of the nonlinear effect produced by even harmonics. By comparing figures 5.33 (b) with 5.29 (b), it can be seen that all five peaks of numerical even harmonics occur at the same frequency, regardless of whether the initial free surface profile is a hump or a trough.

Figures 5.34 depict the analytically predicted free surface elevation time histories of the odd harmonics and the FFT plot of the odd harmonic components. Moreover, Figure 5.35 presents the numerically predicted free surface elevation time history and FFT spectrum of the numerical odd harmonic. Like the trough simulations, the first four spectral peaks of the numerical and analytical odd harmonics occur at the same frequencies, with the magnitudes of the peaks being lower in the numerical spectrum.

To understand whether FFT simulations are produced correctly or not, the area under the spectrum is calculated and the result compared with variance of the mean-zero series. The mean of the series is given by $\bar{\xi} = \frac{1}{N}\sum_{i=1}^{N} \xi$ and so the mean-zero series becomes $\hat{\xi} = \xi - \bar{\xi}$. where $\xi = \frac{h-h_0}{amp}$ (h is the elevation of water, h_0 is the still water depth and amp is the amplitude). The variance is given by $\sigma_\eta^2 = \frac{1}{N-1}\sum_{i=1}^{N} \hat{\xi}^2$. It is obvious from Table 5.3 that there is no significant difference between the calculated variance and the value of the area under FFT plots.

5.2.5 Comparison between second-order and fourth-order simulations of free surface sloshing of an initial Gaussian hump in a square, flat-bottomed basin

A series of test cases are performed to compare results from the second-order tridiagonal matrix solver scheme with those produced by the fourth-order pentadiagonal solver. Again, a closed basin of 7.5 m length and 7.5 m width is considered. The mean depth of the water without the hump, h_0 is 0.45 m. The initial amplitude of the hump a is 0.045 m and the spreading parameter is b = 2 m. The number of grid points is given by $i_{max} = j_{\max} = 201$, and the time step Δt = 0.05 s.

Figures 5.36 and 5.37 present 3D plots and contour maps of the sloshing motions driven by the initial Gaussian hump at different times, showing that there are no significant differences between the results obtained using the two numerical schemes over the duration of the simulations. Figure 5.38 shows the excellent agreement in the free surface elevation time histories at the centre of the basin as predicted by the second-order and fourth-order scheme. This confirms that the use of a second-order difference scheme is acceptable.

5.3 Parameter tests for sloshing in a basin with non-uniform bathymetry

Simulations are now considered of the sloshing behaviour of an initial Gaussian hump of water released in a basin with non-uniform bathymetry. Figure 5.39 presents parameters which govern the Gaussian hump. Here, the bed elevation above a fixed horizontal datum is given by

$$z_b(x,y) = z_{b_0} + a_{z_b} \exp\left\{-b_{z_b}\left[\left(x-\frac{L_x}{2}\right)^2 + \left(y-\frac{L_y}{2}\right)^2\right]\right\} \qquad (5.20)$$

where a_{z_b} is the bed amplitude, b_{z_b} = 2 m is a bed spreading parameter and z_{b_0}=2 m. The initial local water depth is:

$$h(x,y) = h_0 - a_{z_b} \exp\left\{-b_{z_b}\left[\left(x-\frac{L_x}{2}\right)^2 + \left(y-\frac{L_y}{2}\right)^2\right]\right\}$$
$$+a \exp\left\{-b\left[\left(x-\frac{L_x}{2}\right)^2 + \left(y-\frac{L_y}{2}\right)^2\right]\right\} \qquad (5.21)$$

where h_0 = 0.45 m, a is the amplitude of the initial Gaussian hump in free surface elevation, and b = 2 m is a measure of its spread.

Figure 5.40 depicts 3D visualisations and contour maps of the water surface at times t = 2, 4, 6, 8, 10 and 12 s for relatively small value of bed amplitude (a_{z_b} = 0.015 m) and large value of Gaussian hump amplitude (a = 0.225 m). Figure 5.41 shows 3D visualisations and contour maps of the water surface at times t = 2, 4, 6, 8, 10 and 12s for relatively large values of bed amplitude (a_{z_b} = 0.225 m) and Gaussian hump amplitude (a = 0.225 m). The effect of the bed hump on the evolution of the water free surface is most obvious at the centre of the basin exactly where the bed hump has its peak. The large values of bed amplitude (a_{z_b} = 0.225 m) exerts more effect on each simulation.

At first the Gaussian free surface hump drops rapidly to form a trough at the centre of the basin, releasing a circular ring-like wave that propagates towards the basin walls, where reflections occur. The plunging free surface at the centre of the

basin interacts with the bed hump, leading to the recovery of a second clapotis-like hump which peaks and releases a second circular wave. After several cycles of central peaks and troughs, the water surface motions immediately above the hump degenerate into a patch of small waves that heave up and down over the hump (after $t \sim 10$ s); elsewhere the sloshing behaviour is similar to that of the corresponding case without a bed hump, particularly the presence of sloshing components whose wavelength is half the length of the basin.

The following test case concerns the time-dependent motions of an initial Gaussian free surface hump in a basin containing a bed trough at its centre (mirroring the bed hump that has just been considered). Relatively large bed trough amplitude ($a_{z_b} = -0.225$ m, the negative sign denoting a trough) and initial Gaussian hump amplitude ($a = 0.225$ m) are selected. Figure 5.42 depicts 3D visualisations and contour maps of the evolution of the water surface at times $t = 2$, 4, 6, 8, 10 and 12 s.

In a similar manner to the case involving a bed hump in the basin, the presence of the bed trough has greatest effect at the centre of the basin, coincident with the peak position of the initial Gaussian free surface hump. In this case, the water free surface at the centre of the basin is able to fall further before interacting with the bed; localised sloshing of circular waves develops above the bed trough; again the slosh behaviour away from the basin centre is again similar to that in the corresponding basin with a flat bed, with modes at half basin wave length dominating.

The third test case in this section considers the effect of a bed hump located at the south-west corner of basin. Figure 5.43 shows contour maps at times $t = 6$, 8, 10 and 12 s for $a_{z_b} = a = 0.225$ m.

Figure 5.44 compares the numerically predicted free surface elevation time history of an initial Gaussian hump in closed square basin with flat-bottomed and centred bed hump bottomed for a total simulation of 70 s after release of an initial Gaussian hump. Difference between two simulations becomes more evident especially 18 s after releasing the Gaussian hump.

5.4 Parameter tests for sloshing in a rectangular, flat-bottomed basin

The final case considered involves a channel of 15 m length and 7.5 m width in which the mean depth of the water without the hump, h_0 is 0.45 m. Figure 5.45 shows snapshots of the water surface motions using 3D visualisations and contour maps at times t = 4, 6, 8, 10, 12 and 14 s. In this case, the north and south extremes of the initial Gaussian hump are much closer to the walls than the east and west extremes. After the first radial wave is released, it undergoes reflection by the north and south walls before the east and west. After reflection, the combined radial and reflected waves form pairs of humps at the south and north walls that travel in opposite east and west directions along walls. Meanwhile the east and west fronts of the initial radial wave straighten up and to become aligned with the east and west walls by the time they are reached. By t = 4 s, the second and third radial waves have been released, as can be discerned by the ring-like patterns discernible in Figure 5.45(a). A pattern of reflected and re-reflected waves develops progressively dominated by longitudinal and transverse sloshing modes, as can be seen in Figures 5.45(d), (e) and (f).

5.5 Summery

- In this chapter, 2D GN numerical model was verified for nonlinear free surface sloshing motions arising from an initial Gaussian hump in a closed basin. Numerical simulations of initial Gaussian hump were compared with Fourier series semi-analytical solutions of the linearised shallow water equations. Excellent agreement was achieved between the numerical simulation and the analytical solution of the overall free surface patterns in the basin during the first four seconds after the initial release of the hump, after which discrepancies became discernible, in part due to nonlinear wave interaction effects which were not described by the analytical theory. Satisfactory agreement between the numerical and semi-analytical solutions of free surface elevation was achieved for about 10 s at the centre of the basin.

- A reversibility check of the developed numerical code indicated that the reversed hump returned almost to exactly the same shape as the original Gaussian hump, although as the amount of time spent travelling forward and backward lengthened, spurious error tended to accumulate in the vicinity of the basin corners. There was some loss of amplitude at the centre of the basin when the hump was reversed.

- The even and odd harmonics of the initial Gaussian profile were separated from initial crest and trough simulations, with the profiles treated as orthogonal functions. For a small-amplitude initial hump or trough ($amp=h_0/10=0.045$ m) the negligible deviations from zero in the free surface motions of even harmonics indicated that nonlinear effects were quite small. In the equivalent even harmonic results obtained for a larger-amplitude initial disturbance ($amp = h_0/2 = 0.225$ m), it was possible to see evidence of the nonlinearity.

- To understand better the resonant free surface motions driven by an initial Gaussian disturbance in the square basin, an FFT of the free surface elevation component time series was carried out.

- Parameter tests for sloshing of an initial Gaussian hump were carried out in a basin with non-uniform bathymetry with bed humps at the centre of the basin. The deformation in the water free surface Gaussian shapes became more obvious at the centre exactly where the bed hump was located.

Table 5.1: $h - h_0$ (m) at the centre of the basin at $t = 0\ s$

$i_{max}= j_{max}$ / $n=m$	51	101	201	401	1001
51	0.00125	0.08682	0.04500	0.04500	0.04500
101	0.00125	0.36136	0.01679	0.04500	0.04500

Table 5.2: Analytical values of fundamental frequency (Hz) for different modes

n / m	1	2	3	4	5	6	7	8
0	0.140	0.280	0.420	0.560	0. 700	0.840	0.980	1.120
1	0.198	0.313	0.442	0.577	0.714	0.851	0.990	1.129
2	0.313	0.396	0.505	0.626	0.754	0.885	1.019	1.155
3	0.442	0.505	0.594	0.700	0.816	0.939	1.066	1.196
4	0.577	0.626	0.700	0.792	0.896	1.010	1.129	1.252
5	0.714	0.754	0.816	0.896	0.990	1.093	1.204	1.165
6	0.851	0.885	0.939	0.891	1.093	1.188	1.291	1.140
7	0.990	1.019	0.941	1.129	1.204	1.291	1.386	1.488
8	1.129	1.155	1.196	1.252	1.321	1.400	1.488	1.584

Table 5.3: Comparison of calculated variance with the area under the FFT spectrum for initial hump of amplitude = $h_0/2$ = 0.225 m

		σ_η^2	Area under FFt's plots
Analytical solution (amp = $h_0/2$ m)	Crest	19.074	17.639
	Troughs	19.074	17.639
	Odd harmonic	19.074	17.639
Numerical solver (amp = $h_0/2$ m)	Crest	14.198	13.931
	Troughs	13.461	14.838
	Even harmonic	3.107	7.040
	Odd harmonic	10.722	12.603

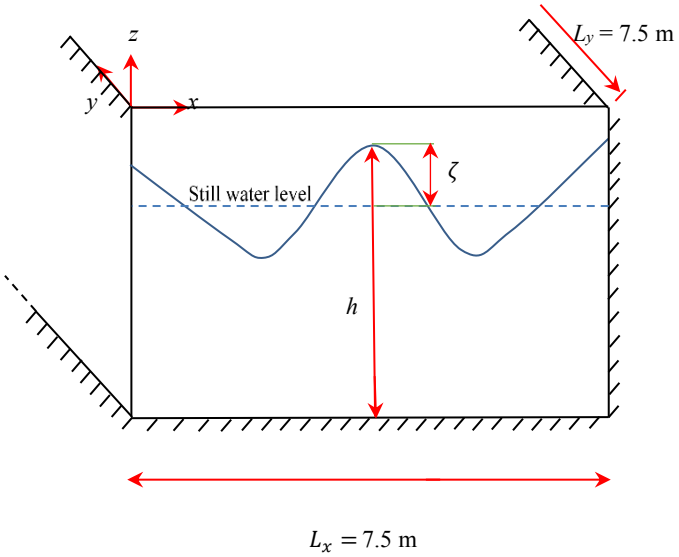

Figure 5.1: A sketch of square basin

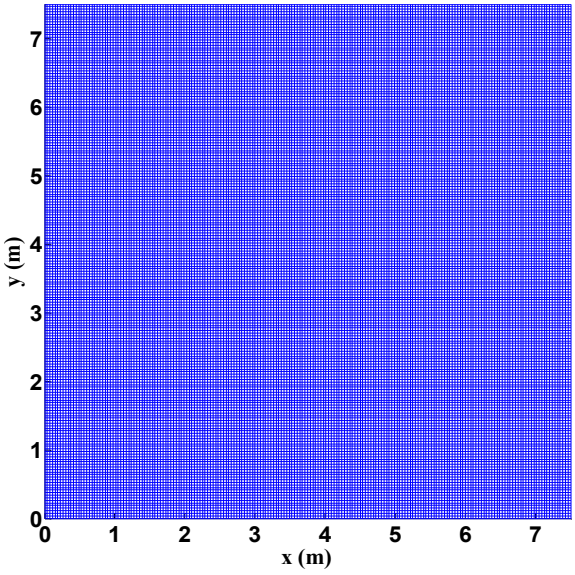

Figure 5.2: Square basin: computational mesh plotted in physical domain

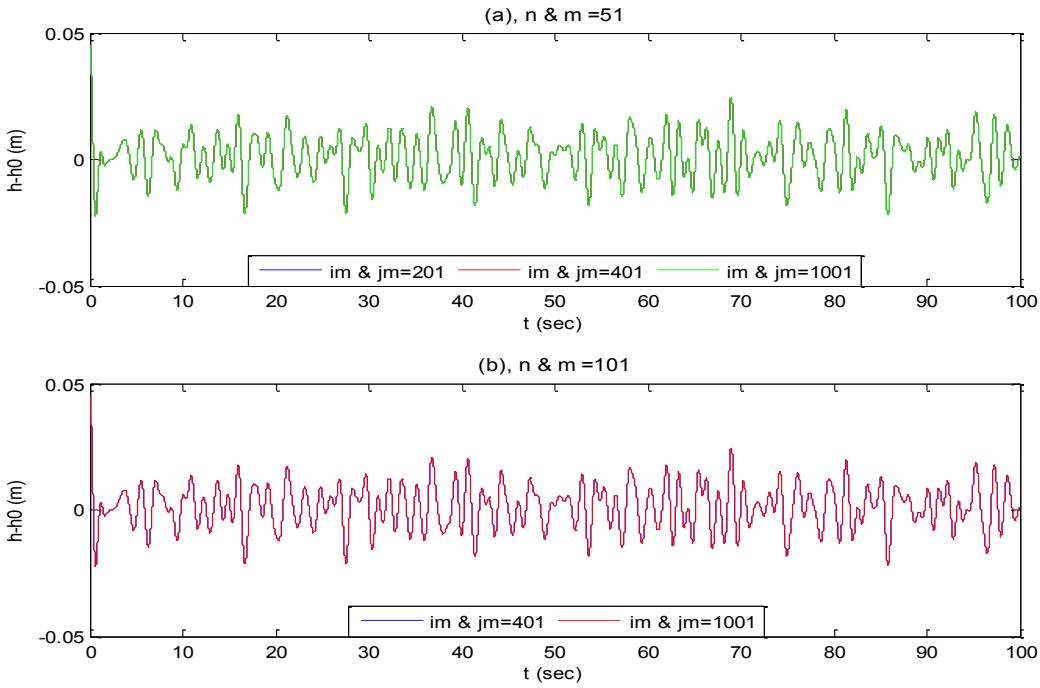

Figure 5.3: Convergence test for analytical solution of different numbers of integration points (i_m, j_m) and numbers of wave components (a) $n = m = 51$; (b) $n = m = 101$.

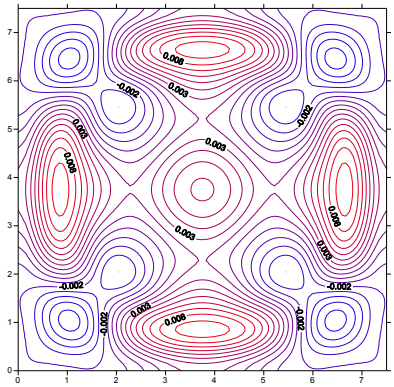

Contours of the analytical solution at $t = 4$ s ($n = m = 51$ and i_m , $j_m = 201$)

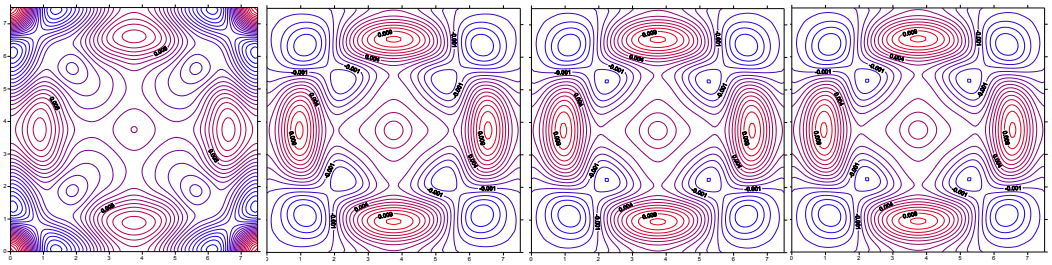

$r = 1$ $r = 2$ $r = 4$ $r = 10$

Figure 5.4: The effect on convergence of number of iterations r for numerical solver on a constant grid of $i_{max} = j_{max} = 201$ at $t = 4$ s.

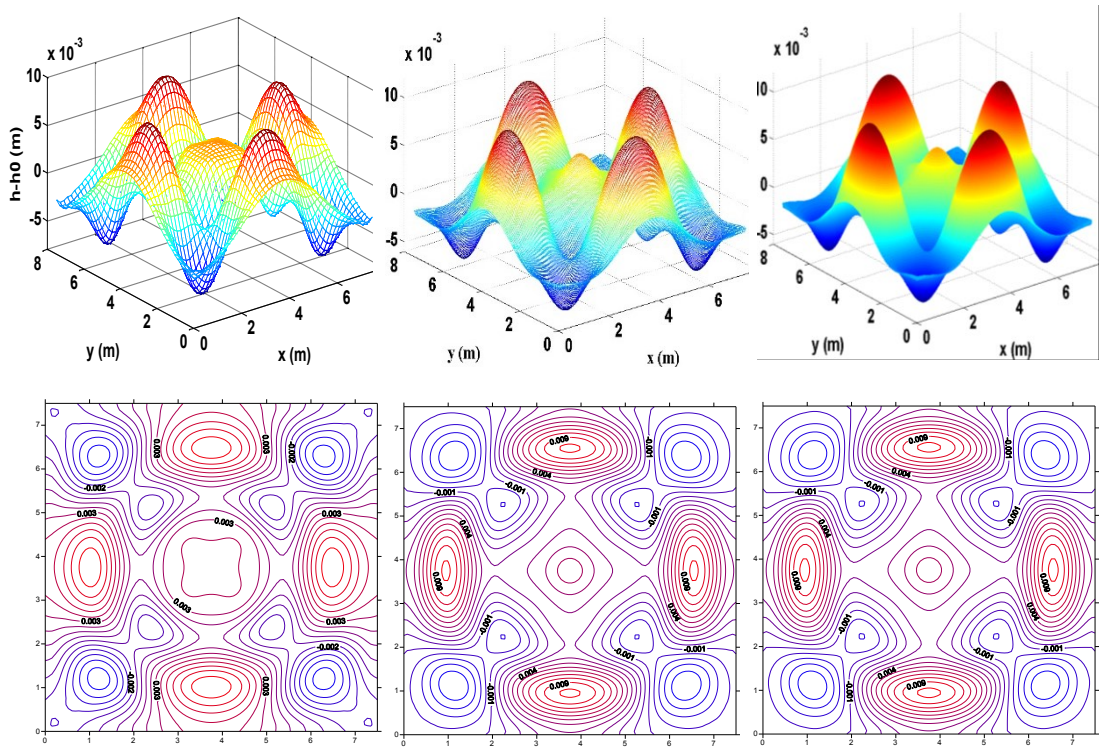

Figure 5.5: Grid convergence results for Gaussian hump in a square, flat-bottomed basin for $r = 4$ at $t = 4$ s: (a) $i_{max} = j_{max} = 51$; (b) $i_{max} = j_{max} = 201$; (c) $i_{max} = j_{max} = 1001$.

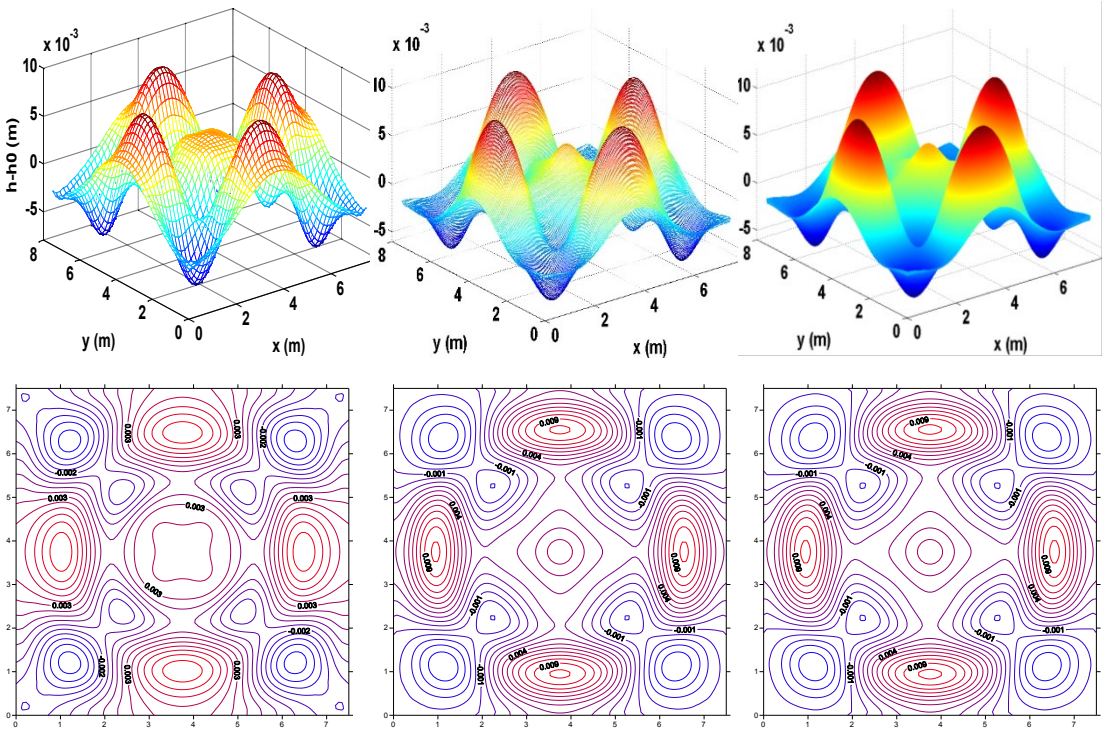

Figure 5.6: Grid convergence results for Gaussian hump in a square, flat-bottomed basin for $r = 10$ at $t = 4$ s: (a) $i_{max} = j_{max} = 51$; (b) $i_{max} = j_{max} = 201$; (c) $i_{max} = j_{max} = 1001$.

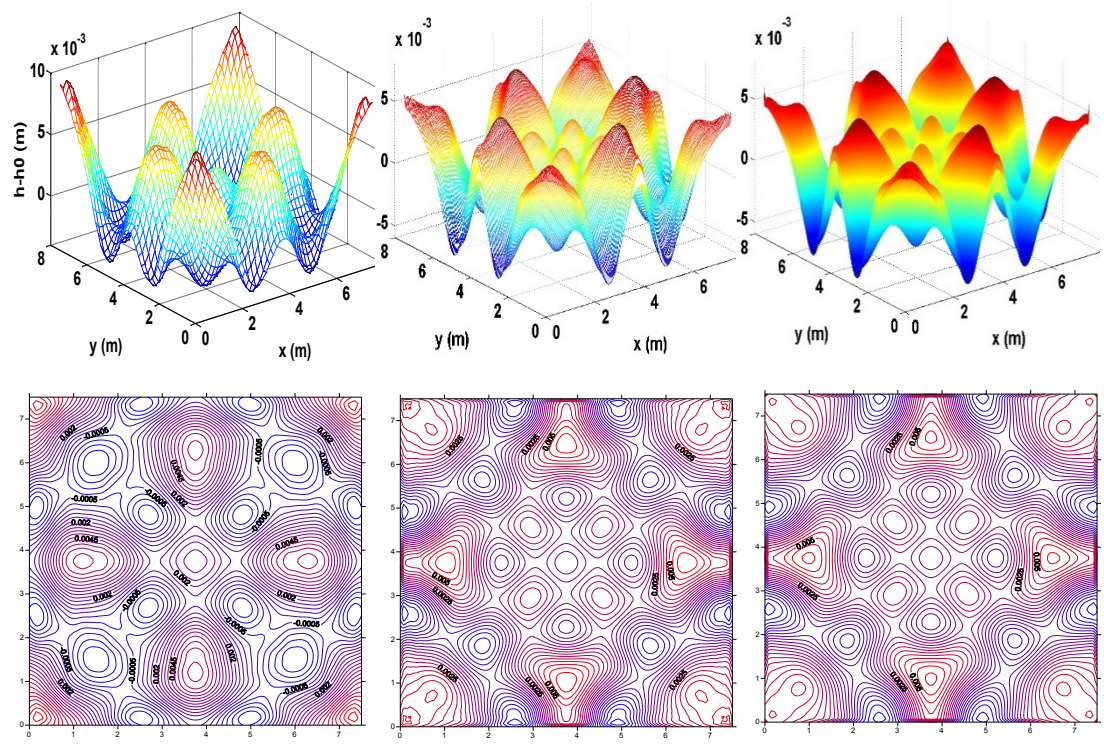

Figure 5.7: Grid convergence results for Gaussian hump in a square, flat-bottomed basin for $r = 4$ at $t = 10$ s: (a) $i_{max} = j_{max} = 51$; (b) $i_{max} = j_{max} = 201$; (c) $i_{max} = j_{max} = 1001$.

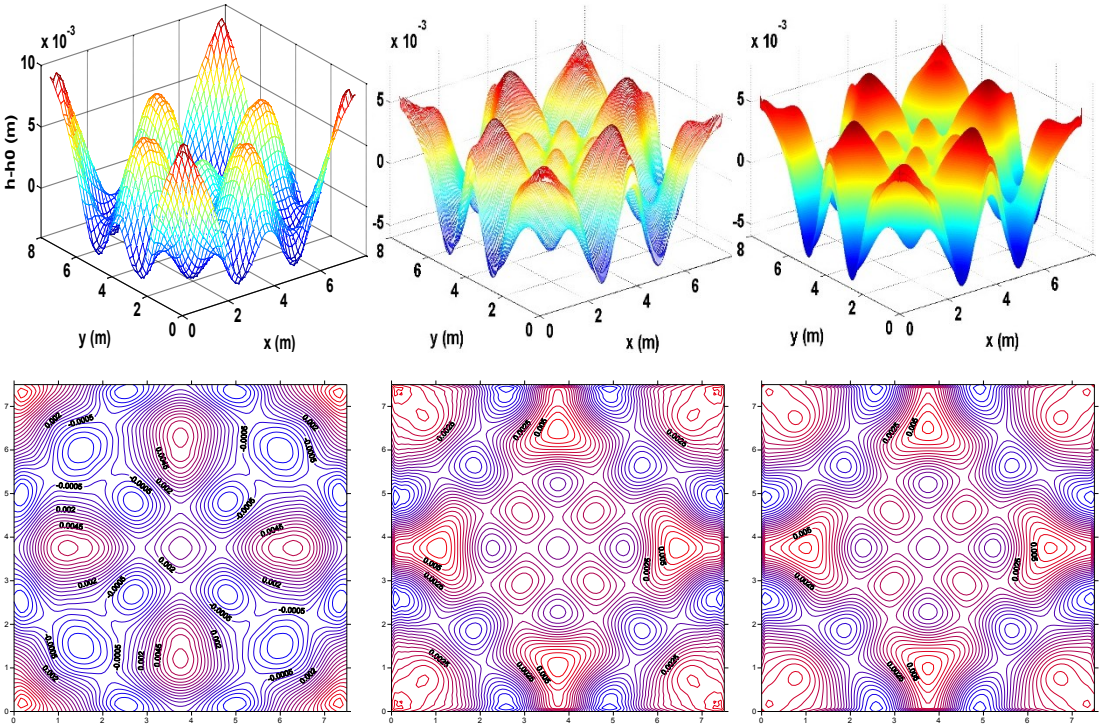

Fig 5.8: Grid convergence results for Gaussian hump in a square, flat-bottomed basin for $r = 10$ at $t = 10$ s: (a) $i_{max} = j_{max} = 51$; (b) $i_{max} = j_{max} = 201$; (c) $i_{max} = j_{max} = 1001$.

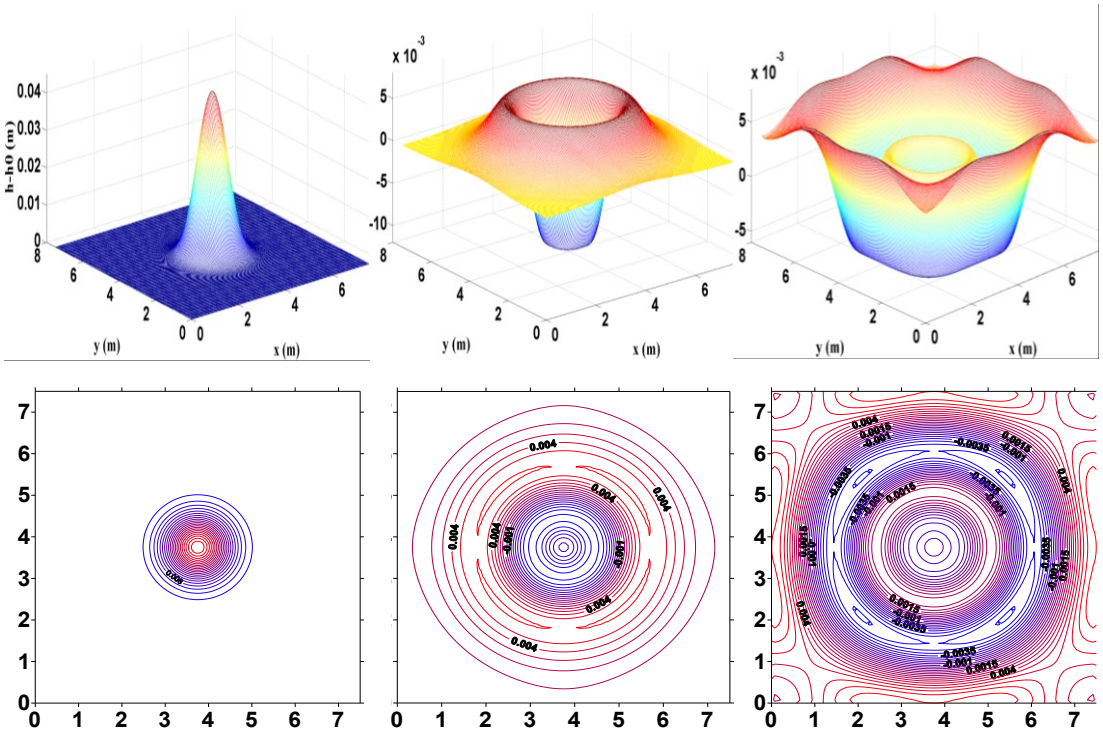

Figure 5.9: Numerical simulations of Gaussian hump sloshing in a square, flat basin for $r = 4$ and $i_{max} = j_{max} = 201$: 3D plots and contour maps at (a) $t = 0$ s, (b) $t = 1$ s; and (c) $t = 2$ s.

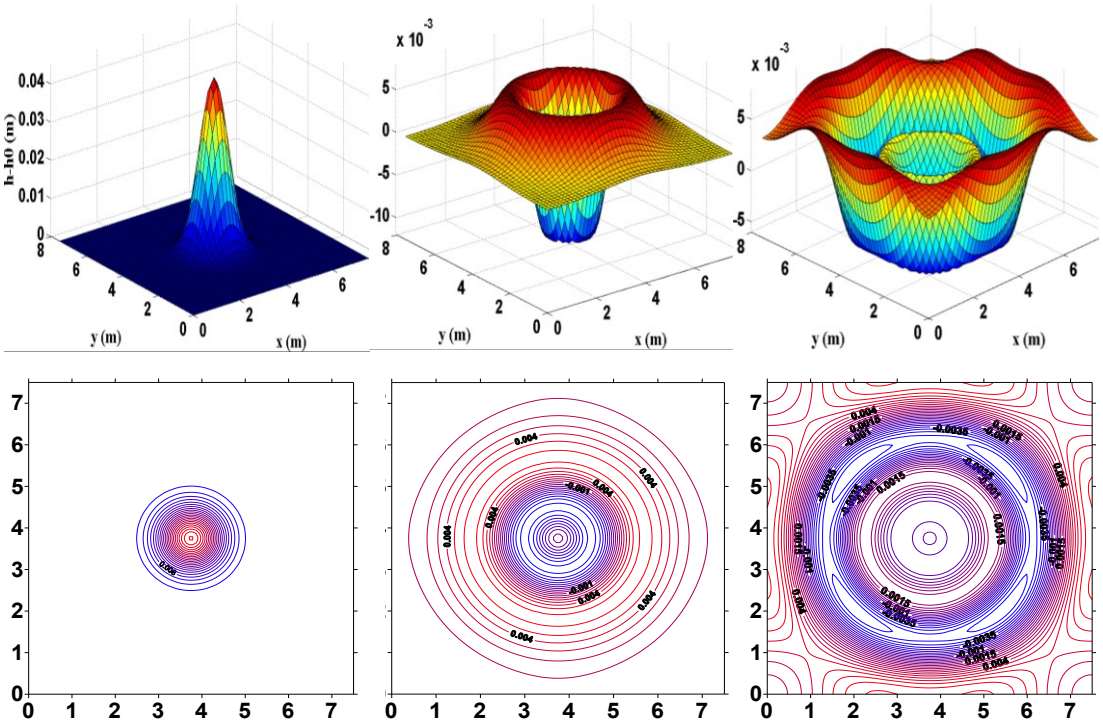

Figure 5.10: Analytical solution of Gaussian hump sloshing in a square, flat basin: 3D plots and contour maps at (a) $t = 0$ s, (b) $t = 1$ s; and (c) $t = 2$ s.

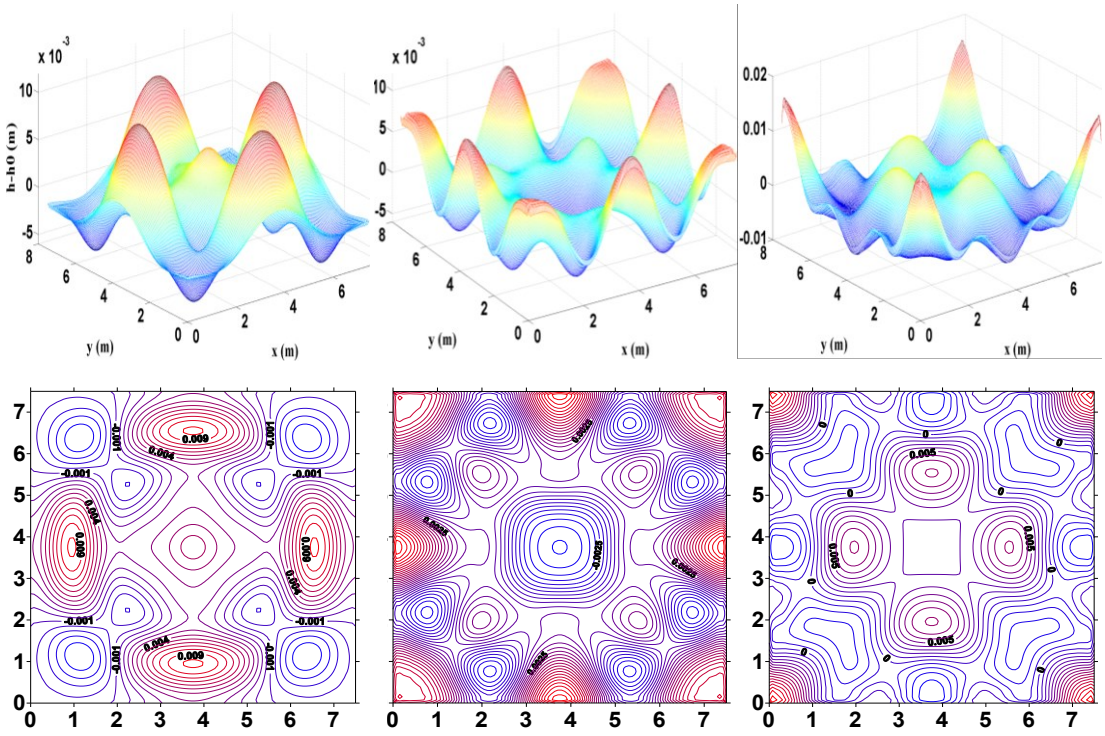

Figure 5.11: Numerical simulations of Gaussian hump sloshing in a square, flat basin for $r = 4$ and $i_{max} = j_{max} = 201$: 3D plots and contour maps at (a) $t = 4$ s, (b) $t = 6$ s; and (c) $t = 8$ s.

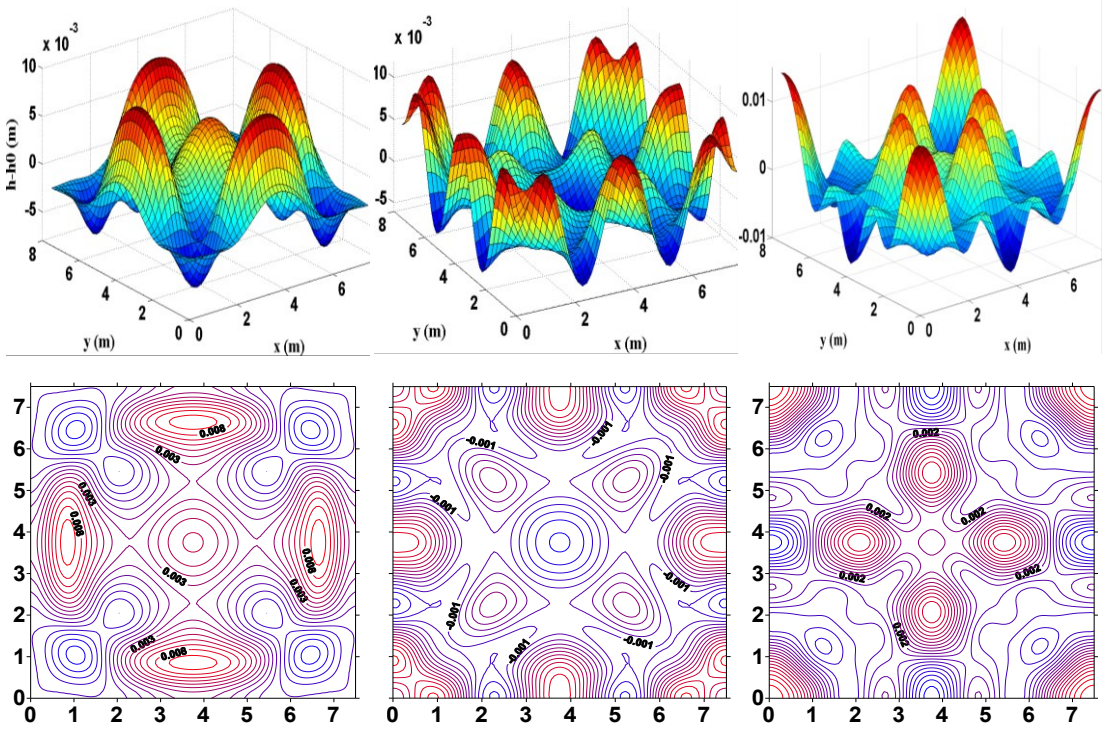

Figure 5.12: Analytical solution of Gaussian hump sloshing in a square, flat-bottomed basin: 3D plots and contour maps at (a) $t = 4$ s, (b) $t = 6$ s; and (c) $t = 8$ s.

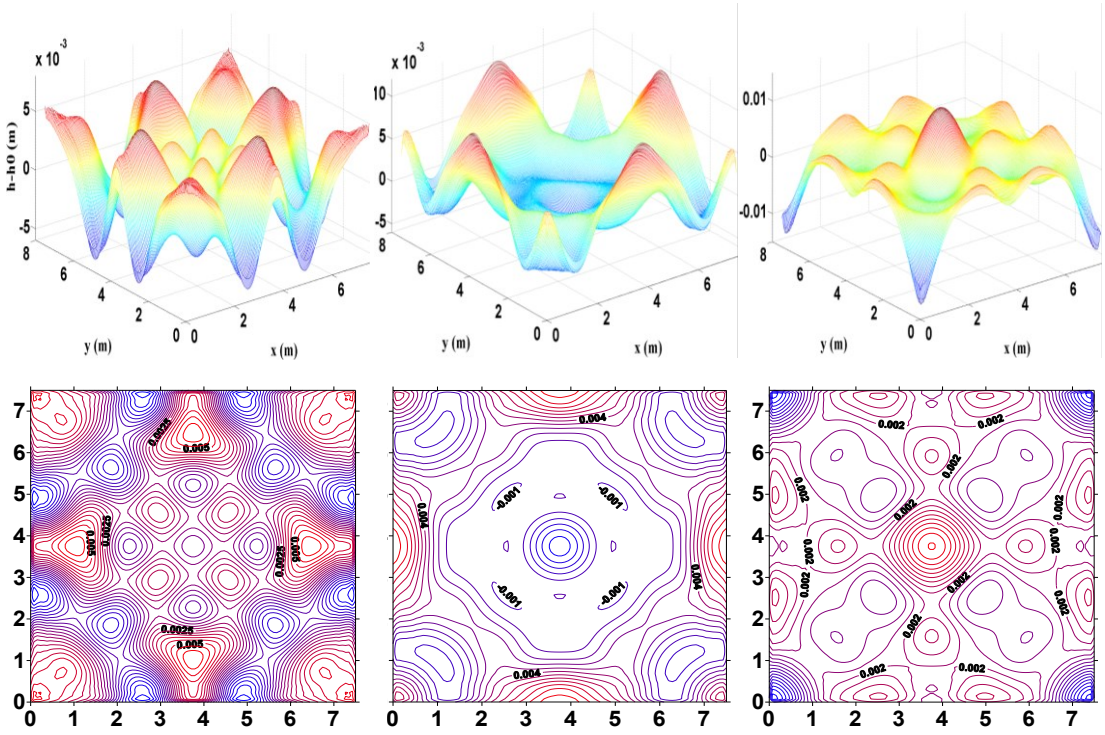

Figure 5.13: Numerical simulations of Gaussian hump sloshing in a square, flat basin for r= 4 and i_{max}= j_{max}= 201: 3D plots and contour maps at (a) t= 10 s, (b) t= 12 s; and (c) t= 14 s.

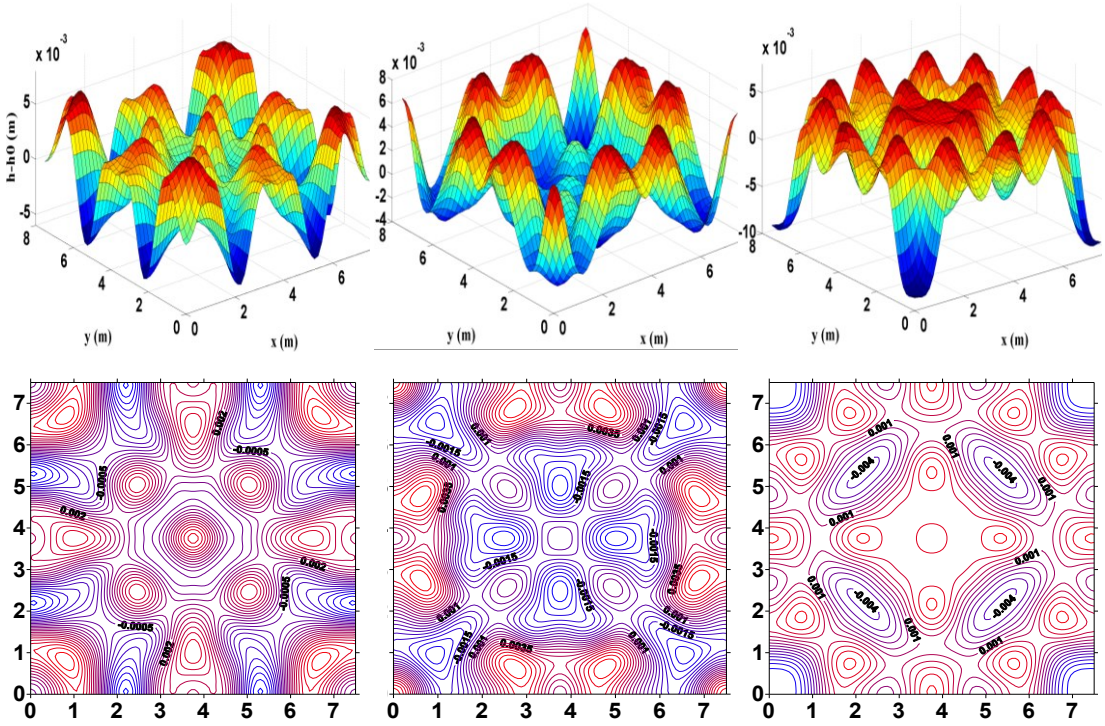

Figure 5.14: Analytical solution of Gaussian hump sloshing in a square, flat basin: 3D plots and contour maps at (a) t = 10 s, (b) t = 12 s; and (c) t = 14 s.

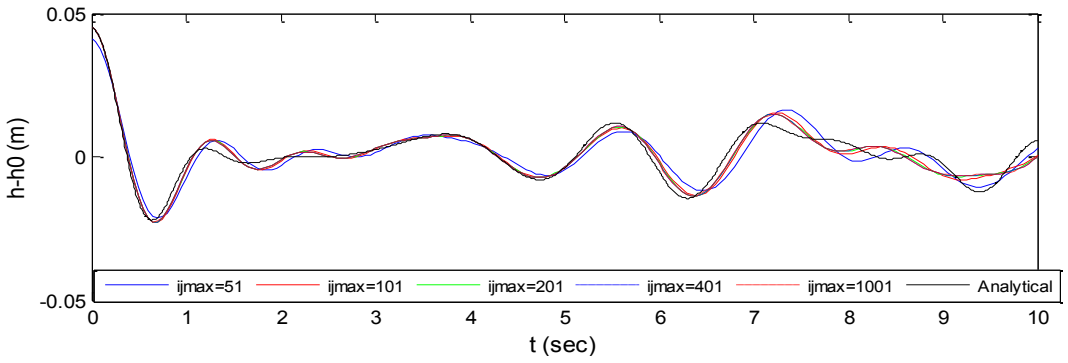

Figure 5.15: Free surface elevation time history at the centre of the basin for Gaussian hump sloshing: numerical results for $r = 4$ on different mesh densities ($i_{max} = j_{max} = 51$, 101, 201, 401, and 1001); analytical solution for $n = m = 51$ and $i_m = j_m = 201$.

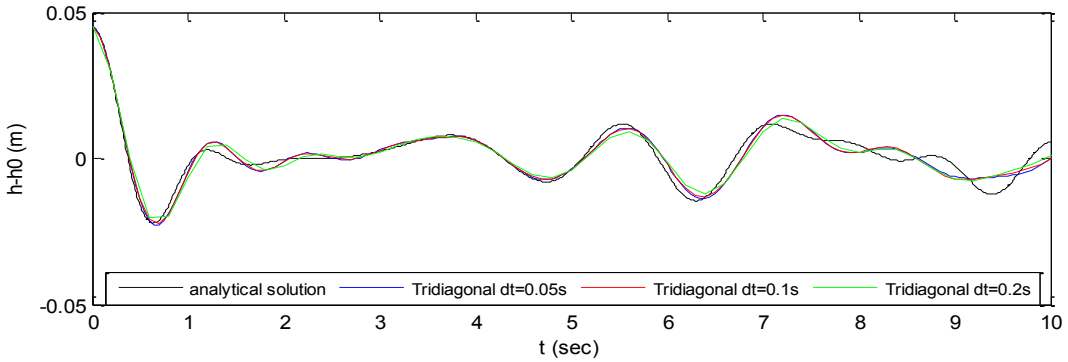

Figure 5.16: Free surface elevation time history at the centre of the basin for Gaussian hump sloshing: numerical results for $r = 4$ and $i_{max} = j_{max} = 201$ using different time steps (Δt = 0.05 s, 0.1 s, and 0.2 s); analytical solution for $n = m = 51$ and $i_m = j_m = 201$.

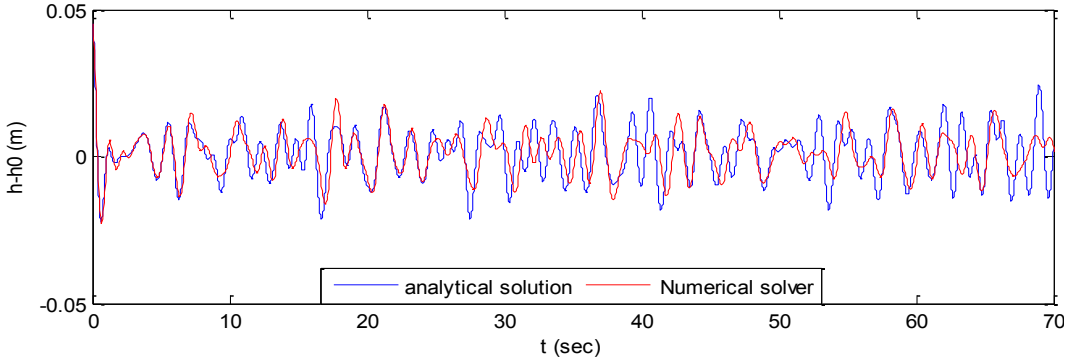

Figure 5.17*a*: Free surface elevation time histories at the centre of a basin for sloshing of an initial Gaussian hump in a square, flat-bottomed basin: numerical solution for $r = 4$ ($i_{max} = j_{max} = 201$) and analytical solution ($n = m = 51$ and $i_m = j_m = 201$).

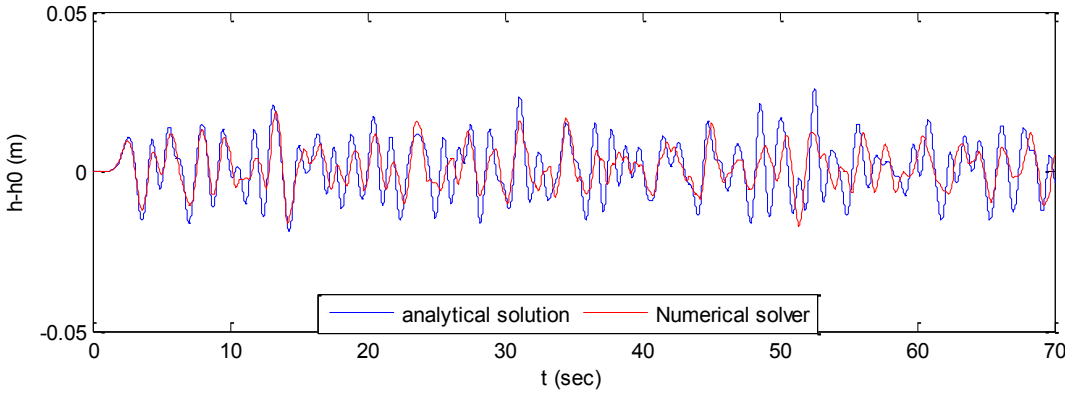

Figure 5.17*b*: Free surface elevation time histories at the corner of a basin for sloshing of an initial Gaussian hump in a square, flat-bottomed basin: numerical solution for $r = 4$ ($i_{max} = j_{max} = 201$) and analytical solution ($n = m = 51$ and $i_m = j_m = 201$).

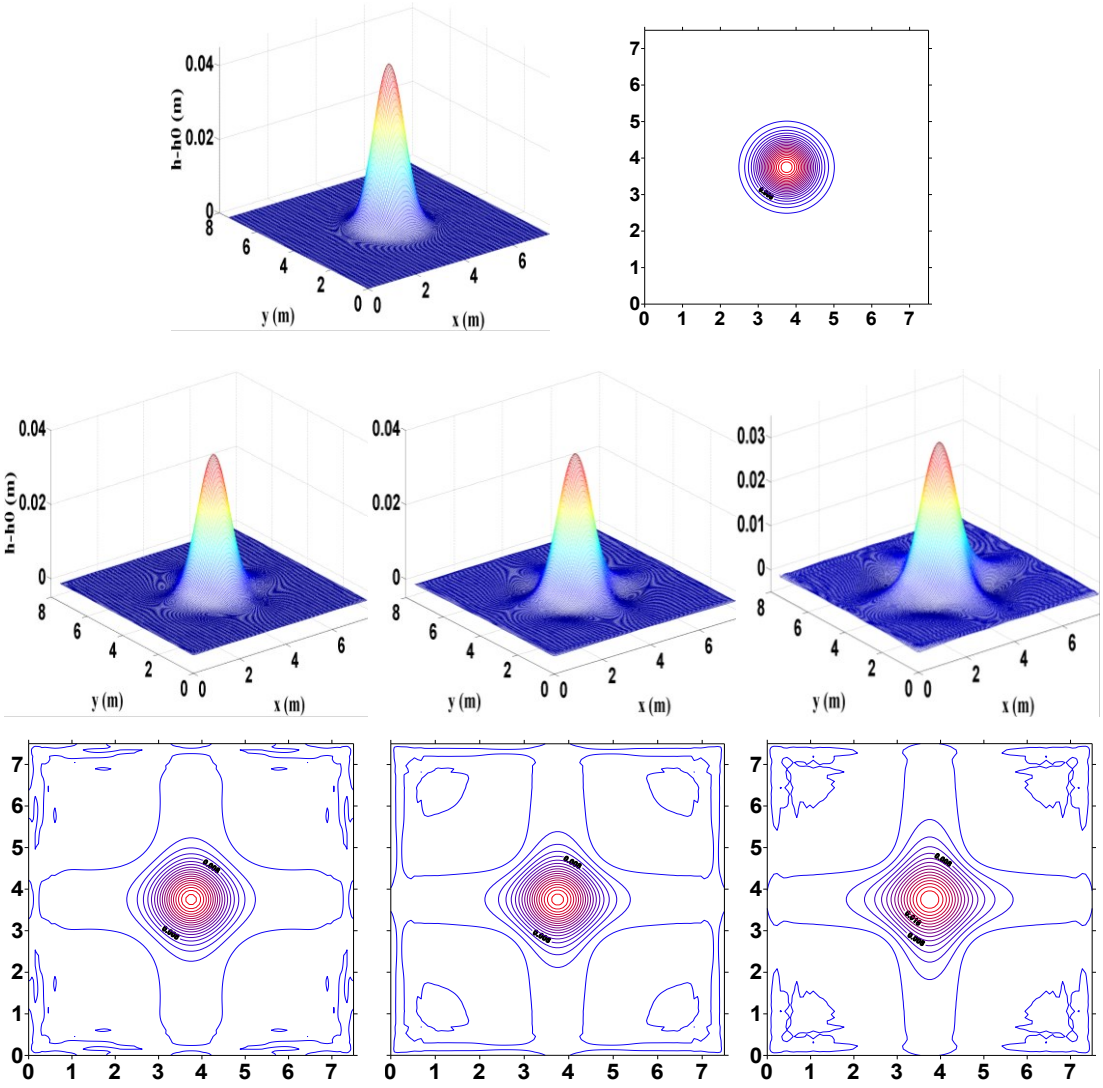

Figure 5.18: Free surface elevation time histories for Gaussian hump sloshing: reversibility tests where the time step is reversed at: (a) $t_1 = 5$ s; (b) $t_2 = 10$ s; and (c) $t_3 = 20$ s.

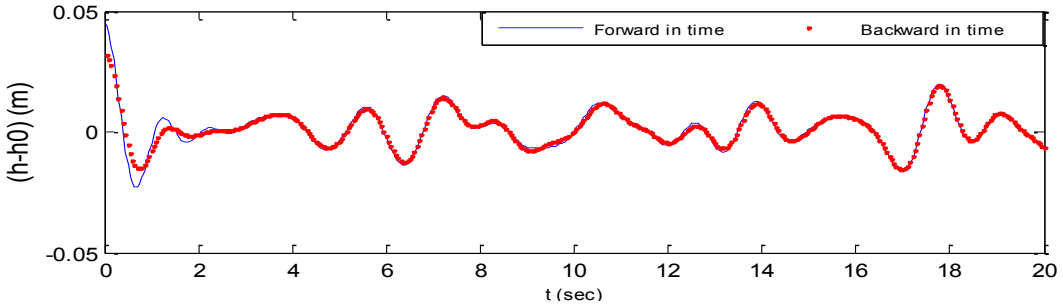

Figure 5.19: Free surface elevation time history at the centre of the basin for Gaussian hump sloshing: reversibility tests where the time step is reversed at $t = 20$ s.

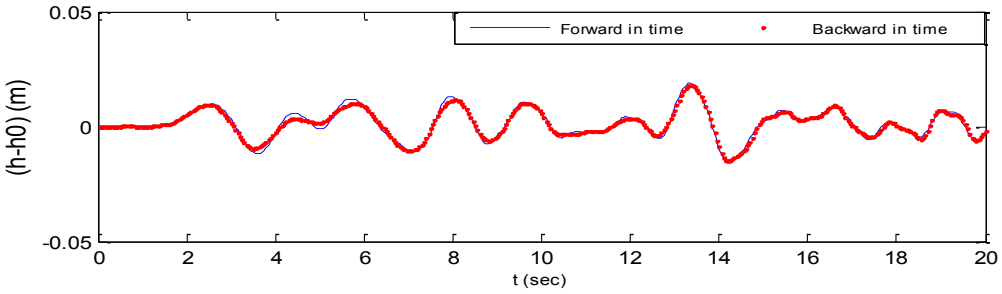

Figure 5.20: Free surface elevation time history at the corner of the basin for Gaussian hump sloshing: reversibility tests where the time step is reversed at $t = 20$ s.

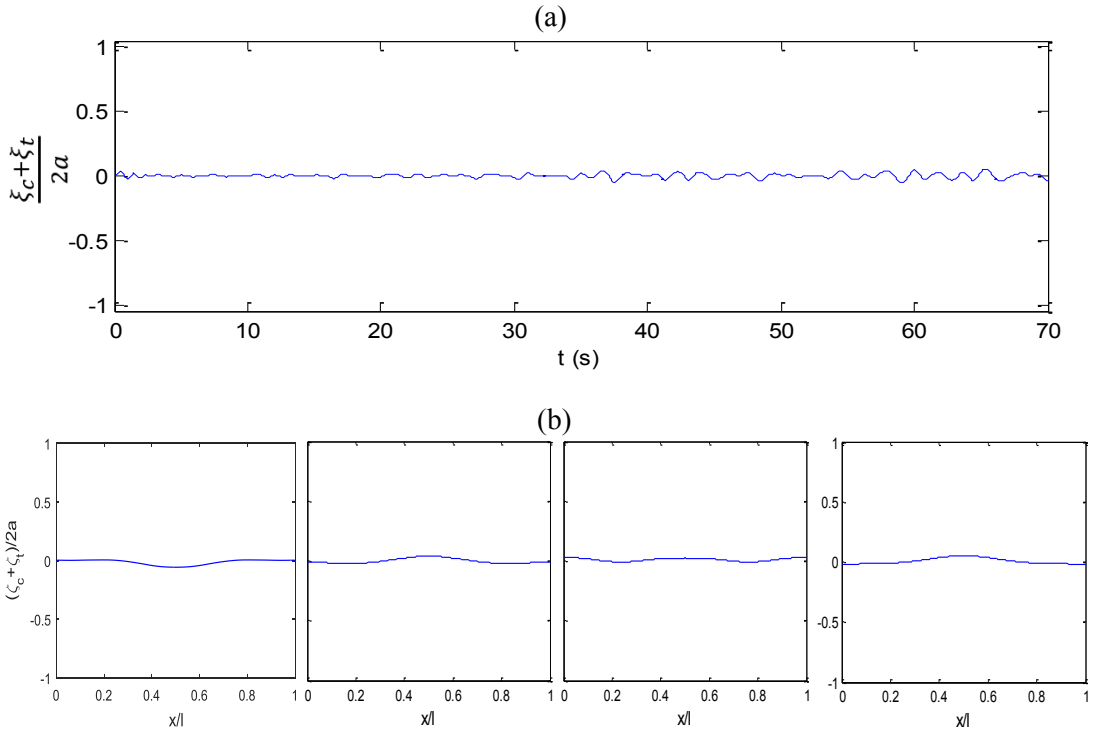

Figure 5.21: Numerically predicted even harmonics of the free surface motions: (a) even harmonic time history for $amp = h_0/10 = 0.045$ m at the centre of the basin; and (b) even harmonic profiles along the centerline of the basin at times $t = 59$, 60, 62 and 65 s.

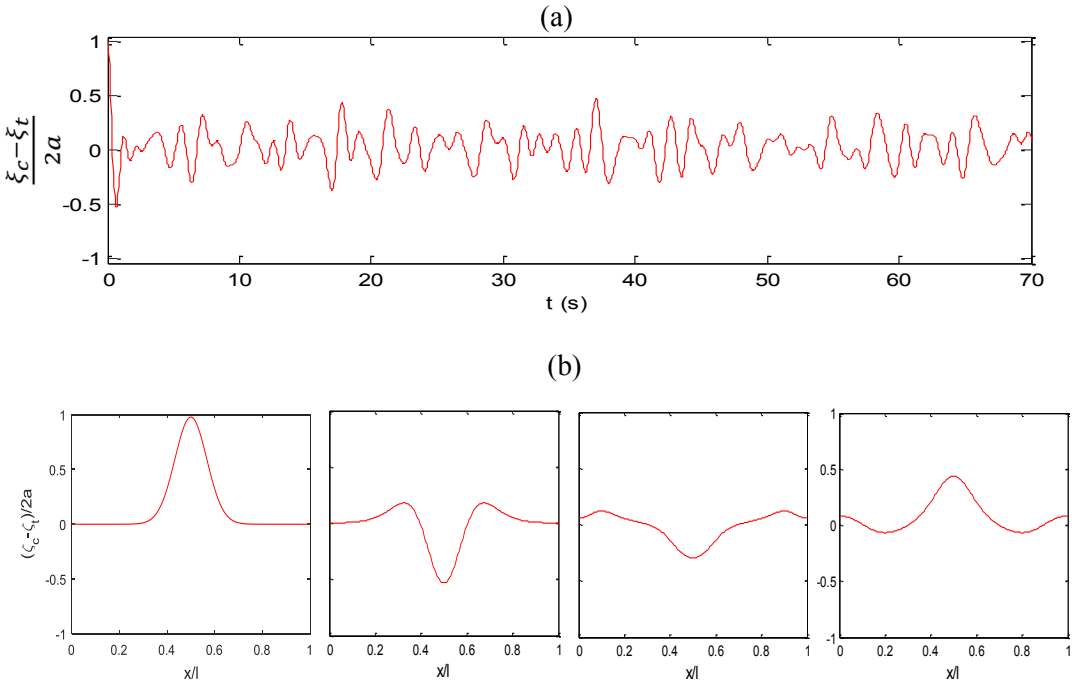

Figure 5.22: Numerically predicted odd harmonics of the free surface motions: (a) odd harmonic time history for *amp* = h_0/10 = 0.045 m at the centre of the basin; and (b) odd harmonic profiles along the centerline of the basin at times t = 0, 0.65, 6.45 and 17.8 s.

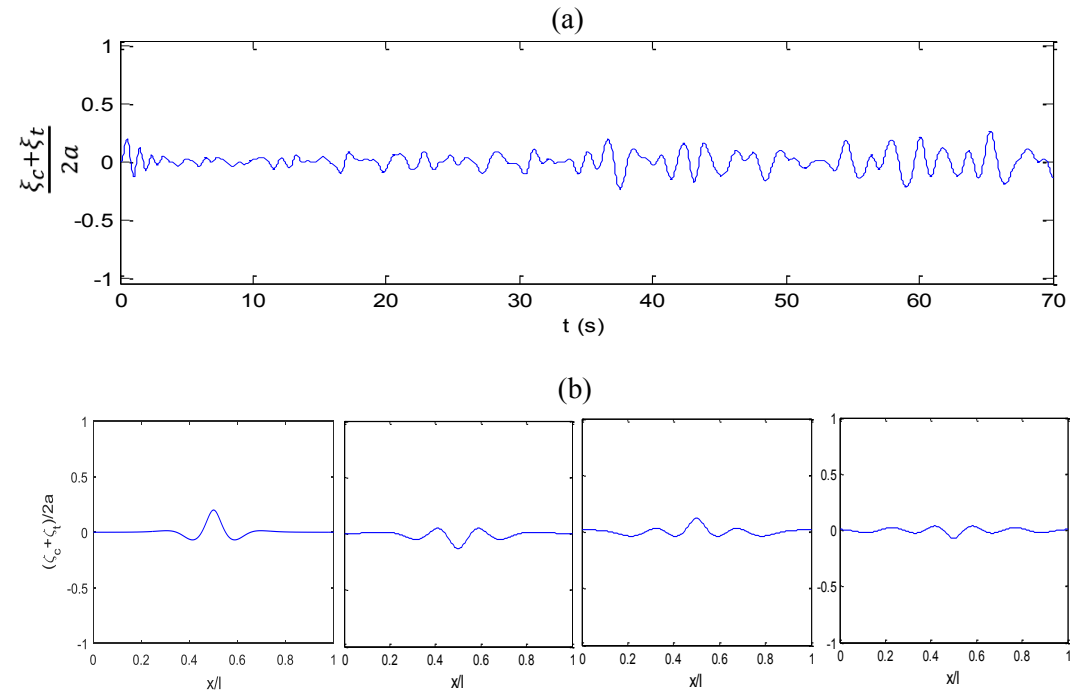

Figure 5.23: Numerically predicted even harmonics of the free surface motions: (a) even harmonic time history for *amp* = h_0/2 = 0.225 m at the centre of the basin; and (b) even harmonic profiles along the centerline of the basin at times t = 0.55, 1.05, 1.5 and 1.95 s.

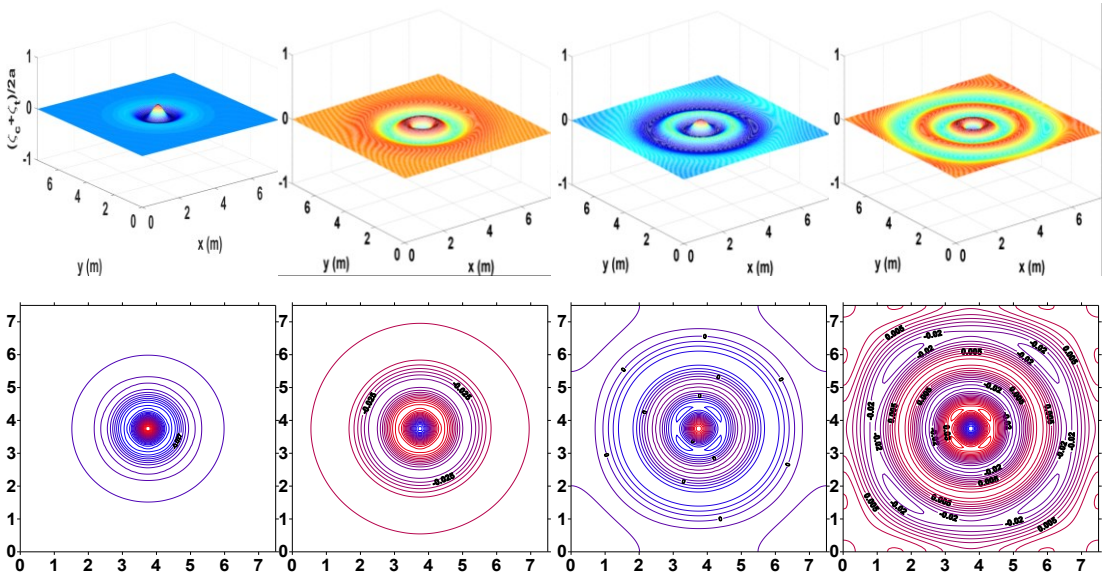

Figure 5.24: Numerical simulations of Gaussian sloshing in a basin for an initial disturbance of amplitude *amp* = $h_0/2$: 3D plots and contour maps of even harmonics at (a) t = 0.55 s, (b) t = 1.05 s; (c) t = 1.5 s; and (d) t = 1.95 s.

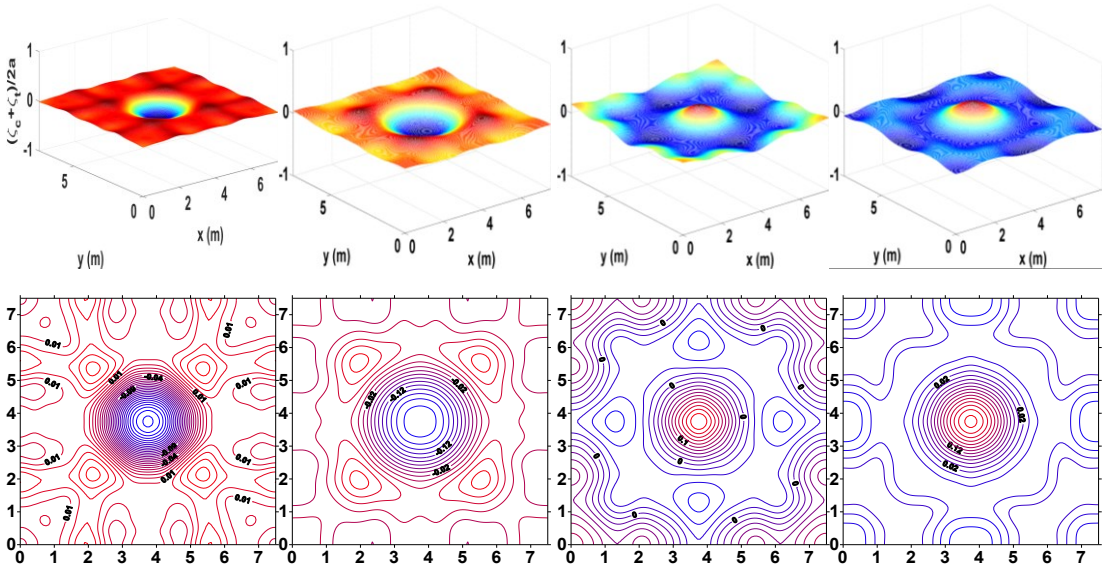

Figure 5.25: Numerical simulations of Gaussian sloshing in a basin for an initial disturbance of amplitude *amp* = $h_0/2$: 3D plots and contour maps of even harmonics at (a) t = 37.55 s, (b) t = 59 s; (c) t = 60.05 s; and (d) t = 65.35 s

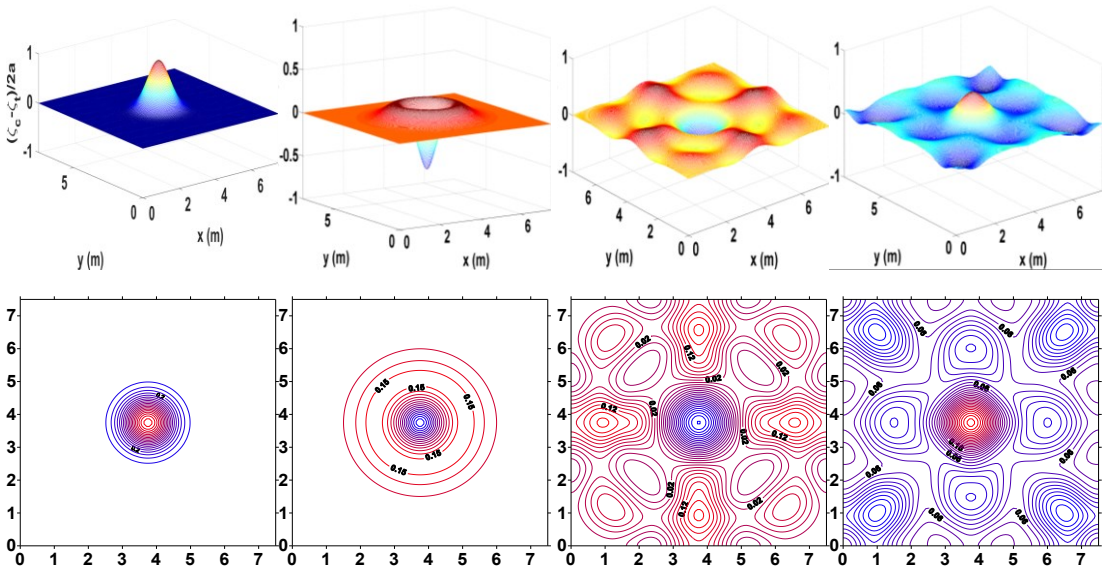

Figure 5.26: Numerical simulations of Gaussian sloshing in a basin for an initial disturbance of amplitude *amp* = $h_0/2$: 3D plots and contour maps of odd harmonics at (a) t = 0 s, (b) t = 0.65 s; (c) t = 17.05 s; and (d) t = 17.8 s.

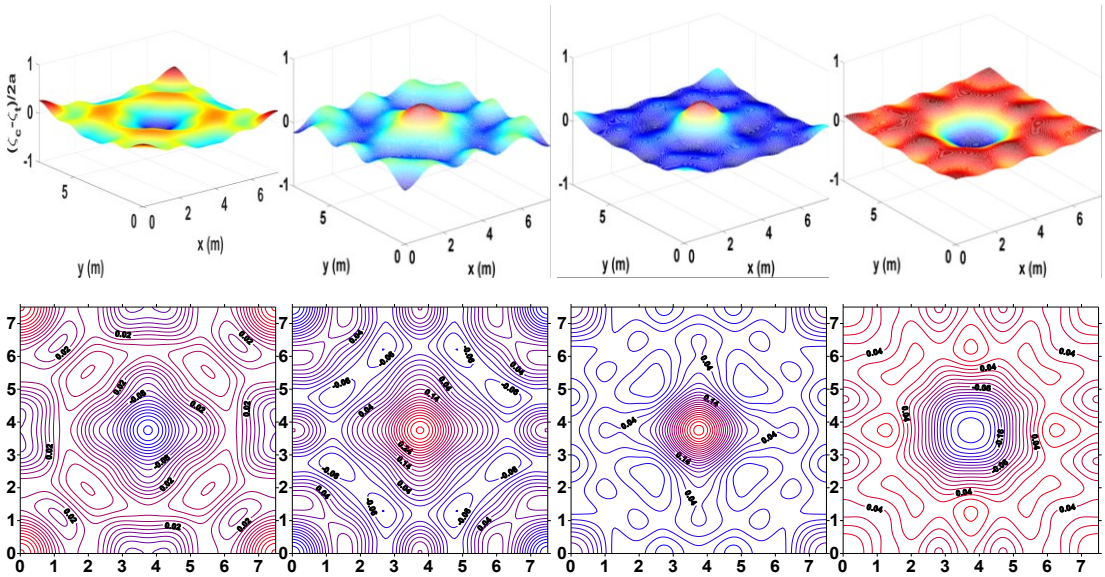

Figure 5.27: Numerical simulations of Gaussian sloshing in a basin for an initial disturbance of amplitude *amp* = $h_0/2$: 3D plots and contour maps of odd harmonics at (a) t = 20.45 s, (b) t = 21.3 s; (c) t = 37 s; and (d) t = 38.15 s.

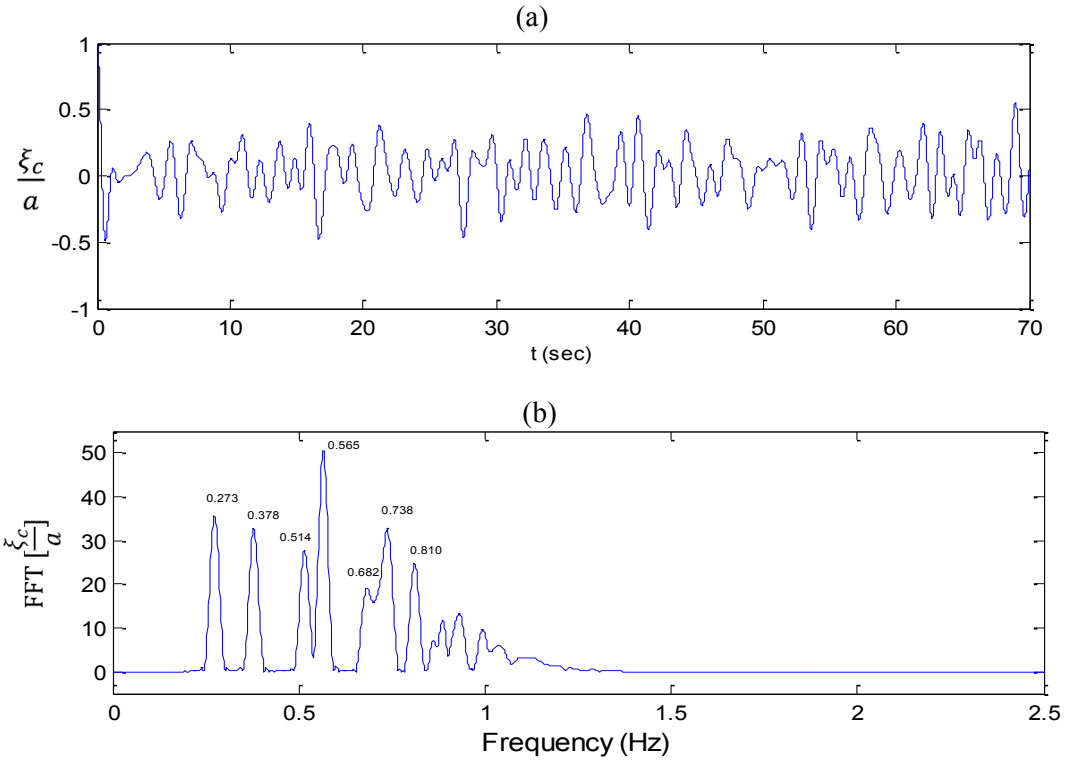

Figure 5.28: Analytical prediction for the initial Gaussian hump for *amp* = $h_0/2$ = 0.225 m at the centre of the basin: (a) free surface elevation time series; and (b) FFT spectrum

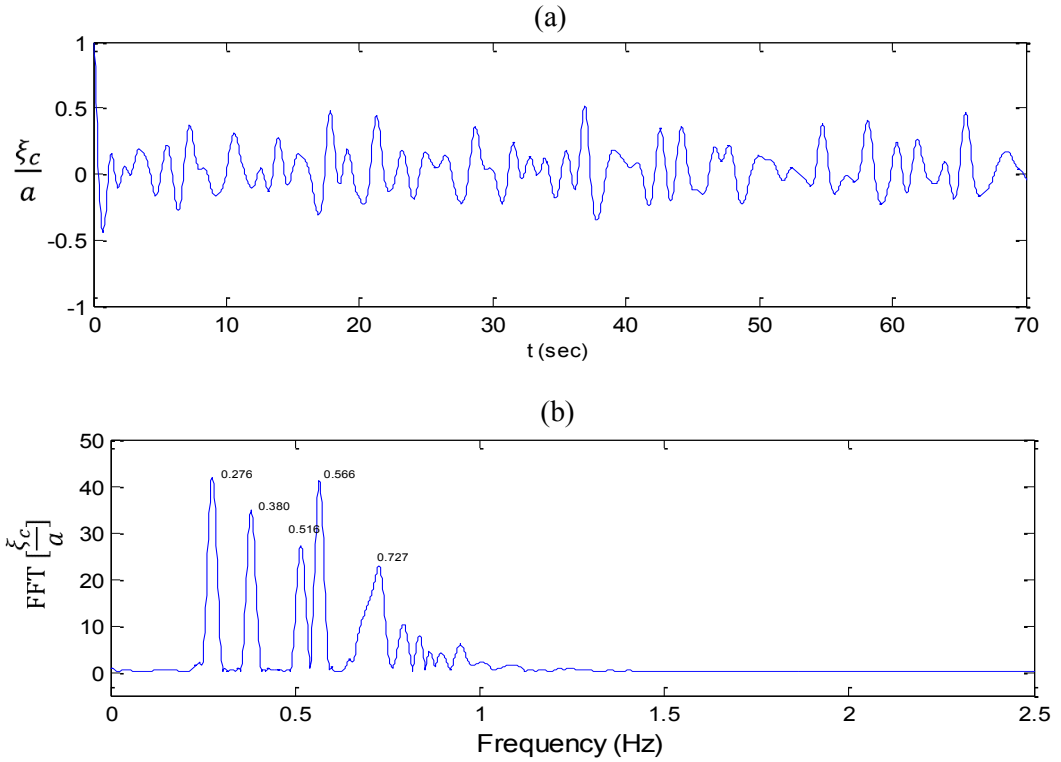

Figure 5.29: Numerical prediction for the initial Gaussian hump for *amp* = $h_0/2$ = 0.225 m at the centre of the basin: (a) free surface elevation time series; and (b) FFT spectrum

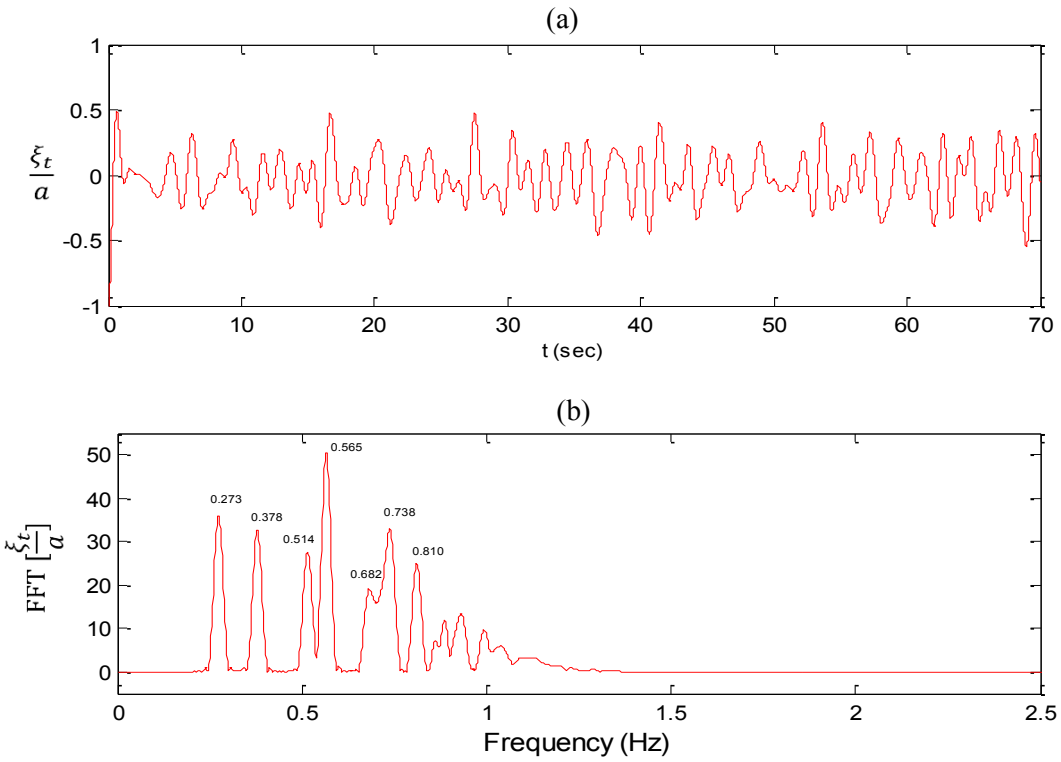

Figure 5.30: Analytical prediction for the initial Gaussian trough for *amp* = $h_0/2$ = 0.225 m at the centre of the basin: (a) free surface elevation time series; and (b) FFT spectrum

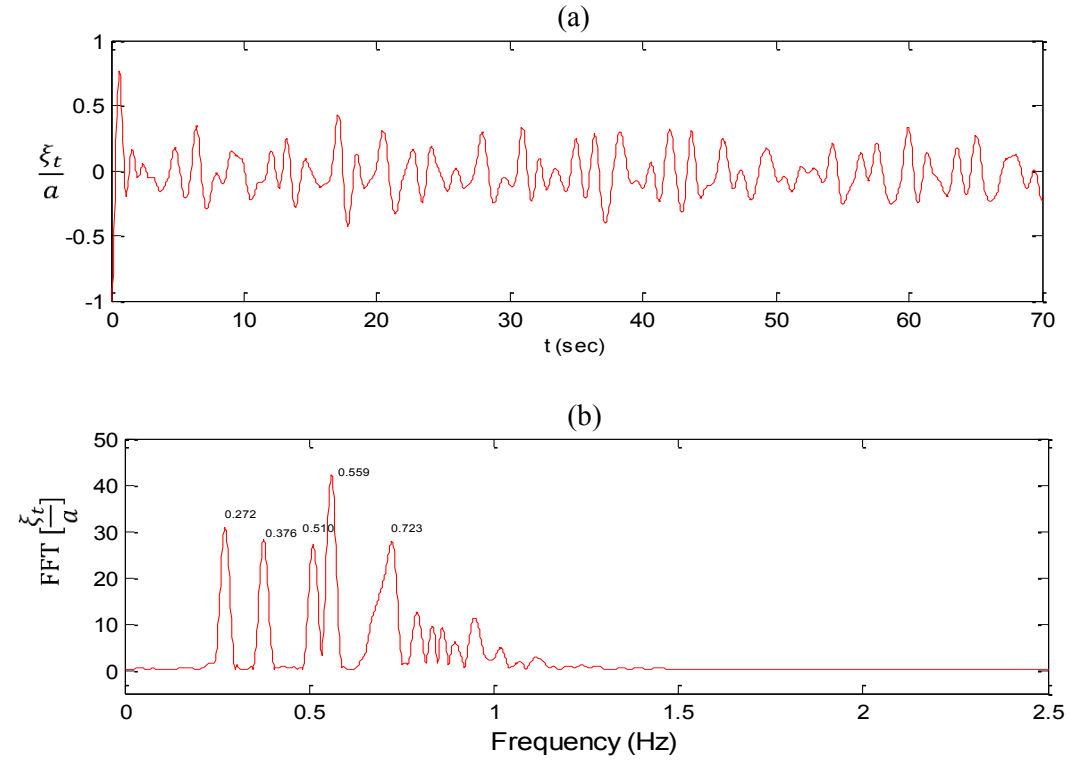

Figure 5.31: Numerical prediction for the initial Gaussian trough for *amp* = $h_0/2$ = 0.225 m at the centre of the basin: (a) free surface elevation time series; and (b) FFT spectrum

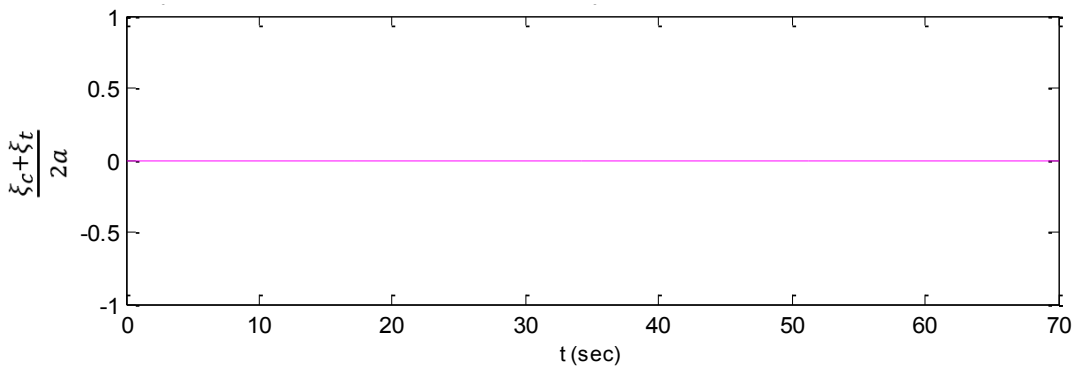

Figure 5.32: Analytical prediction of even harmonic free surface elevation time history for $amp = h_0/2 = 0.225$ m at the centre of the basin

(a)

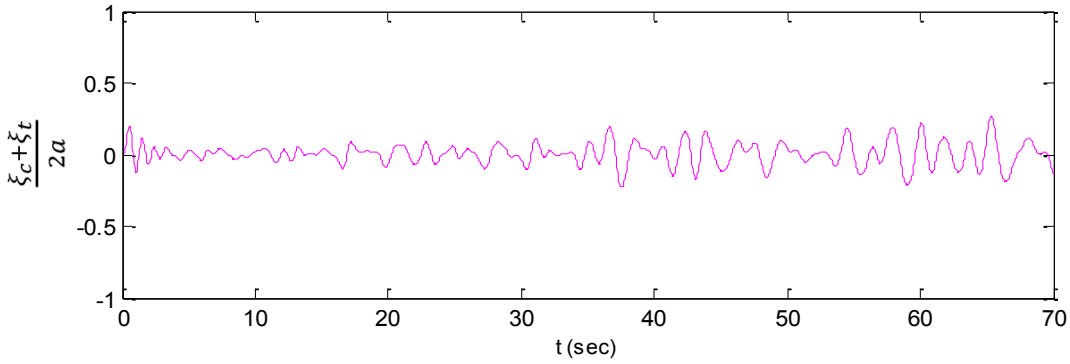

(b)

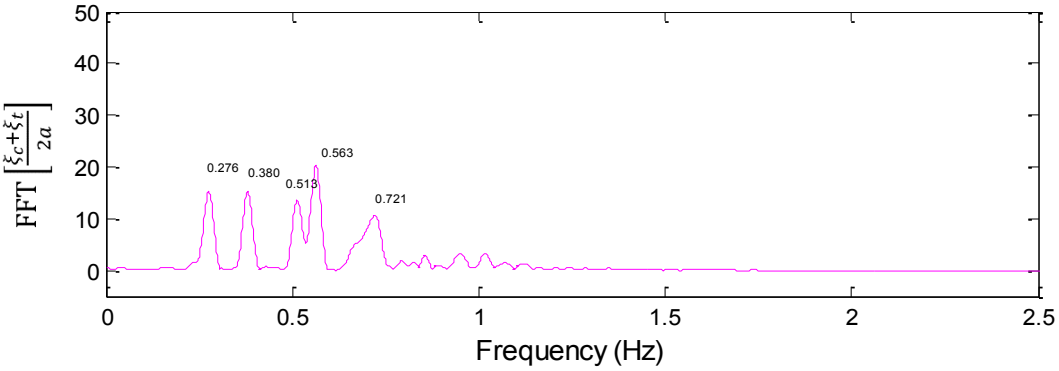

Figure 5.33: Numerical prediction of even harmonic components of sloshing of an initial hump of amplitude $amp = h_0/2 = 0.225$ m at the centre of the basin: (a) free surface elevation time history; and (b) FFT spectrum

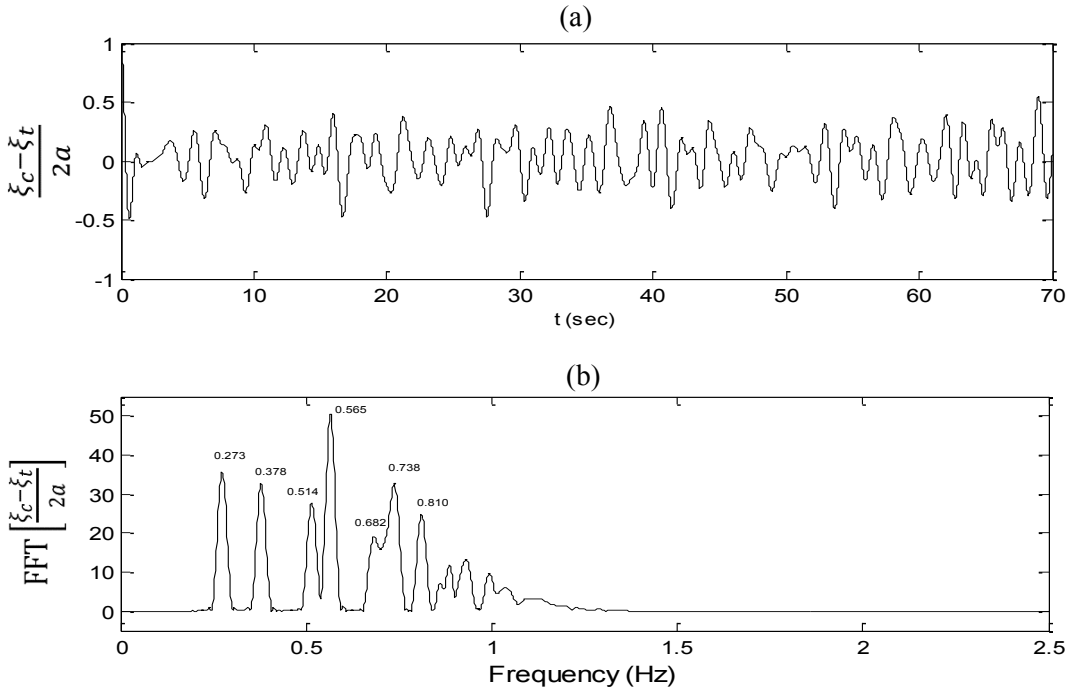

Figure 5.34: Analytical prediction of odd harmonic components of sloshing of an initial hump of amplitude *amp* = $h_0/2$ = 0.225 m at the centre of the basin: (a) free surface elevation time history; and (b) FFT spectrum

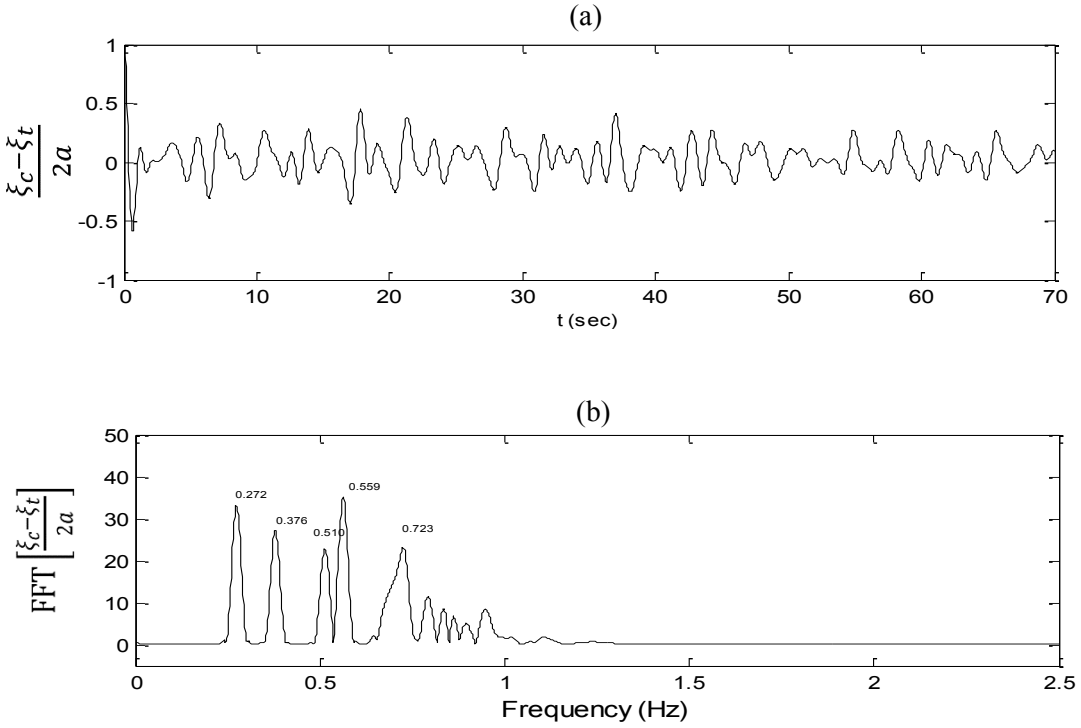

Figure 5.35: Numerical prediction of odd harmonic components of sloshing of an initial hump of amplitude *amp* = $h_0/2$ = 0.225 m at the centre of the basin: (a) free surface elevation time history; and (b) FFT spectrum

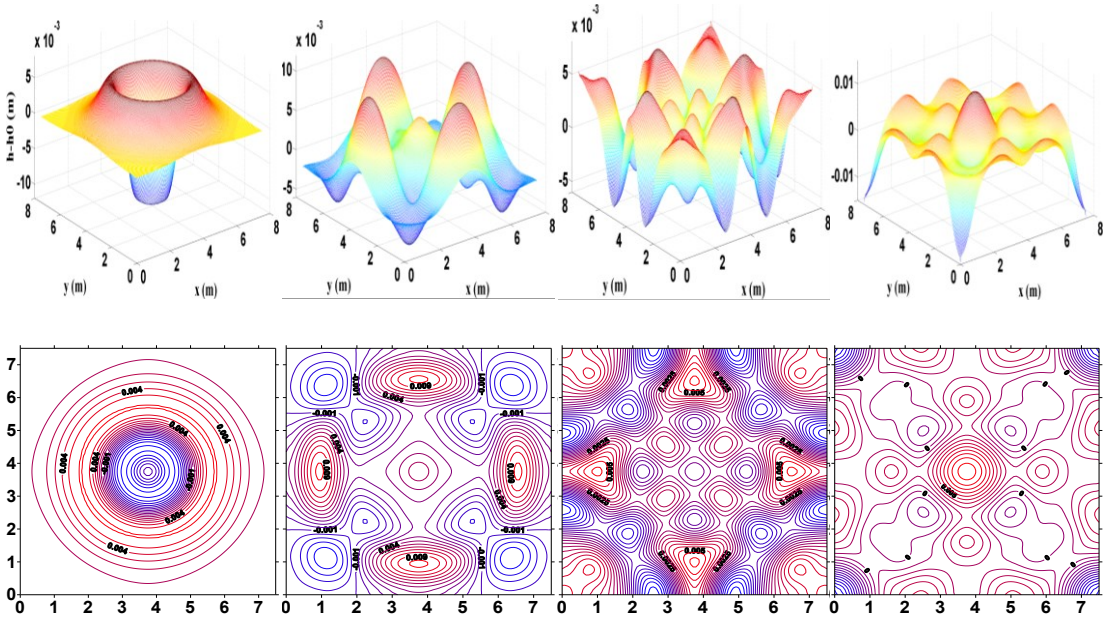

Figure 5.36: Fourth-order simulations of Gaussian hump sloshing in a square, flat-bottomed basin for $r = 4$ and $i_{max} = j_{max} = 201$: 3D plots and contour maps at (a) $t = 1$ s, (b) $t = 4$ s, (c) $t = 10$ s; and (d) $t = 14$ s.

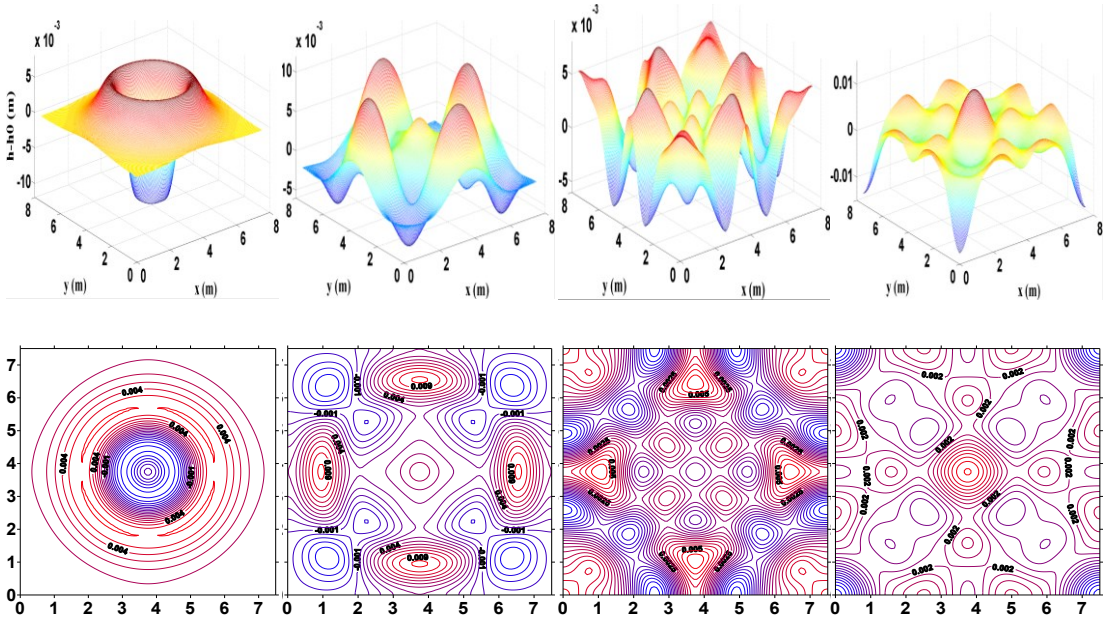

Figure 5.37: Second-order simulations of Gaussian hump sloshing in a square, flat-bottomed basin for $r = 4$ and $i_{max} = j_{max} = 201$: 3D plots and contour maps at (a) $t = 1$ s, (b) $t = 4$ s, (c) $t = 10$ s; and (d) $t = 14$ s.

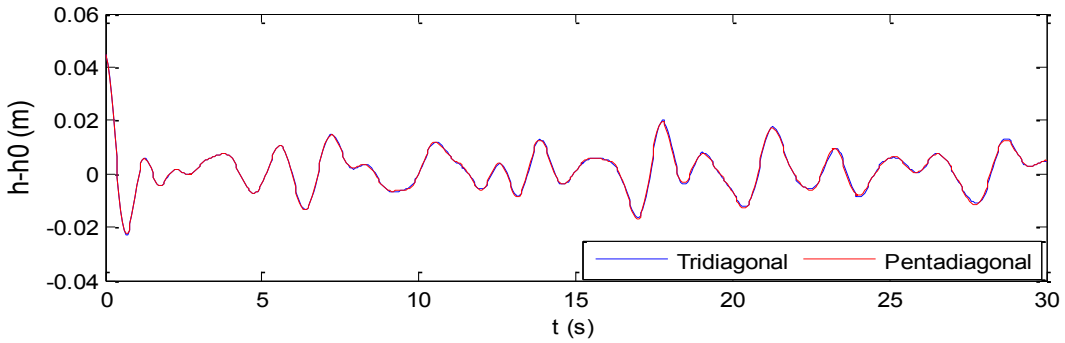

Figure 5.38: Free surface elevation time history at the centre of the basin for Gaussian hump sloshing: second-order solution for $r = 4$ ($i_{max} = j_{max} = 201$) and fourth-order solution for $r = 4$ ($i_{max} = j_{max} = 201$) at the centre of the basin.

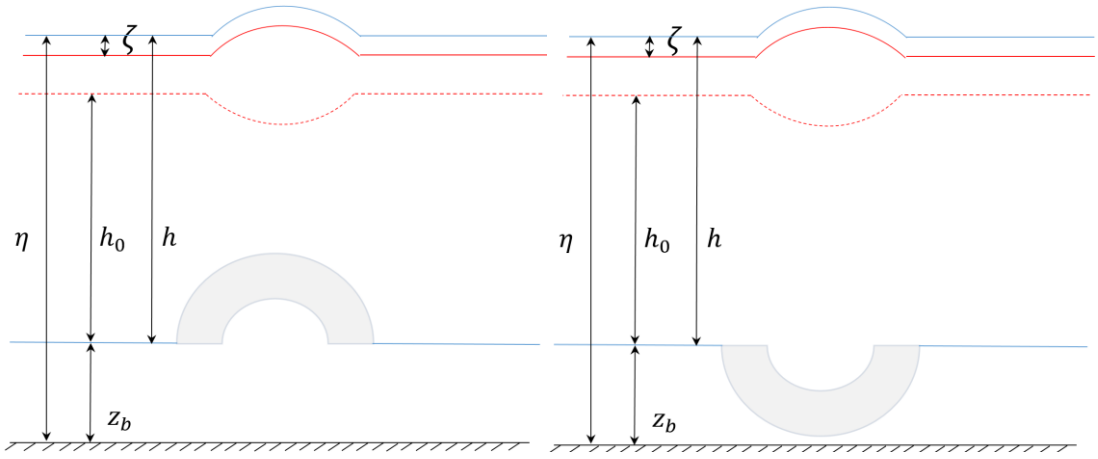

Figure 5.39: illustrates the key variable that defined the flow geometry in the *x*-*z* plate: (a) motions of an initial Gaussian free surface hump in a basin containing a bed hump at its centre (b) motions of an initial Gaussian free surface hump in a basin containing a bed trough at its centre.

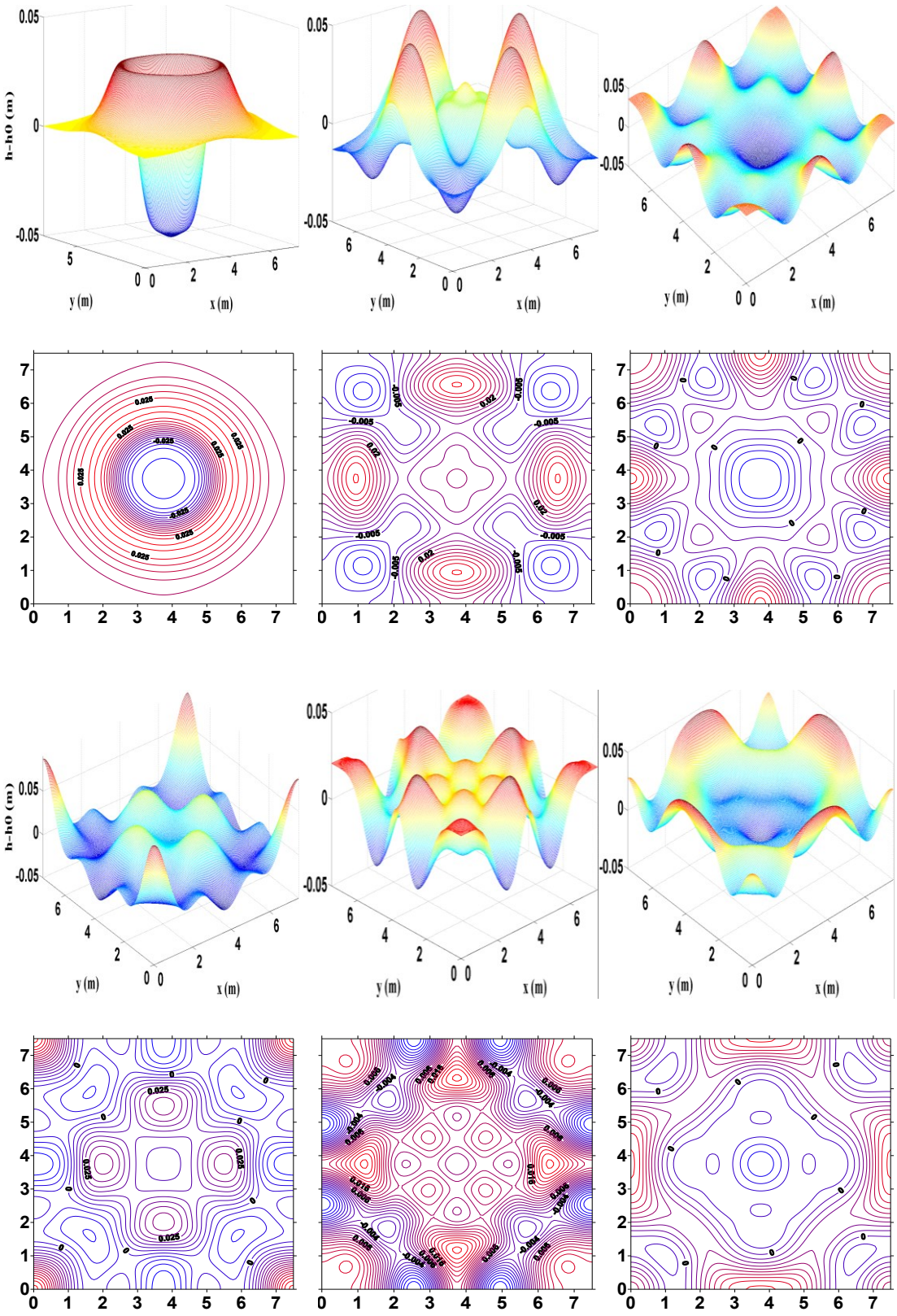

Figure 5.40: Numerical simulations of the sloshing of an initial Gaussian hump in a square basin where the bed topography contains a central hump for a small bed amplitude disturbance a_{z_b}=0.015 m at (a) t= 2 s, (b) t=4 s, (c) t=6 s, (d) t=8 s, (e) t=10 s; and (f) t=12 s.

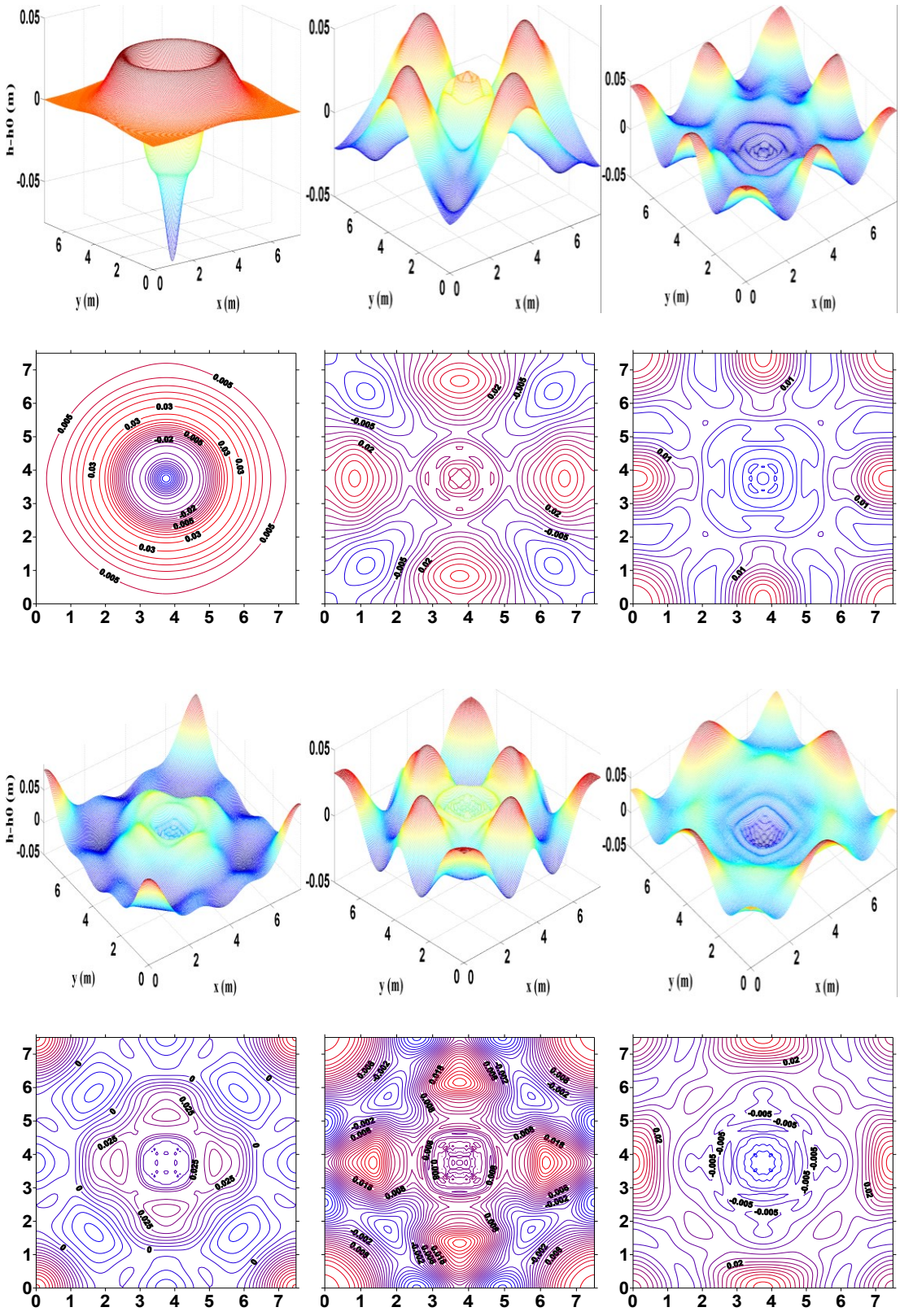

Figure 5.41: Numerical simulations of the sloshing of an initial Gaussian hump in a square basin where the bed topography contains a central hump for a large bed amplitude disturbance a_{z_b} =0.225 m at (a) *t*=2 s, (b) *t*=4 s, (c) *t*=6 s, (d) *t*=8 s, (e) *t*=10 s; and (f) *t*=12 s.

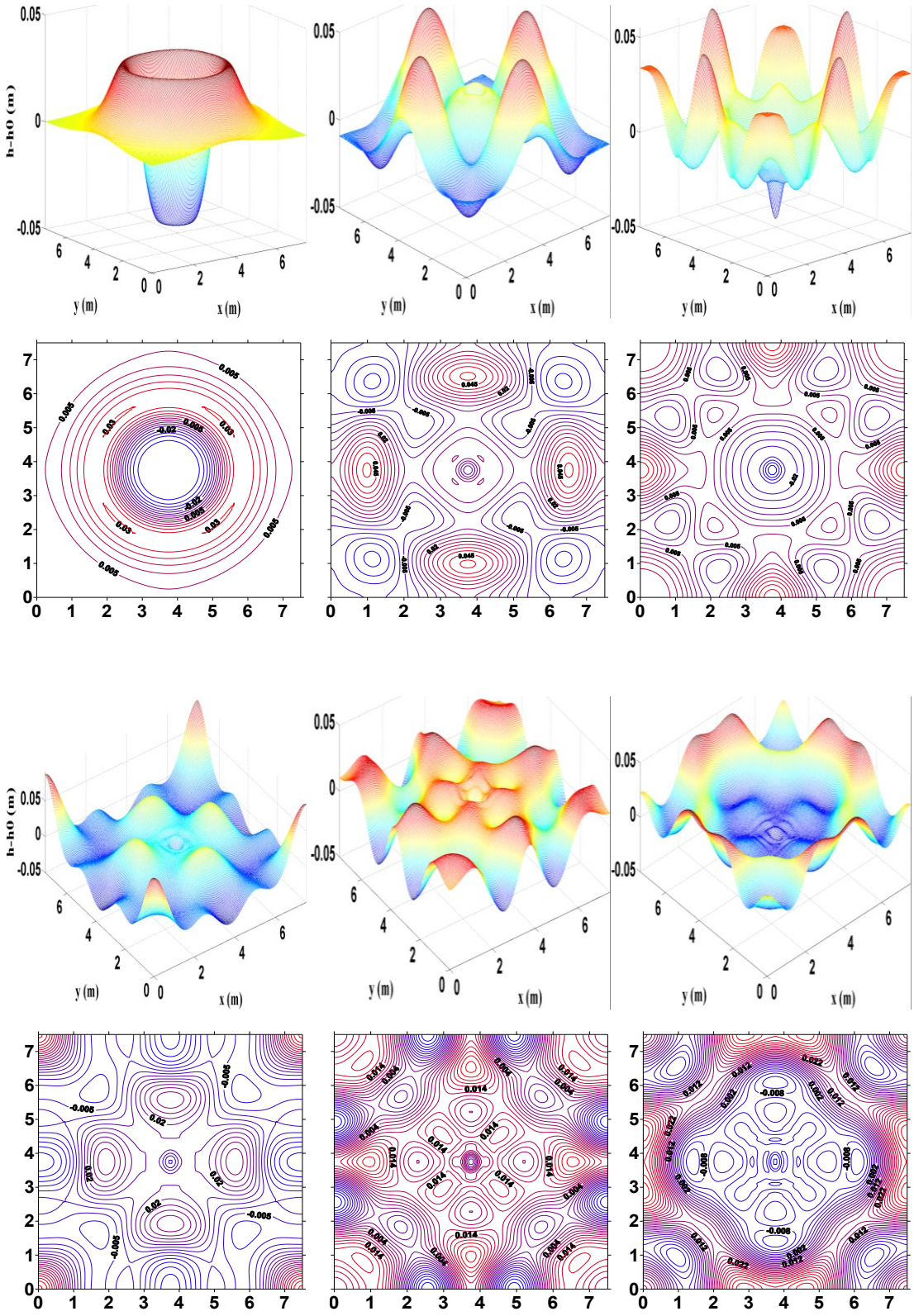

Figure 5.42: Numerical simulations of the sloshing of an initial Gaussian hump in a square basin where the bed topography contains a central trough for a large bed amplitude disturbance a_{z_b}=-0.225m at (a) *t*=2 s, (b) *t*=4 s, (c) *t*=6 s, (d) *t*=8 s, (e) *t*=10 s; and (f) *t*=12 s.

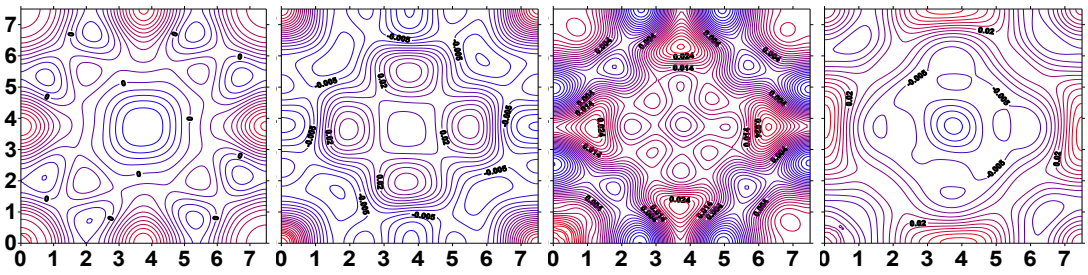

Figure 5.43: Numerical simulations of the sloshing of an initial Gaussian hump in a square basin where the bed topography contains a hump at the south-west corner: contour plots of free surface elevation at (a) t = 6 s, (b) t = 8 s, (c) t = 10 s; and (d) t = 12 s.

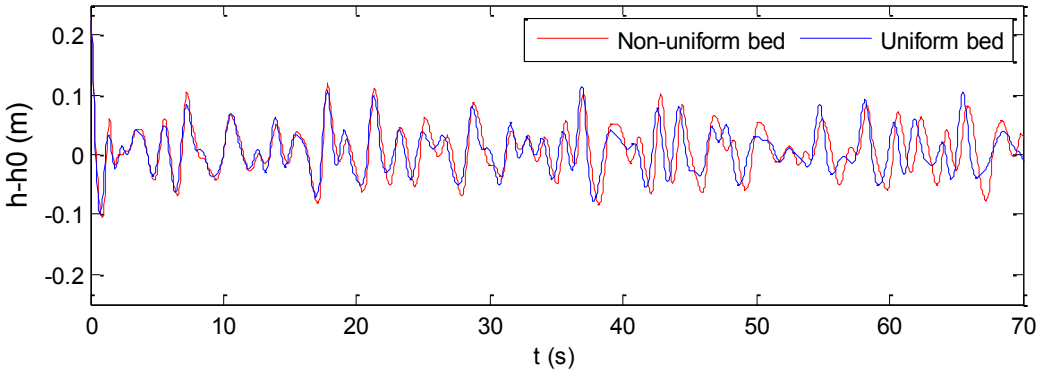

Figure 5.44: Free surface elevation time histories at the centre of a basin for sloshing of an initial Gaussian hump: in a square, flat-bottomed basin (blue line) and in a basin where the bed topography contains a central hump (red line) for a large bed amplitude disturbance a_{z_b} = 0.225 m.

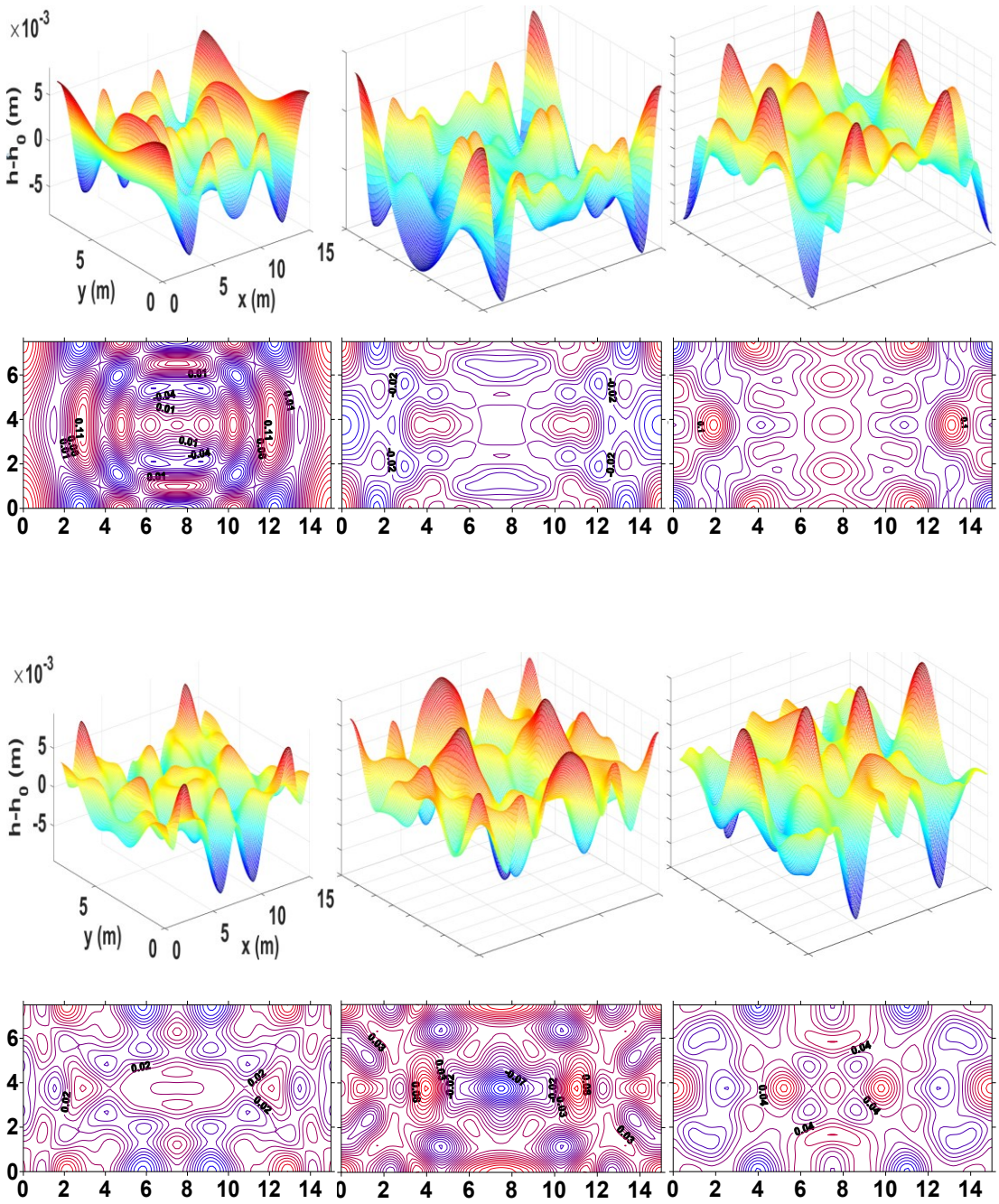

Figure 5.45: Numerical simulations of the sloshing of an initial Gaussian hump in a rectangular, flat-bottomed basin: 3D plots and contour maps of free surface elevation at (a) $t = 4$ s, (b) $t = 6$ s, (c) $t = 8$ s, (d) $t = 10$ s, (e) $t = 12$ s; and (f) $t = 14$ s.

Chapter 6

2D Model Verification and Parameter Tests

Simulation of Solitary Wave Propagation

6.1 Introduction

In this chapter, the horizontal, vertical and oblique propagations of a nonlinear 2D GN solitary wave are simulated. Then, forward and reversed simulations of the solitary wave are compared, and finally interaction between two solitary waves through applying second-order and fourth-order solvers are presented.

6.2 Solitary wave in wall-bounded square channel

The second verification test concerns the simulation of a solitary wave in a closed square basin of plan dimensions $L_x = L_y = 25$ m. The still water depth is $h_0 = 1$ m. The free surface profile of a solitary wave is given by [Metayer *et al*. (2010)]:

$$\xi(x, y, t) = a\,\mathrm{sech}^2\big(b\,(x - ct)\big) \tag{6.1}$$

where ξ is the free surface elevation above still water level, a is amplitude, b is the inverse width and c is the solitary wave speed (see Figure 6.1). The inverse width is defined as

$$b = \frac{1}{2}\sqrt{\left(\frac{3a}{{h_0}^2(h_0+a)}\right)} \tag{6.2}$$

and the wave celerity is

$$c = \sqrt{g(h_0 + a)} \tag{6.3}$$

The local total water depth is given by

$$h(x, y, t) = h_0 + \xi(x, y, t) \tag{6.4}$$

Three solitary wave tests were undertaken; one where the wave propagated from west to east (in the positive *x*-direction); one where the wave propagated from south to north (in the positive *y*-direction); and one where the wave propagated at an angle $\theta = 30^{o}$ to the *x*-axis. The analytical solutions (Metayer *et al*. 2010) for the flow velocity components are as follows:

Case S1: Solitary wave from west to east:

$$\begin{cases} u(x,y,t) = c\left(1 - \frac{h_0}{\xi(x,y,t)+h_0}\right) \\ v(x,y,t) = 0 \end{cases} \tag{6.5}$$

Here, u is the fluid velocity component in the *x*-direction, and v is the fluid velocity component in the *y*-direction.

Case S2: Solitary wave from south to north:

$$\begin{cases} u(x,y,t) = 0 \\ v(x,y,t) = c\left(1 - \frac{h_0}{\xi(x,y,t)+h_0}\right) \end{cases} \tag{6.6}$$

Case S3: Oblique solitary wave, where the coordinate axis is transformed as follows:

$$\begin{bmatrix} x' \\ y' \end{bmatrix} = \begin{bmatrix} \cos\theta & -\sin\theta \\ \sin\theta & \cos\theta \end{bmatrix} . \begin{bmatrix} x \\ y \end{bmatrix} \quad \Rightarrow \quad \begin{cases} x' = x\cos\theta - y\sin\theta \\ y' = x\sin\theta + y\cos\theta \end{cases} \tag{6.7}$$

Hence, u and v are as follows:

$$\begin{cases} u(x',y',t) = c\left(1 - \frac{h_0}{\xi(x',y',t)+h_0}\right) . \cos\theta \\ v(x',y',t) = c\left(1 - \frac{h_0}{\xi(x',y',t)+h_0}\right) . \sin\theta \end{cases} \tag{6.8}$$

In all cases the solitary wave has amplitude of a = 0.6 m. The position of the initial wave crest is set to be 7 m away from the west wall ($L_{xpo} = L_{ypo} = 7$ m). The time step is set to Δt = 0.05 s. The first test case examines the movement of solitary wave in the *x*-direction from west to east. The second test case considers solitary wave propagation in the *y*-direction from south to north. In the third case, the model is used to reproduce the behaviour of an oblique solitary wave ($\theta = 30^{o}$). Figure 6.2 illustrates the computational mesh plotted in physical domain.

A grid convergence test is now performed. Figure 6.3 depicts the non-dimensional free surface profiles obtained for the solitary wave in Case S1 at t = 10 s for three different grids. At this time the solitary wave has reflected at the east wall and is travelling back in the reverse direction from east to west. It can be seen that converged results are obtained on the medium grid ($i_{max} = j_{max} = 251$) and fine grid ($i_{max} = j_{max} = 451$); the results are inaccurate on the coarse grid ($i_{max} = j_{max} = 51$). Figure 6.4 shows the free surface visualisations and contour patterns obtained respectively for a solitary wave propagating from west to east at t = 3 s on the coarse, medium and fine grids. At this time, a trailing wave has appeared behind the main crest on the coarse grid, unlike the results on the medium and fine grids where no trailing wave is evident. Figure 6.5 shows the free surface visualisations and contours at t = 5 s, just as the solitary wave interacts with the solid wall. The spurious trailing wave persists on the coarse grid. These test results that the medium grid is sufficient for accurate simulations. At t = 5 s, the numerically predicted run up reaches 2.355 m which was 0.355 m more than the predicted linear analytical solution due to nonlinear interactions within the wave.

Comparison between the numerical predictions and results from perturbation analysis (Taylor, 2015) confirms that nonlinear interaction between a solitary wave and a solid wall is correctly modelled. The total depth behind the reflected wave (h_w) is:

$$h_w = \left[1 + 2n + \frac{n^2}{2} - \frac{n^3}{4} + \frac{n^4}{4} - \frac{n^5}{4} + \frac{7n^6}{32} - \frac{9n^7}{64} + \frac{n^8}{128} + 0[\mathrm{n}]^9\right] h \qquad (6.9)$$

in which n is upstream amplitude (a) divided by upstream depth (h). By including the second order perturbation term, the approximate analytical solution for the reflected solitary wave elevation is 2.3454 m, a quite similar value to that predicted by the GN model (2.355 m). This analytical approximation was obtained by personal contact with P. H. Taylor on 18 Dec 2015.

It should be noted that identical results and findings were obtained for a solitary wave propagating from south to north, Case S2, only that the axis was rotated. These results are not presented here, for brevity.

Figure 6.6 shows the predicted evolution of the solitary wave at times t = 1, 3, 5, 9, 17, and 19 s on the converged medium grid with $i_{max} = j_{max}$ = 251 and time step Δt = 0.05s. At first, the solitary wave propagates with its free surface profile unchanging in shape (see results at t = 1 and 3 s) as it moves along the channel. At t ~ 5 s, the solitary wave crest hits the wall, and its elevation reaches 2.355 m which is more than twice the elevation prior to contact. The reflected wave sheds some trailing waves which are evident behind the reflected wave as it travels from east to west as shown in the plot for t = 9 s. At t ~ 11 s the solitary wave reflects at the west wall and its elevation again reaches 2.355 m. Figure 6.6e shows the situation at t = 17 s, just before the re-reflected wave reaches the east wall, where the trailing waves are growing in scale as they interact with the channel (through sloshing modes). The final plot in Figure 6.6f shows the wave after it has reflected the second time with the east wall and channel sloshing is even more evident.

Case S3 comprises the simulation of an oblique solitary wave ($\theta = 30^o$) in a 25m by 25m channel. Figure 6.7 shows the predicted surface elevation visualisations and contour maps at t = 0, 0.1 and 0.3 s. The oblique wave retains its shape with time as it moves from west to east, except at the boundaries where wall interactions take place. This indicates that the model can cope properly with a wave at an angle $\theta = 30^o$ to the grid.

6.3 Comparison of GN model simulations and Boussinesq model predictions of solitary wave propagation

The above-mentioned predictions by 2D level I GN model are in reasonable agreement with 1D simulations by Orszaghova (2011) who used Boussinesq model. The present study confirms that the 2D GN second-order numerical solver is able to predict solitary wave behaviour properly. It is worth mentioning that both level I GN equations and Boussinesq equations provide accurate predictions of the post-breaking waves.

6.4 Reverse simulations of solitary wave

In order to test for reversibility, the similar to the aforementioned time travelling tests designed for Gaussian hump simulations, a series of simulations are designed for solitary wave based on time travelling idea. Figure 6.8 shows the free surface elevation time history at the centre of the channel. The total duration of the simulated time is 40 s, of which 20 s is forward in time (blue line) and 20 s is backward in time (red dots). The red dots essentially overlay the blue line. Figure 6.9 shows the solitary wave profiles at t = 0, 0.5, 1, 1.5, 2, 2.5 and 3 s. It is observed that the original profiles (Just going forward in time) and reverse profiles (going forward and backward in time till reaching the specific t_n = 3 s) again overlay each other. Figure 6.10 indicates the excellent agreement between the initial profile from the original simulation and the final profile from the reverse simulation. The foregoing results indicate that the GN simulation of the solitary wave is fully reversible with no energy dissipation evident, as would be expected in the absence of viscosity, turbulence, and bed friction.

6.5 Interaction of two solitons by applying 2th and 4th order solvers

The solitary wave propagations of 0.6 m and 0.3 m initial amplitudes in otherwise still water of depth 1 m along the 100 m x 100 m channel were investigated. Medium grids i_{max} = j_{max} = 251 and a fixed time step $\Delta t = 0.05$ s are selected for second-order and fourth-order numerical simulations. Figure 6.11 presents predicted free surface elevation profile of solitary waves at t = 15.5 s using second-order and fourth-order schemes. In the second-order simulation (Figure 6.11a), large amplitude solitary wave loses amplitude as it dissipates energy into the production of trailing waves (connected to numerical error from lack of spatial resolution). On the other hand, in the fourth-order simulation (Figure 6.11b) the large amplitude solitary wave does not lose amplitude as it does in second-order simulation. Thus, the fourth-order scheme is opted for the remaining simulations, and the second-order results are ignored here, for brevity. Figures 6.12 to 6.14 show the predicted evolution of the solitary wave at times t = 0, 5, 15.5, 15.85, 16.25, 17, 17.75, and 18.1 s. At t = 15.5 s, the large

amplitude solitary wave reaches to the small amplitude one. At t = 16.25 s, interaction occurs between the two solitary waves. The two waves become fully merged at t=17 s and the elevation of the merged wave is ~ 0.9 m. At t = 17.75 s, the two solitary waves start to separate from each other. At t = 18.1 s, they are completely separated, and each of them propagates by its own amplitude.

6.6 Summery

- In this chapter, the numerical model was applied to simulate solitary wave propagation in a closed flat-bottomed channel. Comparison between the numerical predictions and results from perturbation analysis (Taylor, 2015) confirmed that nonlinear interaction between a solitary wave and a solid wall was correctly modelled. When the solitary wave hit a wall, the numerically predicted run up reached 2.355 m which was 0.355 m more than the predicted linear analytical solution. By including the second order perturbation term (Taylor 2015), the approximate analytical solution for the reflected solitary wave elevation was 2.3454 m, a quite similar value to that predicted by the GN model.

- A reversibility check revealed that the original and reverse profiles of solitary wave simulations overlay each other. In the final simulations for 2D level I GN developed model, the interaction between two solitary waves was investigated through applying second- and fourth-order numerical schemes. Both numerical schemes presented accurate simulations for the interaction between the two solitary waves.

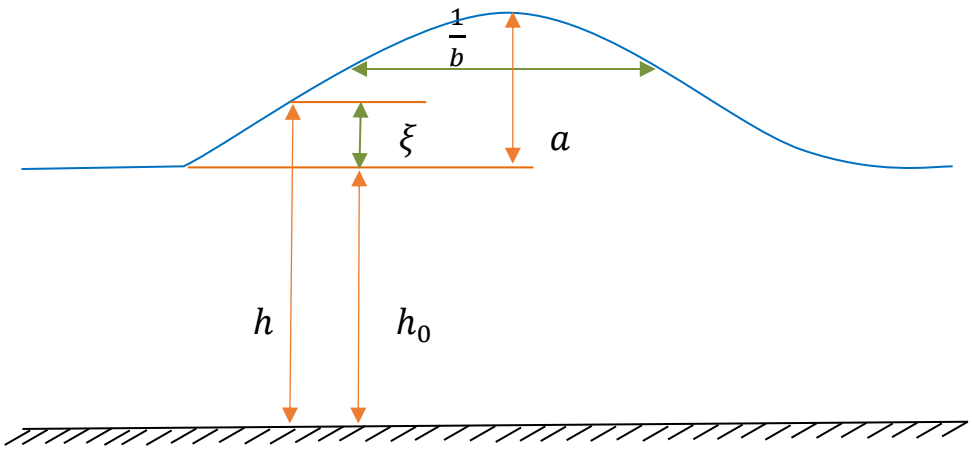

Figure 6.1: Key variables that define the solitary wave flow geometry

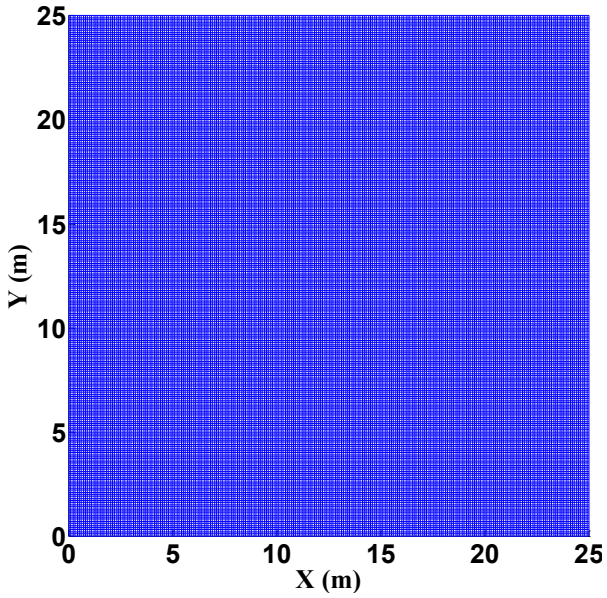

Figure 6.2: Solitary wave problem: computational mesh plotted in physical domain

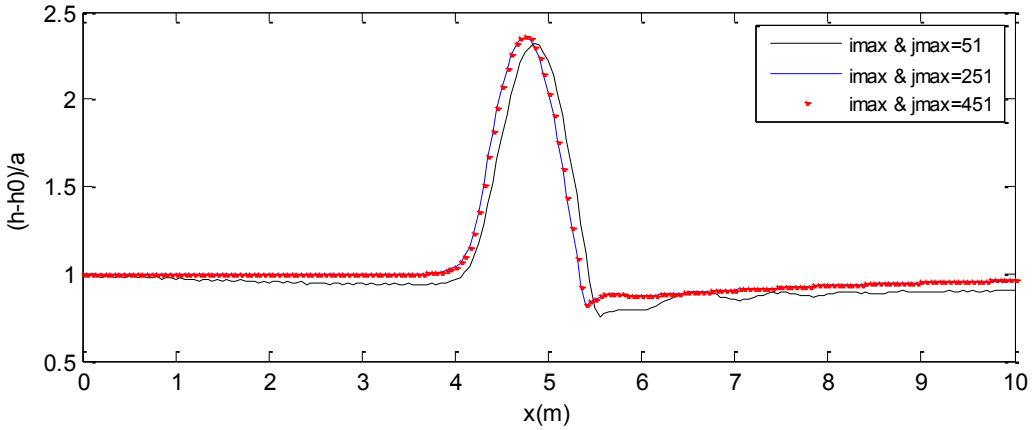

Figure 6.3: Effect of grid convergence on solitary wave simulation

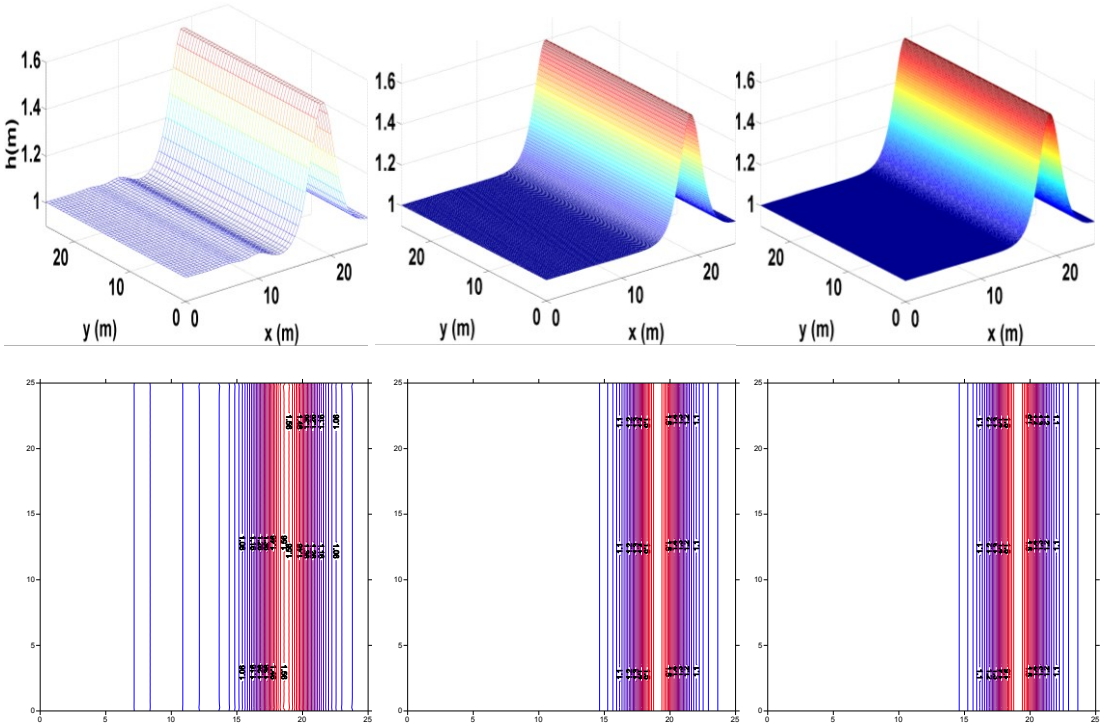

Figure 6.4: Grid convergence results for solitary wave moving west to east at t = 3 s: (a) i_{max} = j_{max} = 51; (b) i_{max} = j_{max} = 251; (c) i_{max} = j_{max} = 451.

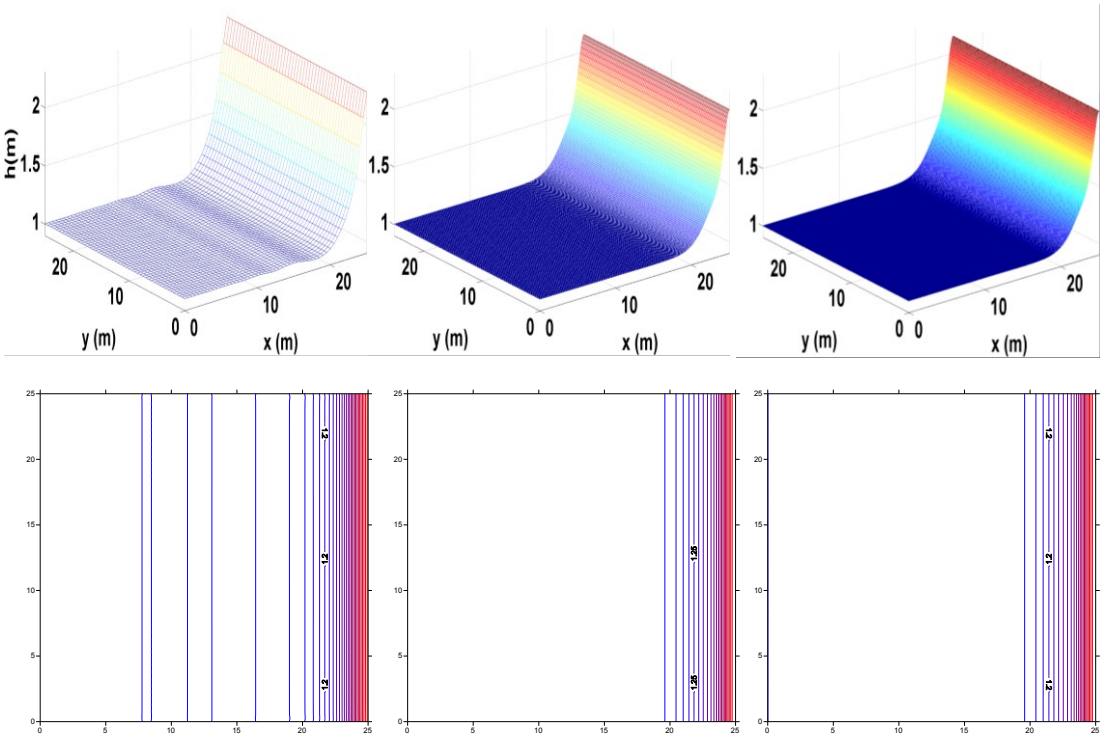

Figure 6.5: Grid convergence results for solitary wave moving west to east at t = 5 s: (a) i_{max} = j_{max} = 51; (b) i_{max} = j_{max} = 251; (c) i_{max} = j_{max} = 451.

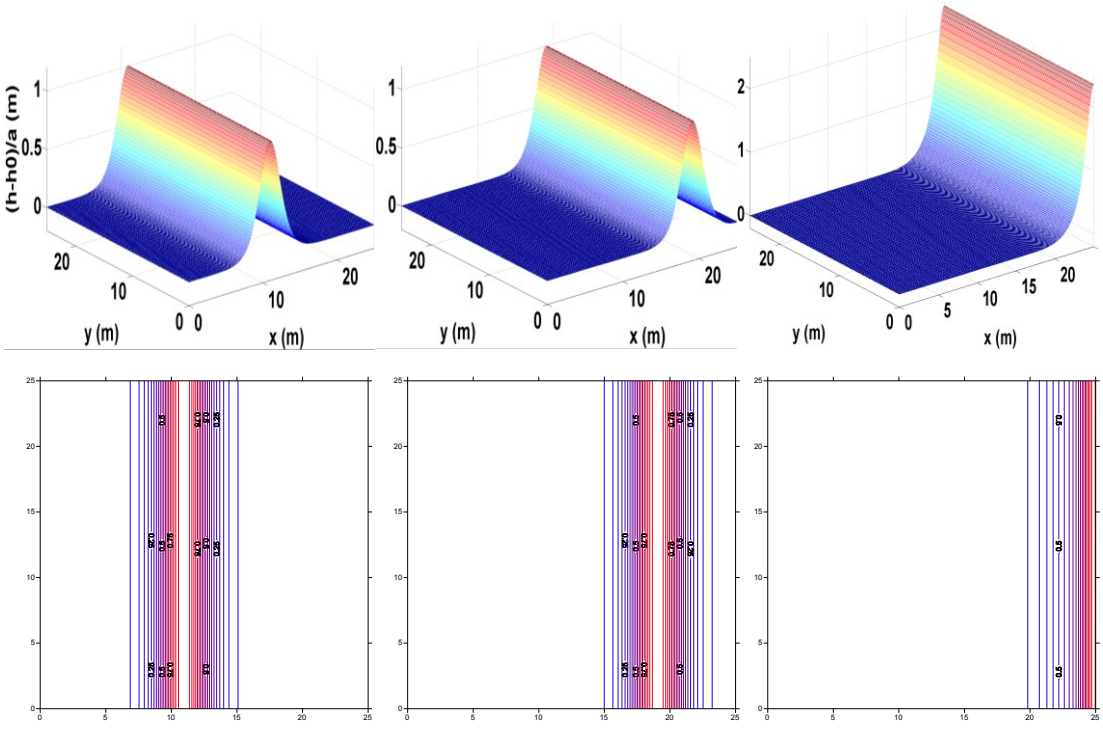

(*a*) $t = 1$ s (*b*) $t = 3$ s (*c*) $t = 5$ s

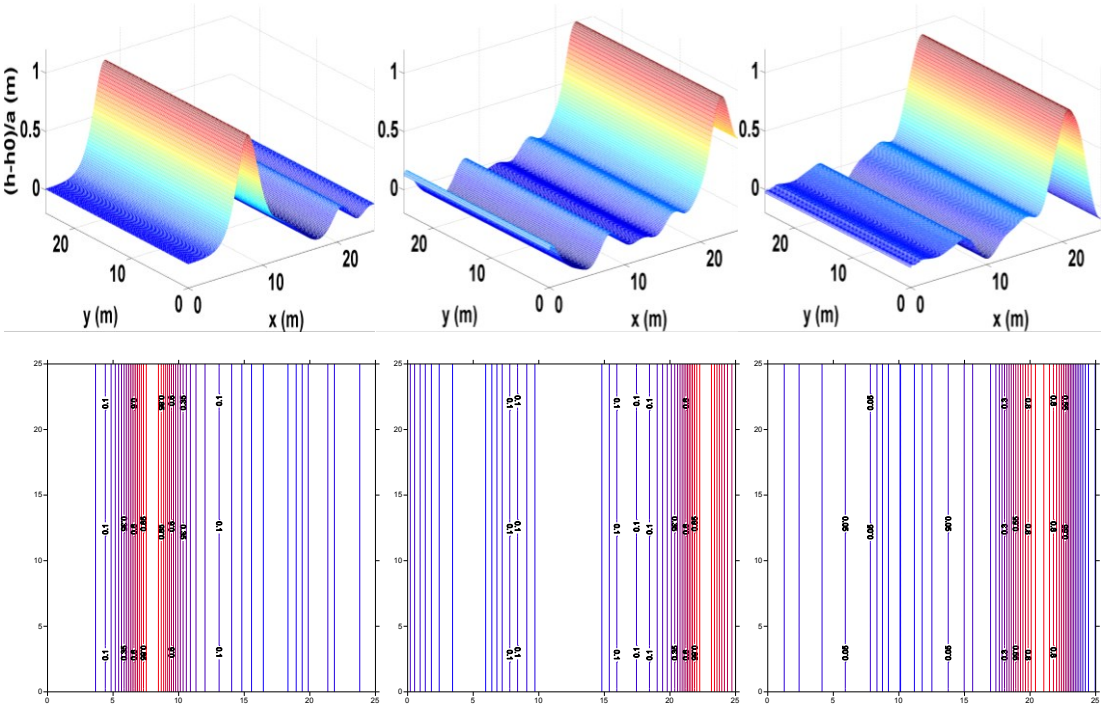

(*d*) $t = 9$ s (*e*) $t = 17$ s (*f*) $t = 19$ s

Figure 6.6: 3D plots and contour maps of solitary wave moving west to east at $t = 1$, 3, 5, 9, 17, and 19 s.

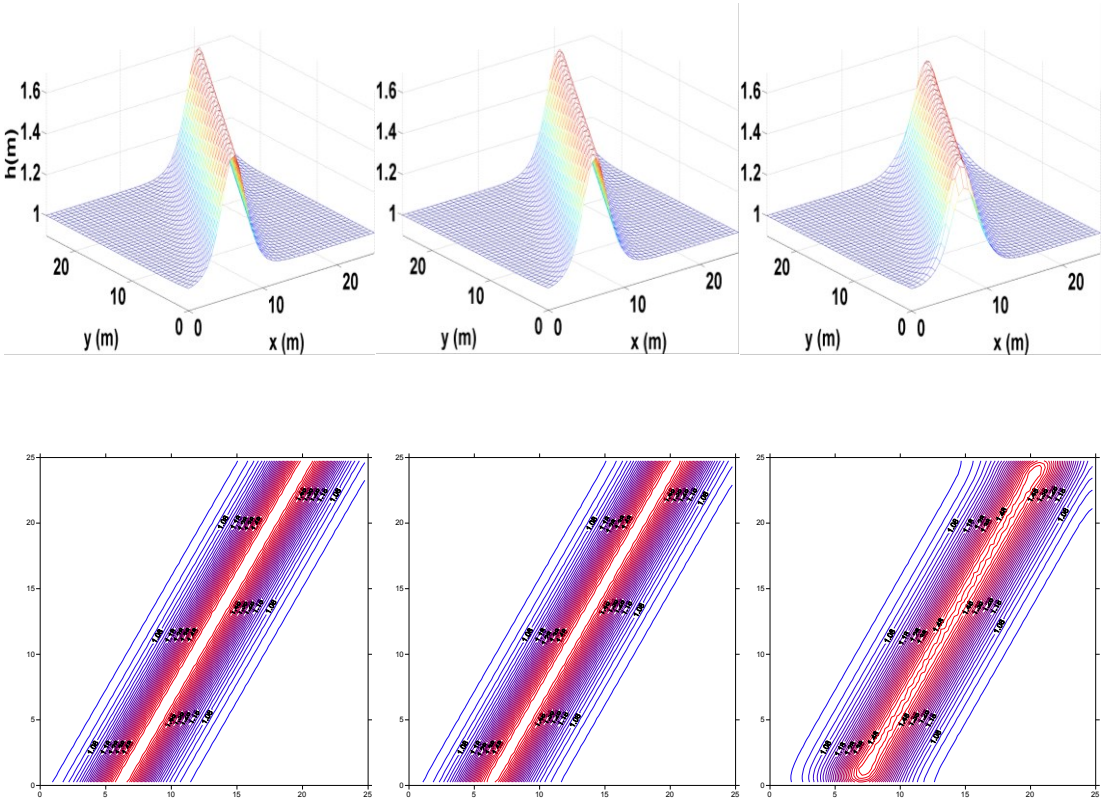

Figure 6.7: 3D plots and contour maps of oblique solitary wave profile ($\theta = 30^{o}$) at t = 0, 0.1 and 0.3 s.

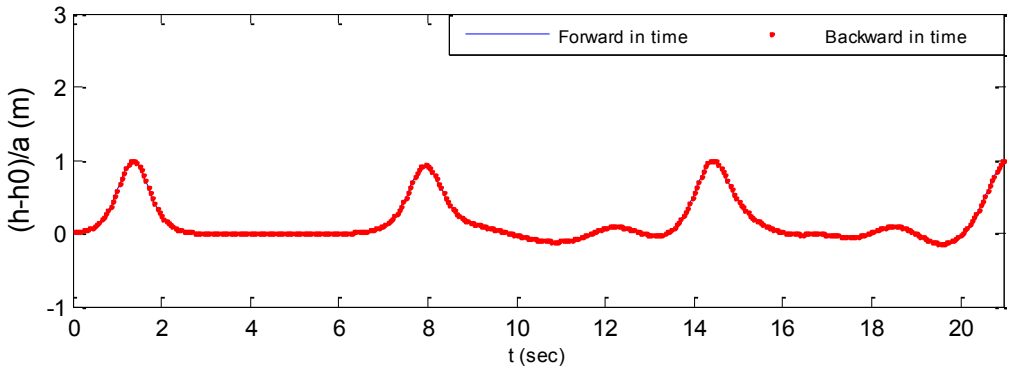

Figure 6.8: Free surface elevation time history indicating the reversibility of the solitary wave simulation.

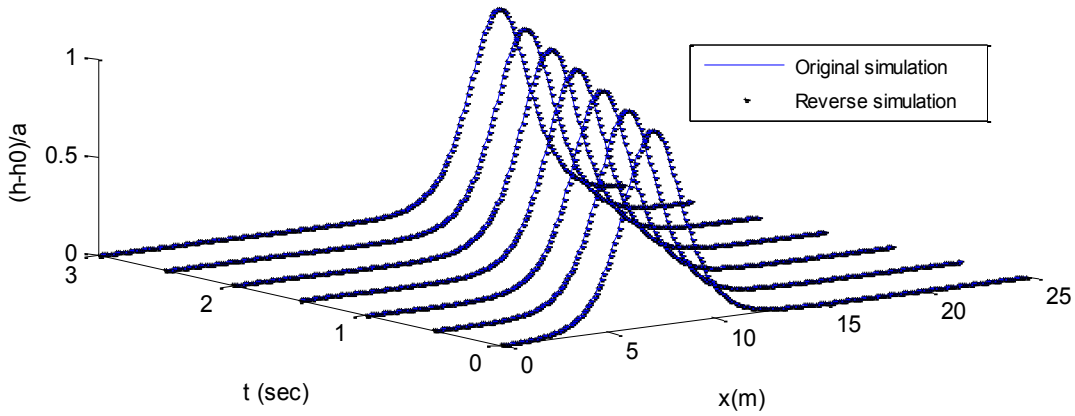

Figure 6.9: Comparison between original and reverse simulations of solitary at different times (t = 0, 0.5, 1, 1.5, 2, 2.5; and 3 s).

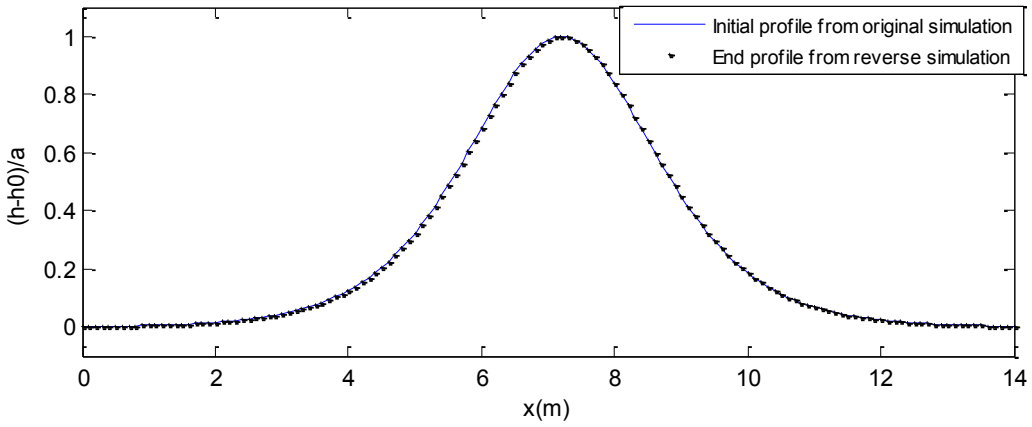

Figure 6.10: Reversibility comparison between original profile and final profile of reverse simulation.

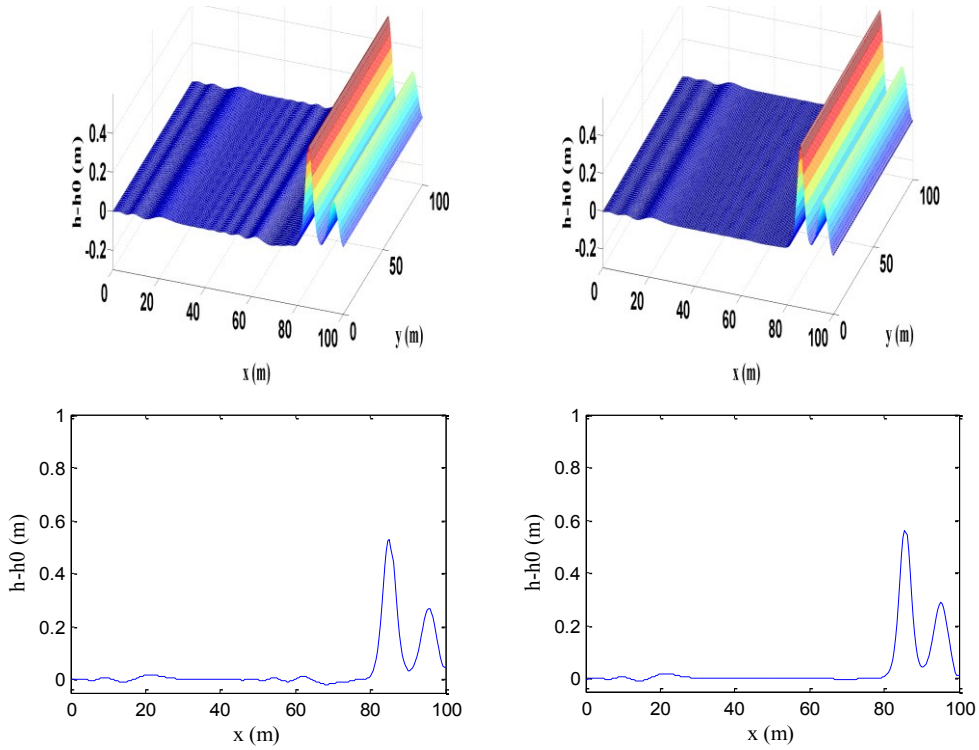

Figure 6.11: Solitary wave propagation: (a) second-order predicted free surface elevation profile at t = 15.5 s; and (b) fourth-order predicted free surface elevation profile at t = 15.5 s.

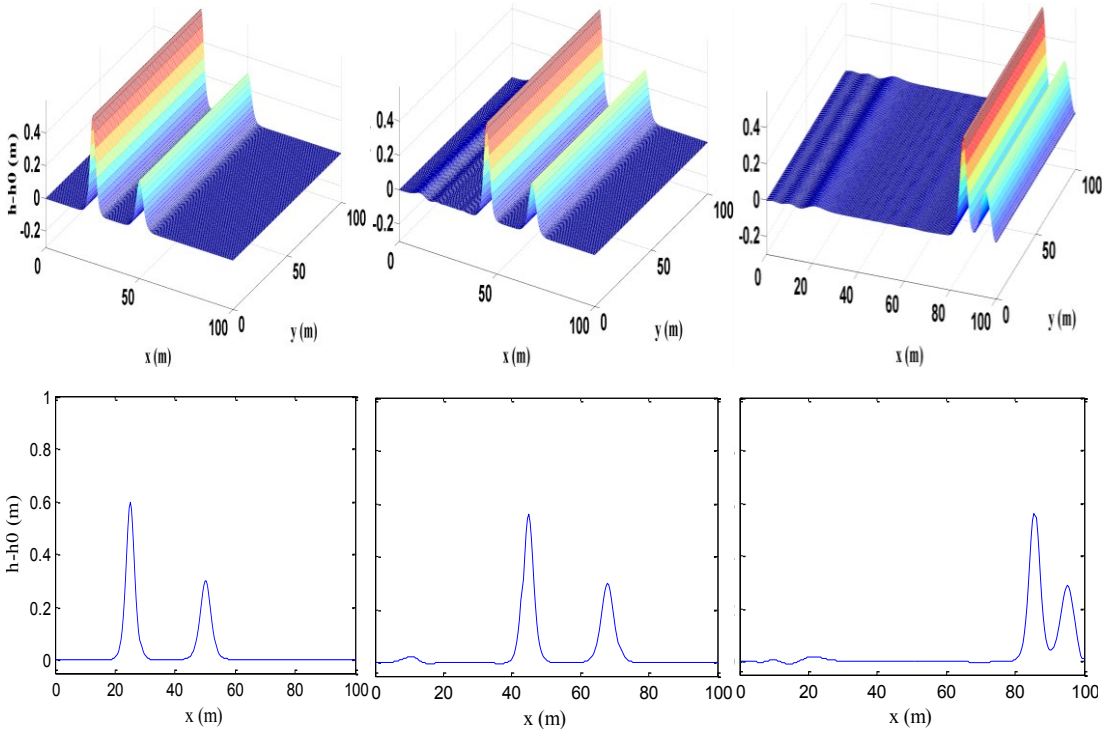

Figure 6.12: Solitary wave propagation: predicted free surface elevation profiles at (a) t =0 s, (b) t = 5 s; and (c) t = 15.5 s using fourth-order solver for $i_{max} = j_{max}$ = 251, Δt = 0.05 s.

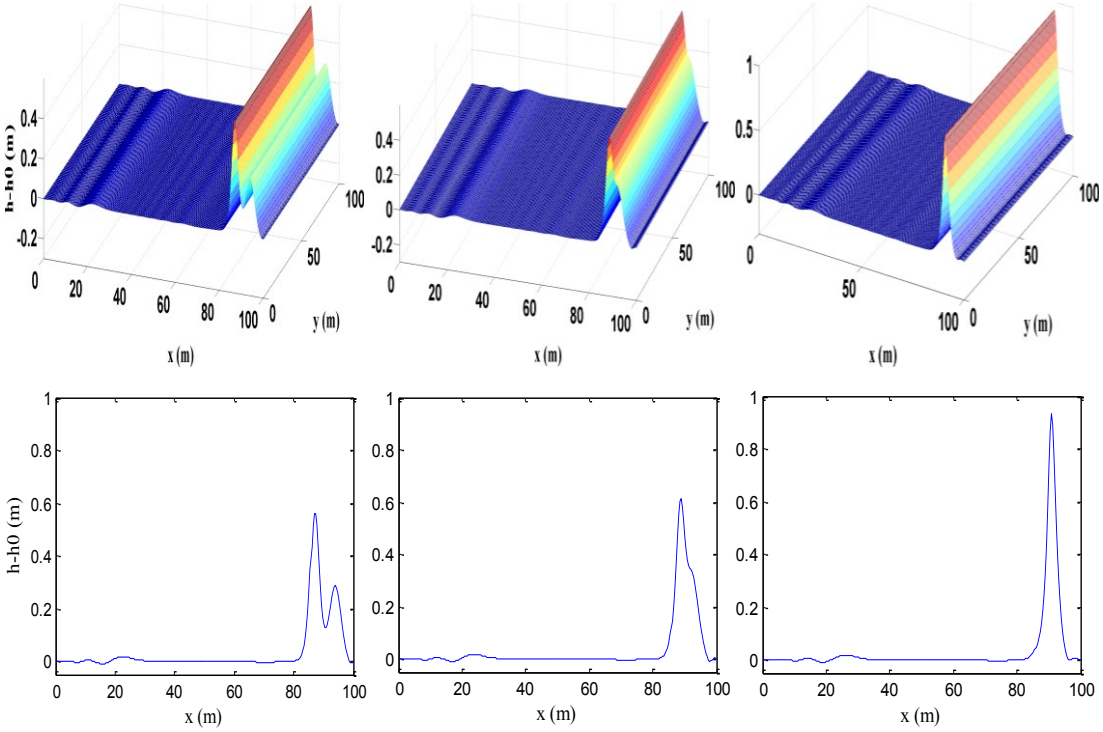

Figure 6.13: Solitary wave propagation: predicted free surface elevation profiles at (a) t = 15.85 s, (b) t=16.25 s; and (c) t=17 s using fourth-order solver for $i_{max} = j_{max} = 251$, Δt=0.05s.

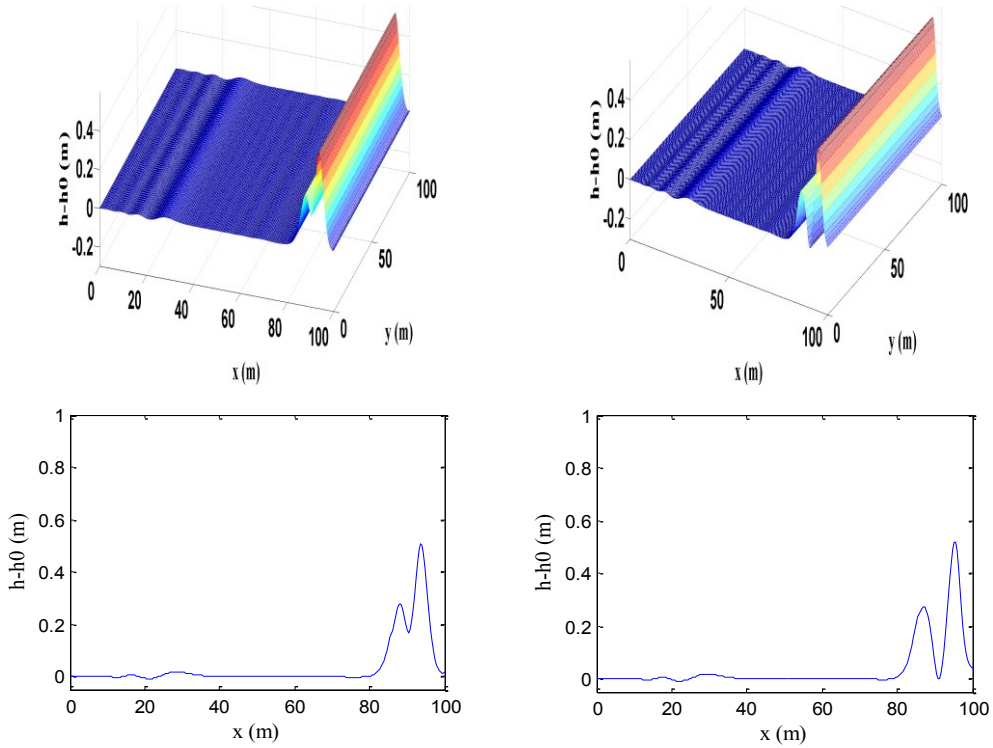

Figure 6.14: Solitary wave propagation: predicted free surface elevation profiles at (a) t = 17.75 s and (b) t = 18.1 s using fourth-order solver for $i_{max} = j_{max} = 251$, Δt = 0.05 s.

Chapter 7

Conclusions and Recommendations

7.1 Introduction

Free surface flows in channels and containers are almost ubiquitous, and include tides in estuaries, flood wave propagation in rivers, seismic-induced sloshing in tanks, etc. Such flows are characterised by free surface waves and currents, the former acting as the liquid's gravitational response to a disturbance. This study has examined the use of Green-Naghdi (GN) Level I equations to represent solitary wave propagation in a channel and free surface sloshing in a basin, both of which were selected as benchmark tests for verification purposes. The thesis has presented a detailed derivation of the 1D and 2D level I GN equations, their discretisation using second- and fourth-order finite differences in space and a fourth-order Runge-Kutta scheme in time. The numerical model utilised a tridiagonal matrix solver and a pentadiagonal matrix solver, the former for the second-order space discretisation, the latter for fourth order. A detailed explanation was given of the numerical procedure, and the boundary conditions necessary to close the model. The results from the two test cases (sloshing in a tank and propagation of a solitary wave in a flat-bottomed channel) demonstrated the model was working satisfactorily by comparison against analytical solutions obtained from linearised shallow water theory. Discrepancies between the GN predictions and the linear analytical solutions were primarily due to the effect of wave nonlinearities arising from the wave amplitude itself and wave-wave interactions. After convergence and stability tests were carried out a parameter study was undertaken to examine the nonlinear behaviour of an initial Gaussian free surface hump in a closed basin. In addition to verification, the GN model was used to test reversibility by simulating the motion of the Gaussian hump first forward, then backward in time, and checking how well the initial conditions were recovered.

In order to understand better the hydrodynamic behaviour of the wavelets comprising the Gaussian hump, both initial hump and hole tests were undertaken (the latter involving a trough instead of a crest). By addition and subtraction of the initial crest and trough signals as they evolved, time series of even harmonics and odd harmonics were extracted. Fast Fourier transform (FFT) analyses were performed to highlight the frequency content of the results. The behaviour of an initial Gaussian hump released in a basin of non-uniform bed topography was also studied, and the results compared against those for sloshing over a flat-bottomed square basin. The second major benchmark test concerned the propagation of a solitary wave in a closed channel. After suitable convergence and stability tests were undertaken, solitary wave propagation was simulated in the positive x-direction, in the y-direction and at an angle $\theta = 30^{o}$ to the x-axis. The model was found to be reversible, again via forward, then backward time-stepping. The interaction between a single solitary wave and a solid wall, and two solitary waves with a wall (and each other) were also studied.

7.2 Conclusions

- A mathematical GN Level I model has been formulated based on the 3-D continuity and momentum equations and kinematic boundary condition applicable to the free surface flow of inviscid, incompressible liquid over a fixed bed. For the first time, to the author's knowledge, the GN Level I mass and momentum equations have been derived in two horizontal dimensions for mild-sloped beds. These equations are summarised by Eqn. (2.18) for mass conservation and Eqns. (2.64) and (2.68) for momentum conservation. The 2D GN level I equations for a horizontal bed were also obtained as a reduced version of the non-uniform bed equations, and are summarised as Eqns. (2.18), (2.66) and (2.70).

- The 1D and 2D GN Level I equations were discretised using second-order and fourth-order schemes, and time integration undertaken using a Runge-Kutta fourth-order scheme.

- Verification tests undertaken for the 1D level I GN equations comprised free surface sloshing of an initial sinusoidal wave in a tank and the propagation of solitary wave over a flat-bed. For sloshing in a tank, excellent agreement was obtained between the model predictions using both second-order and fourth-order schemes and the standard first-order analytical solution for relatively small initial wave amplitude ($a \leq 0.005$ m). At larger amplitudes of initial disturbance, the free surface elevation time history developed saw-tooth profiles. A shock-capturing scheme would be needed to overcome this problem, and is recommended for future work. By means of the FFT analysis, it was found that nonlinear behaviour was particularly pronounced in the even harmonic slosh components. In the second verification test, it was found that both second- and fourth-order solvers produced accurate simulations of soliton propagation when the results were compared against a standard solution.

- The 2D GN numerical model was verified for the case of nonlinear free surface sloshing motions arising from an initial Gaussian hump in a closed basin. Numerical simulations of initial Gaussian hump were compared with Fourier series semi-analytical solutions of the linearised shallow water equations. Excellent agreement was achieved between the numerical simulation and the analytical solution of the overall free surface patterns in the basin during the first four seconds after the initial release of the hump, after which discrepancies became discernible, in part due to nonlinear wave interaction effects which were not described by the analytical theory. Satisfactory agreement between the numerical and semi-analytical solutions of free surface elevation was achieved for about 10 s at the centre of the basin. A reversibility check of the developed numerical code indicated that the reversed hump returned almost to exactly the same shape as the original Gaussian hump, although as the amount of time spent travelling forward and backward lengthened, spurious error tended to accumulate in the vicinity of the basin corners. There was some loss of amplitude at the centre of the basin when the hump was reversed. The even and odd harmonics of the initial Gaussian profile were separated from initial crest and trough simulations, with the profiles

treated as orthogonal functions. For a small-amplitude initial hump or trough (*amp* = $h_0/10$ = 0.045 m) the negligible deviations from zero in the free surface motions of even harmonics indicated that nonlinear effects were quite small. In the equivalent even harmonic results obtained for a larger-amplitude initial disturbance (*amp* = $h_0/2$ = 0.225 m), it was possible to see evidence of the nonlinearity. To understand better the resonant free surface motions driven by an initial Gaussian disturbance in the square basin, an FFT of the free surface elevation component time series was carried out. Parameter tests for sloshing of an initial Gaussian hump were carried out in a basin with non-uniform bathymetry with bed humps at the centre and corner of the basin. The deformation in the water free surface Gaussian shapes became more obvious at the centre exactly where the bed hump was located. The corner bed hump did not have such a significant effect on the free surface simulations.

- Finally, the numerical model was used to simulate solitary wave propagation in a closed flat-bottomed channel. Comparison between the numerical predictions and results from perturbation analysis (Taylor, 2015) confirmed that nonlinear interaction between a solitary wave and a solid wall was correctly modelled. When the solitary wave hit a wall, the numerically predicted run up reached 2.355 m which was 0.355 m more than the predicted linear analytical solution. By including the second order perturbation term (Taylor 2015), the approximate analytical solution for the reflected solitary wave elevation was 2.3454 m, a quite similar value to that predicted by the GN model. A reversibility check revealed that the original and reverse profiles of solitary wave simulations overlay each other. In the final simulations for 2D level I GN developed model, the interaction between two solitary waves was investigated through applying second- and fourth-order numerical schemes. Both numerical schemes presented accurate simulations for the interaction between the two solitary waves with a wall and also with each other.

7.3 Recommendations

The present 2D GN Level I model permits realistic simulations of the free surface hydrodynamic motions of water in tanks and channels, and can incorporate the effect of uneven bed topography. The model represents nonlinear hydrodynamic behaviour, but not wave breaking – for which a hybrid model with shock-capturing would be necessary. On the whole, the results obtained using second-order spatial discretisation were almost as accurate as those using fourth-order. The GN equations have a role as intermediate equations between shallow water equations (which are hydrostatic and non-dispersive) and the more complicated Boussinesq-type equations (which are somewhat dispersive depending on the version utilised). The main recommendations arising from the research conducted in this thesis are as follows:

- Substantial future research effort should be directed towards assessing the applicability of high-level GN equations. At the time of writing, the 1D GN equations are often used for deep water applications where a higher level of GN equations would be more appropriate. In future, it would be worth investigating 2D GN level II, III, and higher equations, noting the greatly increased difficulty that would be encountered in their numerical solution (owing to the presence of high-order cross-derivative terms in time and space).

- In cases where the free surface waves break, such as in shallow coastal waters, the present GN Level I solver could be switched to a Godunov-type shallow water equation solver with a ramping function used to smooth the behaviour between both sets of equations. This would be similar to work undertaken by Orszaghova et al. (2012, 2014) who developed a hybrid Boussinesq-shallow water equation solver. By also including a wetting and drying algorithm, the resultant hybrid GN model could be applied to flow inundation.

- To apply the GN Level I solver to typical environmental flow situations, further attention should be paid to boundary-fitting, perhaps either by means of curvilinear systems mappings (as used in curvilinear shallow water simulations

of flows in rivers and lakes) or by cut-cell techniques with hierarchical or unstructured grids.

- The GN methodology could be extended to deal with flows over erodible beds, and sediment entrainment, transport, and deposition. Similarly, the model could be extended to incorporate the transport of materials, including water quality parameters.

- The present thesis restricted applications to sloshing in tanks and solitary wave propagation in idealised domains. It is recommended that the GN level I solver be applied to more extensive tests including the propagation of regular wave, irregular waves and NewWave groups in the sea and at the coast (where seawall overtopping on beach runup are very important). It would be worth investigating the neting of a 3D CFD code or a smoothed particle hydrodynamics solver within the GN solver. The model could potentially be useful in simulating the behaviour of freak waves, ship waves, tsunami waves and the interaction of such waves with marine structures, ships, oil platforms and renewable energy devices.

References

Bampi, F., Morro, A. (1978). Gravity Waves in Water of Variable Depth. *IL NUOVO CIMENTO*, *1 C*, 377 – 388.

Bonneton, P., Chazel, F., Lannes, D., Marche, F., Tissier, M. (2011). A splitting approach for the fully nonlinear and weakly dispersive Green–Naghdi model. *Journal of Computational Physics*, *230*, 1479 – 1498.

Bonneton, P., Barthelemy, E., Chazel, F., Cienfuegos, R., Lannes, D., Marche, F., Tissier M. (2011). Recent advances in Serre–Green Naghdi modelling for wave transformation, breaking and runup processes. *European Journal of Mechanics B/Fluids*, *30*, 589 – 597.

Chazel, F., Lannes, D., Marche, F. (2011). Numerical Simulation of Strongly Nonlinear and Dispersive Waves Using a Green–Naghdi Model. *Journal of Scientific Computing*, *48*, 105 – 116.

Chow, V. T. (1959). Open-channel hydraulics. McGRAW-HILL Book Company.

Drazin, P. G, Johnson, R. S. (1989). Solitons: an introduction. Cambridge University Press.

Dean, R. G., and Dalrymple, R. A. (2004). Chapter 10: Modeling of Beaches and Shorelines. Coastal Processes with Engineering Applications (pp. 303 – 306). Cambridge University Press.

Demirbilek, Z., Webster, W.C. (1992). Application of the Green-Naghdi Theory of Fluid Sheets to Shallow-Water Wave Problems, Report 1. Model Development. *US Army Engineers Waterways Experiment Station, Coastal Engineering Research Center. Technical Report CERC* – 92 – 11.

Green, A.E., Laws, N., Naghdi, P.M. (1974). On the theory of water waves. *Proceedings of the Royal Society of London. Series A, Mathematical and Physical Sciences*, *338*, 43 – 55.

Green, A.E., Naghdi, P.M. (1976). Directed Fluid Sheets. *Proceedings of the Royal Society of London. Series A, Mathematical and Physical Sciences*, *347*, 447 – 473.

Green, A.E., Naghdi, P.M. (1986). A Nonlinear Theory of Water Waves for Finite and Infinite Depths. *Philosophical Transactions of the Royal Society of London. Series A, Mathematical and Physical Sciences*, *320*, 37 – 70.

Green, A.E., Naghdi, P.M. (1987). Further Developments in a Nonlinear Theory of Water Waves for Finite and Infinite Depths. *Philosophical Transactions of the Royal Society of London. Series A, Mathematical and Physical Sciences*, *324*, 47 – 72.

Hayir, A. (2006). The near-field tsunami amplitudes caused by submarine landslides and slumps spreading in two orthogonal directions. *Ocean Engineering*, *33*, 654 – 664.

Haniffah, M. R. M. (2013). Wave Evolution on Gentle Slopes-Statistical Analysis and Green-Naghdi Modelling. Dphil thesis, *Department of Engineering Science*, *University of Oxford*.

Ibrahim, R. A. (2005). Liquid sloshing dynamics theory and applications. Cambridge University Press.

Kim, J. W., Ertekin, R. C. (2000). A numerical study of nonlinear wave interaction in regular and irregular seas: irrotational Green-Naghdi model. *Journal of Marine Structures*, *13*, 331–347.

Kim, J. W., Bai, K. J., Ertekin, R. C., Webster, W. C. (2001). A derivation of the Green-Naghdi equations for irrotational flows. *Journal of Engineering Mathematics*, *40*, 17 – 42.

Lamb, H. (1916). Chapter 8: Tidal Waves. Hydrodynamics (pp. 274 – 276). Cambridge University Press.

Le Métayer, O., Gavrilyuk, S., Hank, S. (2010). A numerical scheme for the Green-Naghdi model. *Journal of Computational Physics*, *229*, 2034 – 2045.

Miles, J. W. (1980). Solitary waves. *Annual Review of Fluid Mechanics*, *12*, 11 – 43.

Nadiga, B. T., Margolin, L. G., Smolarkiewicz, P. K. (1996). Different approximations of shallow fluid flow over an obstacle. *American Institute of Physics, Phys. Fluids*, *8*, 2066 – 2077.

Orszaghova, J. (2011). Solitary waves and wave groups at the shore. Dphil thesis, *Department of Engineering Science*, *University of Oxford*.

Orszaghova, J., Borthwick, A. G. L., Taylor, P. H. (2012). From the paddle to the beach – A Boussinesq shallow water numerical wave tank based on Madsen and Sørensen's equations. *Journal of Computational Physics*, *231*, 328 – 344.

Pearce, J.D., Esler, J.G. (2010). A pseudo-spectral algorithm and test cases for the numerical solution of the two-dimensional rotating Green–Naghdi shallow water equations. *Journal of Computational Physics*, *229*, 7594 – 7608.

Pozrikidis, C, (2009), MAE 107 - Computational Methods Summer Session II, University of California.

Press, W. H., Teukolsky, S. A., Vetterling, W. T., Flannery, B. P. (2007). Chapter 2: Solution of linear algebraic equations. Numerical recipes the art of scientific computing (pp. 56 – 57). Cambridge University Press.

Sarpkaya, T., Isaacson, M. (1981). *Mechanics of Wave Forces on Offshore Structures*, Van Nostrand Reinhold, New York.

Shields, J. J., Webster, W. C. (1988). On direct methods in water-wave theory. *Journal of Fluid Mechanics, 197*, 171 – 199.

Stewart, R. H. (2008). Chapter 16: Ocean Waves. Introduction to Physical Oceanography (pp. 105, 273 and 280). Department of Oceanography Texas A & M University.

Toro, E. F. (2001). *Shock-Capturing Methods for Free-Surface Shallow Flows*. John Wiley and Sons, Ltd.

Webster, W. C., Shields, J. J. (1991). Applications of high-level Green-Naghdi theory to fluid flow problems. *IUTAM Symposium*. *On the Dynamics of Marine Vehicles and Structures in Waves*. *Brunel University, London. (Ed. W. G. Price, P. Temarel & A. J. Keane) Elsevier Science Publishers B.V.*

Webster, W. C., Duan, W. Y., Zhao, B. B. (2011).Green-Naghdi Theory, Part A: Green-Naghdi (GN) Equations for Shallow Water Waves. Journal of Marine Science and Application, *10*, 253 – 258.

Wei, G., Kirby, J.T. (1995). Time-dependent numerical code for extended Boussinesq equations. *Journal of waterway, port, coastal, and engineering*, *121*, 251 – 261.

Wu, J., Chen, Bo. (2003). Unsteady ship waves in shallow water of varying depth based on Green–Naghdi equation. *Ocean Engineering*, *30*, 1899 – 1913.

Xia, D., Ertekin, R.C., Kim, J.W. (2008). Fluid–structure interaction between a two-dimensional mat-type VLFS and solitary waves by the Green–Naghdi theory. *Journal of Fluids and Structures*, *24*, 527 – 540.

Xu, Qi, Pawlowski, J.S., Baddour, R.E. (1997). Development of Green-Naghdi models with a wave-absorbing beach for nonlinear, irregular wave propagation. *Journal of Marine Science and Technology*, *2*, 21 – 34.

Yao, Y. (2007). Boussinesq-type Modelling of Gently Shoaling Extreme Ocean Waves. Dphil thesis, *Department of Engineering Science*, *University of Oxford*.

Zhang, Y., Kennedy, A. B., Panda, N., Dawson, C., Westerink, J. J. (2013) Boussinesq–Green–Naghdi rotational water wave theory. *Coastal Engineering*, *73*, 13 – 27.

Zhao, B. B., Duan, W. Y. (2010). Fully Nonlinear Shallow Water Waves Simulation Using Green-Naghdi Theory. *Journal of Marine Science and Application*, *9*, 1 – 7.

Zhao, B. B., Duan, W. Y., Webster, W. C. (2011). Tsunami simulation with Green–Naghdi theory. *Ocean Engineering*, *38*, 389 – 396.